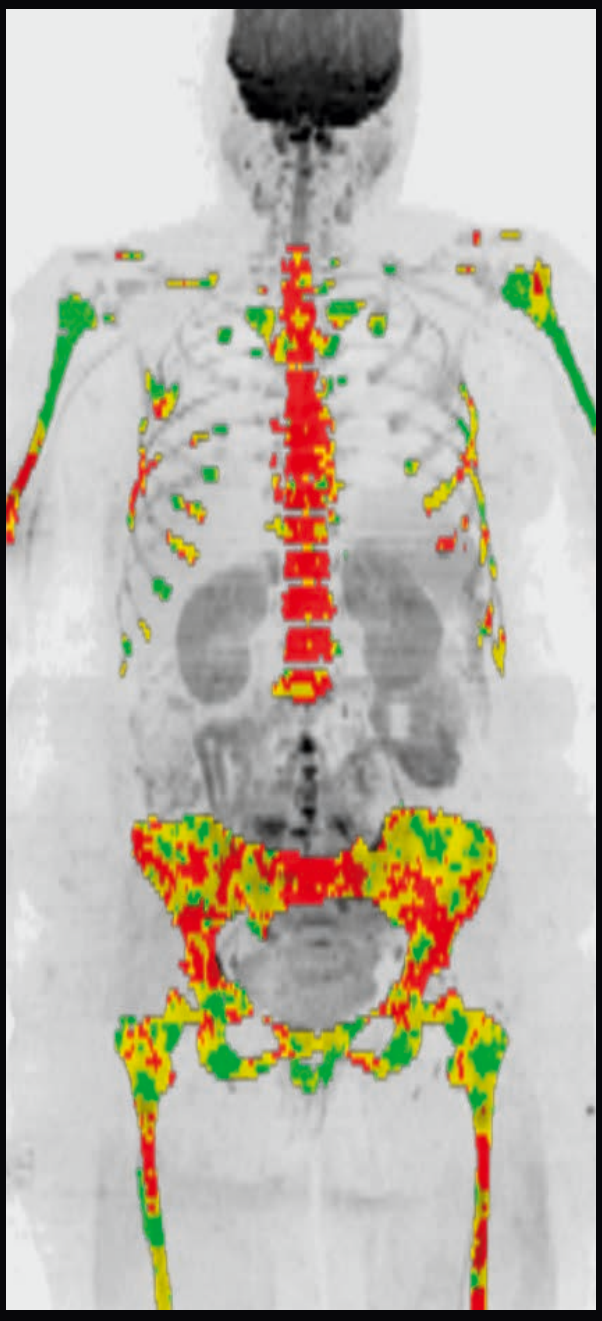

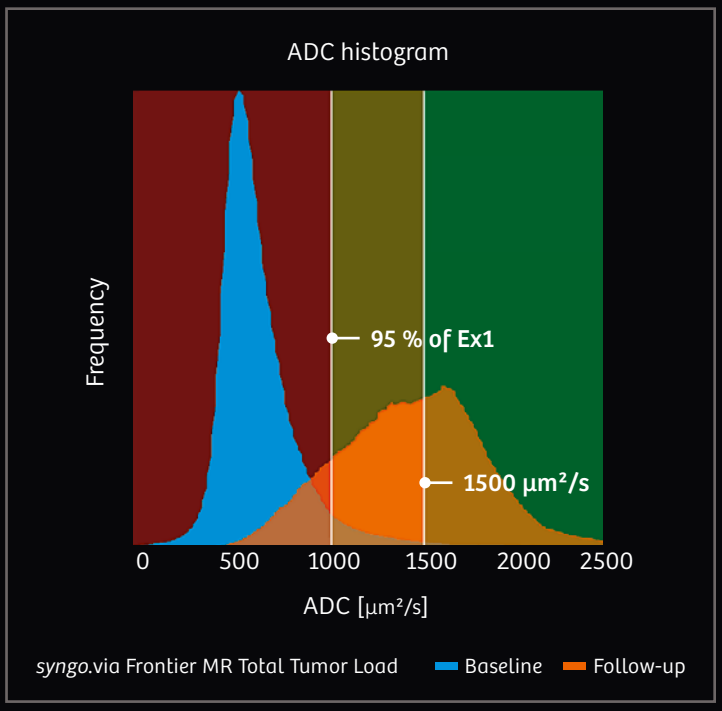

MAGNETOM Flash

Issue Number 68, 2/2017
ISMRM Edition

siemens.com/magnetom-world

SIEMENS Healthineers

Professor Konstantin Nikolaou

Konstantin Nikolaou is Chairman of the Department of Diagnostic and Interventional Radiology in the Department of Radiology at the Eberhard-Karl-University in Tübingen, Germany. Professor Nikolaou received his MD from the Ludwig-Maximilians-University of Munich, Germany, in the year 2000, where he also became an Assistant Professor at the Department of Clinical Radiology, University Hospitals Munich, after finalizing his PhD-thesis on the topic of modern cardiovascular computed tomography techniques in 2007.

After working as a section chief of CT/PET-CT and MRI at the same department, he became Vice Chair of the Department of Clinical Radiology at the Ludwig-Maximilian-University in Munich in April 2007.

Precision Medicine and Adaptive Technologies in Medical Imaging

Dear colleagues, dear readers,

I feel honored and excited to be invited to write an editorial for MAGNETOM Flash on the topic of 'precision medicine' – a term that might seem overused these days. Whilst this term is not new – medicine always wants to deliver the right treatment to the right patient at the right time – our understanding of correlations between genome, habits, and diseases is evolving rapidly and exponentially. It feels like there is a need to re-imagine and re-organize health services.

All fields of medicine are adapting to an increasing and increasingly complex demand of phenotyping and genotyping our patients, identifying precise cohorts, and optimizing health care. To us as radiologists, it may seem obvious, that radiology should certainly play a key role in phenotyping these sub-populations by means of dedicated imaging strategies [1]. This should be complementary, and not compete with other ways of phenotyping, including, for example, advanced laboratory tests, histo-pathology, and immuno-pathology. To integrate our radiological imaging data and reports in a phenotyping system that categorizes patients into well-defined prognostic and therapeutic categories, we will have to learn and adapt to a rising demand of 'imaging biomarkers', 'reproducible parameters' and 'standardized' as well as 'structured' reporting.

I am sure our readers are optimistic as I am that we will be able to successfully master these challenges. However, at the same time, we are facing new opportunities and threats, in terms of increasing economic pressure and increasing workload, 'value-based' healthcare, introducing artificial intelligence in clinical routine, and commoditization of imaging procedures and radiological reports [2, 3]. We need clear and concerted strategies to handle these challenges and these include,

A) accepting and taking on a stronger role of radiologists, as clinical partners and information specialists,

B) setting new standards in quality and workflows, and

C) finding answers to an increasing demand of personalization and parametrization in our daily routine.

In this volume of MAGNETOM Flash, exciting views and reports on advancements in MR technologies, enabling us to improve quality, workflows, flexibility, and standardization, clearly reflect these trends and endeavors – in a way that I find very convincing.

1. A new role for radiologists?

Radiologists will have to adapt. And we will have to adapt quickly, to both an increasing economic pressure and to the 'fourth industrial revolution', i.e., a rapidly improving process automatization on the basis of big data and artificial intelligence (AI) [4, 5]. The first challenge will be to adapt and re-invent our ever more complex imaging procedures and skills in the era of 'value-based healthcare'. Since 'value' is defined as health or patient outcomes, or

He also is president of the European Society of Molecular and Functional Imaging in Radiology (ESMOFIR) and treasurer for the European Society of Cardiac Imaging (ESCR), Member of the Research Committee of the European Society of Radiology (ESR) and Honorary Member of the Greek Society of Radiology.

Professor Nikolaou joined the Eberhard-Karl-University Tübingen in April 2014 as Chairman of the Department of Diagnostic and Interventional Radiology. His main fields of interest are multimodality and multi-parametric imaging modalities in oncology as well as non-invasive imaging of cardiovascular diseases.

Tübingen, Germany

costs, we should therefore be measured on the results and quality of our care and not on the volumes of service delivered. However, if we agree to enter this circle of optimizing our workflows and outcome-centered care, will we be degraded to delivering standardized services and reports within a (short) given time, i.e., will medical imaging become a commodity? The strength of radiology is not only in the delivery of (automated) results from using sophisticated technologies, but even more by providing an optimized diagnostic process and data integration, provided by dedicated, highly skilled, specialized and communicating colleagues in our field, i.e., radiologists and technicians.

Radiology's value chain has to be high-quality, patient-centered, and results-oriented at the same time. This will enable us to develop from volume-based imaging to value-based imaging, demonstrating the added value of imaging in each phase of patient care and transforming imaging results into measurable metrics (e.g., quantitative imaging results, or cost effectiveness). The primary objective is to maintain and improve our visibility and demonstrating our capabilities as radiologists, imaging experts and highly trained specialists to our clinical partners and patients in daily practice, in our conferences, tumor boards, telephone calls, patient interactions, and interven-tional procedures. Optimizing our workflows and constant quality-control of our daily work (scheduling, protocols, procedures, reporting, distribution, and communication) is the foundation, basis, and pre-requisite for this, and should be self-evident, but how our report affects therapeutic decisions will directly influence patient outcome and costs of healthcare.

Will this process include an increasing automatization of our reports, at least in parts? Maybe yes. Is this detrimental or dangerous for our field? No, not, if we lead the way and use these new tools to our and our patients' advantage. Even the best trained colleague will not be able to stay perfectly up-to-date with all medical advancements. At the same time, age distribution in our western societies is changing drastically and imaging volumes are steadily increasing and will continue to do so. Thus, should we not embrace help from technology, rather than to fear it?

There are a number of ways how we could profit from AI. Besides the problem of data, image and information overflow, we will need AI for rare diseases, complex syndromes, or for decision-support systems, to face the growing complexity of our multi-disciplinary, multi-modal, and multi-scale clinical work, combining information from imaging, -omics, lab test, clinical history, and physical exams. The risk is not in the automatization, even of routine reports on frequent imaging procedures such as chest X-rays, mammograms, or CT angiographies to exclude pulmonary embolism. The crucial question will be: Who is in the driver's seat, for technical implementation of these new AI techniques, and for the final decisions. We will have to take action and participate in these developments rather than ignore them, and – if we do it right – we will be able to improve our services and quality. In this process radiologists will transform to information specialists, implementing innovative forms of data handling and data presentation, and focusing on image-guided personalization of our own interventional measures and procedures.

2. New quality standards of radiological services

Multimodal, molecular, and functional imaging is becoming increasingly important in the context of personalized medicine. Our non-invasive diagnostic and imaging procedures are increasingly used to support and complement the data of advanced molecular diagnostics. Complementary qualitative and quantitative imaging parameters play a major role in the assessment of our patients' individual prognosis, the prediction of treatment success and in the monitoring of the therapy effectiveness and outcome, as shown in several articles in the *Oncological Imaging* chapter of this issue. With '-omics' technologies reaching maturity, these will be more and more implemented in clinical practice. Prospective and, where necessary, randomized clinical studies will be

"With recent advances in MR technology, we will optimize workflow and scanning efficiency, while providing consistent, high-quality personalized examination results at the same time, entering a new era in precision medicine."[2]

Professor Konstantin Nikolaou

needed to validate novel imaging biomarkers, imaging phenotypes, and imaging signatures.

High quality collections of biological samples procured in a standardized manner from age- and disease-stratified collections coupled to omics- and imaging-based phenotype information are required for the purpose of identification and validation of new, ideally quantitative, imaging biomarkers. By implementing these reproducible, quantitative, and standardized imaging biomarkers, multimodal image information can be integrated with patient-specific data for the development of individualized and predictive disease models.

To reach this goal, examination protocols and image acquisition must be standardized and homogenized as far as possible, in order to achieve a comparability and transferability of results from the various imaging modalities and between different sites. In addition, strategies for a systematic structuring of our reports and findings will have to be implemented, in order to replace the traditional, descriptive reporting of findings. Structured reporting will lead to the possibility of systematic data extraction from our reports, making them more accessible to statistical correlative analyses and bioinformatics. The term 'structured analysis and reporting' thus describes the establishment of objective, quantitative, extractable, and reproducible standards, e.g., in the context of tumor-specific diagnostic criteria and follow-up. This results in complete and comprehensive reports and considerably increases the objectivity and comparability between different investigators and sites and at the same time creates the possibility to link these image data with those from molecular diagnostics and to scientifically evaluate them or integrate them in complex disease models. The implementation of standardized vocabularies and reporting rules, supported by radiological lexicons and glossaries, established and disseminated by national and international radiological societies, will further harmonize the use or radiological terms and expressions and will enable optimized indexing of our reports.

3. Adaptive imaging technologies in the era of precision medicine

So how, we may ask, do recent MR developments anticipate these challenges and react to the growing demands described above? Due to high levels of exam complexity, patient properties, and user variability, MRI is still considered to be one of the most complex medical imaging modalities. Innovative MR scanner technology should therefore be able to automatically or semi-automatically address anatomical and physiological differences among individual patients, thus, a wider range of routine scanning procedures as well as complex protocols will be applicable to a larger extent of patients, even those formerly not eligible for MRI examinations, delivering more robust and more consistent results. Also, in times of economic pressure, MR scanning will have to be more cost-effective, by greater robustness and acquisition speed, reducing re-scans and increasing productivity.

To provide our patients with individualized and personalized diagnostic strategies and tailored therapies, we need robust, standardized, and reproducible acquisition techniques that are constantly delivering high and comparable quality. Only then we can compare results and link them with additional information, such as data from laboratory medicine or genetic analyses. Recent technologies will allow us to access new and growing clinical fields – for instance, enabling scans in patients with cardiac arrhythmias, excess weight, or other health problems that prevent them from actively supporting the scan.

An impressive array of various innovative MR technologies will be discussed in this present edition of MAGNETOM Flash. For example, dedicated acceleration techniques implementing Compressed Sensing (GRASP-VIBE[1]) enable dynamic, free-breathing liver examinations in one comprehensive scan by the push of button and for every patient, making breath-holds and complex timing of several dynamic contrast phases unnecessary. Optimized shimming technologies based on new hardware and transmit technologies, such as

CoilShim[1], one of the BioMatrix Tuners, homogenize the static magnetic field and significantly improve fat saturation and signal exploitation, e.g., in diffusion-weighted imaging (DWI) of body regions difficult to image, such as the neck. Slice-specific shimming (SliceAdjust[1]) is introduced with MAGNETOM Vida[1] as an effective method to reduce susceptibility effects in whole-body DWI at 3T. Automatization of whole-body MR examinations, e.g. the Whole-Body Dot Engine[1], will significantly reduce overall imaging time, increase patient comfort and will potentially change our use of MRI, e.g., for an increased implementation of whole-body tumor staging. In cardiac imaging, implementation of highly accelerated real-time sequences will preserve diagnostic image quality even in challenging scenarios, such as in arrhythmic patients. Finally, complete free-breathing cardiac examinations[1] will become possible.

The challenges in our field are increasing and may be greater than ever; our clinical and scientific working environment is getting more complex and more demanding. Only if we understand the challenges and take our chances, we will stay in the driver's seat, developing radiology to play an even more central role in clinical care. With recent advances in MR technology, we will optimize workflow and scanning efficiency, while providing consistent, high-quality personalized examination results at the same time, entering a new era in precision medicine.

Konstantin Nikolaou

References

1 Herold CJ, Lewin JS, Wibmer AG, Thrall JH, Krestin GP, Dixon AK, Schoenberg SO, Geckle RJ, Muellner A, Hricak H. Imaging in the Age of Precision Medicine: Summary of the Proceedings of the 10th Biannual Symposium of the International Society for Strategic Studies in Radiology. Radiology 2016;279(1):226-238.

2 Beam AL, Kohane IS. Translating Artificial Intelligence Into Clinical Care. JAMA 2016;316(22):2368-2369.

3 Jha S, Topol EJ. Adapting to Artificial Intelligence: Radiologists and Pathologists as Information Specialists. JAMA 2016;316(22):2353-2354.

4 Forsting M. Hot Topics: Will Machine Learning Change Medicine? J Nucl Med 2017.

5 Kohli M, Prevedello LM, Filice RW, Geis JR. Implementing Machine Learning in Radiology Practice and Research. AJR Am J Roentgenol 2017:1-7.

[1] 510(k) pending. The product is not commercially available. Future availability cannot be guaranteed.

[2] The statements by Siemens' customers presented here are based on results that were achieved in the customer's unique setting. Since there is no 'typical' hospital and many variables exist (e.g., hospital size, case mix, level of IT adoption), there can be no guarantee that other customers will achieve the same results.

Content

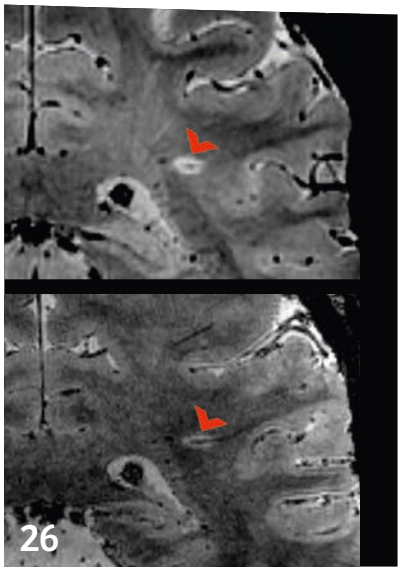

Rapid MR susceptibility imaging using 3D EPI

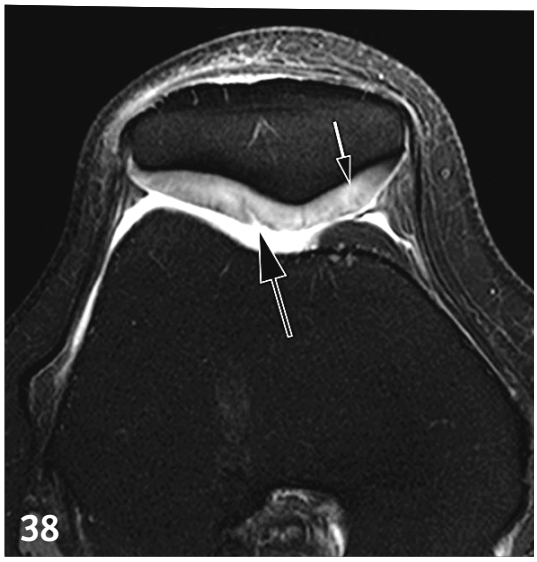

Initial experience with the MAGNETOM Terra 7T system

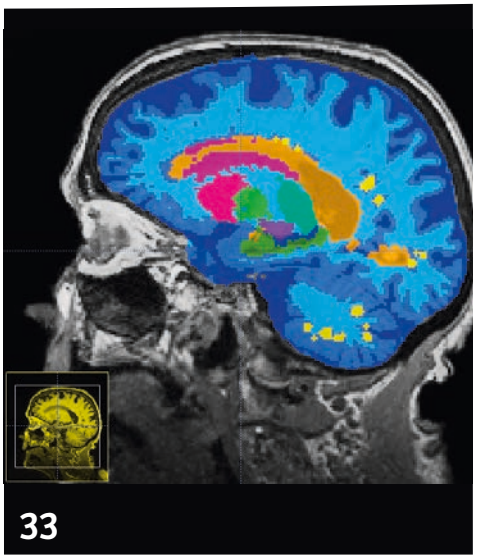

Assessing brain volumes

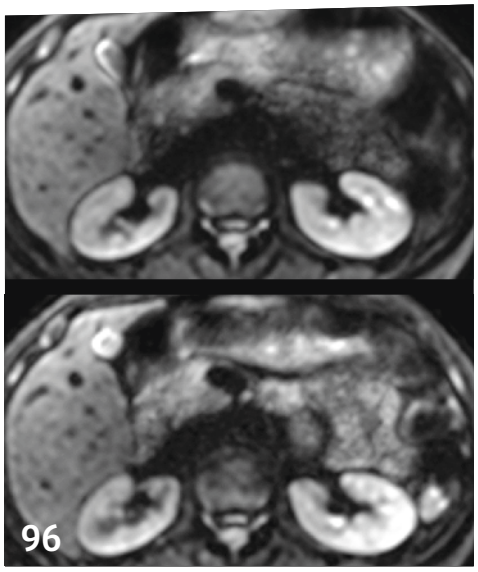

Simultaneous-Multislice in liver diffusion imaging

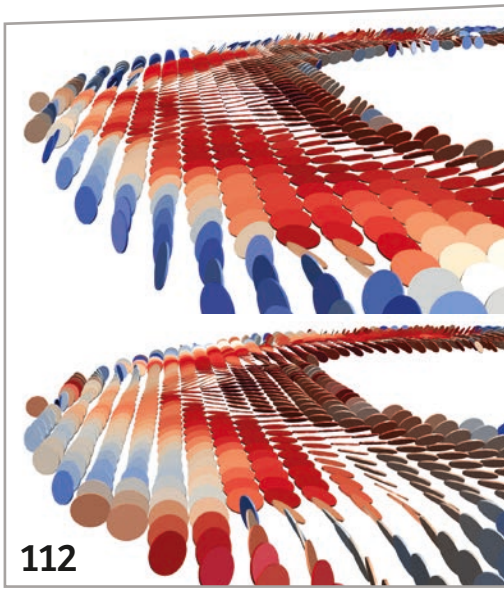

Microstructural dynamics underlying myocardial wall thickening

[1] 510(k) pending. The product is not commercially available. Future availability cannot be guaranteed.
[2] MR scanning has not been established as safe for imaging fetuses and infants less than two years of age. The responsible physician must evaluate the benefits of the MR examination compared to those of other imaging procedures.
[3] WIP, the product is currently under development and is not for sale in the US and in other countries. Its future availability cannot be ensured.
[4] *syngo*.via Frontier is for research only, not a medical device.

First Experiences with the World's First MAGNETOM Vida

Mike Notohamiprodjo, M.D.

Associate Chair and Section Chief MRI, Department of Diagnostic and Interventional Radiology, University Hospital Tübingen, Germany

The Department of Clinical and Interventional Radiology at the University Hospital Tübingen had the rare opportunity to host the world's very first installation of the MAGNETOM Vida, the first BioMatrix equipped scanner, incorporating the latest advances in MR technology.

Current demands for biometrical imaging and personalized medicine

One of the current trends in medicine is the acquisition and analysis of so-called 'big data', to improve disease management and patient outcome.

The University Hospital Tübingen has dedicated itself to this approach and founded the "Center for Personalized Medicine", incorporating all activities in this rapidly developing field. One of the central tasks is a universal database for quantitative data, so that imaging data, for example, can be correlated to histopathology, molecular biology, or clinical outcome.

The Department of Radiology is also part of this inter-disciplinary center, giving us the exciting chance to perform 'Radiomics' on a greater scale by evaluating image phenotypes as a potential biomarker, for example, to predict and assess therapy response and outcome. However, the fundamental requirement for quantitative or at least structured data is robust and reproducible image acquisition (Fig. 1). Up-to-date Computed Tomography is the mainstay of Radiomics since it is highly standardized and accomplishable in most patients. Magnetic Resonance imaging, by contrast, provides more detailed data due to its superior soft-tissue contrast and offers complex functional quantitative methods such as DCE-MRI and diffusion-weighted imaging. However its robustness and reproducibility is often limited due to long acquisition times and the sensitiveness to respiratory and gross motion. One of the focuses of our MR research group is to develop and establish methods for clinical routine to overcome these constraints to acquire robust results in every patient. We have a long-standing experience with advanced parallel imaging methods, free-breathing examinations, compressed sensing, and novel multi-channel coils. Thus, we were very excited to be the first to work with the 3T MAGNETOM Vida[1] and BioMatrix[1], bringing all together work-in-progress- and prototype technology, incorporating and uniting technical and sequence advances.

Our MAGNETOM Vida

Our Magnetic Resonance Department is equipped i.a. with the 1.5T MAGNETOM Espree, Avanto^{fit}, and Aera scanners; the 3T MAGNETOM Skyra and Prisma^{fit} scanners, and the MR-PET scanner Biograph mMR. The focus of our daily clinical work is on oncological, musculoskeletal, and neuro-imaging. We have experienced a steady increase in demand particularly in multiparametric prostate MRI and functional brain MRI. We have also noticed a steady

[1] 510(k) pending. The product is not commercially available. Future availability cannot be guaranteed.

1

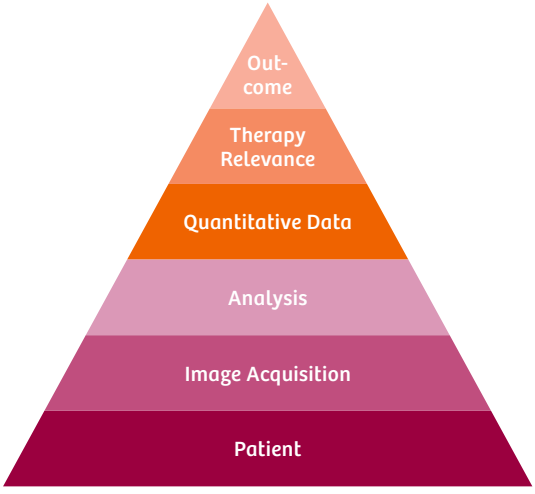

Figure 1: The pyramid of imaging in personalized medicine. Personalized medicine starts with the patient. Only if the patient is feeling comfortable can sufficient data be obtained. Image acquisition should be of high quality, robust and reproducible. The images are then read in PACS; functional imaging is analyzed with postprocessing software. Quantitative or at any rate structured data should then be derived from the analysis. Based on this data individualized therapy can be induced. Therapy response and/or outcome should be monitored and in the best-case scenario predicted by the imaging data acquired before. Optimized scanner hardware, such as BioMatrix and MAGNETOM Vida, help to optimize the fundament of this pyramid. Only if the patient is comfortable and image acquisition optimized can further data analysis and processing be performed.

increase in multi-region oncologic imaging, corresponding to the rapidly growing number of anticancer therapeutics, such as immune or antibody therapy. The latter examinations in particular are repeatedly performed in prospective studies and require a fast and highly reproducible acquisition to reliably assess therapy response.

During the first months of our early installation we performed the initial mandatory conformity marking (CE-certificate), a so-called 'MPG-(medicine devices act)-study'. This means that we had to examine a particular number of patients on both the new scanner and a routine 3T scanner (in our case MAGNETOM Skyra, Prisma^{fit}, and Biograph mMR) and compare image quality.

In short the MAGNETOM Vida features a 70 cm bore, strong 60/200 XT gradients, and a very homogeneous large field-of-view (55 x 55 x 50 cm) (Fig. 2). We believe that it combines the magnet homogeneity of a MAGNETOM Avanto and the performance of a MAGNETOM Prisma, but features the similar comfort of the wider 70 cm bore MAGNETOM Skyra. Furthermore, it features 128 receive channels enabling state-of-the-art coil technology, such as a 72-channel Spine coil, 30-channel Body coils, a 64-channel or a tiltable 20-channel Head coil. The high number of channels is particularly useful for achieving higher parallel imaging acceleration factors, significantly shortening acquisition time while maintaining adequate signal-to-noise ratio (SNR). From our experience, the combination of the 72-channel Spine coil and the 30-channel Body coil delivers up to 30% increase in SNR, particularly at high PAT-factors.

The new scanner also features a novel fully-motorized dockable table concept with an integrated respiratory sensor as well as an updated software with a user interface combining the well-known *syngo* MR E11-software with *syngo*.via functionality for viewing and postprocessing.

First experiences with the user interface

The new user interface and scanner software is now presented on two large 24-inch screens, one for acquisition and one for postprocessing. Thus, the technical staff can view the images and perform postprocessing, without switching the task cards, always keeping acquisition under supervision (Fig. 3).

While the new software looks quite different at first glance, the *syngo* MR E11-functionality is still maintained and only a few minor changes were obvious. We found that all technical staff could operate the scanner after only a short (<5 minutes) basic training. The *syngo*.via-interface was already familiar to our physicians, but the technical staff were also quickly able to perform basic postprocessing, such as composing and advanced postprocessing, e.g. perfusion assessment with Tissue4D was also quite quickly doable.

One of the central aspects of MAGNETOM Vida is to provide optimal reproducibility of MR studies, so that high image and data quality is guaranteed. Several Dot engines enable semi-automated acquisition of e.g. the brain, joints, or the cardiovascular system with a focus on either speed, resolution or, robustness. We were particularly interested in the new Whole-Body Dot Engine, allowing the rapid planning and acquisition of multi-region examinations, giving MRI-acquisition a feeling similar to CT, automatically adjusting the field-of-view, number of stacks, and slices (Fig. 4).

2

Figure 2: Professor Notohamiprodjo and Professor Nikolaou in front of their MAGNETOM Vida, the world's first clinical installation.

3

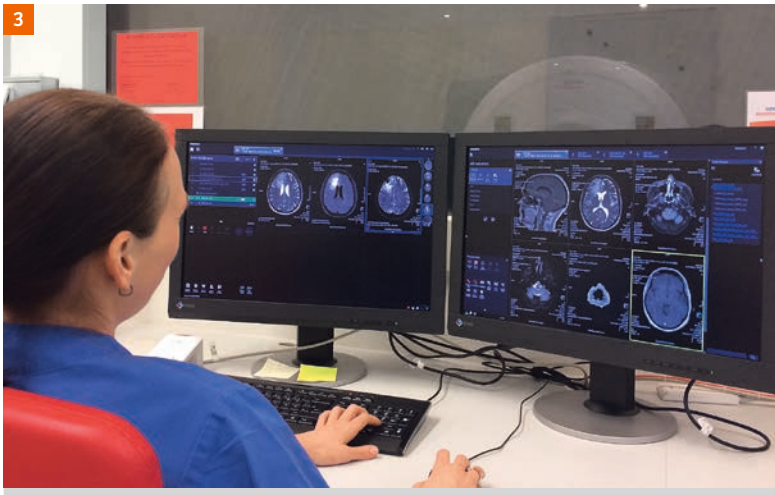

Figure 3: To ease the work of the MR technologist, the new *syngo* MR XA10 software operates on a dual monitor scanning workplace with two large 24-inch monitors.

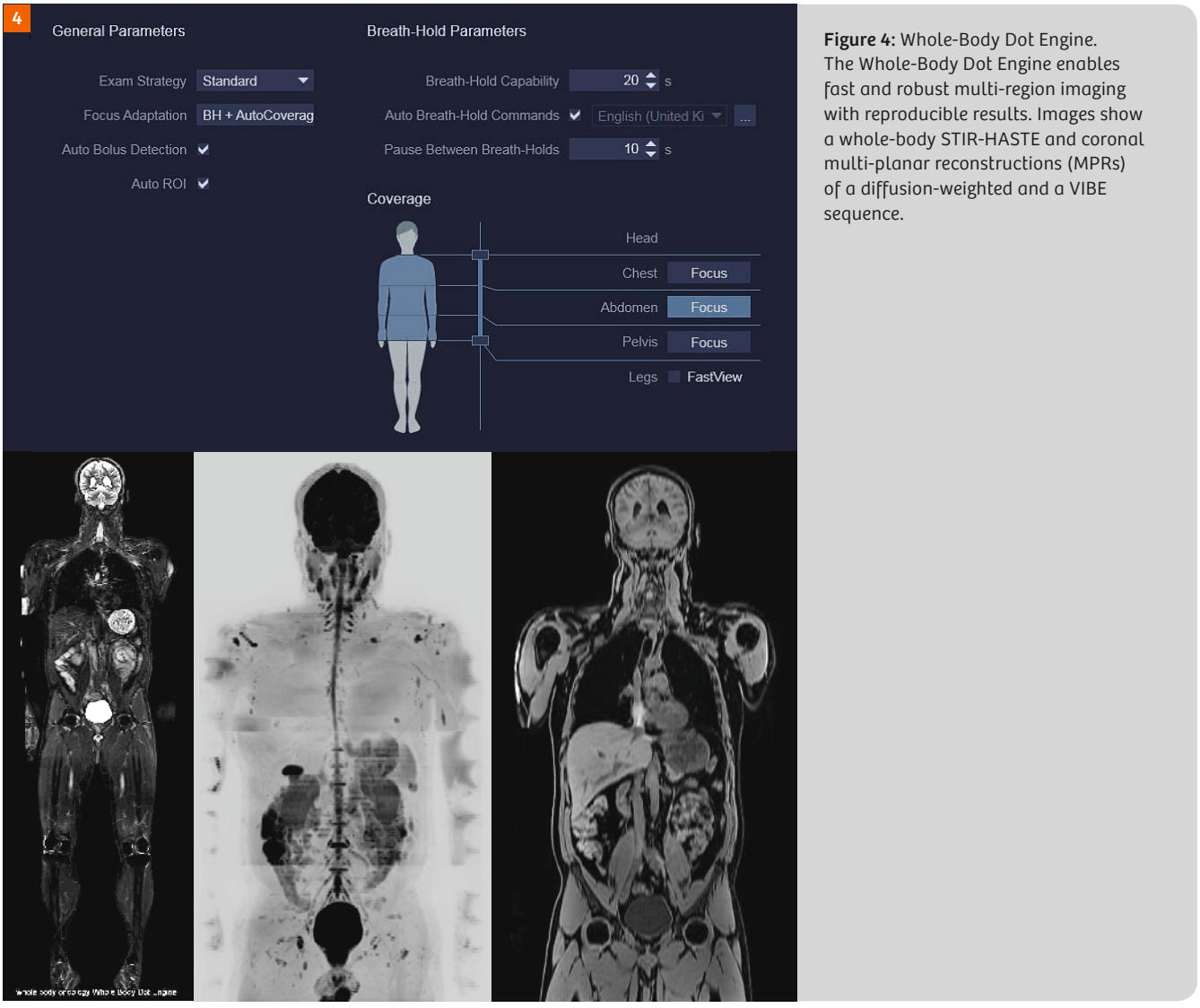

Figure 4: Whole-Body Dot Engine. The Whole-Body Dot Engine enables fast and robust multi-region imaging with reproducible results. Images show a whole-body STIR-HASTE and coronal multi-planar reconstructions (MPRs) of a diffusion-weighted and a VIBE sequence.

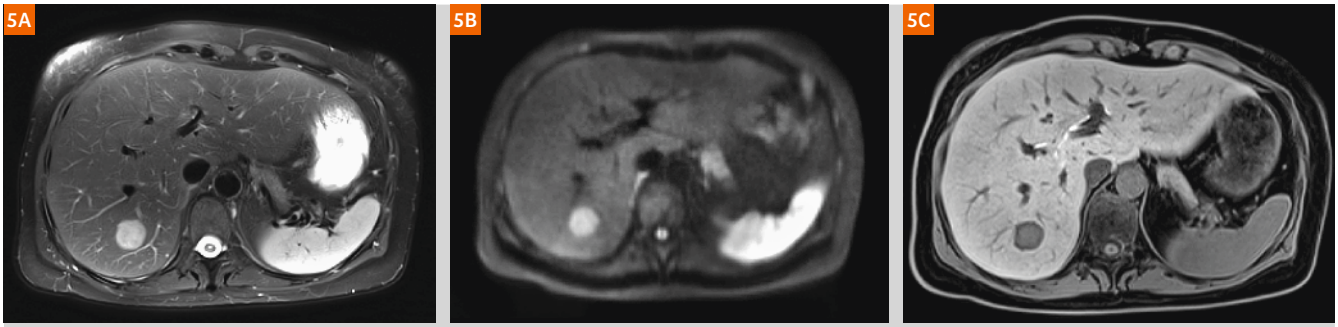

Figure 5: 38-year-old patient with hepatic adenoma. **(5A)** T2-weighted fast BLADE sequence: A hyperintense 2 cm sized mass in the Coinaud-segment VII. The acquisition with optimized radial spokes makes the sequence robust against respiratory motion and reduces typical star and hook artifacts. Furthermore, phase-encodiung artifacts caused, for example, by pulsation, do not occur due to the radial acquisition. **(5B)** Diffusion-weighted sequence with b-value 800 s/mm² with SliceAdjust: The lesion shows diffusion restriction. The strong 60/200 XT gradients provide high signal even at high b-values. Slice selective shimming with SliceAdjust reduces distortion artifacts. **(5C)** Dixon-VIBE sequence with PAT6: The lesion shows some uptake of the hepatocyte specific contrast agent Eovist (Bayer, Berlin, Germany). High acceleration factors are possible with the combination of the 72-channel Spine coil and the 30-channel Body coil. Breath-hold duration is only 8 seconds, still delivering high image quality.

First experiences with the hardware

Our technical staff were very happy with the fully motorized table, making it possible to maneuver even with obese patients with ease. The respiratory sensor enables respiratory triggering even for sequences without navigator. We think that the sensor is particularly useful to monitor if a patient correctly performs the breath-hold maneuvers, so that the duration of sequences can be individually adapted to the patient's respiratory capacity.

The two tablet-like touchscreens at the gantry were also quite popular, giving full control of the room parameters such as ventilation and volume levels. Automated coil position recognition also accelerates the workflow, as positioning of the coil center is not required anymore. The basic coil design was already known and compatible to Tim4G scanners, however many coils feature more elements such as the 72-channel Spine coil, 30-channel Body coil, or 18-channel Knee coil, while others provide more patient comfort, such as the flexible Shoulder coil or the tiltable 20-channel Head/Neck coil, allowing for more comfort in the case of cervical kyphosis.

First clinical experiences

Of course, of greatest interest to us was image quality. The multi-channel coils, particularly the combination of the above mentioned 72-channel Spine coil and a 30-channel Body coil, allow for application of high PAT-factors, such as R = 6 for CAIPIRINHA-imaging (Fig. 5).

We noticed a high diagnostic image quality even for very fast examinations such as a 5 minutes brain (T2, FLAIR, T1, Diffusion) (Fig. 6) or a 6 minutes knee examination (PD fs in 3 planes and T1). Simultaneous Multi-Slice acceleration is also available for diffusion-weighted imaging enabling acquisition of a complete body region in only 2 minutes, so that diffusion-weighted imaging of the chest-abdomen-pelvis can be performed in under 7 minutes. The whole-body-protocol can be further accelerated with a free-breathing or multi-breath-hold STIR-HASTE-sequence, which can also be acquired much faster but with similar image quality than a conventional TSE-STIR (Fig. 4). We currently aim at a 30-minute time slot for a complete whole-body-protocol, allowing for a potential dramatic increase of patient comfort and throughput.

We were also very excited to test the first commercially available version of radial GRASP[1] (Golden Angle Radial Sparse Parallel MRI), enabling continuous free-breathing radial T1-acquisition with a temporal resolution of <2 seconds. The resulting images are of diagnostic quality, similar to breath-hold sequences, while the image reconstruction time (seconds per phase) was considerably faster than the first prototypes, due to the two integrated GPUs.

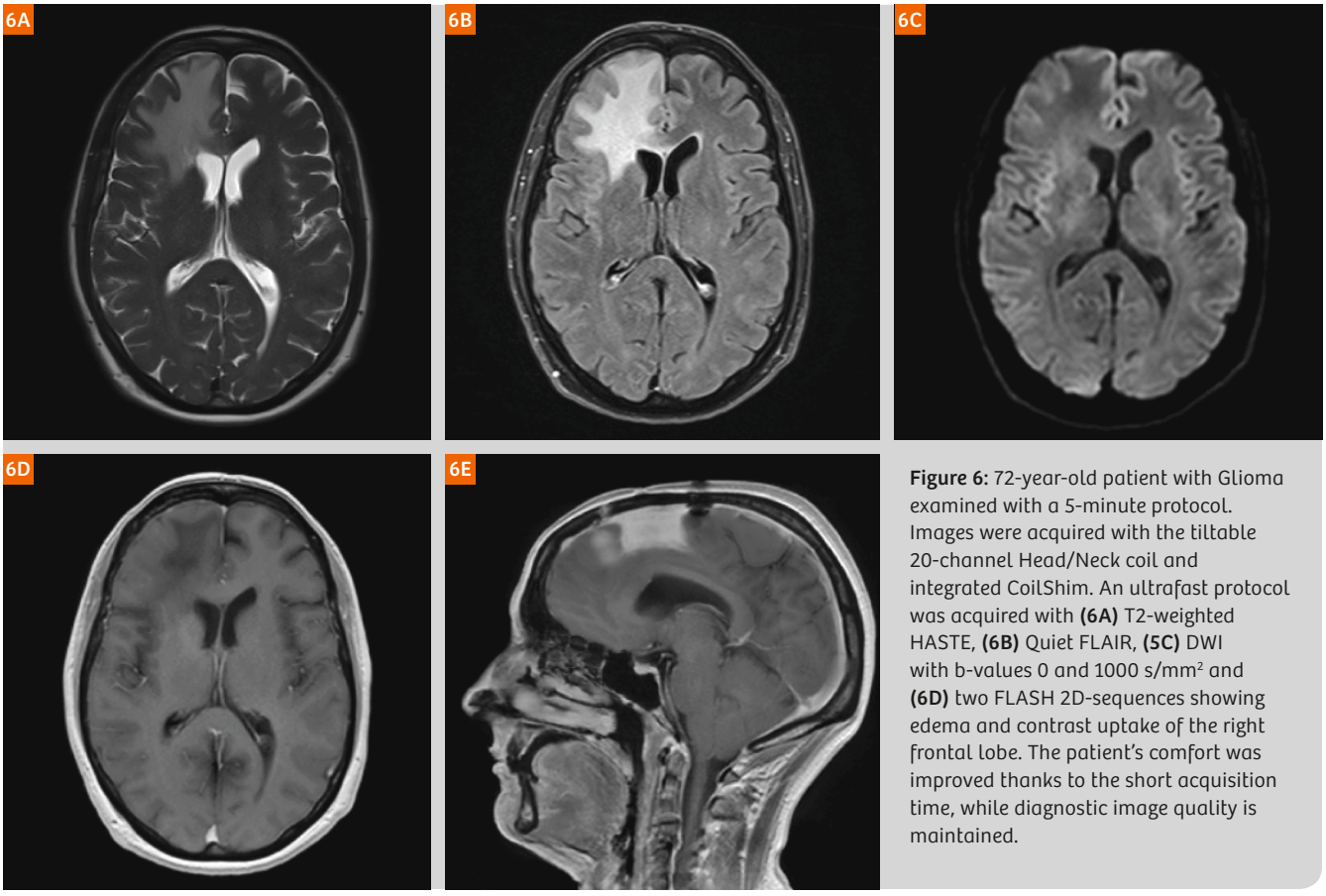

Figure 6: 72-year-old patient with Glioma examined with a 5-minute protocol. Images were acquired with the tiltable 20-channel Head/Neck coil and integrated CoilShim. An ultrafast protocol was acquired with **(6A)** T2-weighted HASTE, **(6B)** Quiet FLAIR, **(5C)** DWI with b-values 0 and 1000 s/mm² and **(6D)** two FLASH 2D-sequences showing edema and contrast uptake of the right frontal lobe. The patient's comfort was improved thanks to the short acquisition time, while diagnostic image quality is maintained.

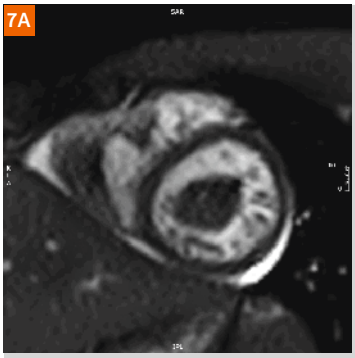

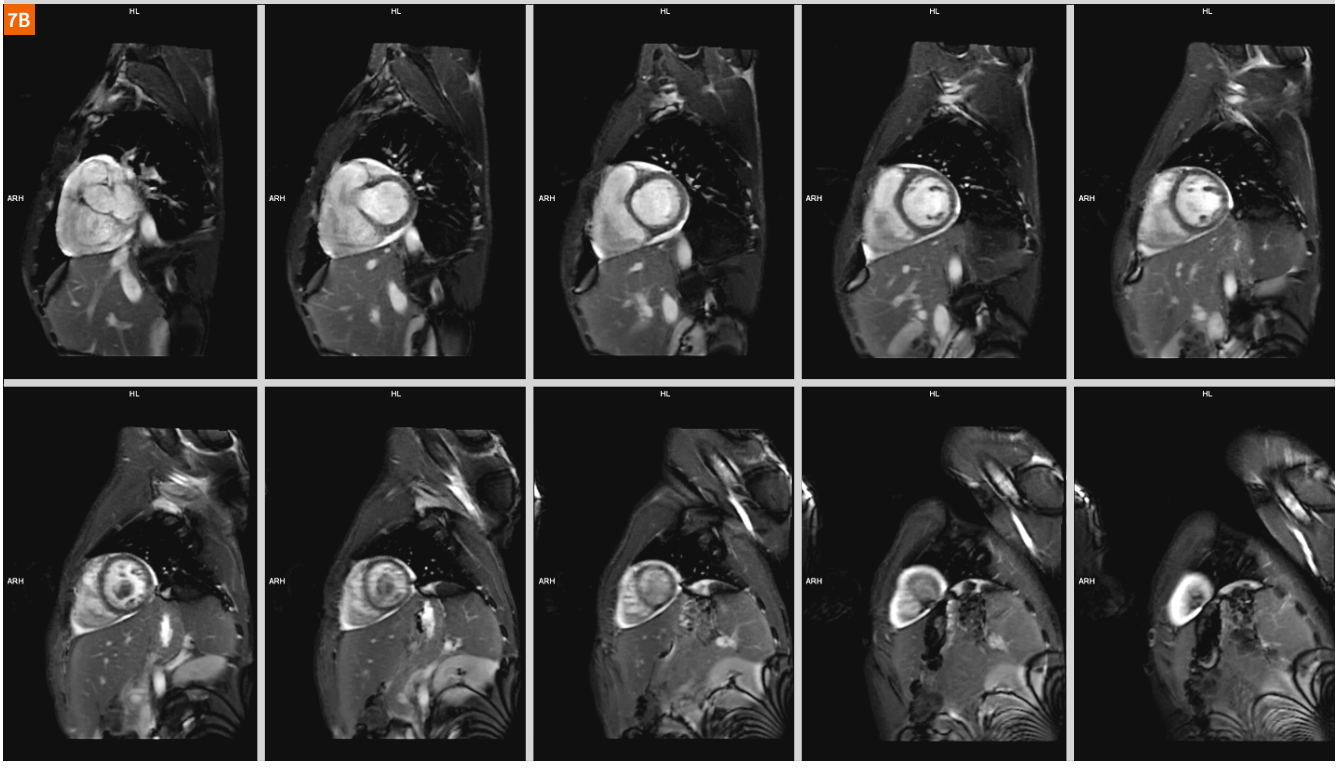

Figure 7: 27-year-old patient with Hughes-Stovinson-Syndrom and M. Behçet with a ventricular thrombus. **(7A)** Single slice short-axis cine sequence acquired during one breath-hold (8 s) at a 3T MAGNETOM Prisma^{fit}. **(7B)** Whole-heart cine sequences accelerated with compressed sensing acquired during one breath-hold (18 s) at the 3T MAGNETOM Vida.

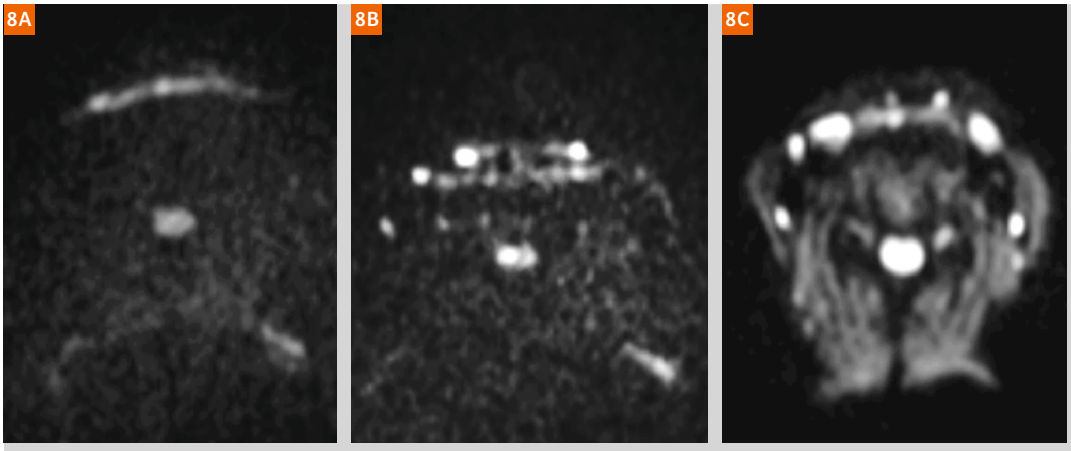

Figure 8: 57-year-old patient with parotid cancer. Diffusion-weighted images (b-value 800 s/mm^2) acquired with the tiltable 20-channel Head/Neck coil. **(8A)** The standard shim shows heavy distortions and almost no anatomical structures. **(8B)** SliceAdjust decreases distortions, however image quality is still impaired. **(8C)** The combination of SliceAdjust and an integrated CoilShim provide good image quality without distortion even of the lower neck, allowing optimal delineation of the cervical lymph nodes.

Other applications profiting from compressed sensing include, for example, cardiovascular examinations. We were able to obtain a complete short axis scan of the whole heart during only a single breath-hold, using Compressed Sensing Cardiac Cine. The diagnostic image quality is similar to that of classic single-slice acquisition requiring multiple breath-holds, so that examinations are significantly shortened, improving patient comfort and workflow (Fig. 7).

The strong gradients and homogenous magnetic field also allow for examination of obese patients, advanced diffusion applications, such as high b-value imaging and high-resolution 3D-imaging. Furthermore slice selective and dedicated coil-shims allow to decrease distortion artifacts e.g. of diffusion-weighted imaging, particularly at problematic body areas, such as the neck (Fig. 8).

Altogether we experienced an image quality, very similar to that of a MAGNETOM Prisma, which however comes with a 60 cm bore. The multi-channel coils may allow further acceleration, making it possible to shorten examination time, so that robust imaging data can be derived from every patient.

Where do we see the MAGNETOM Vida

As the MAGNETOM Vida brings together many advanced hardware and software solutions, we plan to use the scanner for clinical applications related to biometrical disease assessment. In the framework of our 'Center for Personalized Medicine' we will perform multiparametric assessment of primary tumors such as ENT-tumors, sarcoma, glioma, or prostate cancer to gain further insight into tumor biology and predict outcome and therapy response. Highly standardized multi-region examinations to objectify therapy effects will also be performed at this scanner. We also seek to quantify these effects and study tissue and tumor microcirculation and -structure with GRASP and advanced diffusion-weighted imaging. The rapid and free-breathing imaging possibilities allow us to quickly examine children[2] or patients with limited general condition or respiratory status and to obtain adequate image quality in the shortest possible acquisition time.

In summary, the MAGNETOM Vida will enable us to acquire robust and reproducible imaging data in almost all patients, forming the groundwork for biometric MR-imaging, personalized medicine and individually tailored therapies.

[2] MR scanning has not been established as safe for imaging fetuses and infants less than two years of age. The responsible physician must evaluate the benefits of the MR examination compared to those of other imaging procedures.

Contact

Professor Mike Notohamiprodjo, M.D.
Diagnostic and Interventional Radiology
University Hospital Tübingen

Hoppe-Seyler-Str. 3
72076 Tübingen
Germany
Phone: +49 (0)7071 29-86676
mike.notohamiprodjo@uni-tuebingen.de

Case Series: Pediatric GOBrain-5-Minute Protocol MR Imaging at 3 Tesla

Elka Miller, M.D., FRCPC[1]; Barry Smith, MRT (MR)[2]

[1] Chief and Research Director, [2] MRI Supervisor, Medical Imaging Department, Children's Hospital of Eastern Ontario (CHEO), Ottawa, ON, Canada

Background

Fast-brain MRI was first introduced for children[1] with shunt dependent hydrocephalus [1–3] who frequently undertake serial imaging studies through life. The image studies often include a combination of both CT and MRI depending on the child's age, study time, and availability of equipment. CT scans involve exposure to radiation, which has potentially harmful effects, especially for young children [4]. The alternative to a CT scan is MRI, but brain MRI is time consuming and sensitive to motion artifacts. In young patients, MRI studies might require sedation or general anesthesia, which have their own risks of complications [5]. Therefore, fast MRI sequences can avoid the need for sedation or anesthesia, and are thus particularly useful for young and uncooperative patients. Recently, fast MRI sequences have become more popular and these are increasingly being used for non-hydrocephalic indications such as macrocephaly, intracranial cysts, screening for some structural congenital and non-congenital anomalies, and postoperative follow-up [6].

A number of 'fast MRI' protocols have been used; the most popular are modifications of T2-weighted MRI, including Half-Fourier Acquisition Single-shot Turbo Spin Echo (HASTE) [7], Single Shot Fast Spin Echo (SSFSE) [6, 8], and Periodically Rotated Overlapping Parallel lines with enhanced reconstruction (PROP) FSE [2]. These protocols often use a single type of pulse sequence which carries potential pitfalls. Our previous study [9] demonstrated undetected findings in 7/50 (14%) pediatric fast brain MRI including venous sinus thrombosis (one patient), subdural hematoma (three), failure to differentiate blood products (two), and limited evaluation of extra-axial collections (one). This limitation was seen to be due to the lack of other pulse sequences to further characterize tissue and fluid. Consequently, there is a known need to improve image quality using fast MR protocols for all clinically relevant sequences; this is likely to occur when different pulse sequences and planes are used for evaluation of the brain tissues and fluids.

GOBrain [10, 11] was developed as a 5-minute diagnostic brain exam and was clinically validated to be diagnostically

[1] MR scanning has not been established as safe for imaging fetuses and infants less than two years of age. The responsible physician must evaluate the benefits of the MR examination compared to those of other imaging procedures.

	Plane	TR (ms)	TE (ms)	FOV (mm)	Phase FOV (%)	Slices	Slice (mm)	Gap (%)	Matrix	Phase directions	iPAT factor	b-values	Directions (no)	TA (mins)
AutoAlign Head Scout	3D	3.15	1.37	260	100	128	1.6	20	160	A-P	3	NA	NA	0:14
T1 GRE FLASH	Sag	240	2.46	220	100	35	4.0	20	256	A-P	2	NA	NA	0:41
T2 TSE	Axial	6200	78	220	87.5	25	5.0	20	256	R-L	3	NA	NA	1:02
T2 TSE DarkFluid	Axial	8000	119	220	87.5	25	5.0	20	256	R-L	2	NA	NA	1:52
ep2d Diffusion	Axial	4200	72	240	100	31	5.0	12	160	A-P	2	0,800	12	1:16
ep2d T2*W	Axial	6120	30	220	100	25	5.0	20	128	A-P	1	NA	NA	0:06
													Total exam time	5:11

Table 1: Acquisition parameters and scan time for 5-minute GOBrain MRI protocols on the MAGNETOM Skyra with the Head/Neck 20 coil.

equivalent to the longer, conventional exam. The 5-minute examination provides the basic clinical sequences including sagittal T1-weighted, axial T2-weighted, axial T2 TSE Dark Fluid (FLAIR), axial diffusion-weighted (DWI), and axial T2*-weighted sequences. Several factors, like parallel imaging with higher acceleration factors, gradient T1-weighted and EPI-GRE T2*-weighted acquisitions, have made it possible to shorten the scan time but have also alleviated EPI-related susceptibility artifacts and image distortions by reducing the EPI-factors and shortened the inter-echo spacing. The hope is that the 5-minute protocol will reach high diagnostic concordance for the diagnosis of clinically relevant findings compared to the conventional protocol, and therefore become useful in a selected group of pediatric patients that are more prone to motion and the need for anesthesia.

Materials and methods

All images in this case series were acquired on a 3T MAGNETOM Skyra scanner (Siemens Healthcare, Erlangen, Germany). The MRI protocol typically included the routine scan as per the radiologist's request and the additional GOBrain-5-minute sequence appended to the end of the examination (Table 1).

Conclusion

Pediatric fast imaging techniques can shorten scan times, decrease motion-related artifacts, and more importantly in children reduce the need for sedation [1]. In addition, they have the potential to reach diagnostic concordance of clinically relevant findings compared to the conventional protocol and therefore become useful in a selected group of pediatric patients that are more prone for motion and need of anesthesia. Improved patient throughput which decreases wait time can also be an advantage of this protocol.

Acknowledgement

We would like to acknowledge Ms. Wendy Rabbie MRT (R), Director Medical Imaging and Laboratory Medicine.

Case 1

Figure 1: 9-year-old female, congenital hydrocephaly with multiple shunt revisions. Top row GOBrain **(1A–C:** Sagittal T1w, axial T2 TSE, axial T2 TSE FLAIR). Bottom row, conventional fast sequences **(1D–F:** Sagittal T2w, axial T2 HASTE, axial T1 FLASH 2D). No interval change in the asymmetric size of the ventricular system or position of the shunt catheter (arrow). The studies are comparable, adding a T2 FLAIR (1C) sequence has the potential to further characterize fluid and brain findings.

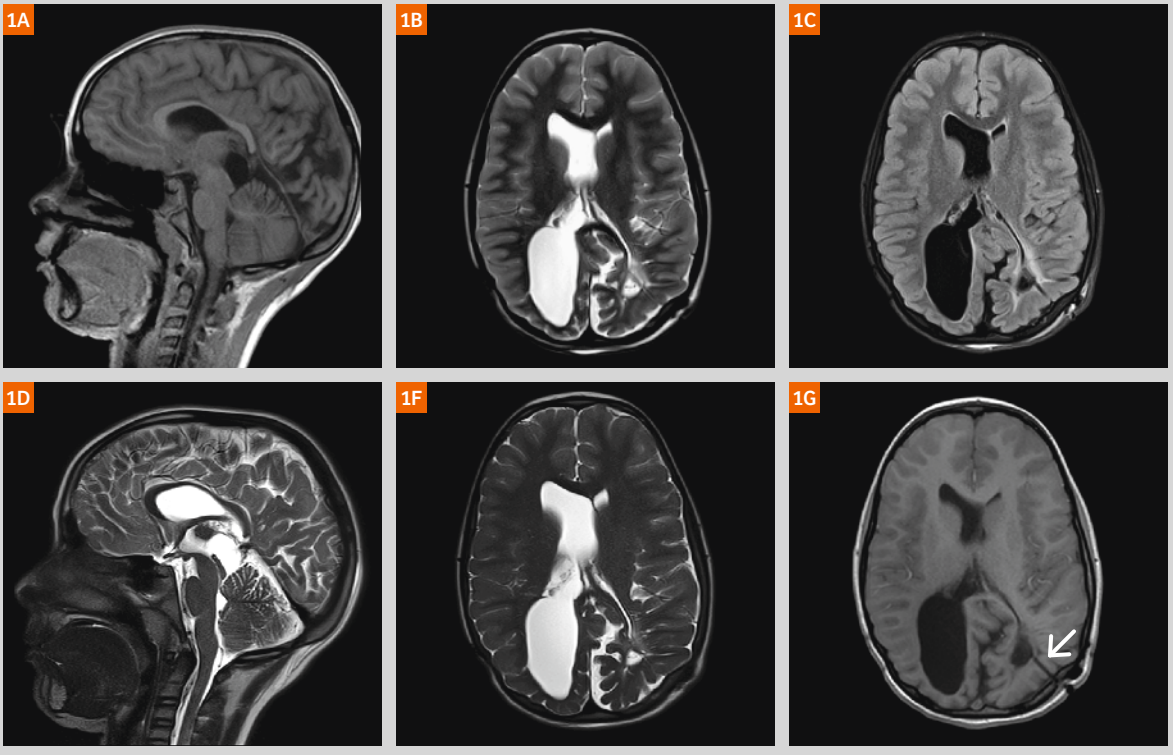

Case 2

Figure 2: 10-year-old female with severe traumatic brain injury. Top row GOBrain **(2A–D:** Sagittal T1w, axial T2 TSE, axial T2 FSE FLAIR, and axial T2*) obtained 3 days after the conventional MRI. Bottom row, routine sequences **(2E–H:** Sagittal T1w, axial T2w, axial FLAIR, and susceptibility-weighted imaging (SWI)). Findings consistent with brain contusion in the posterior parieto-occipital cerebral hemispheres and subdural bleed along the left tentorium (arrow). There is comparable conspicuity of the contusion and blood products with the routine and the GOBrain-5-minute protocol.

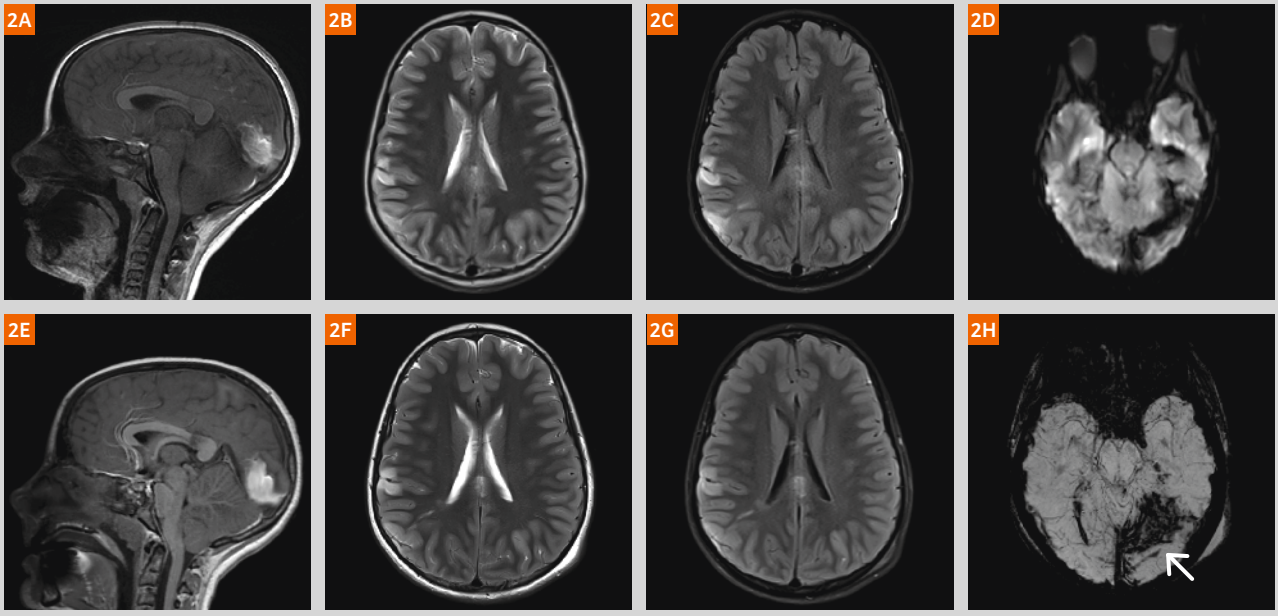

Case 3

Figure 3: 14-year-old male, complicated left frontal sinusitis with a left parasagittal extra-axial collection (arrow) resulting in meningitis. Top row GOBrain **(3A–D:** axial T2 TSE, axial T2 TSE FLAIR, axial DWI, and axial ADC) obtained the same day as conventional MRI. Bottom row, routine sequences **(3E–H:** axial T2w, axial FLAIR, axial DWI, and axial ADC). Diffusion restriction was appreciated in the left frontal sinus (not shown), in the left parasagittal collection (arrowhead). The cortical sulci in the left frontal and parietal lobe demonstrate mild effacement. The images exemplify the comparable image quality in the GOBrain-5-minute protocol (top row), compared to the conventional protocol (bottom row).

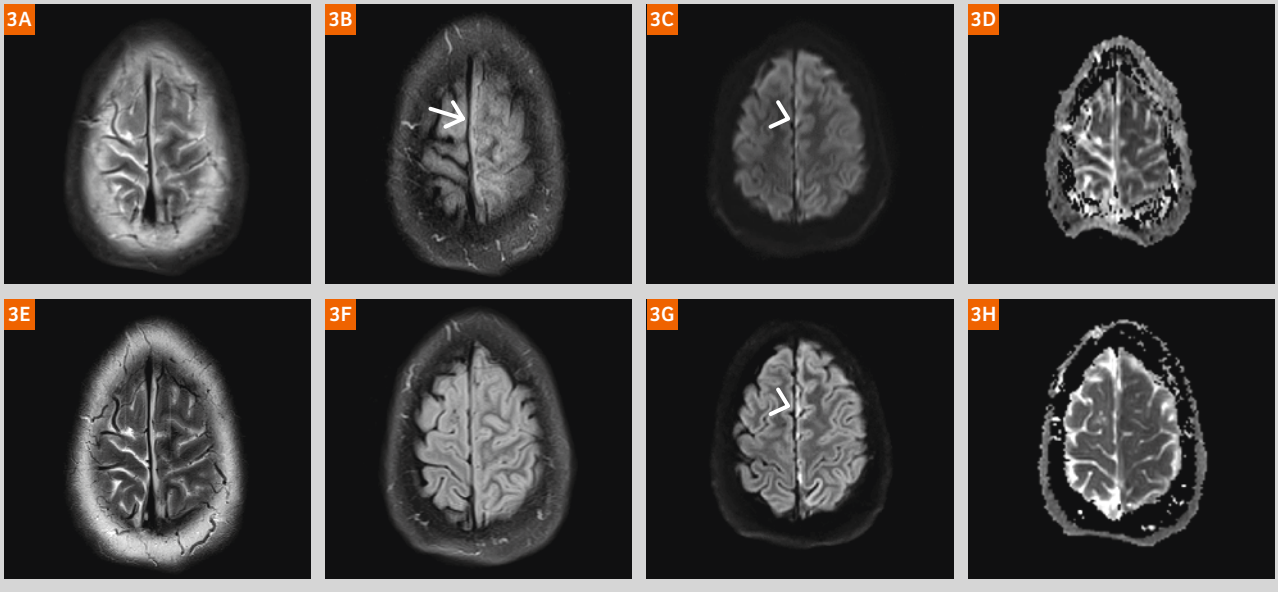

Case 4

Figure 4: 7-year-old female, suprasellar germinoma treated with chemotherapy and radiation. **4A, B**: baseline images before treatment. Top row GOBrain **(4C, D:** axial T2 TSE, and axial T2 TSE FLAIR). Bottom row, routine sequences **(4E, F:** axial T2w, and axial FLAIR) follow-up 2 years after treatment. The follow-up images exemplify the comparable image quality of the suprasellar residual lesion in the GOBrain-5-minute protocol (top row), compared to the conventional protocol (bottom row). Follow-up images using GOBrain and conventional protocols were obtained the same day.

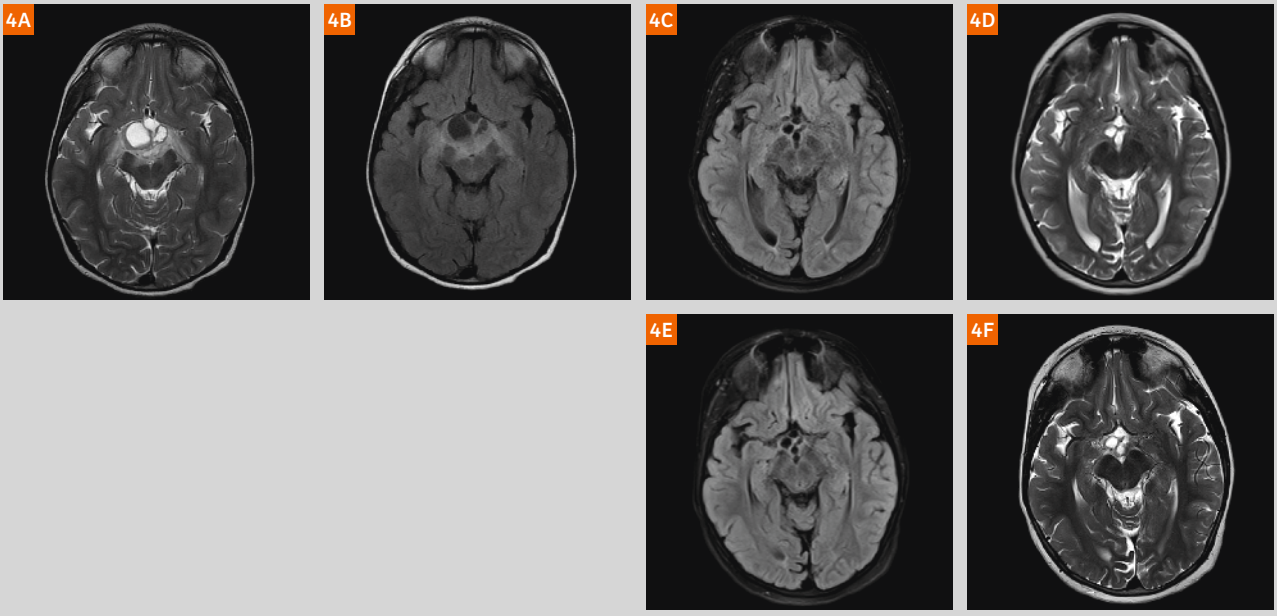

Case 5

Figure 5: 10-year-old male, 2 week history of morning headaches, waking up at night. History of anxiety. Suspected radiological isolated demyelinating type lesions. Top row GOBrain **(5A, B:** axial T2 TSE, and axial T2 TSE FLAIR). Bottom row, conventional sequences **(5C, D:** axial T2w, and axial FLAIR). The images exemplify the same number and size of white matter lesions (arrows) in the GOBrain-5-minute protocol (top row), compared to the conventional protocol (bottom row).

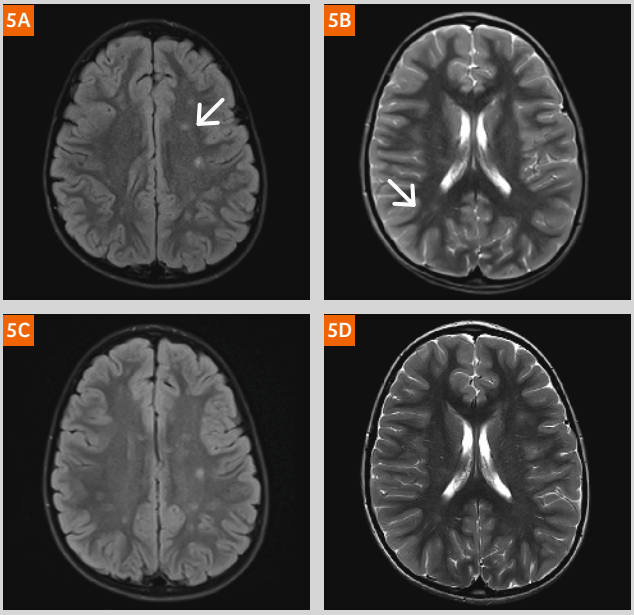

References

1 Ashley WW, Jr., McKinstry RC, Leonard JR, Smyth MD, Lee BC, Park TS. Use of rapid-sequence magnetic resonance imaging for evaluation of hydrocephalus in children. J Neurosurg. Aug 2005;103(2 Suppl):124-130.
2 Forbes KP, Pipe JG, Karis JP, Farthing V, Heiserman JE. Brain imaging in the unsedated pediatric patient: comparison of periodically rotated overlapping parallel lines with enhanced reconstruction and single-shot fast spin-echo sequences. AJNR Am J Neuroradiol. May 2003;24(5):794-798.
3 Miller JH, Walkiewicz T, Towbin RB, Curran JG. Improved delineation of ventricular shunt catheters using fast steady-state gradient recalled-echo sequences in a rapid brain MR imaging protocol in nonsedated pediatric patients. AJNR Am J Neuroradiol. Mar 2010;31(3):430-435.
4 Brenner DJ. Estimating cancer risks from pediatric CT: going from the qualitative to the quantitative. Pediatr Radiol. Apr 2002;32(4):228-221; discussion 242-224.
5 Ramaiah R, Bhananker S. Pediatric procedural sedation and analgesia outside the operating room: anticipating, avoiding and managing complications. Expert Rev Neurother. May 2011;11(5): 755-763.
6 Missios S, Quebada PB, Forero JA, et al. Quick-brain magnetic resonance imaging for nonhydrocephalus indications. J Neurosurg Pediatr. Dec 2008;2(6):438-444.
7 Penzkofer AK, Pfluger T, Pochmann Y, Meissner O, Leinsinger G. MR imaging of the brain in pediatric patients: diagnostic value of HASTE sequences. AJR Am J Roentgenol. Aug 2002;179(2):509-514.
8 Iskandar BJ, Sansone JM, Medow J, Rowley HA. The use of quick-brain magnetic resonance imaging in the evaluation of shunt-treated hydrocephalus. J Neurosurg. Nov 2004;101(2 Suppl):147-151.
9 Rozovsky K, Ventureyra EC, Miller E. Fast-brain MRI in children is quick, without sedation, and radiation-free, but beware of limitations. J Clin Neurosci. Mar 2013;20(3):400-405.
10 Prakkamakul S, Witzel T, Huang S, Boulter D, Borja MJ, Schaefer P, et al. Ultrafast brain MRI: Clinical deployment and comparison to conventional brain MRI at 3T. J Neuroimaging 2016; 26(5): 503-150.
11 Rapalino O, Heberlein K. New strategies for protocol optimization for clinical MRI: Rapid examiniations and improved patient care. MAGNETOM Flash 2016; 65: 22-25.

Contact

Elka Miller, M.D., FRCPC
Chief and Research Director,
Medical Imaging Department
Children's Hospital of
Eastern Ontario (CHEO)

401 Smyth Road
Ottawa, ON K1H 8L1
Canada
Phone: +1 (613) 737-7600 x.2303
Fax: +1 (613) 738-4811
emiller@cheo.on.ca

Download GOBrain & GOBrain+ Protocols

Heightened attention to healthcare costs and value based outcomes in medicine are driving revolutionary changes in the MR industry. Siemens MR and Massachusetts General Hospital (MGH) in Boston collaborate on strategies to develop fast and clinically validated examinations in MR.

GOBrain is a diagnostic brain exam which takes 5 minutes[1]. It consists of five diagnostically-important MR brain protocols acquired with optimized pulse sequences. Integrated with individual anatomical landmark-based AutoAlign technology providing automatic slice positioning, this push-button exam requires minimal interaction from the technologist. The included sequences are a sagittal T1-weighted, axial T2-weighted, axial T2-weighted DarkFluid, axial diffusion-weighted and an axial T2*-weighted contrast.

GOBrain+ expands GOBrain to additionally support brain imaging with contrast medium. New optimized sequences include an axial T1-weighted sequence administred pre- and post-contrast and a post-contrast MPRAGE.

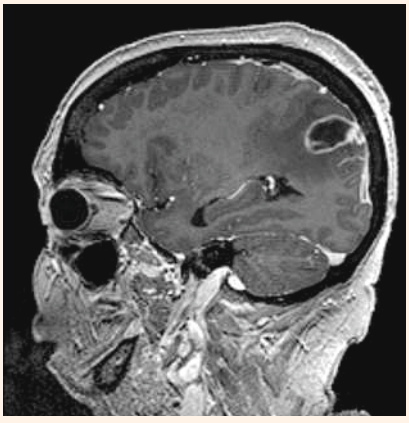

To download the .exar1 files for 1.5T with Head/Neck 20 and for 3T with Head/Neck 20, Head 32 or Head/Neck 64 visit us at

www.siemens.com/GOBrainPlus

[1] Achieved on a MAGNETOM Skyra with the Head 32 coil. Total examination time can take up to 6 minutes depending on system field strength and coil density.

Simultaneous Multi-Slice: a Case-based Presentation of Pre-Operative Brain Tumor Evaluation

Louis-Olivier Bouchard, M.D., MSc[1,3]; Maxime Villeneuve, P.Eng., MSc[2]; Christian Berthelot, M.D., FRCPC[1,3]

[1] CHU de Québec, Hôpital de l'Enfant-Jésus, Radiology Department, Québec, Canada
[2] CHU de Québec, Hôpital de l'Enfant-Jésus, Neurosciences Department, Québec, Canada
[3] Université Laval, Faculté de médecine, Radiology and Nuclear Medicine Department, Québec, Canada

Abstract

Our clinical center, with a neuro-oncologic field of expertise, has recently started using Simultaneous Multi-Slice (SMS) diffusion-weighted imaging for the pre-operative assessment of brain tumors. In our first evaluation, SMS was used to reduce the scan duration of our diffusion tensor imaging sequence. In our second evaluation, SMS was invested in improved data quality by going from a diffusion protocol with a 30% slice gap to a protocol with no slice gap. We indeed found that SMS not only provides a time benefit, but also an improvement to the data quality of our diffusion tensor imaging.

Introduction

Once the initial diagnosis of a brain tumor is made, neurosurgeons are nowadays looking, in addition to the usual clinical investigations, for a thorough imaging evaluation to assess the tumor's location, its extension, and its relation with surrounding white matter, in order to plan their intervention. The paradigm in neuro-oncology is different than in other oncologic fields, as it is not suitable to take wide margins around the tumor; the mass excision has to be balanced with the functional impairment that would result from it, which has to be minimized. Thus, knowing the exact location of functional areas and their connecting white matter tracts is deemed essential when carefully planning the operation; whether the tumor pushes back the tracts or infiltrates them, and the margins (or distance) between the tumor and functionally-important tracts, are important considerations. With that in mind, after acquiring the basic anatomical imaging data, we therefore go further with functional and tractographic data. These supplementary acquisitions, however, raise some issues,

Case 1

Figure 1: We imaged five patients with glial brain tumors, using both non-SMS and SMS imaging. The average examination time was 10 minutes 41 seconds for non-SMS imaging, as opposed to 6 minutes 42 seconds for SMS imaging, a 37% decrease in scan time, while having an average of 223% increase in the number of fibers, representing a significant data quality enhancement.

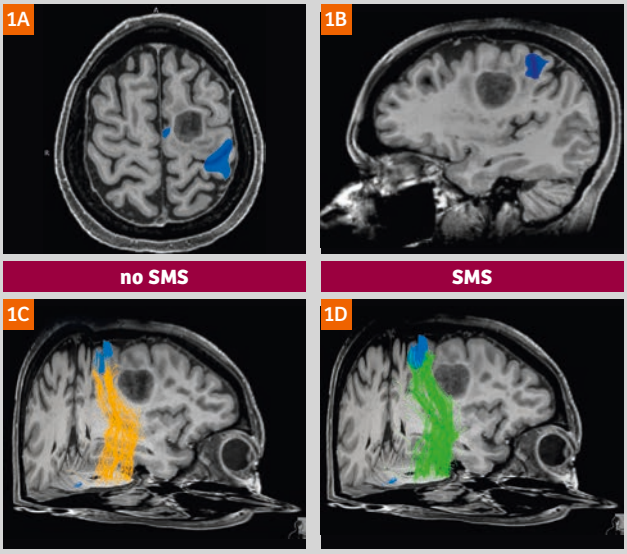

1A–B: In this patient, we found a left frontal glial tumor, which is seen in this T1w sequence as a hypointense lesion. The dark blue area is the superimposed fMRI data, showing the right hand motor area, that will then be used to draw ROIs and seed tracts. It also allows the evaluation of the close relationship between the tumor and functional areas.

1C–D: 1C shows the functional area used as a starting point (dark blue) and display the white matter tracts (as orange fibers), but without SMS imaging. On 1D, the same ROI allows the seeding of the white matter tracts (green fibers), this time with SMS imaging. If in both cases, we identify the corticospinal tract of the right hand, qualitatively, we can see that the green tracts are more numerous and denser, more precise than the orange ones. Quantitatively, this is in line with the results that show for this patient 216 fibers with no-SMS and 957 fibers with SMS.

mainly about time and quality. First, it requires increased time spent by the patients in the machine, stretching their tolerance even more than in a standard MRI acquisition. Second, it slows down considerably the workflow, raising concerns about delays and waiting lists. And third, in order to keep its relevance to clinicians, there can be no compromise on the quality of the data, even if we try to reduce the exam time.

It is in this particular context that Simultaneous Multi-Slice (SMS) imaging was seen as a promising tool in our clinical setting, and we started using it in July 2016. SMS was designed to increase the temporal efficiency [1] of MRI acquisitions, whether to reduce the exam duration or to improve the quality of imaging, for example, using more directions in diffusion imaging to reduce noise and improve tractographic data. With the progress made in parallel imaging and reconstruction algorithms [2], it is now possible to acquire several imaging slices concurrently, without affecting the signal-to-noise ratio [1], for significantly reduced exam durations.

If diffusion tensor imaging has different clinical uses, the one of interest here is the study of white matter tracts through tractographic reconstructions. To do so, we acquire through multiple directions for the whole brain voxel-wise data about diffusivity (as a vector with its strength and directionality, as well as a scalar value). If diffusion tensor imaging (DTI) has been used extensively in the last few years [4], high-angular resolution diffusion imaging (HARDI) is the promising new way to bring further the study of white matter, as it more robustly addresses the issue of crossing fibres [5], paving the way to more valid tractography.

However, diffusion imaging is time consuming to acquire; the conventional sequence used in our practice takes around 10 minutes. With SMS, it would become possible for us to reduce this time or acquire images of higher quality in the same acquisition time.

Together with SMS, we use functional magnetic resonance imaging (fMRI), coupled with Blood-oxygen-level dependent (BOLD) contrast imaging, to display and locate functional brain areas, as activated following certain tasks, for example, soliciting hand mobility or language [3].

Our clinical setting is part of the CHU de Québec – Université Laval, one of the three largest medical centers in Canada. Our teaching hospital has a specialty axis in neuroscience, including expertise in neuro-oncology. For the implementation of this project, our team includes four neurosurgeons, a neuro-radiologist, a radiology resident, and a biomedical engineer, in addition to a neuro-psychologist for fMRI tasks.

Case-based presentation

In our center, when a patient is referred by neurosurgeons for a pre-operative evaluation of a brain tumor, we start by a conventional MRI acquisition, using a 3T MAGNETOM Skyra, with 32-channel head coil (Siemens Healthcare, Erlangen, Germany). Our routine exam includes a 3D MPRAGE T1-weighted (pre- and post-gadolinium), T2-weighted FLAIR and SWI sequences. This allows us to do an anatomical description, to locate the lesion precisely, and describe its extension and impact on surrounding structures (cf. Figures).

Case 2

Figure 2: We imaged five other patients, again with and without SMS, but this time, not using SMS to reduce exam duration, but to go from a 30% gap protocol with 50 slices to a no-gap protocol with 60 slices, without changing other parameters (as TR for example). We found that by doing so, in an equivalent time, we observed an average of 94% increase in the number of fibers, improving data quality significantly.

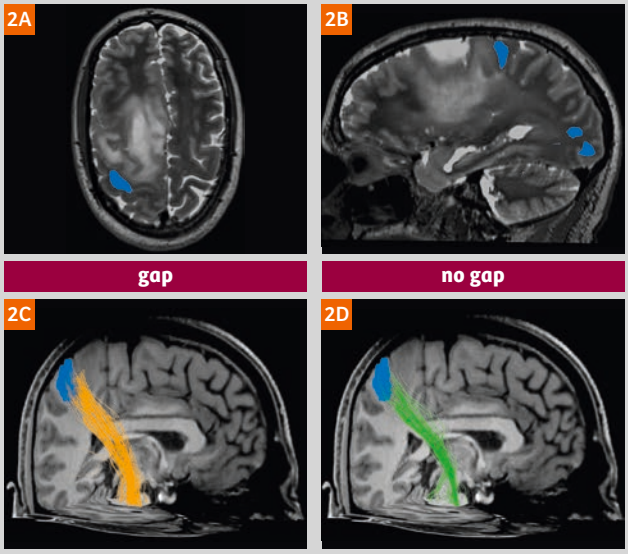

2A–B: In this patient, we found a right parietal glial tumor, with important surrounding infiltration, as shown here with hyper-intensities on a T2 sequence. The dark blue areas are superimposed fMRI data, displaying the relationship between the tumor (and its infiltration) and the functional areas (here the left hand motor area).

2C–D: On these images, we see the same fMRI areas (dark blue) used to draw ROIs and seed the tracts. On 2C, we see the cortico-spinal left hand tracts found using the «gap» protocol (224 orange fibers). On 2D, we see the same tracts, but this time using the «no-gap» protocol (516 fibers). The no-gap protocol is therefore numerically superior and qualitatively easier to interpret with thicker, denser, more precise tracts.

We then proceed to perform the BOLD fMRI data acquisition. A neuropsychologist in our center thoroughly evaluates each patient to determine which paradigms are most adapted to his/her condition and consequently chooses the appropriate series of tasks, for example to define specifically the motor areas of hand, foot and mouth, and the language areas. While resting in the scan, the patient is therefore asked to perform these various tasks to activate these functionally-important areas (cf. Figures). In addition to the clinically-relevant data they give by themselves, these activated zones shown on fMRI sequences will then be used in the next step to draw regions-of-interest (ROI) to seed white matter tracts.

For the DTI, we acquire diffusion tractography data (64 directions, b-value = 1500 s/mm^2), using high-angular resolution diffusion imaging (HARDI). This gives us numerical values for fractional anisotropy (FA), a scalar value which can be used to assess the integrity of the fibers (as FA is known to be a proxy of microstructural damage in white matter tracts, indicating the directionality of diffusion in axons [4]), but also gives us vector values which are then processed to extract tractographic data. Our data post-processing involves the use of FSL 5.0.9 [6], MRtrix [7], Mi-brain by Imeka [8] softwares to make the brain extraction, segmentation, statistics, reformatting and to draw ROIs to seed tracts (cf. Figures).

The combination of anatomical, functional, and tracto-graphic data can now finally be interpreted as a whole to craft the surgical approach.

Conclusion

When we first started using Simultaneous Multi-Slice imaging, we compared our data, with and without SMS (cf. Figure 1), mainly to save acquisition time; lately, we have focused on optimizing the quality of data, using SMS to improve acquisition of diffusion data, comparing protocols with and without gaps (cf. Figure 2).

We found that SMS imaging in a pre-operative evaluation of a brain tumor is useful, with regards to time and quality. By reducing acquisition time, it improves the patient's experience, spending less time in the device, sometimes going as far as to make additional sequence acquisitions possible in patients who would have otherwise asked to stop the exam out of discomfort. Also, the quality of the data was improved, possibly by reducing motion artifacts, as the scanning time was reduced (and patient's restlessness concurrently) [9]. This improvement, paired with the integration of a no-gap technique, allowed for improved spatial resolution. This gave more precise and denser tracts, a precious tool for neurosurgeons when planning their intervention. By clearly drawing the thin line between tumor and sane brain parenchyma, it optimizes the balance between removing as much neoplasm as possible and preserving brain functions; it may also make fully anesthetized surgery possible (instead of the more complicated and patient-displeasing awaken surgery), the full extent of functionally-relevant white matter tracts close to the lesion being known.

Now that we have integrated SMS imaging to our routine and used it to optimize our diffusion tractography data, our next step is to compare the temporal benefit of going from SMS-2 to SMS-3, while maintaining data quality. Then, we will use SMS to try to improve our fMRI-BOLD technique, by doubling acquired volumes to enhance data quality, to further enhance our value-based approach to clinicians.

References

1 Setsompop K et al. Advancing diffusion MRI using SMS EPI. MAGNETOM Flash. 63 (3), 2015.
2 Barth M, Breuer F, Koopmans PJ et al. Simultaneous multislice (SMS) imaging techniques. Magnetic resonance in medicine. 2016, 75 (1): 63-81.
3 Schuknecht B, Barath K. Introduction to advanced techniques in MR neuroimaging. MAGNETOM Flash 52 (2), 2013.
4 Basser PJ, Pierpaoli C. Microstructural and physiological features of tissues elucidated by quantitative-diffusion-tensor MRI. J Magnet Reson B. 1996, 111(3): 209-219.
5 Descoteaux M, Angelinao E, Fitzgibons S. Apparent diffusion coefficients from high angular resolution diffusion imaging: estimation and applications. Magn Reson Med. 2006, 56(2): 395-410.
6 Jenkinson M, Beckmann CF, Behrens TE, Woolrich MW, Smith SM. FSL. NeuroImage. 2012 62:782-90.
7 MRtrix, Tournier JD et al., Brain Research Institute, Melbourne, Australia, 2012;
8 MI-Brain, Imeka Medical Imaging, Descoteaux M et al., Imeka Solutions inc., Sherbrooke, Canada, 2015.
9 Bartsch A. SMS imaging for presurgical BOLD fMRI and diffusion tractography: Case Illustrations, MAGNETOM Flash, 63 (3), 2015.

Contact

Christian Berthelot
CHU de Québec – Université Laval

1401, 18ième rue
Québec, QC, Canada
G1J 1Z4
christianberthelot@gmail.com


Louis-Olivier Bouchard


Maxime Villeneuve


Christian Berthelot

The Assessment of Endolymphatic Hydrops with High-resolution 3D Real Inversion Recovery and 3D Fluid Attenuated Inversion Recovery Sequences

Meng Long Zhao[1]; Zhuang Liu[3]; Yan Sha[1]; Ru Jian Hong[1]; Yu Shu Cheng[1]; Fang Zhang[1]; Qian Ru Wu[2]; Wen Lin Tang[4]; Chun Fu Dai[2]

[1] Department of Radiology, Eye, Ear, Nose and Throat Hospital, Fudan University, Shanghai, China
[2] Department of Otology and Skull Base Surgery, Eye, Ear, Nose and Throat Hospital, Fudan University, Shanghai, China
[3] Department of Radiology, Cancer Hospital, Fudan University, Shanghai, China
[4] Siemens Healthineers, MR Scientific Marketing, Shanghai, China

Introduction

Since the initial study by Nakashima et al. [1] who demonstrated that endolymphatic hydrops in patients with Ménière's disease can be visualized using MR imaging following an intratympanic injection of gadolinium, this topic has gained strong clinical interest internationally [2–13]. The two most common sequences used in the evaluation of endolymphatic hydrops are a 3D Fluid Attenuated Inversion Recovery with variable flip angles turbo spin echo sequence (3D SPACE FLAIR) and a 3D real inversion recovery sequence (3D real IR) [1–3]. However, the use of the two sequences varies across different countries. The aim of this study was to compare and contrast the two sequences in terms of the imaging results to best determine their use in clinical practice.

Methods

Patients who have received a diagnosis of Ménière's disease or delayed endolymphatic hydrops from the otolaryngologist (in the period October 2013 to May 2014) were retrospectively identified and their MR images analyzed. Ménière's disease was diagnosed according to the diagnostic criteria established by the Chinese Society of Otolaryngology of the Chinese Medical Association in 2006 [14] while delayed endolymphatic hydrops was diagnosed according to the criteria of Komatsuzaki et al. [15]. Patients must have undergone MR imaging of their endolymphatic system with no significant head movement during imaging and have no history of otitis media or inner ear surgery. 40 patients were identified; 26 males and 33 females ranging in age from 19 to 67 years (mean = 48 ± 13 years), with 52 affected ears. The main symptoms reported by the patients include dizziness, hearing loss, tinnitus and ear stuffiness.

All patients underwent MR imaging 24 hours following an injection of contrast media into the tympanum through the tympanic membrane. An otology clinician with long experience in auripuncture injected a Magnevist solution (Bayer Healthcare, Berlin, Germany) that has been diluted 8-fold with saline into the tympanum through the tympanic membrane of the patient. The injection was performed using a 23-G needle with a 1 ml syringe and approximately 0.4–0.5 mm of the diluted solution was injected. Following the injection, patients were advised to rest their head for an hour, speak as little and swallow as little as possible. Patients were imaged 24 hours later on a MAGNETOM Verio with a 32-channel Head coil (see Table 1 for sequence parameters).

The images were assessed for differences in signal-to-noise ratio (SNR) and contrast-to-noise ratio (CNR) and also for the ability to visualize the presence of endolymphatic hydrops. Analyses for SNR and CNR were performed by

	3D SPACE FLAIR	3D real IR
Repetition time (TR) (ms)	6000	9000
Echo time (TE) (ms)	387	181
Inversion time (TI) (ms)	2100	1730
Echo train length	173	--
Voxel resolution (mm)	0.7 x 0.7 x 0.6	0.4 x 0.4 x 0.8
Field-of-view (FOV) (mm)	220 x 220	160 x 160
Acquisition time (TA) (mins)	6:26	14:32

Table 1: Imaging parameters of the 3D SPACE FLAIR and 3D real IR sequences.

first identifying the 3D real IR image where the vestibule is clearly visible and a circle region-of-interest (ROI) of 0.02 cm^2 was drawn in the perilymph within the perilymphatic space. The ROI was replicated on the corresponding 3D SPACE FLAIR image and manually matched in location. Similar ROIs were created in the cerebrospinal fluid (0.1 cm^2) within the cerebellopontine angle and in the brainstem (0.5 cm^2). SNR ratio was defined as:

$$\frac{(S_{vestibule} - S_{cerebrospinal\ fluid})}{\sigma_{brainstem}}$$

$S_{vestibule}$ = vestibular ROI average signal intensity

$S_{cerebrospinal\ fluid}$ = cerebrospinal fluid ROI average signal intensity

$\sigma_{brainstem}$ = brainstem ROI signal intensity standard deviation

Evaluations for the presence of endolymphatic hydrops in the inner ear, vestibule and the basal, middle and apical turns of the cochlea of all affected ears were performed. For each turn of the cochlea, the diagnosis was made according to the standards proposed by Nakashima et al. [16]. The absence of endolymphatic hydrops is defined by no displacement of Reissner's membrane inside the cochlea (Fig. 1). The presence of cochlear endolymphatic hydrops is visualized by the significant expansion of the non-enhancing endolymphatic space relative to the contrast-enhanced perilymphatic area (Fig. 2). The vestibule is considered normal if the area of low signal in the vestibule is confined to a level above the horizontal semicircular canal; an extension of the low signal area downwards below the horizontal semicircular canal is considered to be indicative of endolymphatic hydrops [5]. When endolymphatic hydrops are seen in either the cochlea or vestibule, a positive diagnosis of endolymphatic hydrops is made for the inner ear.

Results

SNR of the 3D real IR (28.06 ± 12.71) was significantly higher than the 3D SPACE FLAIR (17.46 ± 6.38; $t = 6.37$, $p < 0.05$). CNR was likewise significantly higher for the 3D real IR (33.79 ± 13.52) compared to the 3D SPACE FLAIR (15.40 ± 6.04; $t = 11.11$, $p < 0.05$). In the 3D real IR images, the endolymphatic space (low signal), the perilymphatic space (high signal) and bone (intermediate signal) can be differentiated (Fig. 2B, D). In comparison, with the 3D SPACE FLAIR, it is more difficult to differentiate between the endolymphatic space and the surrounding low-signal bone (Fig. 2A, C).

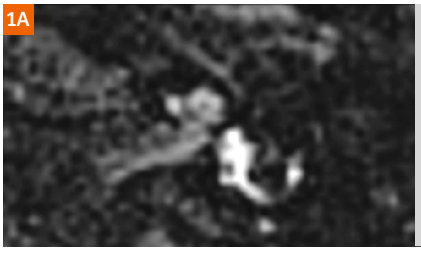

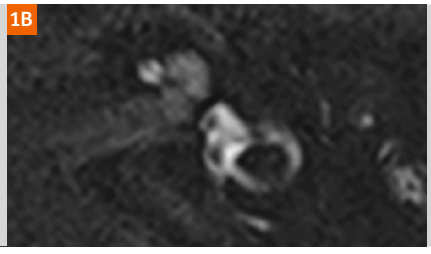

Figure 1: 3D SPACE FLAIR **(1A)** and 3D real IR **(1B)** imaging of a normal left inner ear. There are no indications of enlarged endolymphatic spaces and displacement of Reissner's membrane.

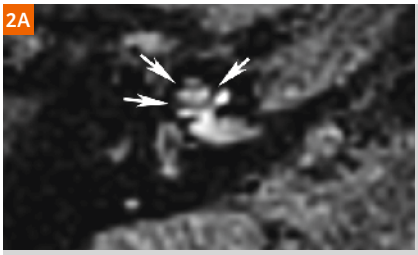

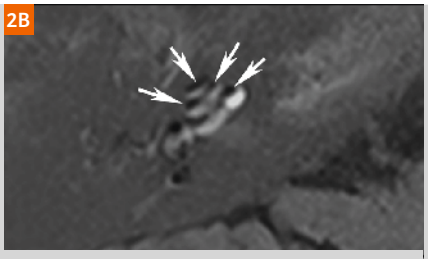

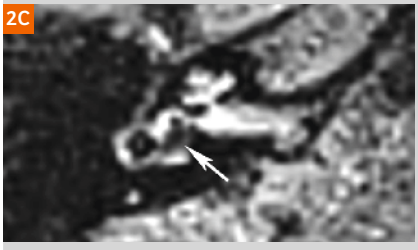

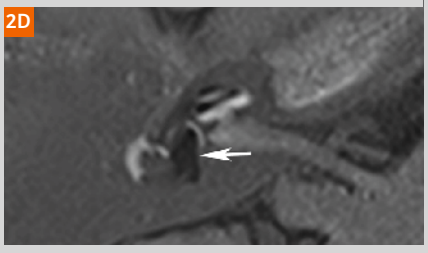

Figure 2: 3D SPACE FLAIR **(2A, C)** and 3D real IR **(2B, D)** imaging of the right ear of a patient with Ménière's disease. The presence of endolymphatic hydrops (marked by arrows) can be visualized within the cochlea (2A and B) and within the vestibule (2C and D). While the presence of endolymphatic hydrops within the cochlea is visible on the 3D SPACE FLAIR image (2A), the 3D real IR image clearly shows a severe presence at each turn of the cochlea (2B). The presence of vestibular endolymphatic hydrops is visible as an enlarged area of low signal in the patient's right vestibule on the 3D SPACE FLAIR (2C) and 3D real IR (2D). Note that in the 3D real IR image, there is clear differentiation between the endolymphatic space (low signal), the perilymphatic space (high signal) and the surrounding bone (intermediate signal) while it is more difficult to differentiate between the endolymphatic space from the surrounding low-signal bone in the 3D SPACE FLAIR image.

Comparing the 3D real IR to the 3D SPACE FLAIR, the detection rates of endolymphatic hydrops were identical for the vestibule while significantly higher in all turns of the cochlea for the 3D real IR (Table 2). In all cases, endolymphatic hydrops which could be detected in the 3D SPACE FLAIR could also be visualized in the 3D real IR (Figs. 2A–D). In addition, there were a significant number of cases where milder cochlear endolymphatic hydrops were visible only in the 3D real IR images (Figs. 3 and 4). In particular, detection rate for endolymphatic hydrops at the apical turn of the cochlea was much lower for the 3D SPACE FLAIR (19.2%) images compared to the 3D real IR images (88.5%; Fig. 4).

Discussion and conclusions

The two most commonly used MR sequences for imaging endolymphatic hydrops are the 3D SPACE FLAIR and 3D real IR. The 3D SPACE FLAIR, using variable flip angles, achieves high-resolution 3D imaging in relatively short scan times and enables differentiation between the low-signal endolymphatic space and the high-signal perilymphatic space. However, with this sequence, the endolymphatic space cannot be distinguished from the surrounding low-signal bone (Figs. 3 and 4). The 3D real IR sequence is an inversion-recovery turbo spin-echo (TSE) sequence with real reconstruction [2, 3]. Information about the magnetization polarity is preserved and the contrast reflects the real signal value instead of the absolute value. With the appropriate T1 (≈ 1700 ms for 3T), the endolympatic space will be hypo-intense (negative value), the perilymphatic space will be hyper-intense (positive value) while the surrounding bone will be iso-intense (near 0), which enables differentiation between these three structures with a single scan. In addition, the higher resolution used for the 3D real IT may help in the differentiation of finer structures in the inner ear and have been adopted more in recent studies [2, 7, 9, 10]. To our knowledge, this is the first study, to date, which reports a systematic comparison of the diagnostic quality of these two sequences.

Significantly higher signal-to-noise and contrast-to-noise ratios were found for the 3D real IR sequence compared to the 3D SPACE FLAIR sequence. The higher contrast-to-noise ratio reflects the difference in signals between the endolymphatic space and the perilymphatic space, with the 3D real IR sequence being clearly superior.

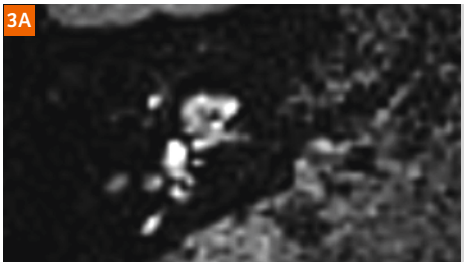

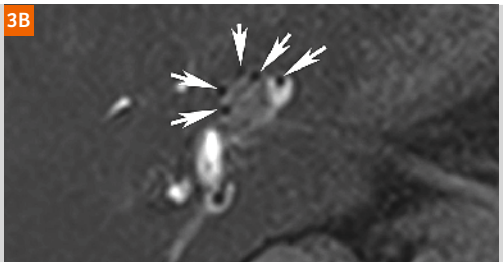

Figure 3: A patient with Ménière's disease of the right ear. The endolymphatic hydrops were not detected on the 3D SPACE FLAIR image **(3A)** while they were clearly visible at each turn of the cochlea in the 3D real IR image **(3B; arrows)**.

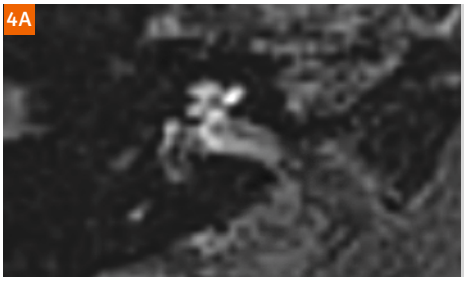

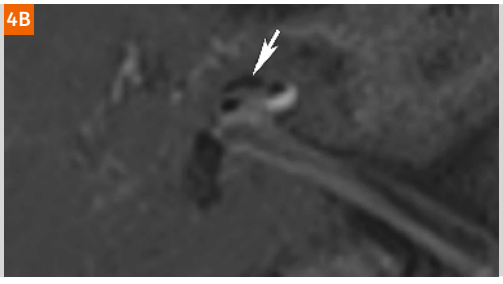

Figure 4: Endolymphatic hydrops in the cochlear and vestibule were visible in the 3D SPACE FLAIR **(4A)** image of this patient with Ménière's disease. However, hydrops at the apical turn of the cochlea were only visible in the 3D real IR **(4B)** image (arrow).

	3D SPACE FLAIR		3D real IR		*p* value
	Ear	Rate (%)	Ear	Rate (%)	
Affected side's inner ear[1]	41	78.8	49	94.2	0.008
Vestibule	39	75.0	39	75.0	1.000
Basal turn of the cochlea	33	63.5	46	88.5	0.000
Middle turn of the cochlea	37	71.2	46	88.5	0.004
Apical turn of the cochlea	10	19.2	46	88.5	0.000

Table 2: Detection rate for endolymphatic hydrops in the affected ears (n = 52).

[1] Noted as positive if endolymphatic hydrops were detected in any part of the inner ear.

As endolymphatic hydrops occurs mainly in the cochlea and balloon and less frequently in the utricle and semicircular canal [17, 18], our assessment was limited to the cochlea and the vestibule. A significantly higher detection rate for endolymphatic hydrops in the cochlea, especially in the apical turn, was achieved for the 3D real IR sequence relative to the 3D SPACE FLAIR while detection rates were the same in the vestibule.

The cochlear structure is small and highly detailed; there are 2.50–2.75 turns, and the diameter of each turn is very small (the diameter of the basal turn is about 1.4 mm) [21]. In the early stage of Ménière's disease, endolymphatic hydrops start in the apical turn of the cochlea and will grow downward when the extent of the hydrops increases. For the 3D SPACE FLAIR sequence, the detection rate of hydrops was much lower in the apical turn (n = 10) compared to the middle (n = 37) and basal (n = 33) turns, which is inconsistent with the known clinical evolution of this disease. In contrast, the detection for the 3D real IR sequence was consistent across the three turns and better reflects the evolution of the disease (Figs. 3 and 4).

There are two reasons as why it is more difficult to visualize hydrops at the apical turn of the cochlea with the 3D SPACE FLAIR sequence. First, the endolymphatic space is virtually indistinguishable from surrounding bone which makes it extremely difficult to visualize hydrops in small structures such as the apical turn. Secondly, the signal-to-noise ratio and the resolution of the sequence are lower, again making it difficult to appreciate the smaller structures of the inner ear.

The 3D-real IR sequence has a higher CNR and resolution with a contrast that provides strong advantage in the display of endolymphatic hydrops. However, the scan time of the 3D real IR is significantly longer, generally taking around 12 to 16 minutes, which has limited its use on a wider clinical basis. With further optimization of the sequence parameters and the development of new MR hardware, this problem is expected to be resolved in the near future.

In conclusion, the 3D real IR sequence is superior to the 3D-FLAIR-VFL sequence for the MR assessment of endolymphatic hydrops and may help in the early diagnosis of Ménière's disease and other diseases of the inner ear.

References

1 Nakashima T, Naganawa S, Sugiura M, Ternaishi M, Sone M, Hayashi H et al. Visualization of endolymphatic hydrops in patients with Ménière's disease. Laryngoscope 2007; 117(3): 415-420.
2 Naganawa S, Satake H, Kawamura M, Fukatsu H. Separate visualization of endolymphatic space, perilymphatic space and bone by a single pulse sequence; 3D-inversion recovery imaging utilizing real reconstruction after intratympanic Gd-DTPA administration at 3 Tesla. Eur Radiol, 2008, 18(5): 920-924.
3 Naganawa S, Ishihara S, Iwano S, Sone M, Nakashima T. Three-dimensional (3D) visualization of endolymphatic hydrops after inversion-recovery turbo spin-echo (TSE) sequence and application of a 32-channel head coil at 3T. J Magn Reson Imaging 2010; 31(1): 210-214.
4 Chen X, Zhang XD, Gu X, et al. Clinical application of inner ear imaging technology by gadolinium injection through the tympanum. National Medical Journal of China 2011; 91(46): 3246-3249. DOI: 10.3760/cma.j.issn.0376-2491.2011.46.003.
5 Fang ZM, Liu Y, Cao DR, et al. Gadolinium imaging MR scoring for perilymphatic space and its diagnostic value for Ménière's disease. Chinese Journal of Radiology 2012; 46(8): 719-723.
6 Iida T, Teranishi M, Yoshida T, Otake H, Sone M, Shimono M, et al. Magnetic resonance imaging of the inner ear after both intratympanic and intravenous gadolinium injections. Acta Otolaryngol 2013; 133(5): 434-438.
7 Baráth K, Schuknecht B, Monge Naldi A, Schrepfer T, Bockisch CJ, Hegemann. Detection and grading of endolymphatic hydrops in Ménière's disease using MR imaging. Am J Neuroradiol 2014; 35: 1-6.
8 Liu Y, Cao DR, Fang ZM, et al. Inner ear perilymphatic fluid enhanced MRI characteristics of patients with vertigo and sudden deafness. Chinese Journal of Radiology, 2014; 48(12): 996-999.
9 Naganawa S, Yamazaki M, Kawai H, Bokura K, Iida T, Sone M, et al. MR imaging of Ménière's disease after combined intratympanic and intravenous injection of gadolinium using HYDROPS2. Magn Reson Med Sci 2014; 13(2): 133-137.
10 Naganawa S, Nakashima T. Visualization of endolymphatic hydrops with MR imaging in patients with Ménière's disease and related pathologies: current status of its methods and clinical significance. Jpn J Radiol 2014; 32(4): 191-204.
11 Shi HB, Li YH, Yin SK, Zou J. The predominant vestibular uptake of gadolinium through the oval window pathway is compromised by endolymphatic hydrops in Ménière's disease. Otol Neurotol 2014; 35(2): 315-322.
12 Gürkov R, Berman A, Dietrich O, et al. MR volumetric assessment of endolymphatic hydrops. Eur Radiol 2015; 25(2): 585-595.
13 Wu Q, Dai C, Zhao M, Sha Y. The correlation between symptoms of definite Ménière's disease and endolymphatic hydrops visualized by magnetic resonance imaging. Laryngoscope 2016; 126(4): 974-979.
14 Editorial Committee of the Chinese Journal of Otorhinolaryngology Head and Neck Surgery, Otolaryngology Subcommittee of the Chinese Medical Association. Diagnosis Basis and Efficacy Assessment of Ménière's disease (2006, Guiyang). Chinese Journal of Otorhinolaryngology Head and Neck Surgery 2007; 42(3):163.
15 Komatsuzaki A, Futaki T, Harada Y, Hozawa J, Ishii T, Kamei T, et al. Delayed endolymphatic hydrops. The guideline for standardization of diagnostic criteria in vertiginous diseases. Equilib Res 1987; 47: 249-250.
16 Nakashima T, Naganawa S, Pyykkö I, Gibson WPR, Sone M, Nakata S et al. Grading of endolymphatic hydrops using magnetic resonance imaging. Acta Otolaryngol 2009; 129: 5-8.
17 Schuknecht HF. Endolymphatic hydrops: can it be controlled? Ann Otol Rhinol Laryngol 1986; 95(1): 36-39.
18 Wang ZM. Class II Vertigo Surgery. Chin J Otolaryngol 2002; 2(3):198-200.

Contact

Professor Yan Sha
Department of Radiology
Eye, Ear, Nose and Throat Hospital
Fudan University

No. 83 Fenyang Road
Xuhui District, Shanghai 200031
China
cjr.shayan@vip.163.com

Rapid MR Susceptibility Imaging of the Brain Using Segmented 3D Echo-Planar Imaging (3D EPI) and its Clinical Applications

Pascal Sati[1]; Sunil Patil[2]; Souheil Inati[3,4]; Wen-Tung Wang[5]; J. Andrew Derbyshire[6]; Gunnar Krueger[7]; Daniel S. Reich[1,8]; John A. Butman[5,8]

[1] Translational Neuroradiology Section, National Institute of Neurological Disorders and Stroke, National Institutes of Health, Bethesda, MD, USA
[2] Siemens Healthineers, HC NAM USA DI MR COLLAB, Bethesda, MD, USA
[3] Functional MRI Core, National Institute of Mental Health, National Institutes of Health, Bethesda, MD, USA
[4] InatiAnalytics, Potomac, MD, USA
[5] Center for Neuroscience and Regenerative Medicine, Henry Jackson Foundation, Bethesda, MD, USA
[6] Section of Functional Imaging Methods, Laboratory of Brain and Cognition, National Institute of Mental Health, National Institutes of Health, Bethesda, MD, USA
[7] Siemens Healthineers, HC NAM USA DI MR COLLAB NE, Boston, MA, USA
[8] Radiology and Imaging Sciences, Clinical Center, National Institutes of Health, Bethesda, MD, USA

Abstract

MR susceptibility imaging (e.g., T2*, SWI, QSM) is a powerful tool for imaging blood vessels, hemorrhage, calcifications, and iron deposition in the normal and diseased brain with exquisite detail. To obtain such images at high resolution, very long image acquisition times are typically needed when using the conventional 3D gradient-echo sequence. Using a novel acquisition strategy called segmented (or multi-shot) 3D echo planar imaging (3D EPI)[1], we have found that MR susceptibility images can be produced with high resolution and no loss in diagnostic clarity. Our experience at the NIH across the range of field strengths indicates that the 3D EPI acquisition may be used to obtain very short scan times (1–3 min) at standard image resolutions or to increase the resolution to obtain submillimeter isotropic images in scan times on the order of 5–6 minutes. The ability to perform

[1] WIP, the product is currently under development and is not for sale in the US and in other countries. Its future availability cannot be ensured.

1

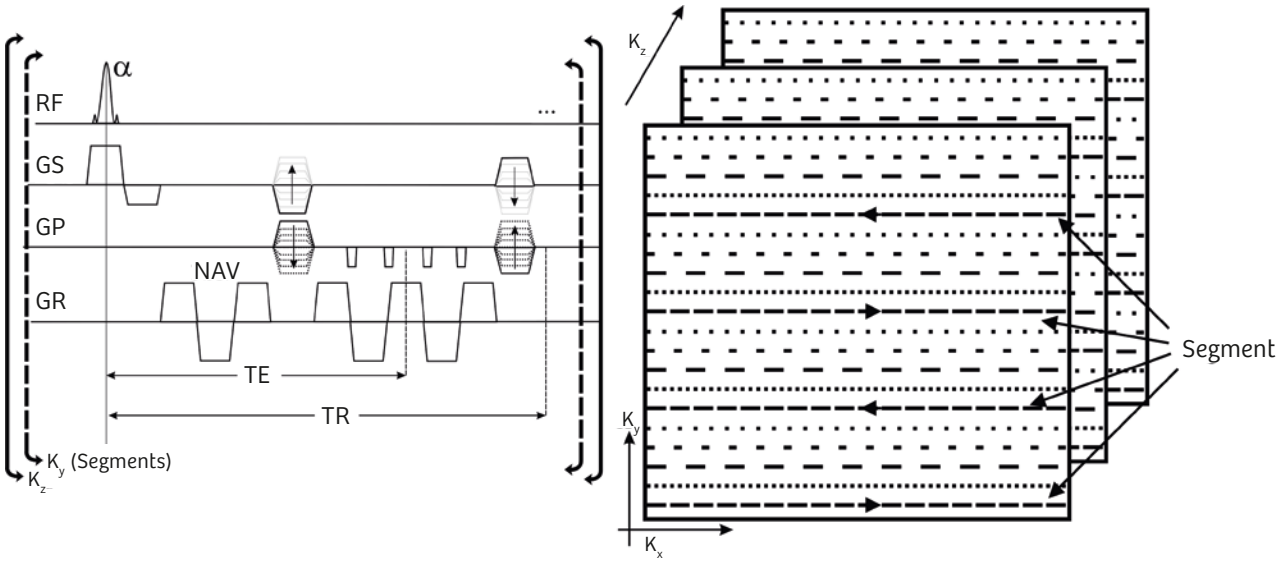

Figure 1: 3D EPI sequence diagram and its corresponding *k*-space trajectory.

rapid susceptibility imaging allows for its integration into routine clinical imaging, reduces the likelihood of motion artifact, and may be of particular benefit in the acute clinical setting such as stroke or traumatic brain injury where minimizing time in the scanner is paramount. Furthermore, the new capability to perform submillimeter isotropic imaging in clinically acceptable scan times opens up new avenues of clinical research in demyelinating diseases through the investigation of the relationship between central veins and white matter lesions.

Introduction

MR susceptibility imaging has become an essential clinical tool to visualize blood vessels, hemorrhage, calcifications, and iron deposits in the brains of people with neurological disorders. Susceptibility-based MR images can take various forms, including T2* contrast, susceptibility-weighted imaging (SWI), phase imaging, and quantitative susceptibility mapping (QSM). Because the image acquisition typically relies on a spoiled gradient echo (GRE) sequence with a relatively long TE to allow for susceptibility effects to influence contrast, scan time can be quite long, particularly when whole brain coverage and/or high resolution are required (e.g. > 15 min for 1 mm isotropic whole brain). Long acquisition times are problematic in a clinical setting, where subjects are likely to move during the scan resulting in blurred or unusable images. Therefore, slice thickness is usually limited to 2–4 mm while the field-of-view (FOV) covers only the supratentorial brain in order to maintain clinically compatible scan time.

To speed up the acquisition of MR susceptibility imaging, we recently developed a prototype volumetric (3D) segmented echo-planar imaging (EPI) sequence[1] that allows rapid imaging of the entire brain at submillimeter resolution. In a manner analogous to the use of an echo train in turbo spin echo to accelerate the acquisition of 3D spin echo, we use an echo train in segmented EPI to accelerate the acquisition of a 3D gradient echo. In this article, we describe this novel approach and present acquisition protocols developed across the range of magnetic field strengths to illustrate the application of this technique in different clinical and research applications.

MRI technique

The 3D EPI approach was originally introduced for whole-brain functional MRI with high-resolution at 7T [1]. It was then demonstrated to be a viable solution for fast high-resolution anatomical imaging of the brain at 7T when using a segmented approach with relatively short EPI train lengths in order to limit distortions and image blurring [2]. Through a collaboration between different institutes at the National Institutes of Health (NIH, Bethesda, MD) and Siemens MR, we implemented a segmented 3D EPI technique as a WIP on *syngo* MR E11A and as a prototype sequence on *syngo* MR B17A, B20P, D13A/D (available as C2P from NIH) and tested on a variety of Siemens scanners (1.5T MAGNETOM Aera, 3T Biograph mMR, 3T MAGNETOM Skyra, 3T MAGNETOM Prisma, and 7T Research System, Siemens Healthcare, Erlangen, Germany), all sited at the NIH Clinical Center. The pulse sequence diagram of the 3D seg EPI and its corresponding *k*-space trajectory are depicted in Figure 1. The segmentation used a conventional interleaved *k*-space trajectory along the primary phase encoding direction (K_Y), while the secondary phase encoding (K_Z) was used to select partitions. In order to reduce the artifacts due to B_0 variation and odd-even line discrepancy; which is typical in EPI, state-of-the-art navigator approach (shown as "NAV" in Figure 1) was integrated. The EPI factor was typically set to 15 which acquires 15 phase-encoded lines of *k*-space data for each excitation as a compromise between improving imaging efficiency while limiting the level of image distortion and blurring. Different acquisition protocols were setup according to the scanner field strength (Table 1) to produce high isotropic resolution T2*-weighted (T2*w) images of the brain under 6 min (Fig. 2). Despite a short TR, T2*-weighting is the dominant contrast on the magnitude images due to the use of prolonged TE and a low flip angle which minimize the T1-weighting. Although no obvious

	Plane	TR (ms)	TE (ms)	FOV (mm)	Phase FOV (%)	Slices	Voxel size (mm)	Matrix	Phase direction	EPI factor	TA (mins)
1.5T MAGNETOM Area, Head/Neck 20 ch	Sag	64	37	228	94.1	256	0.75 iso	304	A >> P	15	5:23
3T MAGNETOM Biograph mMR, Head/Neck 16 ch	Ax	64	25	220	78.1	72	0.5 x 0.5 x 2.0	448	R >> L	15	1:30
	Sag	57	25	228	96.6	288	0.65 iso	352	A >> P	15	4:45
3T MAGNETOM Skyra, Head 32 ch & 3T MAGNETOM Prisma, Head 32 ch	Sag	64	35	250	81.3	256	0.65 iso	384	A >> P	15	5:46
7T research system, Head 32 ch	Ax	52	23	220	81.8	176	0.5 iso	440	R >> L	15	3:40

Table 1: 3D EPI acquisition protocols running on different Siemens scanners at NIH.

distortions could be detected on T2*w images, some noticeable areas of signal loss could be observed in the areas of poor B_0 field homogeneity (e.g. inferior frontal and temporal lobes). The 3D EPI protocol allows for reconstruction of magnitude, phase, SWI, and minimum intensity projection images which well depict the cerebral venous vasculature (Fig. 3). The phase images can be used to generate QSM images to map out the local magnetic susceptibility of brain tissues [3] (Fig. 3).

Application in multiple sclerosis

High-resolution T2*-weighted images are particularly useful to research clinicians for the purpose of detecting small veins inside cerebral white matter (WM) lesions, as this detection may aid with the diagnosis of multiple sclerosis (MS) [4]. When searching for central veins in WM lesions, whole-brain coverage is particularly important, since MS lesions can be found anywhere in the brain. Moreover, isotropic resolution is particularly useful to reformat images in any desired plane, a feature that is available on many radiology viewing platforms that enables veins to be well visualized irrespective of their orientation (Fig. 4).

Based on our experience with scanning 100+ MS patients using the high-resolution 3D EPI protocols at different field strengths, central veins are most conspicuous at 7T due to the increased resolution and contrast (Fig. 5). While central veins are visible at 1.5T and 3T, their detection can be facilitated by injecting a gadolinium-based contrast agent during the first minutes of the 3D EPI acquisition (Fig. 5). This is straightforward to implement when the MRI protocol already involves the use of contrast agent to detect newly enhancing MS lesions on T1-weighted images. Because there is usually a recommended 5-minute wait before running post-contrast imaging [5], the 3D EPI acquisition can be performed at that time, thus not prolonging the total scan time of the MRI exam.

Unlike T2-weighted fluid-attenuated inversion recovery (FLAIR) images, T2*-weighted and SWI images lack cerebrospinal fluid suppression and are, therefore, less able to demonstrate contrast between lesions and surrounding tissues, making the detection of lesions more difficult for the clinicians. To overcome these issues, our laboratory has developed and routinely generates an MR combined contrast, which we have called FLAIR* [6]. The FLAIR* approach uses the Siemens product sequence (SPACE IR) to acquire a 1 mm isotropic 3D FLAIR (for lesion detection) and our 3D EPI prototype sequence for 0.65 mm isotropic T2*-weighting (for vein detection); total acquisition time is <12 min. FLAIR* images are generated using simple processing steps: rigid co-registration, interpolation, and image multiplication (Fig. 6). Because of its close resemblance to the conventional FLAIR images, 3T FLAIR* can be readily interpreted by radiologists and neurologists.

Over the past couple of years, our fast, high-resolution 3D EPI protocols have been disseminated to a dozen

2

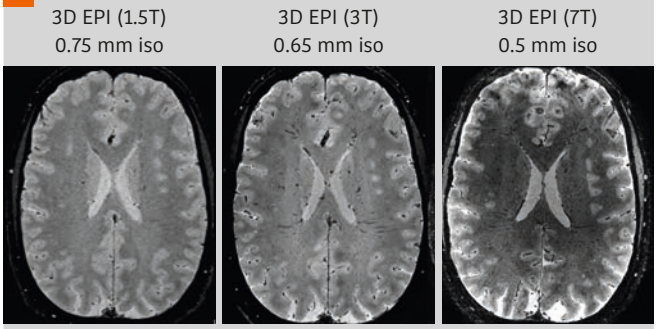

Figure 2: Representative 3D EPI images acquired on the same healthy volunteer at three different field strengths (1.5T, 3T and 7T). Submillimeter voxel dimensions were used for all scans (1.5T: 0.75 mm isotropic, 3T: 0.65 mm isotropic and 7T: 0.5 mm isotropic).

3

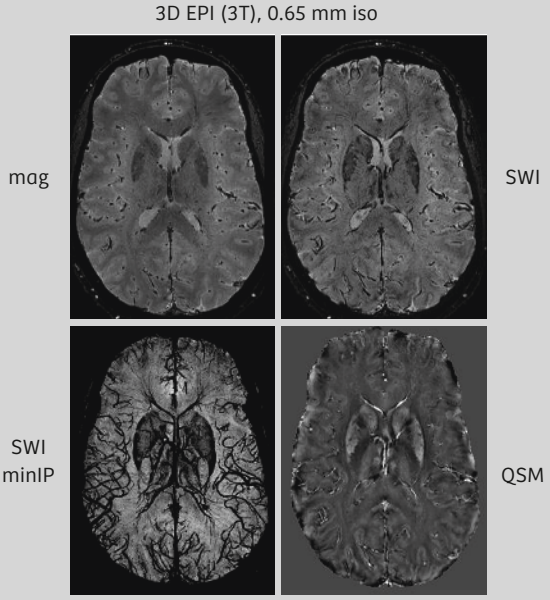

Figure 3: Different susceptibility-based contrasts obtained with 3D EPI protocol at 3T. T2*w contrast corresponds to the native magnitude images produced by the scanner. SWI and SWI mIP contrasts can also be generated by the scanner when using the WIP. QSM images are generated offline using the QSM reconstruction algorithm from Langkammer et al. (http://www.neuroimaging.at/pages/research/quantitative-susceptibility-mapping.php).

MRI centers specialized in MS across the US and Europe, resulting in several publications that illustrate its potential clinical value in MS [7–10]. Recent guidelines on the use of MRI in MS from the MAGNIMS group [5, 11] and the NAIMS cooperative [4] also mentioned 3D EPI and its combined FLAIR* contrast as promising MRI techniques for the clinical evaluation of the central vein sign in MS diagnosis.

4

3D EPI (3T), 0.65 mm iso

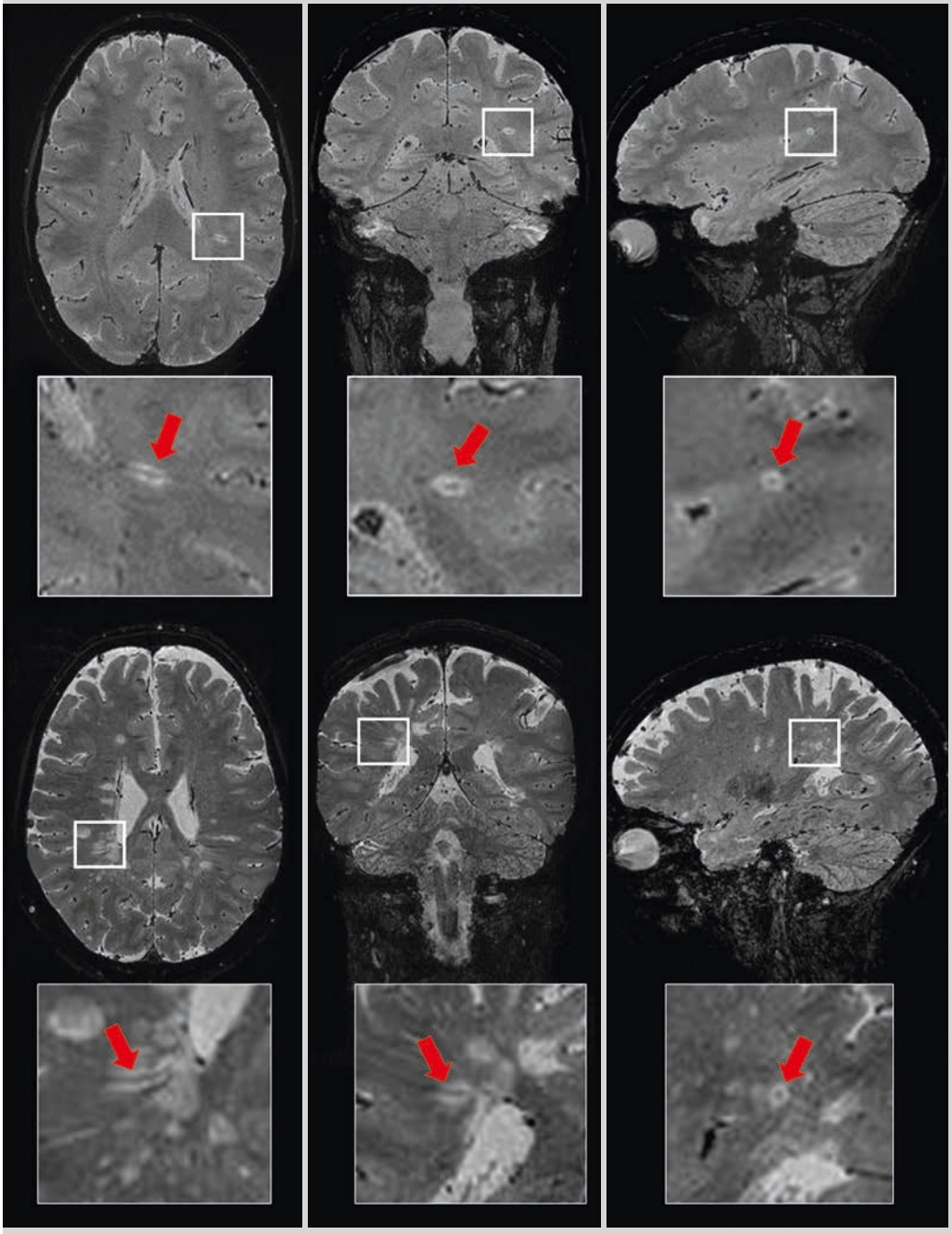

Axial Coronal Sagittal

Figure 4: 0.65 mm isotropic 3D EPI (magnitude) T2*w images acquired at 3T in two different MS patients. Images can be reformatted for multiplanar viewing, thus allowing the identification of small parenchymal veins running centrally through MS lesions (red arrows in the magnified boxes).

Application in the acute clinical setting (e.g. traumatic brain injury (TBI) and stroke)

One major limitation of MRI in the acute clinical evaluation of traumatic brain injury and stroke is the simple fact that the extended MRI exam can be quite long. Thus, despite the additional information that may be gained by MRI relative to CT for these indications [12], clinicians continue to rely on CT to rule out intracranial hemorrhage and to rely on clinical evaluations to guide therapy. Any rapid and comprehensive MRI examination must be able to evaluate for intracranial hemorrhage using gradient echo based techniques [13]. In the setting of TBI, SWI is preferred over GRE T2* [14] due to its greater sensitivity for microhemorrhage and is typically performed as an axial acquisition with 2.0 mm slice thickness and in plane resolution of 0.5 to 1.0 mm.

5

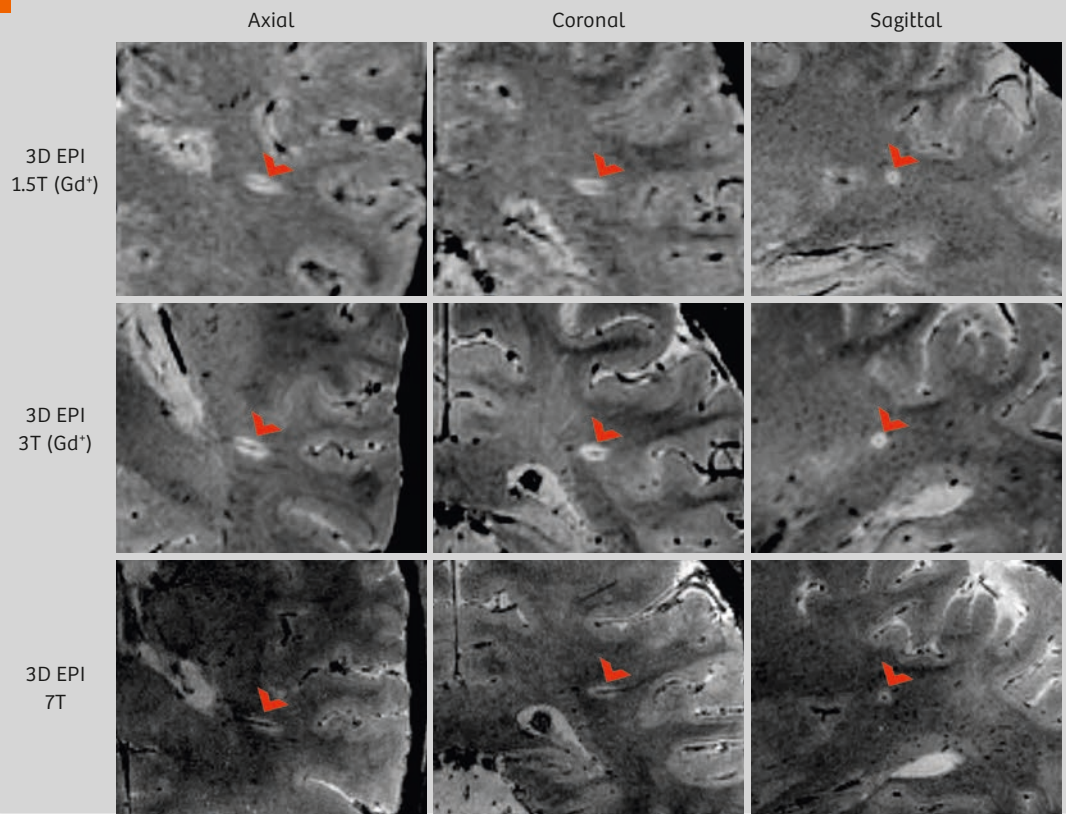

Figure 5: 3D EPI (magnitude) T2*w images in the same MS patient brain at three different field strengths (0.75 mm isotropic at 1.5T, 0.65 mm isotropic at 3T, and 0.5 mm isotropic at 7T). The same central vein inside an MS lesion can be detected at all field strengths and on all imaging planes (red arrows). Note that at 1.5T and 3T, images were acquired during the injection of gadolinium-based contrast agent (Gd+) to enhance the conspicuity of the parenchymal veins.

6

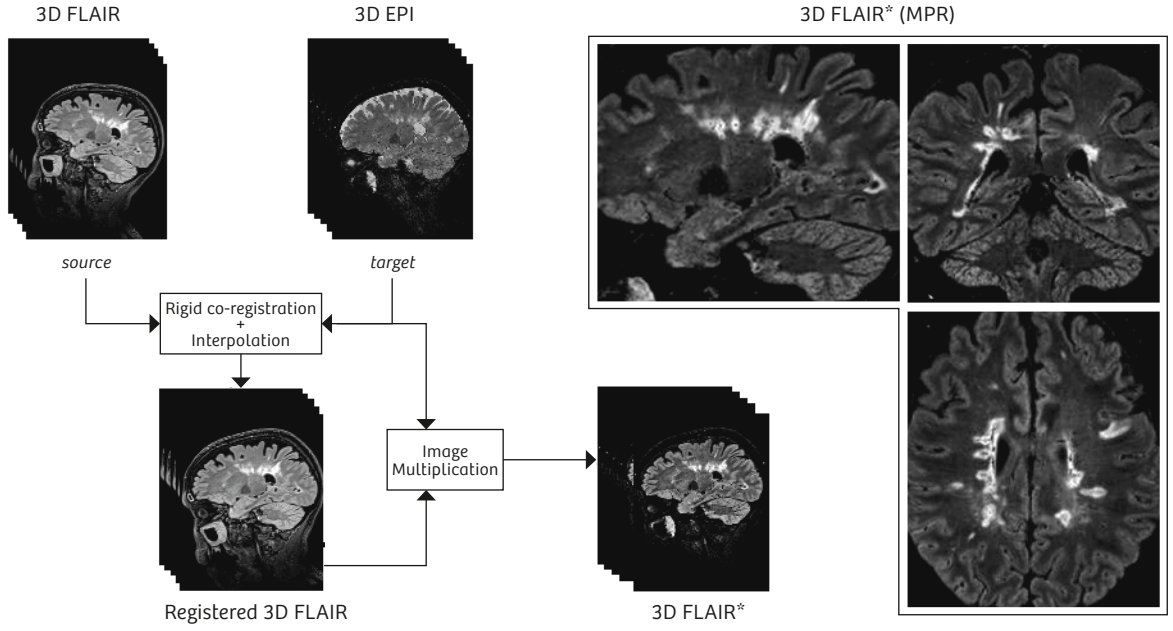

Figure 6: Workflow of the 3T FLAIR* processing pipeline. Native 3D FLAIR (1 mm isotropic) images are co-registered (rigid, 6 degrees of freedom) to native T2*w 3D EPI (0.65 mm isotropic) and interpolated (windowed sinc) to match the 3D EPI resolution. FLAIR* images are then generated by multiplying the registered 3D FLAIR images to the native 3D EPI images. Because FLAIR* images retain the high-isotropic-resolution from the native 3D EPI images, multiplanar reformatting (MPR) enables the reader to view FLAIR* images in any desired orientation. Our FLAIR* pipeline is currently performed offline after downloading the DICOM images from the NIH Radiology PACS system. Once the processing is completed, FLAIR* images are imported back into the PACS system to be read by NIH clinicians. Note that FLAIR* processing could also be done using the MR Arithmetics prototype[1] available under *syngo*.via Frontier.

7

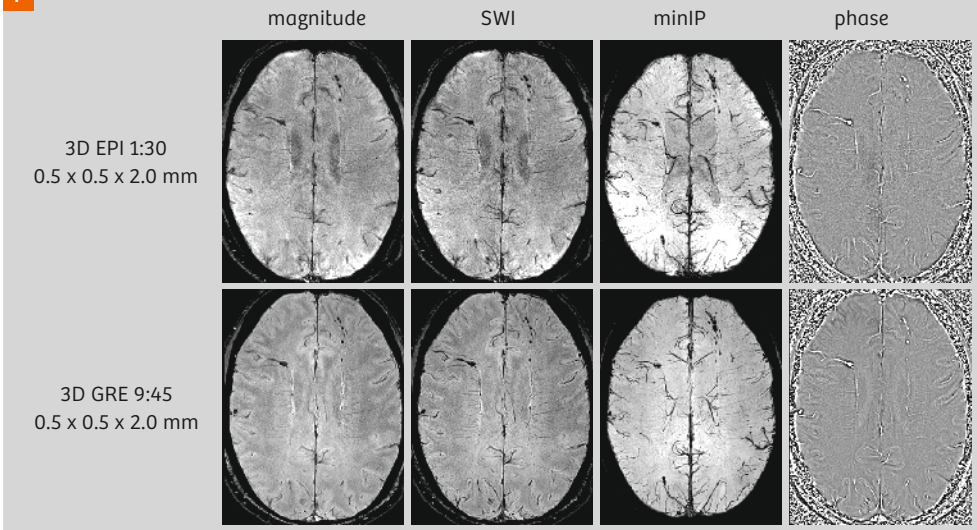

Figure 7: An ~ 1½-minute 3D EPI sequence compares favorably with an ~ 10-minute 3D GRE sequence for the depiction and characterization of traumatic axonal injury characterized by clustered curvilinear and punctate microhemorrhages scattered throughout the frontal lobes bilaterally. Identical image resolution and echo time (TE = 25 ms). 3D GRE was performed using iPAT2 and a TR of 40 ms and 6/8 partial phase encode. 3D EPI was performed with an EPI of 15 and a TR of 64 ms for a net ~ 6 fold acceleration. Minimum intensity projection (minIP) used a 10 mm slab thickness.

For the characterization of TBI associated microhemorrhage, consensus imaging protocols prefer GRE based SWI over the conventional 2D GRE T2*-weighted methods, but acknowledge, even using iPAT, that this demands imaging times on the order of 5–10 minutes for whole brain coverage [15]. With 3D EPI, equivalent or higher resolution is easily obtained in 1.5–3 minutes. Figure 7 compares 3D GRE based SWI to that of the 3D EPI SWI performed with identical in-plane resolution (0.5 × 0.5 mm) and slice thickness (2.0 mm) with imaging times of 9:45 and 1:30 respectively on a 3T Biograph mMR platform. Qualitatively, the images are quite similar, and, despite the somewhat lower SNR of the rapid SWI scan, the SNR is more than sufficient to detect and characterize small microhemorrhages and also to generate phase data and subsequent SWI processing.

Alternatively, one can spend more time imaging and obtain higher (e.g. 0.65 mm isotropic) resolution to allow for characterization of microhemorrhage in any plane of interest (Fig. 8) allowing for demonstration of the curvilinear microhemorrhages characteristic of traumatic axonal injury. In addition, such high resolution imaging can demonstrate other hemorrhagic pathologies such as subarachnoid hemorrhage, cortical contusion, and superficial siderosis.

Conclusions

In summary, we present a novel approach to acquire susceptibility-based MR images using a segmented 3D EPI prototype sequence. Our experience at the NIH has shown that this method can be used either to reduce the imaging time of standard resolution 3D GRE/SWI images, or to increase the resolution to acquire submillimeter isotropic images of the whole brain at a variety of field strengths, as low as 1.5T. One current limitation of our prototype sequence is the lack of parallel imaging capability acquisition (e.g., GRAPPA, CAIPIRINHA), which was recently demonstrated to be feasible at 7T [16]. Clinically, we believe

8

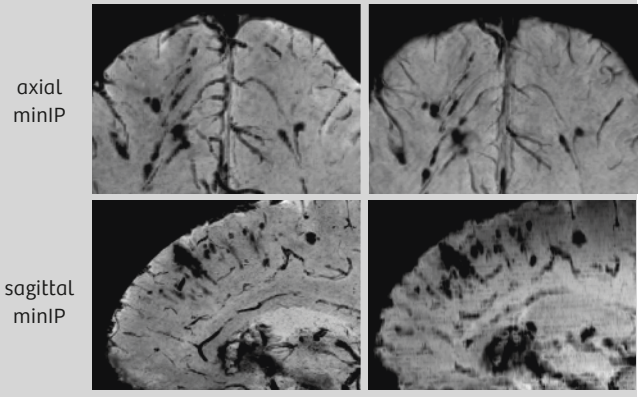

Figure 8: Comparison of microhemorrhage characterization using isotropic 0.65 mm 3D EPI vs. traditional 0.5 x 0.5 x 2.0 mm 3D GRE. Axial minimum intensity projections are comparable but the projections in the sagittal plane demonstrate the superiority of isotropic acquisition. Acquisition time for 3D EPI was 4:45 min and for GRE was 9:45 min.

the 3D EPI approach is a promising tool for MS diagnosis, but it could have many other applications in variety of neurological disorders, such as detecting microhemorrhage in neurovascular disease or traumatic brain injury, or assessing iron deposition in the substantia nigra in Parkinson's disease [17].

Acknowledgements

Research described in this article was supported in part by the Intramural Research Program of the National Institute of Neurological Disorders and Stroke, NIH. We also acknowledge the Center for Neuroscience and Regenerative Medicine for support.

Appendix

Currently, the 3D EPI prototype sequence[1] is available for *syngo* MR D13A/D through C2P exchange with NIH (Please contact Dr. Pascal Sati, satip@ninds.nih.gov). It is also available for *syngo* MR E11A as a WIP through Siemens (Please contact Dr. Sunil Patil, patil-sunil@siemens-healthineers.com). The collaborative work between the National Institute of Neurological Disorders and Stroke, the National Institute of Mental Health, and Siemens Healthcare USA was conducted under a Cooperative Research and Development Agreement.

References

1 B.A. Poser, P.J. Koopmans, T. Witzel, L.L. Wald, M. Barth, Three dimensional echo-planar imaging at 7 Tesla, Neuroimage, 51 (2010) 261-266.

2 J.J. Zwanenburg, M.J. Versluis, P.R. Luijten, N. Petridou, Fast high resolution whole brain T2* weighted imaging using echo planar imaging at 7T, Neuroimage, 56 (2011) 1902-1907.

3 C. Langkammer, K. Bredies, B.A. Poser, M. Barth, G. Reishofer, A.P. Fan, B. Bilgic, F. Fazekas, C. Mainero, S. Ropele, Fast quantitative susceptibility mapping using 3D EPI and total generalized variation, Neuroimage, 111 (2015) 622-630.

4 P. Sati, J. Oh, R.T. Constable, N. Evangelou, C.R. Guttmann, R.G. Henry, E.C. Klawiter, C. Mainero, L. Massacesi, H. McFarland, F. Nelson, D. Ontaneda, A. Rauscher, W.D. Rooney, A.P. Samaraweera, R.T. Shinohara, R.A. Sobel, A.J. Solomon, C.A. Treaba, J. Wuerfel, R. Zivadinov, N.L. Sicotte, D. Pelletier, D.S. Reich, N. Cooperative, The central vein sign and its clinical evaluation for the diagnosis of multiple sclerosis: a consensus statement from the North American Imaging in Multiple Sclerosis Cooperative, Nat Rev Neurol, 12 (2016) 714-722.

Contact

Pascal Sati, Ph.D.
Translational Neuroradiology Section
National Institute of Neurological Disorders and Stroke
National Institutes of Health

10 Center Drive MSC 1400
Building 10 Room 5C103
Bethesda, MD 20892-1400
USA
satip@ninds.nih.gov

Pascal Sati

John A. Butman

5 A. Rovira, M.P. Wattjes, M. Tintore, C. Tur, T.A. Yousry, M.P. Sormani, N. De Stefano, M. Filippi, C. Auger, M.A. Rocca, F. Barkhof, F. Fazekas, L. Kappos, C. Polman, D. Miller, X. Montalban, M.s. group, Evidence-based guidelines: MAGNIMS consensus guidelines on the use of MRI in multiple sclerosis-clinical implementation in the diagnostic process, Nat Rev Neurol, 11 (2015) 471-482.

6 P. Sati, I.C. George, C.D. Shea, M.I. Gaitan, D.S. Reich, FLAIR*: a combined MR contrast technique for visualizing white matter lesions and parenchymal veins, Radiology, 265 (2012) 926-932.

7 I.D. Kilsdonk, A. Lopez-Soriano, J.P. Kuijer, W.L. de Graaf, J.A. Castelijns, C.H. Polman, P.R. Luijten, J.J. Geurts, F. Barkhof, M.P. Wattjes, Morphological features of MS lesions on FLAIR* at 7 T and their relation to patient characteristics, J Neurol, 261 (2014) 1356-1364.

8 I.D. Kilsdonk, M.P. Wattjes, A. Lopez-Soriano, J.P. Kuijer, M.C. de Jong, W.L. de Graaf, M.M. Conijn, C.H. Polman, P.R. Luijten, J.J. Geurts, M.I. Geerlings, F. Barkhof, Improved differentiation between MS and vascular brain lesions using FLAIR* at 7 Tesla, Eur Radiol, 24 (2014) 841-849.

9 A.P. Samaraweera, M.A. Clarke, A. Whitehead, Y. Falah, I.D. Driver, R.A. Dineen, P.S. Morgan, N. Evangelou, The Central Vein Sign in Multiple Sclerosis Lesions Is Present Irrespective of the T2* Sequence at 3 T, J Neuroimaging, 27 (2017) 114-121.

10 A.J. Solomon, M.K. Schindler, D.B. Howard, R. Watts, P. Sati, J.P. Nickerson, D.S. Reich, "Central vessel sign" on 3T FLAIR* MRI for the differentiation of multiple sclerosis from migraine, Ann Clin Transl Neurol, 3 (2016) 82-87.

11 M. Filippi, M.A. Rocca, O. Ciccarelli, N. De Stefano, N. Evangelou, L. Kappos, A. Rovira, J. Sastre-Garriga, M. Tintore, J.L. Frederiksen, C. Gasperini, J. Palace, D.S. Reich, B. Banwell, X. Montalban, F. Barkhof, M.S. Group, MRI criteria for the diagnosis of multiple sclerosis: MAGNIMS consensus guidelines, Lancet Neurol, 15 (2016) 292-303.

12 M. Chiara Ricciardi, R.P. Bokkers, J.A. Butman, D.A. Hammoud, D.L. Pham, S. Warach, L.L. Latour, Trauma-Specific Brain Abnormalities in Suspected Mild Traumatic Brain Injury Patients Identified in the First 48 Hours after Injury: A Blinded Magnetic Resonance Imaging Comparative Study Including Suspected Acute Minor Stroke Patients, J Neurotrauma, 34 (2017) 23-30.

13 C.S. Kidwell, J.A. Chalela, J.L. Saver, S. Starkman, M.D. Hill, A.M. Demchuk, J.A. Butman, N. Patronas, J.R. Alger, L.L. Latour, M.L. Luby, A.E. Baird, M.C. Leary, M. Tremwel, B. Ovbiagele, A. Fredieu, S. Suzuki, J.P. Villablanca, S. Davis, B. Dunn, J.W. Todd, M.A. Ezzeddine, J. Haymore, J.K. Lynch, L. Davis, S. Warach, Comparison of MRI and CT for detection of acute intracerebral hemorrhage, JAMA, 292 (2004) 1823-1830.

14 K.A. Tong, S. Ashwal, B.A. Holshouser, L.A. Shutter, G. Herigault, E.M. Haacke, D.K. Kido, Hemorrhagic shearing lesions in children and adolescents with posttraumatic diffuse axonal injury: improved detection and initial results, Radiology, 227 (2003) 332-339.

15 C.A. Mutch, J.F. Talbott, A. Gean, Imaging Evaluation of Acute Traumatic Brain Injury, Neurosurg Clin N Am, 27 (2016) 409-439.

16 R. Stirnberg, J. Acosta-Cabronero, B.A. Poser, T. Stocker, 2D-segmented, multi-TE 3D-EPI for high-resolution R2* and quantitative susceptibility mapping at 7 Tesla, Proceedings of the International Society of Magnetic Resonance Imaging in Medicine, 2015.

17 C. Langkammer, L. Pirpamer, S. Seiler, A. Deistung, F. Schweser, S. Franthal, N. Homayoon, P. Katschnig-Winter, M. Koegl-Wallner, T. Pendl, E.M. Stoegerer, K. Wenzel, F. Fazekas, S. Ropele, J.R. Reichenbach, R. Schmidt, P. Schwingenschuh, Quantitative Susceptibility Mapping in Parkinson's Disease, PLoS One, 11 (2016) e0162460.

Assessing Brain Volumes Using MorphoBox Prototype

Alexis Roche[1,2,3]; Bénédicte Maréchal [1,2,3]; Tobias Kober [1,2,3]; Gunnar Krueger [4]; Patric Hagmann[1]; Philippe Maeder [1]; Reto Meuli [1]

[1] Department of Radiology, University Hospital (CHUV), Lausanne, Switzerland
[2] Advanced Clinical Imaging Technology, Siemens Healthineers, Lausanne, Switzerland
[3] Signal Processing Laboratory (LTS 5), École Polytechnique Fédérale de Lausanne, Lausanne, Switzerland
[4] Siemens Medical Solutions USA, Boston, MA

Introduction

Brain morphometry from routine structural MR images is useful to detect abnormal regional brain volumes that may be indicative of a disease [1]. For instance, hippocampus atrophy is known to be associated with memory impairment commonly experienced by individuals with dementia [2]. When combined with other volumetric measurements such as frontal lobe atrophy and white matter lesions, it may help diagnose a particular form of dementia (Alzheimer's disease, fronto-temporal or vascular dementia among others).

The MorphoBox algorithm[1] was developed by the Advanced Clinical Imaging Technology group in Lausanne in close collaboration with the University Hospital's Radiology Department. As an integral part of a Siemens prototype sequence, it automatically estimates a number of brain volumes from a single T1-weighted MR image acquired with the MPRAGE sequence, and compares these volumes with normative ranges adjusted for head size, age, and sex. The results are presented to the user in the form of a DICOM report, where brain structures that are found to be abnormally small (or abnormally large, e.g. for ventricular structures) are indicated with an asterisk.

Owing to its full incorporation into the MRI system, MorphoBox runs during image reconstruction. Results can be read with the *syngo* standard viewers or sent to the PACS system in order to seamlessly integrate into the radiological workflow. As of early 2016, more than 10,000 patients had benefited from this prototype worldwide.

[1] WIP, the product is currently under development and is not for sale in the US and in other countries. Its future availability cannot be ensured.

Methodology

Image processing

MorphoBox implements a processing pipeline consisting of several steps, as outlined in Figure 1. After the incoming MR scan has been checked for protocol compliance with a widely accepted standard for MPRAGE sequences [3], it is

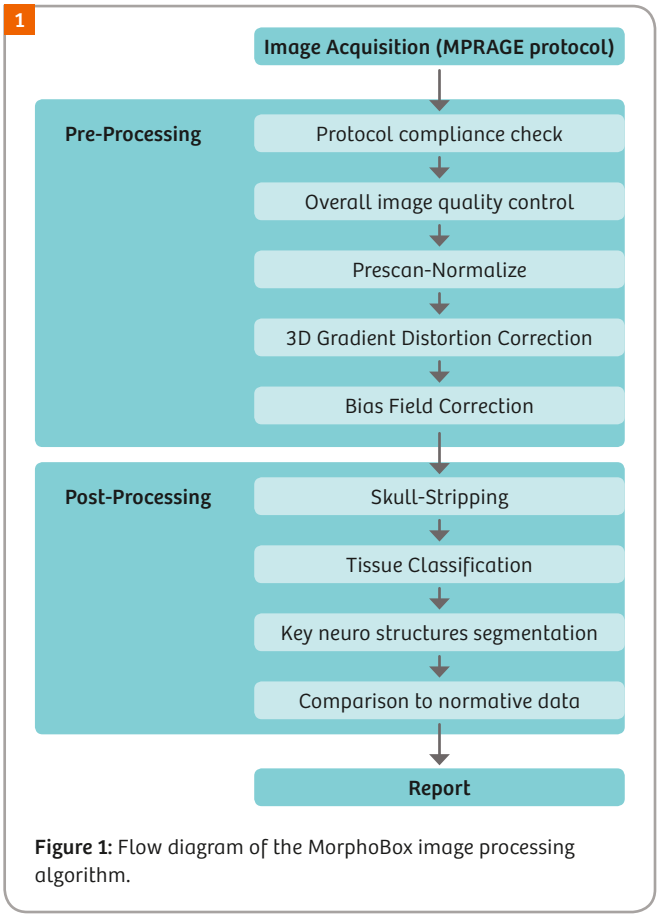

Figure 1: Flow diagram of the MorphoBox image processing algorithm.

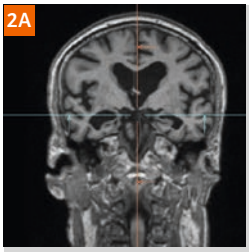

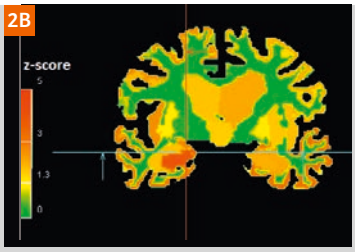

2C

Brain Morphometry Report - 4/7

Lobar GM/structure	Absolute [ml]	Normalized^ [%]	Normative Range^^ [%]
Frontal lobe			
GM left	67.4	* 4.93	[5.27 - 6.47]
GM right	64.2	* 4.69	[5.20 - 6.35]
Parietal lobe			
GM left	49.2	3.59	[3.48 - 4.46]
GM right	47.7	3.49	[3.41 - 4.31]
Occipital lobe			
GM left	15.4	* 1.12	[1.21 - 1.80]
GM right	15.9	* 1.16	[1.37 - 1.98]
Temporal lobe			
GM left	39.4	* 2.88	[3.32 - 4.00]
GM right	42.4	* 3.09	[3.52 - 4.30]
Cingulate gyrus			
GM left	6.3	0.46	[0.44 - 0.59]
GM right	6.5	0.47	[0.43 - 0.56]
Insula			
Left	3.8	* 0.28	[0.30 - 0.40]
Right	4.1	* 0.30	[0.34 - 0.44]

not approved for diagnostic purpose

Figure 2: Screenshots of MorphoBox results on the *syngo* viewer for an Alzeimer's Disease patient. **(2A)** an MRI coronal slice, **(2B)** the corresponding deviation map, and **(2C)** three pages from the report.

Brain Morphometry Report - 3/7

Patient Demographics	80 yrs	Male	
Image quality	high	0.72	[0 - 0.82]
Segmentation Quality	high	0.82	[0.7 - 1]

Tissue	Absolute [ml]	Normalized^ [%]	Normative Range^^ [%]
TIV	1368.4		
GM	474.8	* 34.7	[37.6 - 43.9]
cortical GM	349.5	* 25.5	[28.3 - 33.6]
WM	426.3	31.2	[26.0 - 31.4]
WMab	0.3	0.0	
CSF	467.3	34.2	[26.7 - 35.3]

^ Percentage of TIV (Total Intracranial Volume)
^^ 10th and 90th percentiles of healthy age-matched population
* Out-of-range volumes

not approved for diagnostic purpose

Brain Morphometry Report - 3/7

Structure	Absolute [ml]	Normalized^ [%]	Normative Range^^ [%]
Hippocampus	4.3	* 0.31	[0.38 - 0.48]
Hippocampus left	2.3	* 0.17	[0.19 - 0.24]
Hippocampus right	2.0	* 0.14	[0.19 - 0.24]
Ventricles	107.4	* 7.85	[1.94 - 5.38]
lateral ventricle left	55.3	* 4.04	[0.81 - 2.56]
lateral ventricle right	44.1	* 3.22	[0.79 - 2.41]
3rd ventricle	4.6	* 0.34	[0.14 - 0.29]
4th ventricle	3.5	0.25	[0.13 - 0.26]

not approved for diagnostic purpose

submitted to different image quality checks based on both signal-to-noise ratio and contrast-to-noise ratio assessments as well as motion-/aliasing-related artifact detection [4]. Subsequently, the images are corrected for gradient distortion [5] and radio-frequency field inhomogeneity [6, 7]. A tissue classification algorithm [8] is applied to the corrected image, the results of which are combined with a deformed anatomical template to segment various brain structures in the image [9], including: lobe-wise gray and white matter, insula, cingulate, hippocampi, central nuclei, subcortical white matter, corpus callosum, ventricular system, cerebellum, and different brainstem structures. Volumes are computed for each segmented structure.

Normative range analysis

A cohort of 437 subjects with balanced sex and age ranging from 19 to 91 years was used to construct normative ranges for each brain volume measure output by MorphoBox. Specifically, the volumes produced by MorphoBox on the normative cohort were divided by the corresponding total intra-cranial volume, also estimated by MorphoBox, and regressed against age and sex using a log-linear model [9]. The normative ranges were then defined depending on age and sex by the regression prediction intervals corresponding, respectively, to the 10th and 90th percentiles of the TIV-normalized volume distribution, as seen in Figures 2–7 for various brain structures.

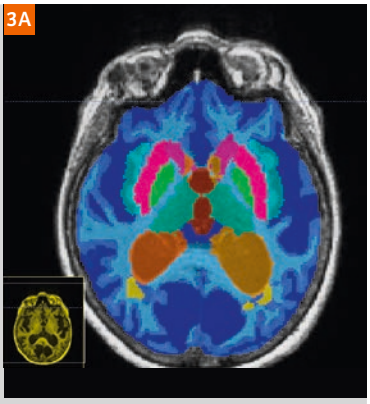

Figure 3: (3A) Axial slice of a 77-year-old woman with chronic vascular atrophy. Structures of interest segmented by MorphoBox and overlaid in color are the insula, putamen, pallidum, caudate nucleus, thalamus, lateral and third ventricles. In yellow are detected white matter lesions. **(3B–C)** Display of normative ranges for women as a function of age, respectively for the total normalized gray matter volume **(3B)** and the total normalized cerebrospinal fluid volume **(3C)**. The red dots indicate the volumes assessed by MorphoBox.

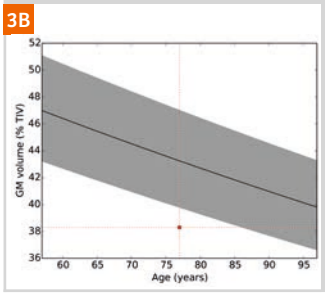

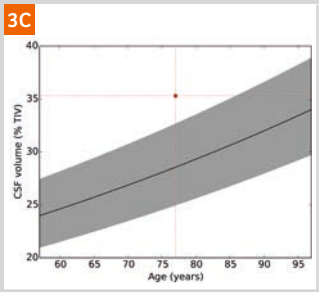

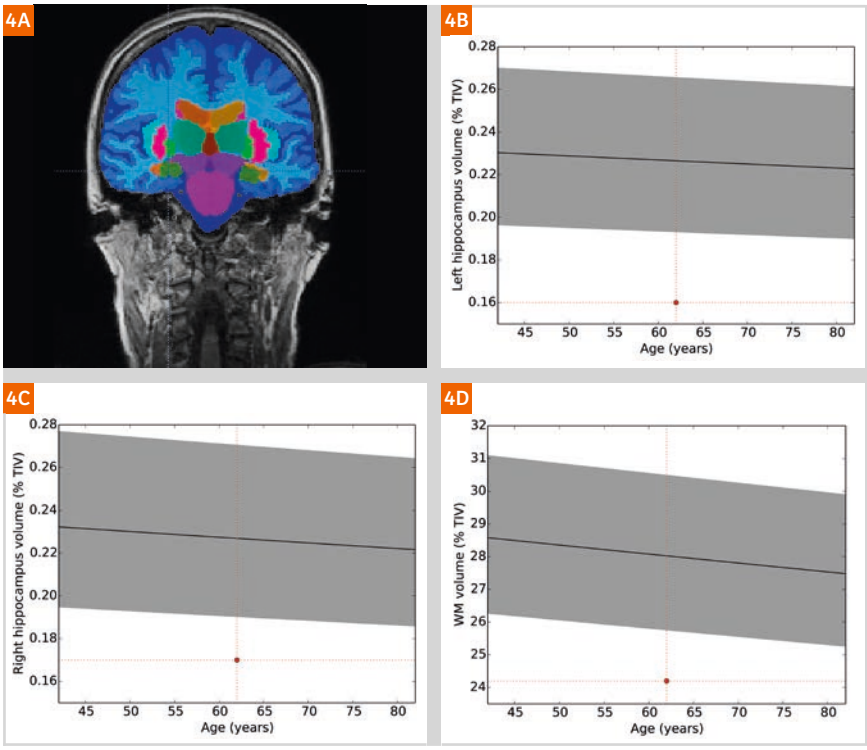

Figure 4: (4A) Coronal view of a 62-year-old woman with suspected Alzheimer's disease. The segmented hippocampi are shown in green. Other colored structures are the insula, putamen, pallidum, caudate nucleus, thalamus, lateral and third ventricles, mesencephalon, and pons. **(4B–D)** Display of normative ranges of TIV-normalized volumes for women as a function of age, **(4B)** for the left hippocampus, **(4C)** the right hippocampus and **(4D)** the total white matter, respectively.

Creation of report and deviation map
Finally, a report in form of a DICOM image is created containing patient identification, the result of the performed image quality assessment as well as a list of evaluated volumes, divided by hemispheres. Beside the absolute volumes, the TIV-normalized measures are reported and displayed in relation to the normative ranges. Detected deviations from the normative ranges are indicated with an asterisk (see Fig. 2). In addition, MorphoBox produces an image called "deviation map" displaying abnormal regions in hot colors (orange to red depending on the severity of deviation from normality). Since this information is stored as a DICOM image, it can be exported to the PACS like any other image and is available in other viewing software along with the imaging data.

Clinical examples

In the following examples, all brain MR slices are displayed in radiological convention (with the left hemisphere shown on the right of the image).

Results of applying MorphoBox on a 77-year-old female patient with chronic vascular atrophy are depicted in Figure 3A. Both global gray matter atrophy and global cerebrospinal fluid expansion, which are clearly visible in the MR scan, are appropriately detected by MorphoBox, as reflected in the normative range plots in Figure 3B. Other smaller structures are indicated as out-of-range in the MorphoBox report, including the ventricles, the frontal, temporal, parietal lobes, and the insula, in both hemispheres. Figure 4 shows the case of a 62-year-old woman with suspected Alzheimer's disease. Abnormal hippocampi are detected in both hemispheres, suggesting hippocampal atrophy. The total white matter volume is also flagged as abnormally low, which is common in early-age-of-onset Alzheimer's disease [10]. This case is in contrast with that of a 78-year-old woman with suspected early mild cognitive impairment, where the hippocampi like most brain structures are found normal, although insula atrophy is detected mainly on the left, see Figure 5.

As another example, the case of an 88-year-old man with probable cognitive disorder is shown in Figure 6A, for which cortical atrophy can be suspected from visual inspection of the MR scan. Quantitative analysis using MorphoBox (Fig. 6B) reveals that both frontal lobes are small, yet within the bounds of normality, and that both temporal lobes are clearly out-of-range, although the right hippocampus is normal and the left hippocampus is only slightly below the 10th percentile.

MorphoBox can also provide clinically relevant quantitative information on young patients, such as the 20-year-old woman with brain stem disorder shown in Figure 7A. The pons and medulla oblongata are found abnormal by MorphoBox, while the mesencephalon is borderline within normal range, as illustrated in Figure 7B.

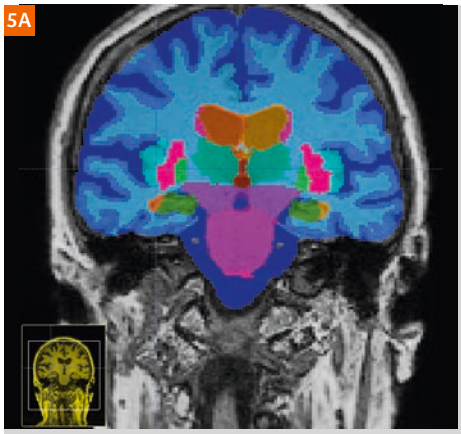

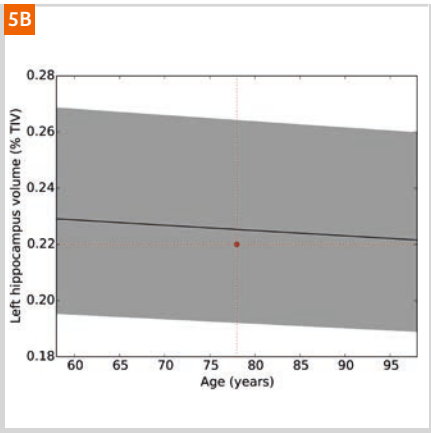

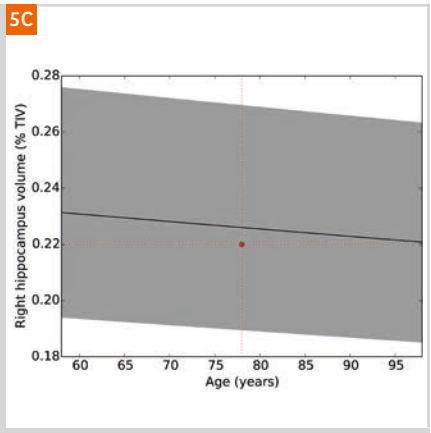

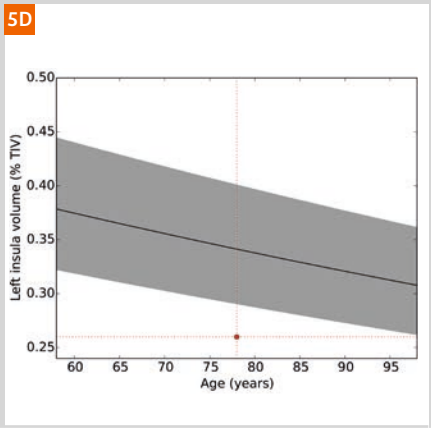

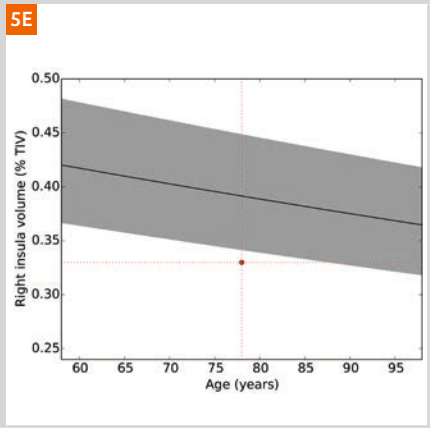

Figure 5: (5A) Coronal view of a 78-year-old woman with suspected MCI. The hippocampi (highlighted in green) are normal contrary to the left and right insulae (in light blue). Other structures shown in color (the central nuclei, ventricles, and brain stem) are normal. **(5B–E)** Display of normative ranges of TIV-normalized volumes for women as a function of age, **(5B)** for the left hippocampus, **(5C)** the right hippocampus, **(5D)** the left insula, and **(5E)** the right insula, respectively.

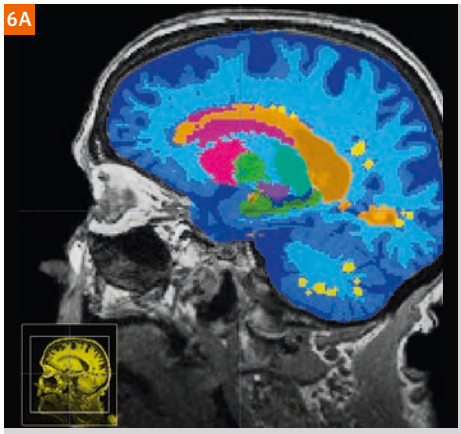

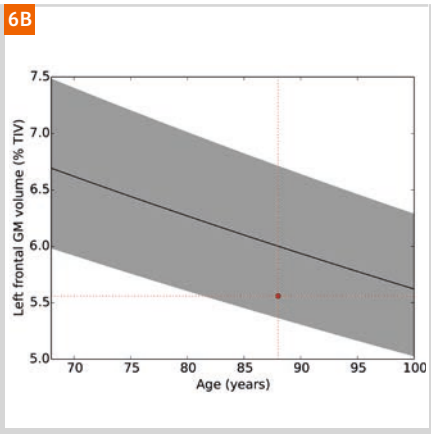

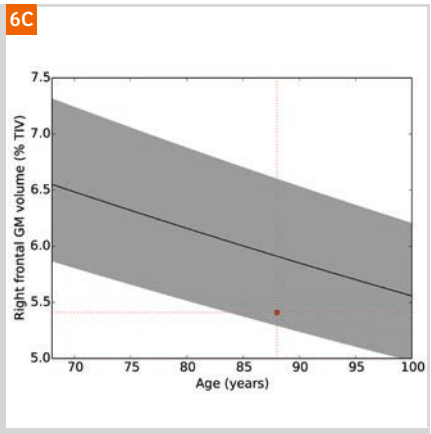

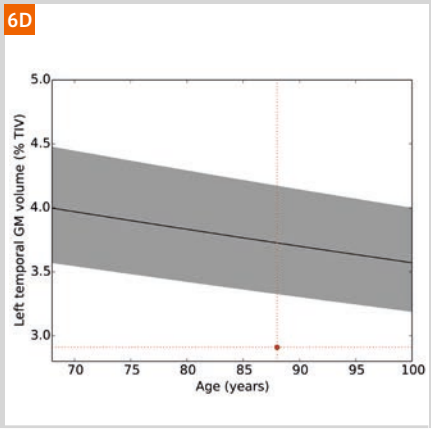

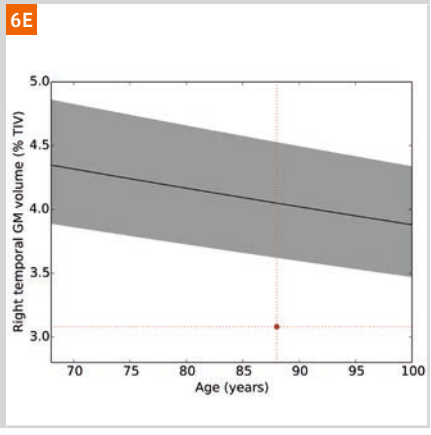

Figure 6: (6A) Sagittal view of an 88-year-old man with suspected cognitive disorder (left hemisphere). **(6B–E)** Display of normative ranges of TIV-normalized volumes for men as a function of age, **(6B)** for the left frontal lobe gray matter, **(6C)** the right frontal lobe gray matter, **(6D)** the left temporal lobe gray matter, and **(6E)** the right temporal lobe gray matter, respectively.

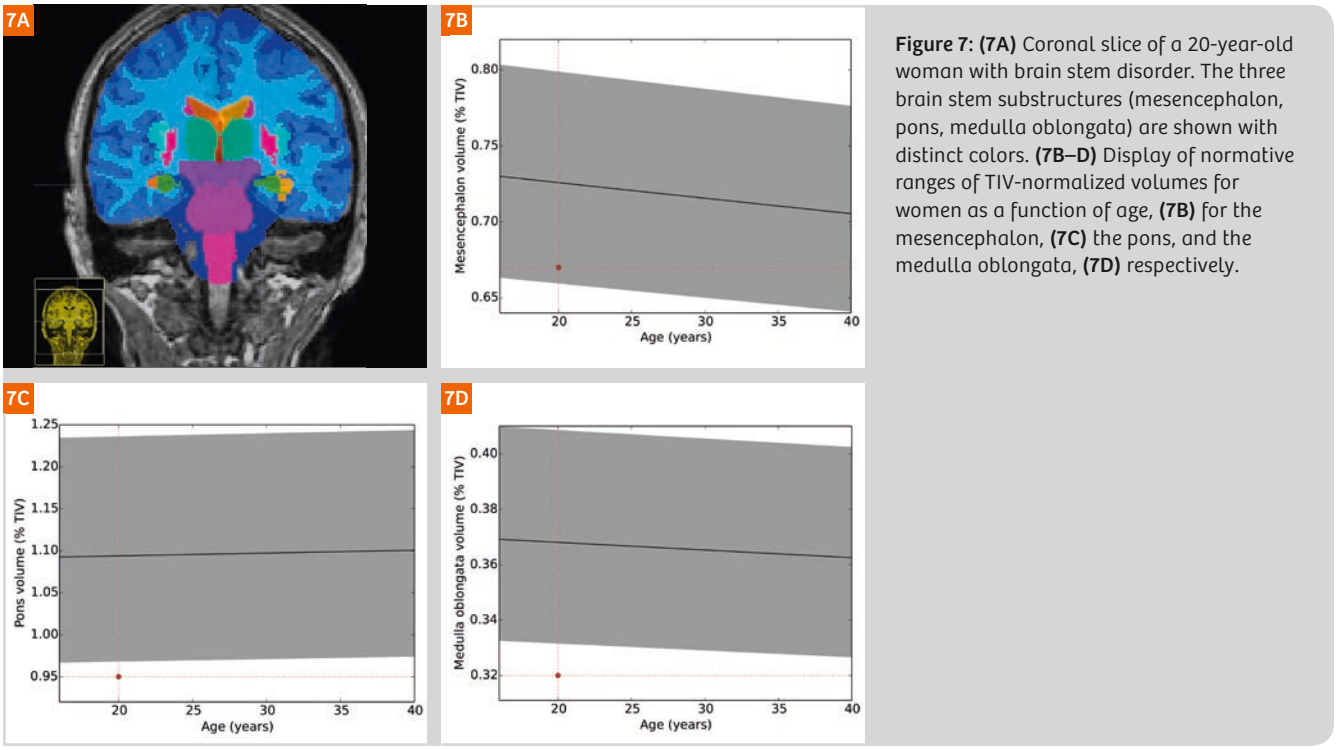

Figure 7: (7A) Coronal slice of a 20-year-old woman with brain stem disorder. The three brain stem substructures (mesencephalon, pons, medulla oblongata) are shown with distinct colors. **(7B–D)** Display of normative ranges of TIV-normalized volumes for women as a function of age, **(7B)** for the mesencephalon, **(7C)** the pons, and the medulla oblongata, **(7D)** respectively.

Conclusion

MorphoBox is a user-friendly brain volumetry prototype software compatible with clinical workflow constraints and intended for routine use. It provides quantitative information that can help radiological reading for patients with suspected neurodegeneration, as briefly exemplified in this article, and it is fully integrated in a clinical workflow. Our current objective is to further develop MorphoBox as a decision support tool for differential diagnosis of brain diseases.

References

1 D. Mietchen, and C. Gaser. Computational morphometry for detecting changes in brain structure due to development, aging, learning, disease and evolution. Frontiers in neuroinformatics 3: 25, 2009.
2 M.P. Laakso, et al. Hippocampal volumes in Alzheimer's disease, Parkinson's disease with and without dementia, and in vascular dementia: An MRI study. Neurology 46(3):678-681, 1996.
3 C.R. Jack, et al. The Alzheimer's disease neuroimaging initiative (ADNI): MRI methods. Journal of Magnetic Resonance Imaging 27(4):685-691, 2008.
4 B. Mortamet, M. Bernstein, J. C. Jack, J. Gunter, C. Ward, P. Britson, R. Meuli, J.-P. Thiran, and G. Krueger. Automatic Quality Assessment in Structural Brain Magnetic Resonance Imaging. Magnetic Resonance in Medicine 62:365–372, 2009.
5 P. Narayana, W. Brey, M. Kulkarni, and C. Sievenpiper. Compensation for surface coil sensitivity variation in magnetic resonance imaging. Magnetic Resonance Imaging 6:271–274, 1988.
6 K. Van Leemput, F. Maes, D. Vandermeulen, and P. Suetens. Automated model-based bias field correction of MR images of the brain. IEEE Transactions on Medical Imaging 18(10):885–896, 1999.
7 F. Schmitt. Correction of geometric distortion in MR Images. In Proceedings of the computer assisted radiology (CAR), pages 15–25. Springer, 1985.
8 A. Roche, D. Ribes, M. Bach-Cuadra, and G. Krueger. On the Convergence of EM-Like Algorithms for Image Segmentation using Markov Random Fields. Medical Image Analysis 15(6): 830–839, 2011.
9 D. Schmitter, A. Roche, B. Maréchal, D. Ribes, A. Abdulkadir, M. Bach-Cuadra, A. Daducci, C. Granziera, S. Klöppel, P. Maeder, R. Meuli, and G. Krueger. An evaluation of volume-based morphometry for prediction of mild cognitive impairment and Alzheimer's disease. NeuroImage: Clinical 7:7–17, 2014.
10 R. Migliaccio, et al. White matter atrophy in Alzheimer's disease variants. Alzheimer's & Dementia 8(5): S78-S87, 2012.

Contact

Alexis Roche, Ph.D.
Lead Clinical Research
Advanced Clinical Imaging Technology
Siemens Healthcare /
CHUV / EPFL
HC CEMEA SUI DI BM PI

1015 Lausanne
Switzerland
Phone: +41 21 545 9972
alexis.roche@gmail.com

Initial Experience with the MAGNETOM Terra 7T System. Focus on Neuroradiology and Knee Imaging

Manuel A. Schmidt, M.D.[1]; Tobias Engelhorn, M.D.[1]; Frank Römer, M.D.[2]; Angelika Mennecke, Ph.D.[1]; Frederik B. Laun, Ph.D.[2]; Armin M. Nagel, Ph.D.[2]; Michael Uder, M.D.[2]; Arnd Doerfler, M.D.[1]

[1] Department of Neuroradiology, University Hospital Erlangen, Germany
[2] Department of Radiology, University Hospital Erlangen, Germany

Clinical MRI scanners with a magnetic field strength up to 3T have become the state-of-the-art imaging modality for clinical neuroimaging and for most musculoskeletal applications and contribute significantly to patient care. Continuous progression in the development of scanner technology has led to remarkable progress in gradient and radiofrequency performance, magnet coil design and field strength. After the initial demonstration of feasibility at a few academic institutions, MR systems with magnetic field strengths of 7T are now at the forefront of MR research [1–8]. Especially for neuroimaging, 7T research has significantly improved the potential for high-resolution morphologic and functional imaging. The main advantages of ultra high-field (UHF) MRI scanners are a higher signal-to-noise ratio (SNR) and a higher contrast-to-noise ratio (CNR). Some applications benefit from both effects, such as susceptibility-weighted imaging (SWI) or time-of-flight angiography (TOF). The inherent higher SNR at 7T allows for submillimeter spatial resolution that gives accurate anatomical insight to reveal valuable diagnostic information for clinical applications. However, before 7T can be used in clinical routine, it is necessary to demonstrate the equivalence of a 7T scanner for clinical use compared to a clinical 3T scanner. In this article, we show the first 3T/7T comparison of patient data acquired on the new Siemens 7T MRI scanner MAGNETOM Terra[1].

In April 2015, the first MAGNETOM Terra was installed at the University Campus in Erlangen, Germany. This generation of 7T scanners will be the first generation of UHF MRI scanners to apply for European CE certification and FDA clearance for neuro and musculoskeletal (MSK) applications.

After an initial implementation period with technical testing and volunteer scanning, patient scanning was started at the beginning of 2017 for planned CE and FDA clearance in close cooperation with Siemens Healthcare. More than 60 patients were examined – including patients with brain tumors, multiple sclerosis, epilepsy, and neurodegenerative diseases such as Parkinson's disease, glaucoma, and spastic

[1] 510(k) pending. The product is not commercially available. Future availability cannot be guaranteed.

	Sequence	TR/TE [ms]	FOV [mm²]	Matrix	Number of slices	Slice thickness [mm]	Acceleration factor	Scan time [min:sec]
Neuro	2D FLAIR	10000/66	280 x 280	400 x 400	34	3	3	7:02
	MP2RAGE	4500/2.27	240 x 225	320 x 320	208	0.75	3	9:15
	SWI	27/15	230 x 173	640 x 640	96	1.2	3	5:38
	TSE	5940/120	235 x 235	608 x 608	34	3	2	5:46
MSK	TSE tra	4200/36	160 x 160	432 x 410	40	2.5	2	3:15
	TSE sag	4200/36	160 x 160	432 x 410	31	2.5	2	3:15
	DESS	8.67/2.54	160 x 160	320 x 320	224	0.5	3	3:43

Table 1: Sequences and parameters MAGNETOM Terra 7T.

	Sequence	TR/TE [ms]	FOV [mm²]	Matrix	Number of slices	Slice thickness [mm]	Acceleration factor	Scan time [min:sec]
Neuro	3D FLAIR	5000/253	250 x 250	256 x 256	160	1	2	11:42
	MPRAGE	1900/2.38	250 x 250	256 x 256	176	1	2	4:29
	SWI	28/20	230 x 230	384 x 384	120	1.2	3	7:50
	TSE	6420/91	220 x 220	512 x 512	35	3	2	4:25
MSK	TSE tra	6050/30	150 x 150	384 x 307	40	2.5	2	4:40
	TSE sag	3760/26	150 x 150	448 x 358	32	2.5	2	4:40

Table 2: Sequences and parameters MAGNETOM Trio 3T.

paraplegia as well as traumatic and degenerative lesions of the knee joint. The protocol of this prospective study was approved by the Clinical Investigation Ethics Committee of the University of Erlangen-Nuremberg and all examinations were performed in accordance with the Declaration of Helsinki. All participants gave written informed consent prior to all measurements. Exclusion criteria included implants in general, claustrophobia, and the inability to lie motionless during the scan time.

In this early phase we focused on – and we continue to focus on – the implementation and optimization of sequences and clinical protocols by fully exploiting the advantages of ultra high-field imaging with special regard to neuroimaging and musculoskeletal applications. In parallel with the 7T exams, 3T exams were performed for all patients on a MAGNETOM Trio (Siemens Healthcare, Erlangen, Germany). For neuroimaging, 32-channel receive (Rx) array head coils were used on both scanners (7T: 32 Rx/1 Tx RF coil, Nova Medical, Wilmington, MA, USA; 3T: Siemens Healthcare, Erlangen, Germany). For MSK applications, at 7T, a 28-channel receive (1 Tx) knee coil and at 3T, a 15-channel receive (1 Tx) knee coil were used (both RF coils: Quality Electrodynamics, Mayfield Village, OH, USA). Protocol parameters with the corresponding sequences are summarized in Tables 1 and 2 for 7T and 3T, respectively.

Compared to 3T, regarding T1-weighted imaging the high-resolution MP2RAGE showed a similarly stable and in general equally high image quality with ultra-fine anatomical resolution in a reasonable scan time. MP2RAGE had an improved gray/white matter contrast at 7T, which might be exploited to allow for better delineation of cortical malformations such as focal cortical dysplasia. This may be especially of benefit in the diagnostic work-up of patients suffering from medically refractory focal epilepsy.

Ultra high-field MRI shows higher sensitivity to magnetic susceptibility differences. By taking advantage of the susceptibility difference between deoxyhemoglobin and tissue, microvasculature as small as 200 µm can be depicted. As expected, SWI naturally benefited from the inherent strengths of 7T and showed greater CNR as well as greater SNR. Even very small structures such as tiny cortical veins (diameter 200–500 µm) were identified. In contrast, these structures could not be identified at 3T. This may be useful in diagnostic imaging, as SWI can visualize the formation of perivascular inflammatory lesions in multiple sclerosis. A clinical application might be imaging in inflammatory central nervous system (CNS) diseases. Multiple sclerosis lesions are frequently associated with vascular pathology and are located in the perivascular tissue, typically adjacent to a central vein [9, 10]. Visualization of small (cortical) lesions may thus be improved and a 7T scan may help to make the diagnosis in patients with so-called 'clinically isolated syndrome'. These patients clinically show features of an inflammatory CNS disease, but standard neuroimaging fails to confirm (post-) inflammatory lesions [11]. Here, 7T MRI might be more effective for detection of small lesions.

Ultra-fine SWI may also be useful in patients with brain tumors to help differentiate high grade glioma from primary CNS lymphoma [12]. 7T SWI offers improved evaluation of intratumoral susceptibility signals, thus intratumoral hemorrhage and microbleeds as well as tumor microvessels can be reliably detected. High resolution SWI can facilitate the diagnosis, as these lesions are uncommon in lymphoma.

Furthermore, 7T SWI may deliver insight into iron accumulation in the smallest anatomical structures in neurodegeneration such as Parkinson's disease. Nigrosome-1, a small defined cell cluster in the substantia nigra, returns a high signal on SWI and can be directly visualized with high resolution SWI [13]. Its degradation leads to a hypointense signal and in consequence to the absence of the typical swallow-tail appearance of the healthy substantia nigra,

possibly making 7T SWI a screening tool for early diagnosis of Parkinson's disease.

T2-weighted turbo spin echo sequences generally showed stable results with high diagnostic image quality. Even small anatomical structures such as pontocerebellar fibers in the brainstem were noticeable and the high SNR helped visualize the microstructure and exact localization of post-inflammatory multiple sclerosis plaques. Detailed T2w anatomical imaging of the hippocampus may be beneficial for diagnosis of hippocampal sclerosis as well as for visualization of early, subtle volume loss in subfields of the hippocampus as sign of neuronal degradation in Alzheimer's disease [14].

3D-FLAIR SPACE imaging is prone to B1 inhomogeneities which results in variable CNR over the whole image data. Therefore, 3D SPACE sequences, which were used routinely for comparative 3T imaging, were replaced with 2D FLAIR TSE sequences. Thus, we were able to achieve stable diagnostic image quality when FLAIR contrast was required or appropriate for diagnosis.

Higher gradient strengths and submillimeter spatial resolution make clinically important structural diffusion-weighted imaging promising at 7T. Diffusion tensor imaging (DTI) at 7T resolves small tracts and allows for measurement of diffusion indices in small anatomical structures [15]. Together with the high anatomical resolution that could be achieved with MP2RAGE sequences, preliminary results of a cohort of 20 patients with glaucoma revealed atrophy of the corpus geniculatum laterale (CGL), an important relay station of the visual system. Due to the high spatial resolution, we were able to perform direct volumetry of the CGL and use it as seed point for tractography of the optic tract and the optic radiation. This revealed marked atrophy of the optic radiation in these patients.

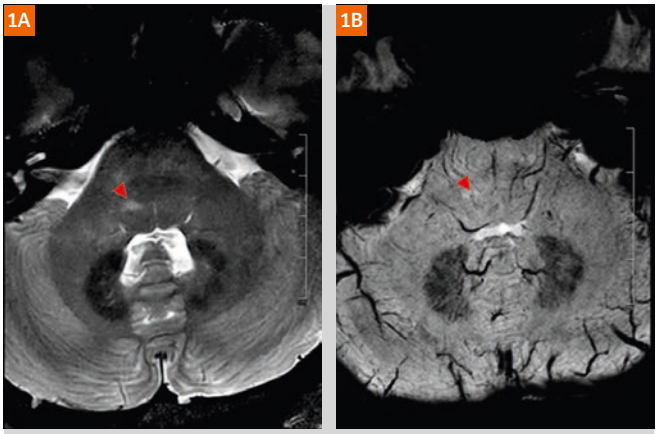

Figure 1: (1A) 7T axial T2w TSE shows infratentorial multiple sclerosis lesion. **(1B)** Corresponding SWI confirms the perivenular location.

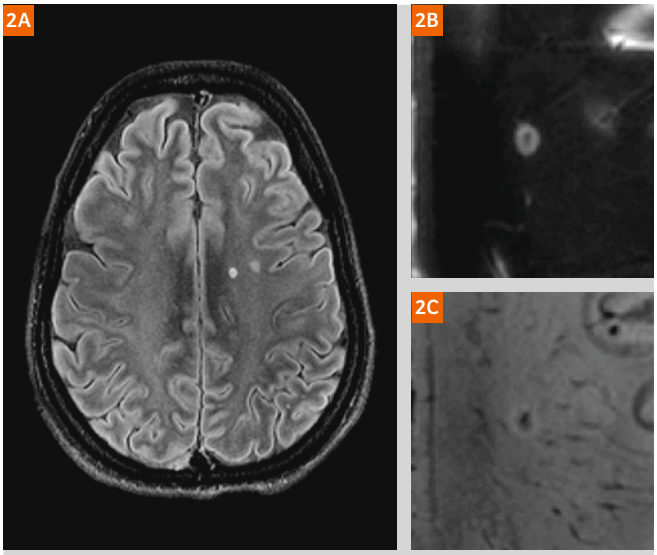

Figure 2: (2A) 7T axial FLAIR (2D TSE) shows hyperintense MS lesion with hypointense center. **(2B)** Corresponding T2w TSE. **(2C)** High-resolution SWI shows typical central vein and perivenular demyelination.

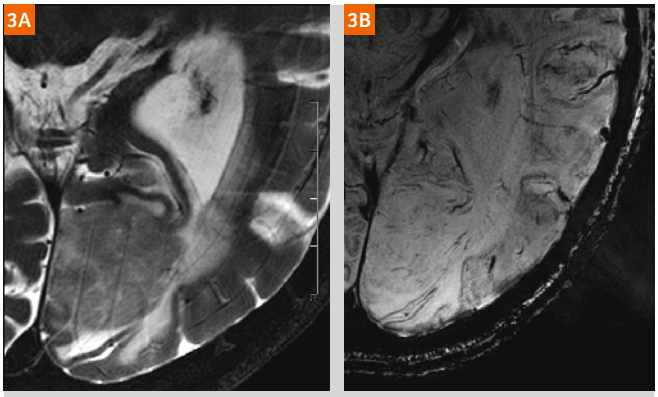

Figure 3: (3A) 7T T2w TSE shows a left occipital mass confirmed as secondary CNS lymphoma by histology. **(3B)** 7T SWI shows absence of microbleeds and tumor microvessels.

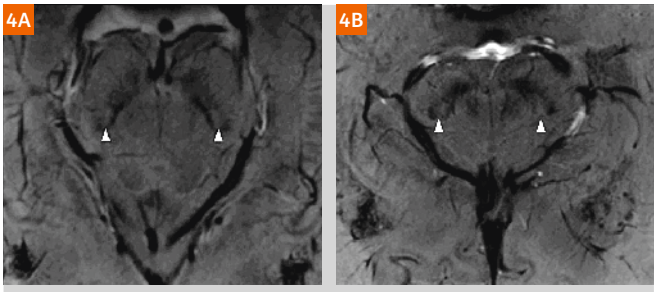

Figure 4: 7T SWI shows hyperintense signal of nigrosome-1 and the swallow-tail sign of the healthy substantia nigra.

In addition to optimized anatomical and structural sequences for clinical applications, 7T high-field MR imaging will facilitate metabolic imaging as metabolite resonances increase with field strength. Spectroscopic imaging might thus become more accurate for differential diagnosis of various neurological disorders such as tumors and tumefactive inflammatory lesions. Furthermore, UHF-spectroscopy may improve the detection of onco-metabolites (2-hydroxyglutarate) for grading and estimation of prognosis of gliomas [16]. Imaging and spectroscopy of non-proton nuclei such as sodium and phosphorus also largely benefit from ultra-high magnetic field strengths as the acquisition of reasonable voxel resolutions becomes achievable within clinically acceptable scan times. The sodium signal is increased in brain tumors and the combination of total sodium images and relaxation-weighted sodium images may be beneficial for tumor grading [17]. Phosphorous spectroscopy might provide important insights into phospholipid metabolism and phosphate energy metabolism [18].

In this early stage of clinical 7T imaging, a significant potential for future improvements naturally exists. Scan time was longer at 7T for most sequences compared to the corresponding 3T examinations. Magnetic field inhomogeneities, chemical shift displacement, and inhomogeneous B1 field are still challenges. These inherent limitations of ultra high-field imaging could be observed especially in regions close to the skull base, i.e. the lower parts of the temporal lobes and in the cerebellum and brainstem. Necessary adjustments to overcome these issues (TR↑, flip angle↓) were partly responsible for longer acquisition times at 7T compared to 3T. Further improvements of specialized pulse sequences and protocols as well as new hardware solutions, i.e. implementation of advanced parallel transmit technologies (pTx) will be addressed by a multidisciplinary team of MR physicists, engineers, and

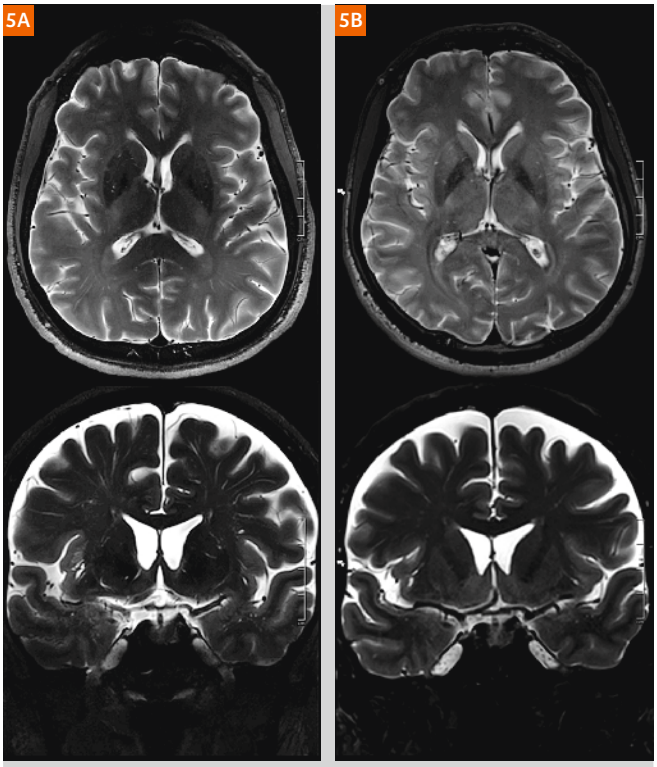

Figure 5: (5A) 7T axial and coronar T2w TSE images show diagnostic quality with high anatomic detail, even near the skull base. **(5B)** Same patient, images acquired at 3T (2D T2w TSE).

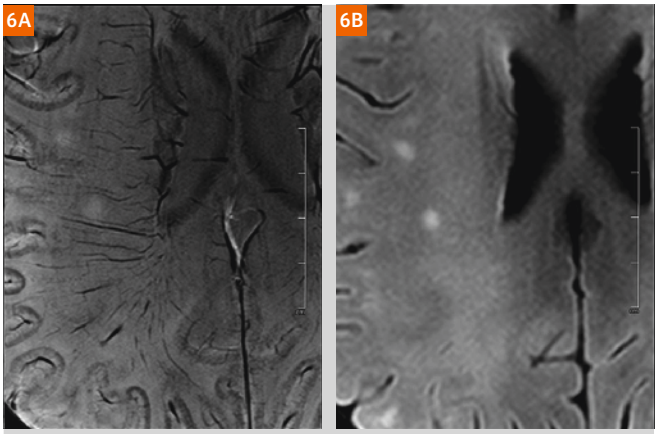

Figure 6: (6A) 7T axial SWI shows perivascular multiple sclerosis lesions. **(6B)** Corresponding FLAIR (2D TSE).

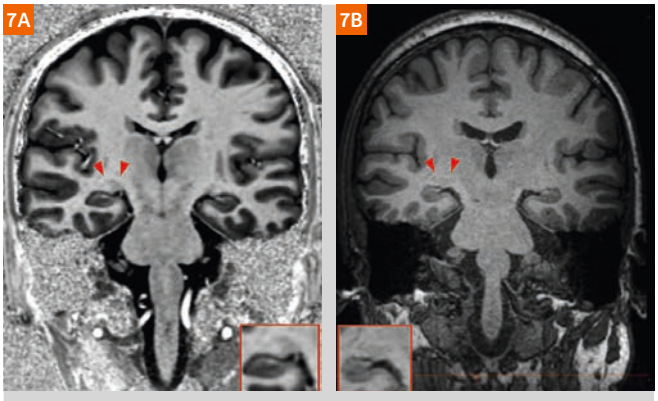

Figure 7: (7A) 7T MP2RAGE shows normal appearance of the corpus geniculatum laterale. Superior visibility compared to **(7B)** 3T MPRAGE of the same patient.

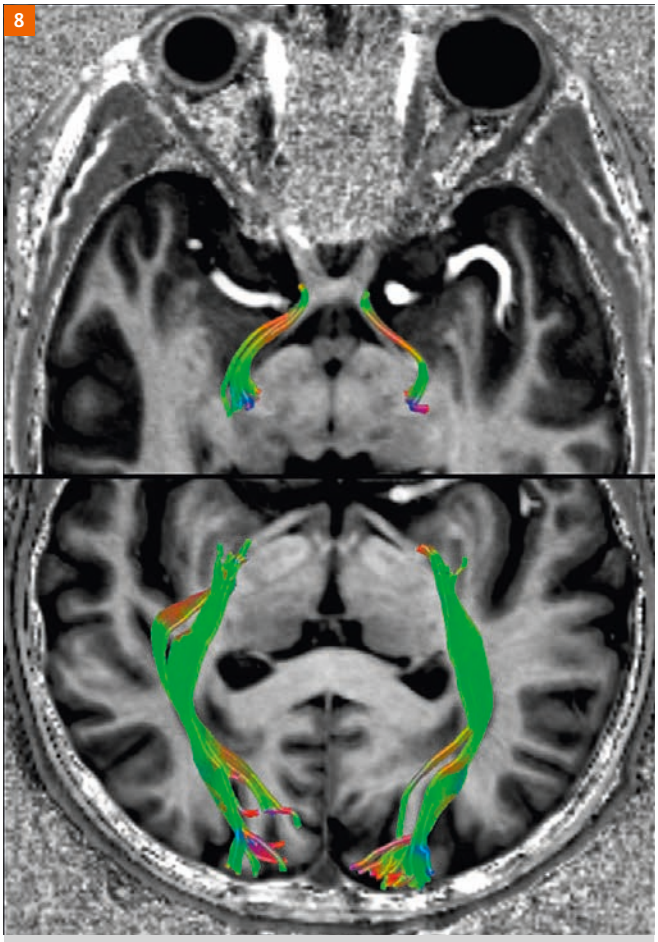

Figure 8: Selective tractography of the optic tract and the optic radiation using high resolution DTI fused with axial MP2RAGE.

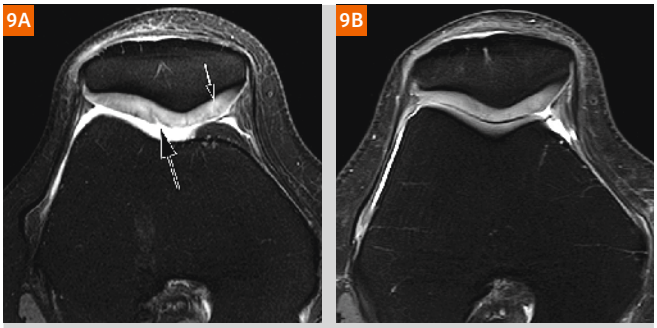

Figure 9: Retropatellar cartilage damage. **(9A)** 7T fat suppressed proton density-weighted image shows superficial cartilage fissure not reaching the subchondral bone in the lateral patellar facet (large arrow). In addition there is a high intensity intrachondral signal change at the medial patella indicating early cartilage degeneration without surface pathology (small arrow). **(9B)** Corresponding 3T image does not visualize cartilage fissure laterally. Medial signal change is markedly less pronounced.

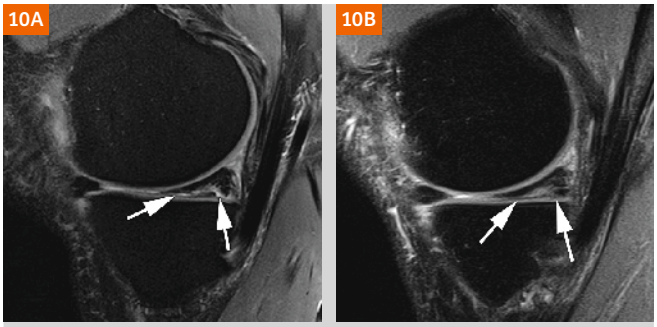

Figure 10: Meniscal tear. **(10A)** Sagittal 7T proton density-weighted fat suppressed image shows a degenerative horizontal-oblique tear of the posterior horn of the medial meniscus. Tear opens to the inferior meniscal surface anteriorly and near its base posteriorly (arrows). **(10B)** Corresponding 3T image shows intrameniscal high intensity signal change (arrows). Surface involvement is not depicted.

technicians in close contact with clinical radiologists and will further maximize the high-field gain in signal and contrast.

As has been demonstrated in previous work, ultra high-field MRI at 7T is capable to improve the diagnostic confidence in routine MRI of the knee joint compared to examinations acquired at 3T [3]. Our preliminary results obtained with the new MAGNETOM Terra system are in line with these observations as exemplified by several corresponding image examples of 7T vs. 3T. Ongoing sequence optimization will most likely result in further improved image quality in the future, and additional evaluation comparing 3T and 7T in regard to diagnostic performance using a surgical gold standard is planned to eventually be able to fully appreciate the potential added value of 7T in clinical knee imaging.

Official clinical authorization of the MAGNETOM Terra would strongly support the transition of 7T high-field MRI into clinical application. In addition to research projects, the community will then be able to start evaluation of clinical benefits of 7T high-field imaging. To put it another way: as a next step, we have to demonstrate that 7T not only provides crisp images but that it also has the potential to significantly improve the diagnostic workup and patient outcome. This can only be accomplished within clearly defined imaging protocols for defined larger patient cohorts, ideally in a multicenter approach.

Overall, our preliminary results give a first impression of what is already possible with clinical ultra high-field MRI and what interesting clinical perspectives can be expected for well-selected patients mainly in structural and

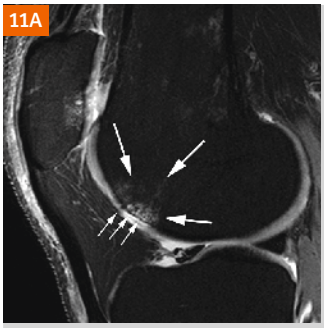

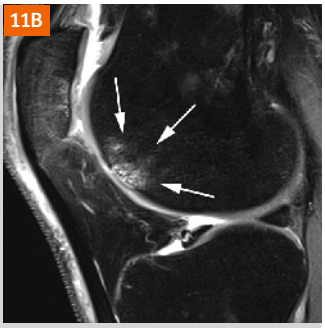

Figure 11: Cartilage delamination at the femoral trochlea. **(11A)** 7T sagittal fat suppressed image shows cartilage delamination of a focal cartilage lesion at the anterior lateral torchlea. There is fluid equivalent signal at the interface between the deep cartilage layer and the subchondral bone (small arrows). The most anterior small arrow points to cartilage surface disruption at the most superior aspect of lesion. In addition there is a concomitant subchondral bone marrow lesion, a finding commonly associated with focal cartilage pathology (large arrows). **(11B)** Corresponding 3T image shows a signal change at the same location subchondrally that is less pronounced and cannot definitely be diagnosed as a delamination. Bone marrow lesion is depicted in slightly larger fashion at 3T compared to 7T, a finding that is likely due to decreased susceptibility at lower field strengths (arrows).

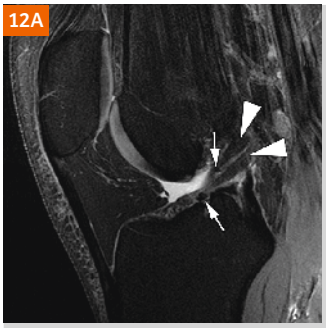

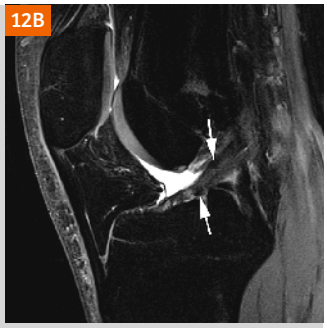

Figure 12: Anterior cruciate ligament (ACL) reconstruction. **(12A)** Sagittal proton density-weighted 7T MRI shows two intact hypointense bundles of an ACL reconstruction performed two years earlier (arrowheads). Note minor intraligamentous hypointense spot-like signal alterations representing minor metallic surgical remnants (arrows). **(12B)** Corresponding 3T image does not allow for differentiation of the two bundles as shown in 12A. Intraligamentous susceptibility is less pronounced at 3T compared to 7T.

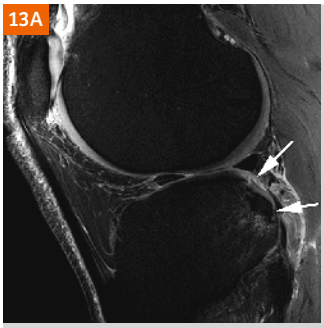

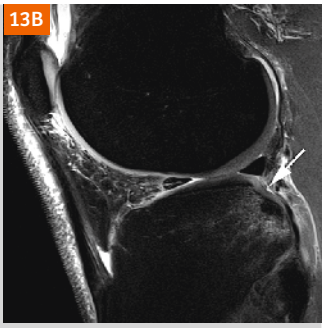

Figure 13: Osteochondral fracture. **(13A)** 7T sagittal proton density-weighted image shows an osteochondral fracture of the posterior lateral tibia with definite surface disruption of the chondral articular surface and slight depression of the osteochondral fragment (arrows). In addition, there is concomitant traumatic bone marrow lesion. **(13B)** Corresponding 3T MRI shows osteochondral fracture but differentiation between articular surface depression with a preserved chondral surface from chondral surface disruption is not possible (arrow). Bone marrow lesion appears more pronounced at 3T compared to 7T MRI.

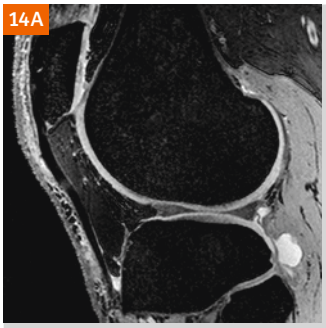

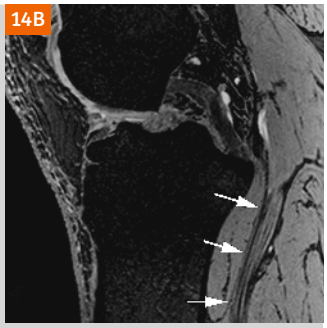

Figure 14: High resolution morphologic 3D joint imaging at 7T. **(14A)** Sagittal 3D dual echo at steady state (DESS) image at 7T MRI shows cartilage as high intensity tissue with marked contrast between the cartilage layer and subchondral bone. Commonly DESS is used for cartilage quantification of thickness and volume based on manual or automated segmentation approaches. **(14B)** Sagittal 7T DESS image shows tibial nerve as a multi-fasciculated structure posteriorly to the tibia (arrow). Intraneural nerve bundles can clearly be differentiated at high resolution 7T imaging.

functional neuroimaging in the future. Improved imaging methods may be applied to detect subtle anatomic, functional, and metabolic abnormalities associated with a wide range of neurologic disorders, including epilepsy, brain tumors, multiple sclerosis, neurodegenerative disease, and psychiatric conditions making the future of ultra high-field imaging very exciting.

References

1 van der Kolk AG, Hendrikse J, Zwanenburg JJ, Visser F, Luijten PR: Clinical applications of 7 T MRI in the brain. Eur J Radiol 2013, 82(5):708-718.
2 Ugurbil K: Magnetic resonance imaging at ultrahigh fields. IEEE Trans Biomed Eng 2014, 61(5):1364-1379.
3 Springer E, Bohndorf K, Juras V, Szomolanyi P, Zbyn S, Schreiner

MM, Schmitt B, Trattnig S: Comparison of Routine Knee Magnetic Resonance Imaging at 3 T and 7 T. Invest Radiol 2017, 52(1):42-54.
4 Trattnig S, Springer E, Bogner W, Hangel G, Strasser B, Dymerska B, Cardoso PL, Robinson SD: Key clinical benefits of neuroimaging at 7T. Neuroimage 2016.
5 Balchandani P, Naidich TP: Ultra-High-Field MR Neuroimaging. AJNR American journal of neuroradiology 2015, 36(7):1204-1215.
6 Niendorf T, Paul K, Oezerdem C, Graessl A, Klix S, Huelnhagen T, Hezel F, Rieger J, Waiczies H, Frahm J et al: W(h)ither human cardiac and body magnetic resonance at ultrahigh fields? technical advances, practical considerations, applications, and clinical opportunities. NMR Biomed 2015.
7 Kraff O, Fischer A, Nagel AM, Monninghoff C, Ladd ME: MRI at 7 Tesla and Above: Demonstrated and Potential Capabilities. J Magn Reson Imaging 2015, 41(1):13-33.
8 Moser E, Stahlberg F, Ladd ME, Trattnig S: 7-T MR – from research to clinical applications? NMR Biomed 2012, 25(5):695-716.

Contact

Prof. Dr. Arnd Doerfler, M.D., Ph.D.
Department of Neuroradiology
University Hospital Erlangen
Germany

arnd.doerfler@uk-erlangen.de

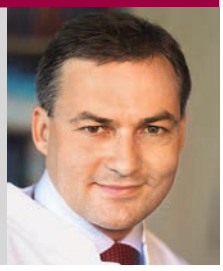

Contact

Prof. Dr. Michael Uder, M.D., Ph.D.
Department of Radiology
University Hospital Erlangen
Germany

michael.uder@uk-erlangen.de

9 Ge Y, Law M, Herbert J, Grossman RI: Prominent perivenular spaces in multiple sclerosis as a sign of perivascular inflammation in primary demyelination. AJNR American journal of neuroradiology 2005, 26(9):2316-2319.
10 Grabner G, Dal-Bianco A, Schernthaner M, Vass K, Lassmann H, Trattnig S: Analysis of multiple sclerosis lesions using a fusion of 3.0 T FLAIR and 7.0 T SWI phase: FLAIR SWI. J Magn Reson Imaging 2011, 33(3):543-549.
11 Kollia K, Maderwald S, Putzki N, Schlamann M, Theysohn JM, Kraff O, Ladd ME, Forsting M, Wanke I: First clinical study on ultra-high-field MR imaging in patients with multiple sclerosis: comparison of 1.5T and 7T. AJNR American journal of neuroradiology 2009, 30(4):699-702.
12 Radbruch A, Wiestler B, Kramp L, Lutz K, Baumer P, Weiler M, Roethke M, Sahm F, Schlemmer HP, Wick W et al: Differentiation of glioblastoma and primary CNS lymphomas using susceptibility weighted imaging. European journal of radiology 2013, 82(3):552-556.
13 Lehericy S, Bardinet E, Poupon C, Vidailhet M, Francois C: 7 Tesla magnetic resonance imaging: a closer look at substantia nigra anatomy in Parkinson's disease. Movement disorders: official journal of the Movement Disorder Society 2014, 29(13):1574-1581.
14 Prudent V, Kumar A, Liu S, Wiggins G, Malaspina D, Gonen O: Human hippocampal subfields in young adults at 7.0 T: feasibility of imaging. Radiology 2010, 254(3):900-906.
15 Heidemann RM, Porter DA, Anwander A, Feiweier T, Heberlein K, Knosche TR, Turner R: Diffusion imaging in humans at 7T using readout-segmented EPI and GRAPPA. Magnetic resonance in medicine 2010, 64(1):9-14.
16 Ganji SK, An Z, Tiwari V, McNeil S, Pinho MC, Pan E, Mickey BE, Maher EA, Choi C: In vivo detection of 2-hydroxyglutarate in brain tumors by optimized point-resolved spectroscopy (PRESS) at 7T. Magnetic resonance in medicine 2017, 77(3):936-944.
17 Nagel AM, Bock M, Hartmann C, Gerigk L, Neumann JO, Weber MA, Bendszus M, Radbruch A, Wick W, Schlemmer HP et al: The potential of relaxation-weighted sodium magnetic resonance imaging as demonstrated on brain tumors. Invest Radiol 2011, 46(9):539-547.
18 Klomp DW, van de Bank BL, Raaijmakers A, Korteweg MA, Possanzini C, Boer VO, van de Berg CA, van de Bosch MA, Luijten PR: 31P MRSI and 1H MRS at 7 T: initial results in human breast cancer. NMR Biomed 2011, 24(10):1337-1342.

How to Create a 'True' T1-weighted BLADE Measurement for Musculoskeletal Imaging

Thomas Illigen

Application Specialist MR, Siemens Healthineers, Mannheim, Germany

Introduction

With the BLADE trajectory, Siemens Healthcare offers a robust method to reduce 2D inplane movement artifacts. In the Siemens tree you can find various dedicated default protocols using the BLADE trajectory. Even though there are T1-weighted dark-blood measurements with inversion recovery (IR) pulses to gain a T1 contrast for brain examinations, such IR measurements are not desired for muscolosceletal imaging.

In this article I will describe how it is possible to create a 'true' T1-weighted BLADE protocol that might be used, for instance, for shoulder examinations which are very often negatively influenced by patient movement and the consequential artifacts.

What is meant by 'true' T1-weighted?

There are some definitions in literature of a 'true' T1-weighting for a (T)SE based protocol.

For a BLADE trajectory I define it – based on my own experience – as an effective echo time (TE) below 30 ms and an echo train length (ETL) of below 50 ms with a repetition time (TR) of between 400 and 700 ms for a 1.5T scanner or between 500 and 800 ms for a 3T scanner.

Although they are open to debate, adhering to the above values will guarantee an adequate T1 contrast – and by refocusing on the intention of BLADE trajectories, acquisition with a little longer TE is preferable to a (T)SE that is affected by motion artifacts.

Protocol set-up

In order to create the T1-weighted BLADE protocol, you can start with a default PD-weighted BLADE protocol (Fig. 1).

The T1-weighted BLADE protocols have to be designed with iPAT mode GRAPPA – because herein lies the key to implementing a shorter echo train length. Changing the GRAPPA reference lines from 8 to 4, allows you to reduce the turbo-factor (TF) from 9 to 7.

1

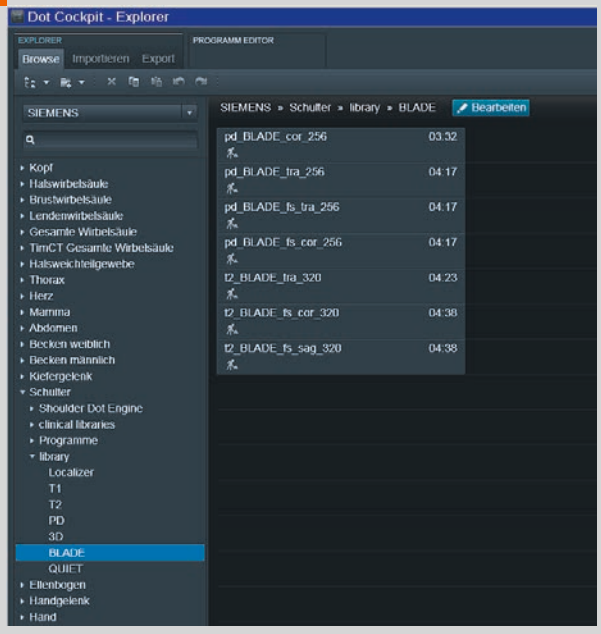

Figure 1: Siemens library

2

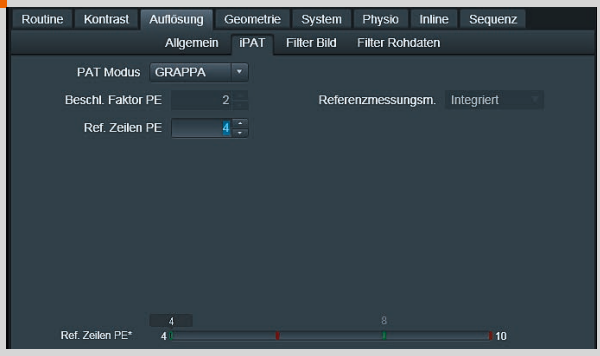

Figure 2: iPAT

3

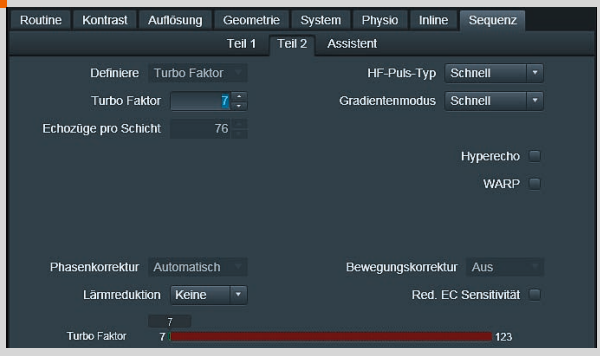

Figure 3: Turbo Factor (TF) 7

Note that a BLADE protocol has no preferred phase-encoding direction, due to the rotating trajectory, although during the planning of the measurement in the GSP, the following may be suggested:

4

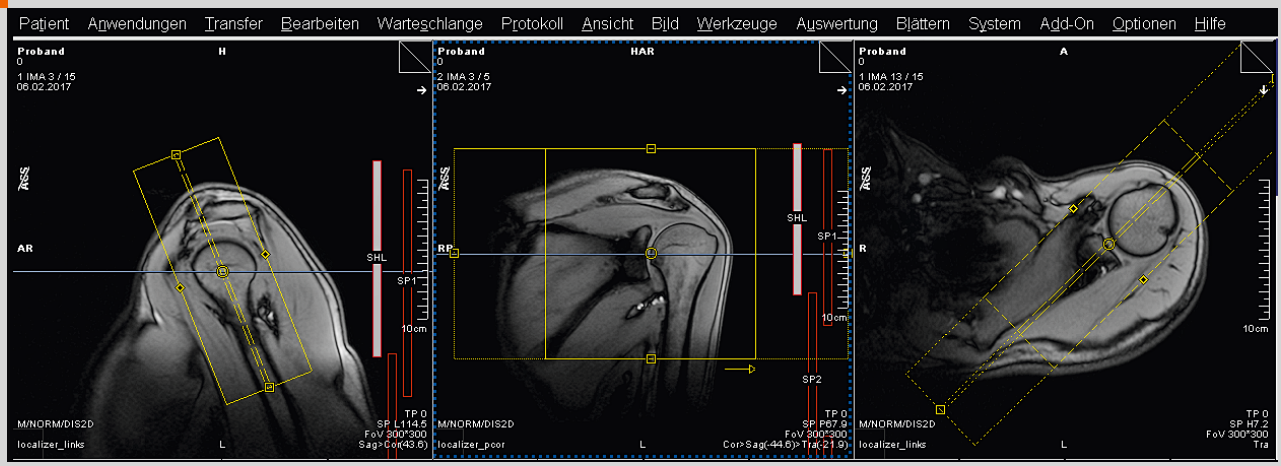

Figure 4: Planning

5

Figure 5: Matrix

These are the requirements for sufficient phase-oversampling in all directions and/or sat-bands. The disadvantage of an additional sat-band is a higher SAR deposition, which can become a problem, especially at a 3T scanner. Therefor I prefer a higher phase-oversampling. With 100% phase-oversampling you can be sure that there will be no infolding, because the maximum coil sensitivity will be below this. In addition, you get a higher signal-to-noise ratio (SNR). The field-of-view (FOV) has been enlarged from 160 mm to 180 mm, since the large 16-channel shoulder coil (SHL) can capture this.

By adapting the acquisition matrix – maximum for BLADE trajectories is 384, but it will work with lower matrices anyway – you can change the bandwidth to minimize the echo spacing (ES) at or below 7 ms, since TF x ES = ETL.

6

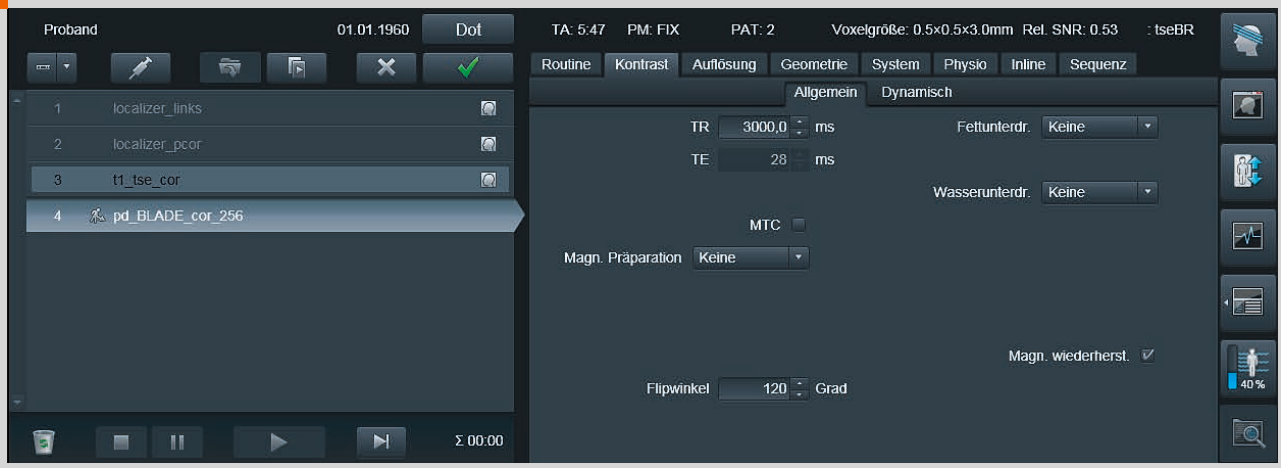

Figure 6: TE

7

Figure 7: BW + ES

The TE represents the central *k*-space line. For a BLADE acquisition this is always the central echo. Due to the ETL of below 50 ms, TE will be about 25–30 ms, which is acceptable for a 'true' T1 contrast, as defined above.

As a last step you have to arrive at an acceptable TR. Changing the concatenations to 2 or 3 allows you to achieve a TR between 500–700 ms. Even though – especially with a 3T scanner – at least two concatenations are recommended for a T1-weighted (T) SE-based protocol, and you also have to respect a buffer in TR due to the SAR deposition, a scan time (TA) below 3 minutes should nevertheless be achievable.

8

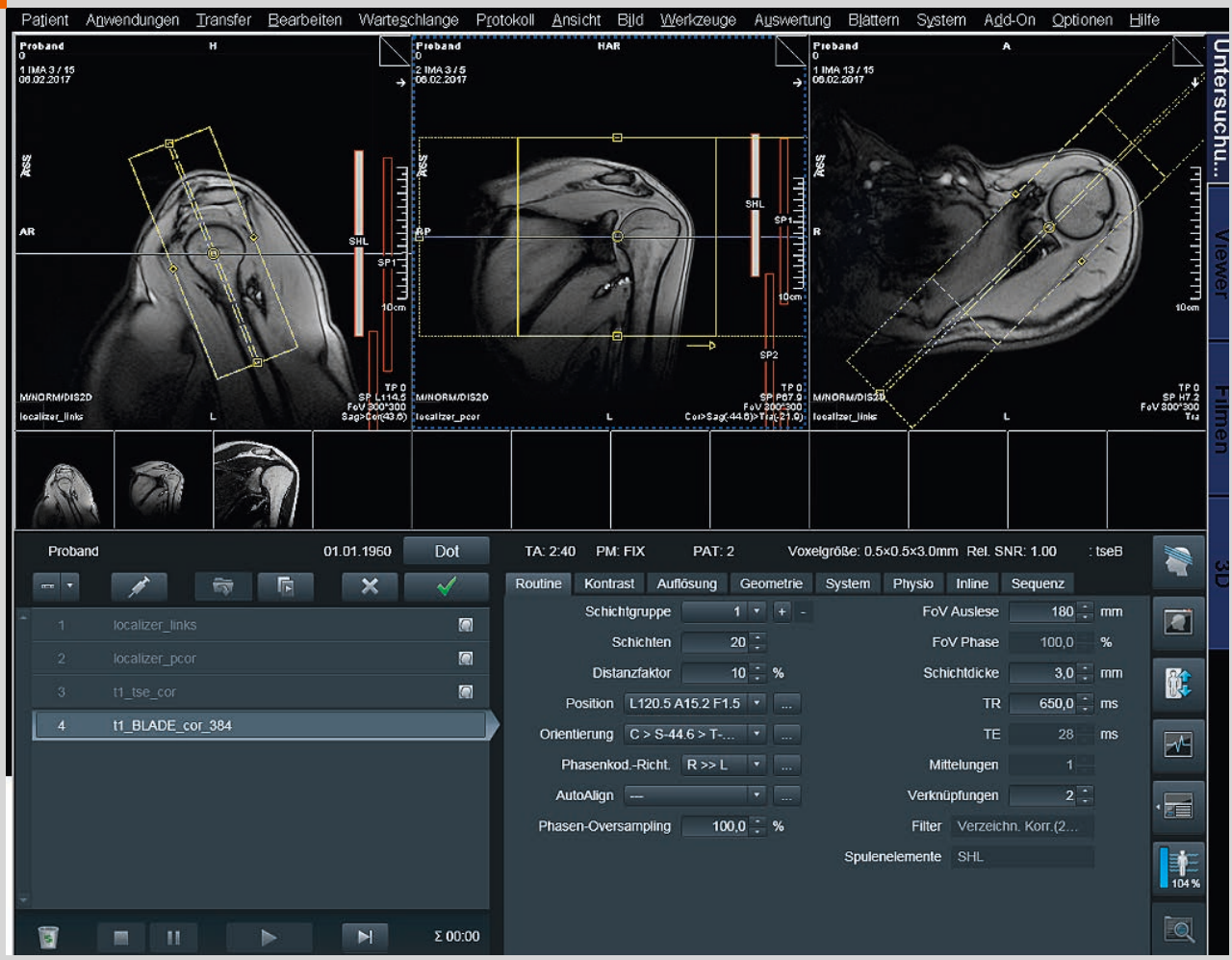

Figure 8: TR

9

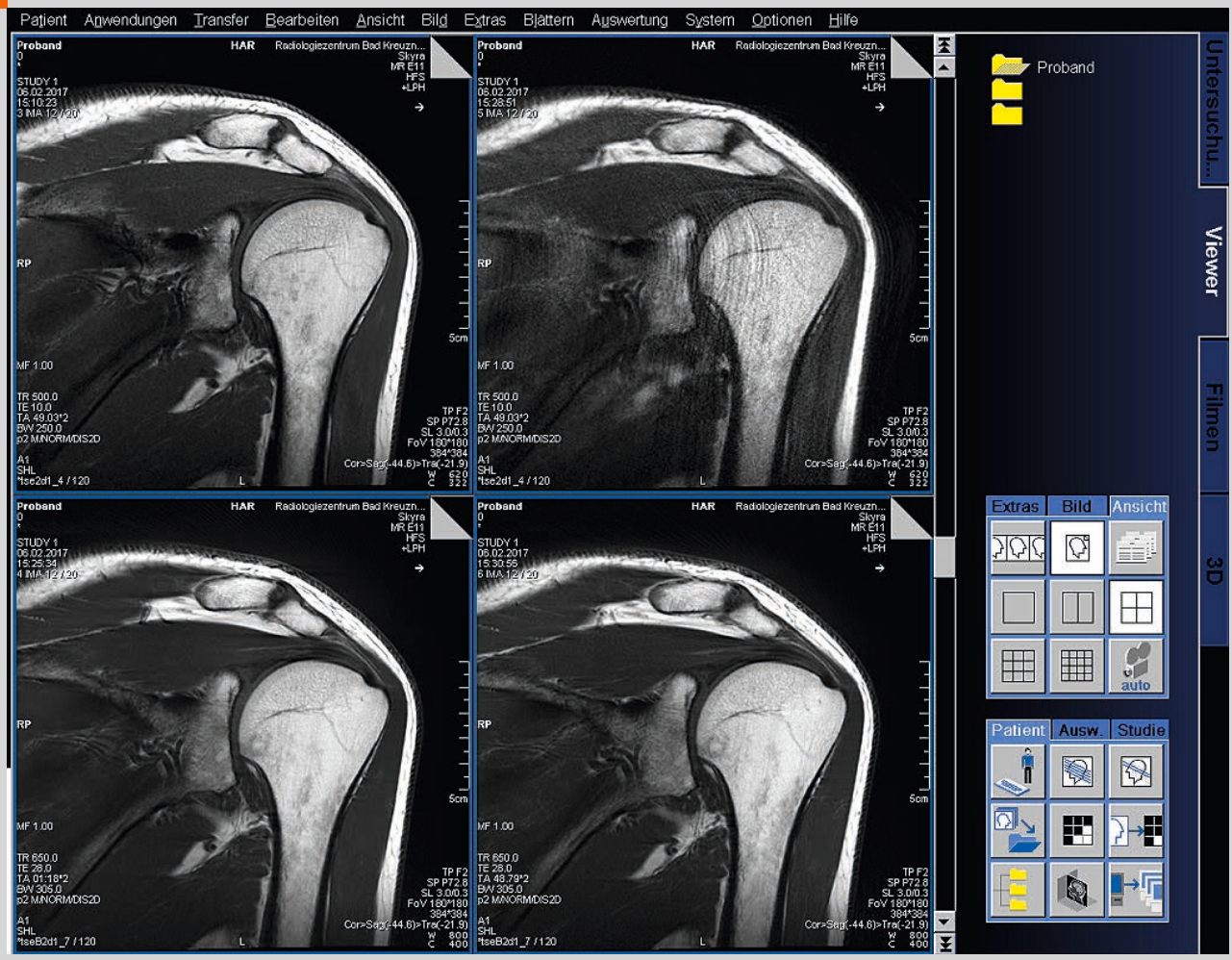

Figure 9: The upper left image shows a coronal T1 TSE with good image quality and a scan time of 1.40 mins. The upper right image shows the same measurement with artifacts caused by patient movement. The lower left image shows the 'true' T1-weighted BLADE with an equal image quality and contrast as the TSE. Possible artifacts, caused by patient movement, are suppressed.

The lower right image shows a faster version of the BLADE with reduced BLADE coverage of 83.5% and reduced Phase-oversampling of 50%, leading to a scan time of 1.38 mins. Contrast was not affected and image quality is still convincing.

Images courtesy of Radiologiezentrum Bad Kreuznach, Germany.

Result

The images in Figure 9 show a comparison of T1-weighted TSE and BLADE images acquired with a MAGNETOM Skyra 24-channel scanner, using the dedicated 16-channel shoulder coil.

Please visit us at
www.siemens.com/magnetom-world
to download the .exar1 file of the shoulder protocol for 3T MAGNETOM Skyra.

Contact

Thomas Illigen
Application Specialist MR
Customer Solutions, Region Germany, Central Region
Siemens Healthcare GmbH
HC CX DE MTE CS

Dynamostr. 4
68165 Mannheim
Germany
Phone: +49 174 2011898
thomas.illigen@siemens.com

Case Report: Lisfranc/Tarsometatarsal Joint Injury

Richard C. Shin, M.D.; Charles P. Ho, Ph.D., M.D.

Steadman Philippon Research Institute, Vail, CO, USA

History of present illness

The patient is a 44-year-old female who has left foot pain and swelling following acute injury. She notes symptoms following an episode where she was carrying her sick 8-year-old son down the stairs when she missed the last step and fell, twisting her left foot and falling to the ground. She then tried to stand up and put weight on her left foot, but due to severe pain she states she 'passed out' and fell again and her husband found her at the bottom of the steps. She presented at the local emergency department, where X-rays were taken and she was told she bruised her foot. Due to her pain and inability to bear weight fully, she spoke to her orthopedic surgeon, who ordered an MRI and consultation with a foot and ankle specialist. Prior to the fall, she was in her normal state of health. In addition to her left foot pain and swelling and limited weight-bearing, she notes bruising in the area. Review of symptoms was otherwise negative, outside of exacerbation of her pre-existing left knee symptoms.

Physical examination

She was noted on physical examination not to be able to stand for alignment evaluation due to left foot pain. Left knee was noted to have slight swelling. Tenderness to palpation was noted at the pes anserinus. No MCL insertion tenderness was noted. There was severe swelling throughout the left foot. There was no ankle swelling. Tenderness to palpation was noted over multiple areas of the dorsal aspect of the left foot, as well as plantar aspect of the metatarsal heads. No tenderness to palpation was noted over the lateral or medial malleolus.

Radiographs

Left foot radiographs obtained while in the emergency department were reportedly negative for fracture.

Differential diagnosis for midfoot pain and swelling

- Tarsometatarsal joint fracture/dislocation
- Metatarsal fracture/stress fracture
- Tarsometatarsal osteochondral injury
- Cuboid/navicular fracture and/or compression injury
- Posterior tibial and peroneal tendon injury
- Soft tissue injury/hematoma/fluid collection
- Synovitis/arthritis
- Neuropathic change

Plan

Following emergency department evaluation, the patient was placed on crutches, and arrangements made for orthopedic follow-up and MR imaging.

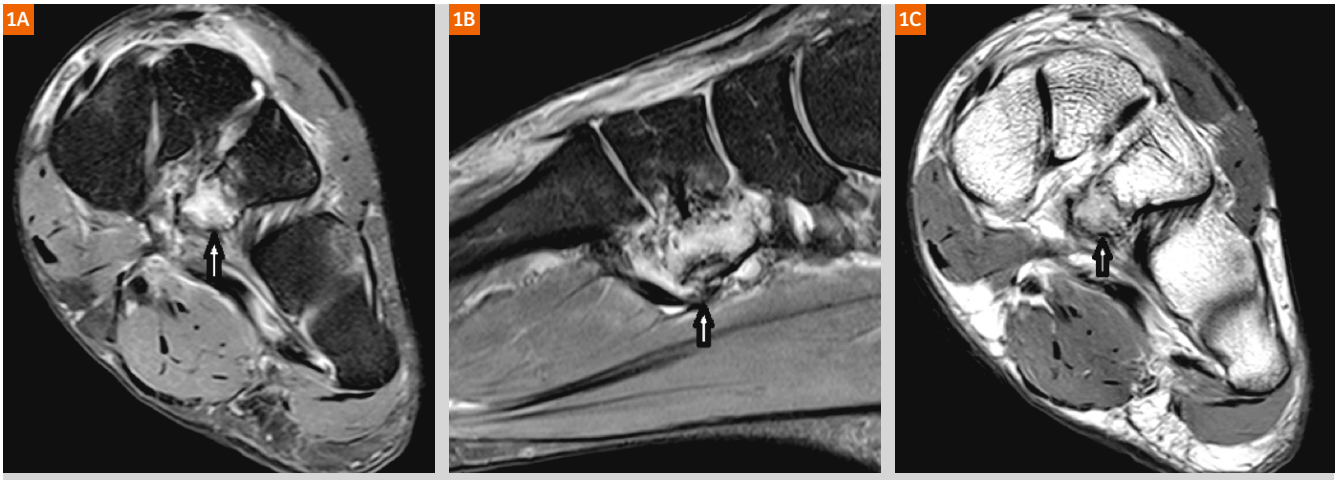

Figure 1: Coronal and sagittal proton density-weighted TSE FS **(1A, B)** and coronal proton density TSE **(1C)** images of the left foot demonstrate comminuted fracture and bone edema at the plantar aspect of the lateral cuneiform with mild plantar displacement/distraction (arrows).

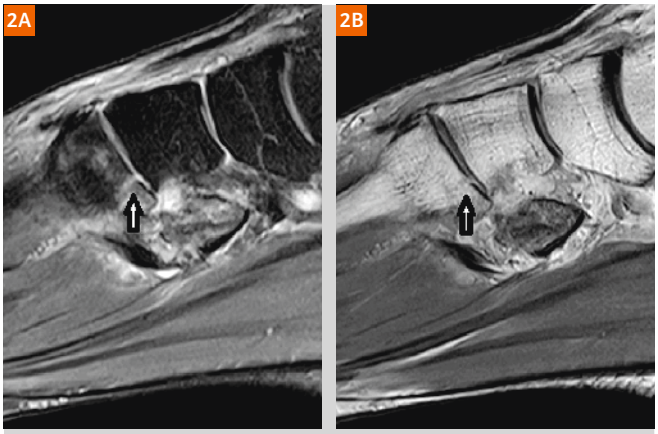

Figure 2: Sagittal proton density-weighted TSE FS **(2A)** and TSE **(2B)** images of the left foot demonstrate fracture at the plantar aspect of the second metatarsal base with intraarticular extension and slight 1 mm displacement/distraction and overlying chondral fracture (arrows).

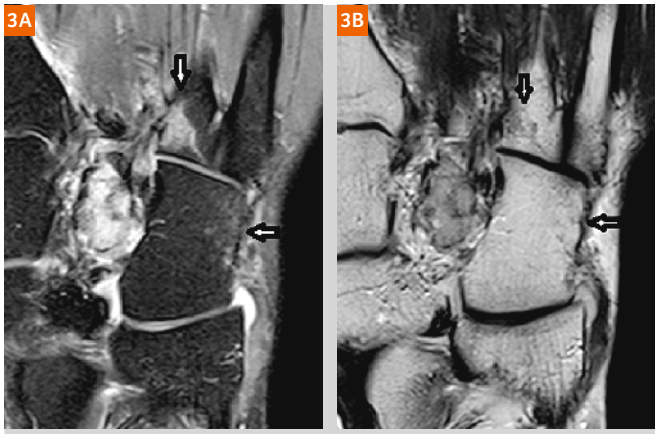

Figure 3: Fourth metatarsal base (vertical arrow) and lateral cuboid (horizontal arrow) contusion/mild impaction injury/ fracture on axial proton density-weighted TSE FS **(3A)** and T2 TSE **(3B)** images.

Midfoot MRI protocol

1. Sagittal Proton Density (PD) Turbo Spin Echo (TSE)
2. Sagittal PD TSE Fat Saturation (FS)
3. Coronal PD TSE
4. Coronal PD TSE FS
5. Axial T2 TSE
6. Axial PD TSE FS

MR imaging findings

1. Comminuted fracture and bone edema at the plantar aspect of the lateral cuneiform with mild plantar displacement/distraction.

2. Fracture at the plantar aspect of the second metatarsal base with intraarticular extension and slight 1 mm displacement/distraction and overlying chondral fracture.

3. Multiple additional areas of contusion/mild impaction fracture/injury with cortical and subcortical fracture lines at the first, second, and fourth tarsometatarsal joints, as well as at the cuboid, anterior calcaneus, and calcaneal and navicular junction, with little or no displacement.

4. Complete tear and stripping of Lisfranc's ligament with possible avulsion from the second metatarsal base with possible small thin curvilinear cortical avulsion fragment. There is severe sprain and possible areas of tearing of tarsal, tarsometatarsal, and intermetatarsal ligaments about the tarsometarsal joint.

Discussion

Lisfranc's fracture was named after Jacques Lisfranc, a field surgeon in Napoleon's army who described a fracture/ dislocation injury pattern at the tarsometatarsal articulation in cavalry riders who fell from the saddle but were

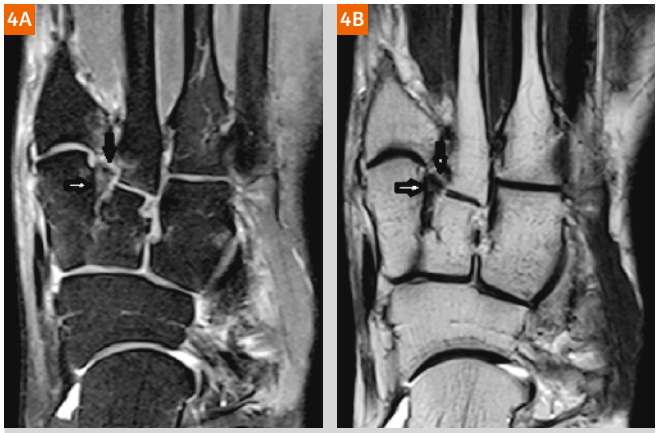

Figure 4: Tear and stripping of Lisfranc's ligament (horizontal arrow) with possible avulsion fragment (vertical arrow) from the second metatarsal base on axial proton density TSE FS **(4A)** and T2 TSE **(4B)** images.

dragged with foot still in the stirrup [1]. The term has now come to refer to any injury to the tarsometatarsal joint, with the joint now bearing Lisfranc's name.

The tarsometatarsal joint is a complex structure comprising the metatarsal bases with the three cuneiforms as well as cuboid, with numerous associated supporting ligaments including the eponymous Lisfranc's ligament which usually bridges the proximal medial margin of the second metatarsal with the distal lateral margin of medial cuneiform. The joint has been classically divided into three longitudinal columns, with the medial column composed of the medial cuneiform and the base of the first metatarsal, the middle column of the middle and lateral cuneiforms and the second and third metatarsal bases, and the lateral column of the cuboid and fourth and fifth metatarsal bases [2].

A classification system for Lisfranc injury has been described, with homolateral injury having all 5 metatarsals displaced in the same direction, isolated injury with one or two metatarsals displaced from the others, and divergent injury with metatarsals displaced and separated in sagittal and coronal planes. The homolateral pattern has been associated with cuboid fracture, and divergent injury with intercuneiform extension and navicular fracture, although multiple other complex injury patterns are also possible [3].

Lisfranc injuries can result from both indirect and direct trauma. Direct injuries, including crush and other high-energy mechanisms are frequently associated with significant soft tissue trauma, and compartment syndrome and vascular compromise are common sequela. Two classic indirect trauma mechanisms, axial loading of the foot in a fixed equinus position, as well as forced external rotation have been described, the latter corresponding to Lisfranc's originally-described injury mechanism [4].

On physical examination, pain and swelling of the midfoot, with tenderness along Lisfranc's joint with passive abduction and pronation of the forefoot with the hindfoot held fixed is the classic finding. Plantar midfoot ecchymosis and frank midfoot instability may be seen with more severe injuries, and assessment for vascular compromise and compartment syndrome should always be made with tarsometatarsal trauma [5].

Imaging

Radiographs

Conventional radiographic findings may range from frank fracture and dislocation with more severe injuries, but findings may be more subtle or absent with less severe injuries. Stress radiographs and/or fluoroscopy as tolerated may increase sensitivity.

Computed tomography

The superior bone demonstration capability of CT, in combination with 2D and 3D reconstruction techniques may be very helpful in the detection and characterization of more subtle or complex fractures.

MR imaging

MRI soft tissue demonstration capability may be useful in direct assessment for ligamentous injury, particularly when there is a high clinical concern with routine radiographs being inconclusive [6]. MRI is also helpful for suspected more acute bone injury, with benefit of acute bone and surrounding soft tissue edema and hemorrhage, when radiographically occult.

Treatment and prognosis

Non-displaced or slightly-displaced Lisfranc injury can initially be treated conservatively, but continued instability often necessitates subsequent surgery, particularly given high rates of post-traumatic arthritis. Injuries with 2 mm of displacement or more, or tarsometatarsal angulation of 15 degrees or more are treated primarily, with open/internal fixation and arthrodesis being much preferred over closed fixation, in the absence of contraindication such as skin disruption. Recent meta-analysis suggests that ORIF and arthrodesis yield “satisfactory and equivalent” results, with perhaps a slight advantage to primary arthrodesis in terms of clinical outcomes [7].

References

1 Matar HE, Atkinson HD, Toh EM, Akimau PI, Davies MB. Surgical interventions for treating tarsometatarsal (Lisfranc) fracture dislocations. Cochrane Database of Systematic Reviews 2014, Issue 7. Art. No.: CD011235. DOI: 10.1002/14651858.CD011235.
2 Scolaro JA, Ahn J, Mehta S. Lisfranc Fracture Dislocations. Clin Orthop Relat Res (2011) 469:2078–2080 DOI 10.1007/s11999-010-1586-z.
3 Wheeless, CR. Lisfranc's Fracture/Tarsometatarsal Injuries. (2016) Retrieved from http://www.wheelessonline.com/ortho/lisfrancs_fracture_tarsometatarsal_injuries. Accessed on July 22, 2016.
4 Gotha HE, Lareau CR, Fellars TA. Diagnosis and management of Lisfranc injuries and metatarsal fractures. R I Med J (2013). 2013 May 1;96(5):33-6. PubMed PMID: 23641461.
5 Myerson MS. The Diagnosis and Treatment of Injury to the Tarsometatarsal Joint. J Bone Joint Surg [Br] 1999;81-B:756-63.
6 Weerakkody Y and Gaillard F. Lisfranc Injury. Retrieved from http://radiopaedia.org/articles/lisfranc-injury. Accessed on July 22, 2016.
7 Sheibani-Rad S, Coetzee JC, Giveans MR, DiGiovanni C. Arthrodesis versus ORIF for Lisfranc fractures. Orthopedics. 2012 Jun;35(6):e868-73. doi:10.3928/01477447-20120525-26. Review. PubMed PMID: 22691659.

Contact

Charles P. Ho, Ph.D., M.D.
Steadman Philippon Research Institute

181 West Meadow Drive, Suite 1000
Vail, CO 81657
USA
Phone: +1 (970) 479-9797
Fax: +1 (970) 479-9753
charles.ho@sprivail.org

High-resolution, Anatomically-accurate Diffusion-weighted Imaging of Orbital and Sinonasal Lesions with RESOLVE

Yan Sha[1]; Hailin Wan[1]; Menglong Zhao[1]; Feng Wang[1]; Ping Lu[1]; Fang Zhang[1]; Wen Lin Tang[2]; Yushu Cheng[1]

[1] Department of Radiology, Eye, Ear, Nose and Throat Hospital, Fudan University, Shanghai, China
[2] Siemens Healthineers, MR Scientific Marketing, Shanghai, China

Diffusion-weighted imaging is a core sequence in clinical routine imaging for many anatomical regions including the brain, abdomen, breasts, and pelvis [1, 2]. Conventionally, diffusion-weighted imaging is acquired using a single-shot diffusion-weighted echo planar imaging (EPI) sequence with the primary advantages of insensitivity to motion-induced phase errors and relatively short acquisition times. However, this sequence also suffers from lower spatial resolution as well as susceptibility-based, geometric distortions in certain regions (such as fluid/air interfaces). This has posed challenges for high-quality, diffusion-weighted imaging of the eyes, ears, nose, and throat.

	Conventional SS-EPI	RESOLVE
TR (ms)	8000	4700
TE (ms)	88	66
Echo spacing (ms)	1.08	0.34
FOV	240 x 240 or 220 x 220	240 x 240 or 220 x 220
Matrix	154 x 192 or 164 x 164	154 x 192 or 192 x 192
Slice / Gap (mm)	4.0 / 0.6	4.0 / 0.6
b-values (s/mm²)	0, 1000	0, 1000
Averages	4	1
GRAPPA factor	2	2
Readout segments	-	7
Total acquisition time (min)	2:34	2:55

Table 1: Imaging parameters of the SS-EPI and RESOLVE sequences as used in Zhao et al. (2016) [6].

RESOLVE (**RE**adout **S**egmentation **O**f **L**ong **V**ariable **E**cho trains) [3, 4] is a multi-shot, diffusion-weighted sequence with a readout-segmented EPI sampling scheme. This sequence includes a 2D non-linear correction for motion-induced phase errors together with GRAPPA [5] functionality. The significantly shortened EPI echo spacing (as only a subset of raw data points in the readout direction is sampled with each shot) enables a significant reduction in the level of susceptibility and blurring, making it possible to acquire diffusion-weighted images of higher resolution.

In this paper, we review four of the recently published studies from our Institution where RESOLVE was shown to be clinically effective in the diffusion-weighted imaging of sinonasal and optic pathologies. We additionally demonstrate the clinical value that RESOLVE brings to the detection and characterization of the diseases in these regions.

RESOLVE in the imaging of sinonasal lesions

Our first evaluation of RESOLVE in the imaging of sinonasal lesions involved a comprehensive comparison of image quality relative to conventional single-shot EPI (SS-EPI) (see Table 1 for the imaging parameters of these two sequences) in 32 patients with sinonasal lesions [6]. Image quality was evaluated qualitatively by two head and neck radiologists with decisions made on consensus where there is divergence. In addition, a quantitative evaluation of the geometric distortion was also performed.

RESOLVE ADC maps had significantly higher ratings compared to SS-EPI on the scales of image quality, lesion conspicuity, and image distortions (Table 2 and Fig. 1). During the analyses, we also observed that RESOLVE was capable of revealing the otitis media of five patients (e.g., via the effusion of mastoid cells) more clearly than SS-EPI. RESOLVE also exhibited the orbit, skull base, and upper neck with significantly reduced distortion, ghosts, and blurring. The delicate structures of the orbit, such as the globe, optic nerve, extraocular muscle, and lacrimal gland

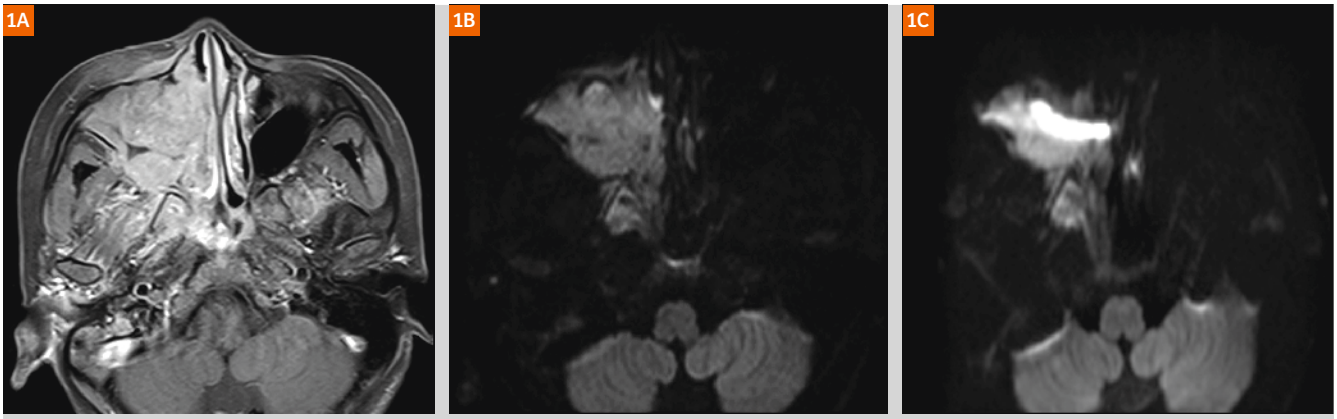

Figure 1: Contrast-enhanced T1 TSE **(1A)**, RESOLVE b1000 **(1B)** and SS-EPI b1000 **(1C)** of a mass that involved the right nasal cavity, maxillary sinus, pterygopalatine fossa and pterygospinous process. The RESOLVE b1000 image was relatively artifact free, enabling detailed observation of the mass which was not possible in the SS-EPI b1000 image due to significant susceptibility artifacts [6].

		N	SS-EPI (mean ± SD)	RESOLVE (mean ± SD)	p-value
Qualitative evaluation	Image quality	32	2.36 ± 0.57	3.72 ± 0.68	<.001
	Lesion conspicuity	32	2.24 ± 0.83	4.00 ± 0.87	<.001
	Distortion	32	2.20 ± 0.50	0.16 ± 0.37	<.001
Quantitative evaluation	ADC (x10^{-3} mm^2/s)				
	Lesion	20	1.31 ± 0.73	1.25 ± 0.68	.001
	Brainstem	32	0.74 ± 0.42	0.75 ± 0.44	.350
	SNR (b1000)				
	Lesion	20	150.72 ± 118.97	90.64 ± 56.08	.002
	Brainstem	32	108.42 ± 32.74	81.58 ± 31.21	<.001
	CNR	20	2.46 ± 1.51	2.51 ± 1.50	.798

Table 2: Results of the qualitative and quantitative evaluations of RESOLVE and SS-EPI images [6].

could be visualized with RESOLVE. The image qualities of the nasopharynx and upper neck were also improved by the introduction of RESOLVE, which resulted in significantly reduced ghosts and distortions and enabled us to observe nasopharynx disease and neck lymph nodes.

To evaluate extent of geometric distortions, key anatomical landmarks (bilateral frontal-internal points, lateral points, and back points of the maxillary sinus, bilateral back points, of the inferior nasal concha, and bilateral frontal-lateral points of the sphenoid sinus) were identified and their coordinates were marked on the T2w TSE, T1w TSE, and the B_0 images for SS-EPI and RESOLVE. The differences in the coordinate locations (in mm) between the T2w and the other images (T1w, SS-EPI, and RESOLVE) were measured and compared. Our findings indicated that while some minimal residual distortions remain with RESOLVE (relative to the T1w images), the extent of the deviation from the T2w images was, on average, 3 times higher for SS-EPI compared to RESOLVE [6].

We also evaluated for differences in ADC as well as signal-to-noise ratio (SNR) and contrast-to-noise ratio (CNR) between RESOLVE and SS-EPI using regions-of-interest (ROIs) carefully matched to the lesions together with ROIs placed in the brainstem. There were significantly lower ADC values for RESOLVE compared to SS-EPI for the lesions while the ADC values for the brainstem were similar (Table 2). For us, the elevated lesion ADCs seen for SS-EPI is likely the result of the more inhomogeneous ADC maps due to susceptibility and ghosting artifacts which are prevalent in conventional diffusion-weighted imaging of the nasal cavity. This is bolstered by the finding of similar ADC values in the brainstem.

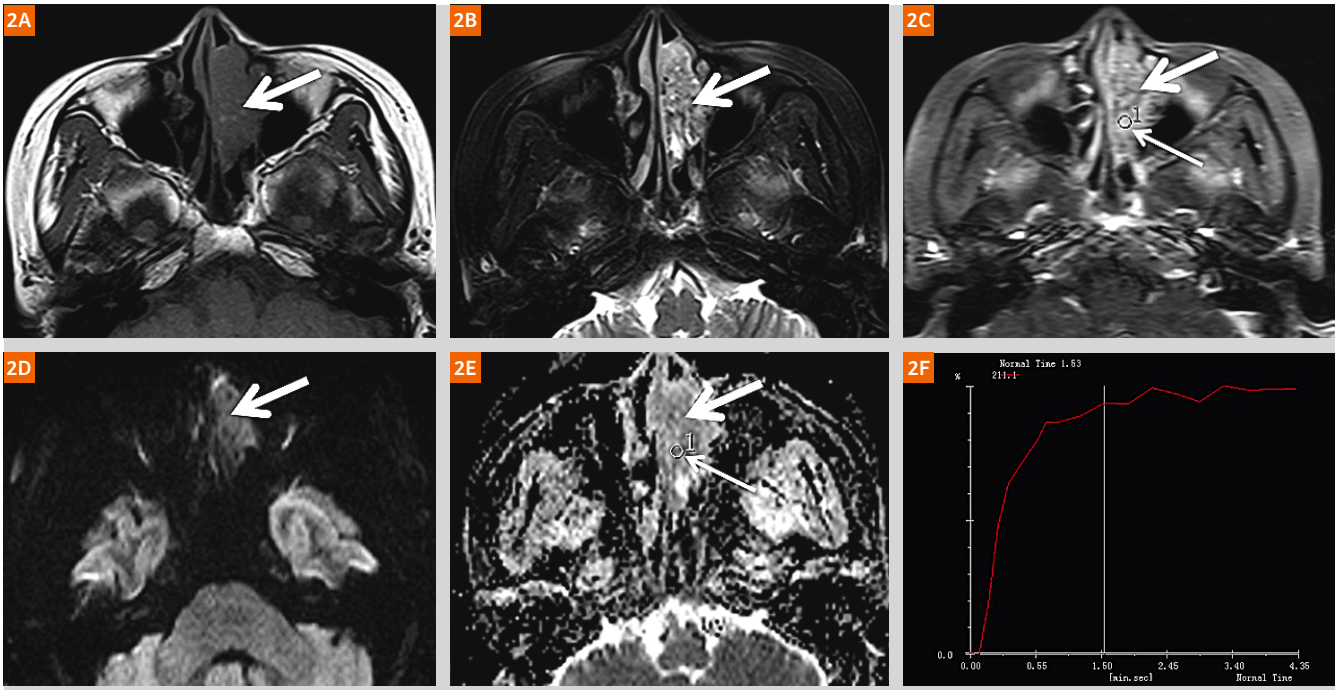

Figure 2: A 43-year-old man diagnosed with rhabdomyosarcoma. The lesion is indicated by the thick arrow and ROI by the thin arrow. **2A**: Axial T1-weighted with isointense mass in right nasal cavity and maxillary sinus; **2B**: Axial fat-suppressed T2-weighted; **2C**: Axial, contrast-enhanced T1-weighted showing marked heterogeneous enhancement; **2D**: b-value 1000 s/mm² RESOLVE with high signal intensity in the lesion; **2E**: ADC map with low signal intensity in the lesion and mean absolute ADC of 0.482 x 10^{-3} mm²/s within the ROI; **2F**: DCE-MRI time-signal intensity curve in this patient is categorized as type 3 with washout enhancement [8].

SNR was lower for RESOLVE compared to SS-EPI, however, there were no significant differences for CNR. This finding is not surprising as SS-EPI has more efficient *k-space* coverage compared to RESOLVE [7] which necessitates the loss of the advantage of a short acquisition time. However, the higher SNR of SS-EPI does not translate to increased resolution or image quality. In contrast, RESOLVE has the potential to achieve higher resolution with reduced susceptibility artifacts and T2* blurring compared to SS-EPI. Critically, there is no difference in the CNR ratio, consistent with a previous study on breast cancer [7].

Following our establishment of the improved image quality provided by RESOLVE in sinonsal lesions, we sought to investigate the clinical utility of RESOLVE; specifically we tested if the addition of RESOLVE may improve the differentiation of benign and malignant sinonasal lesions over DCE-MRI [8].

This study involved 98 patients (61 females, mean age 47 years) who underwent RESOLVE and DCE-MRI examinations. 58 patients had histologically-proven malignant lesions while the remaining 40 were established as benign (see Fig. 2 for a case example). The images were post-processed and the data analyzed by an experienced radiologist who was blinded to the histopathological results [8]. Parameters derived from DCE-MRI included several parameters uptake characteristics (see [8] for more details).

Logistic regression and receiver operator characteristic (ROC) curve analyses were performed, first with DCE-MRI parameters alone, followed by DCE-MRI together with RESOLVE ADC values. With DCE parameters alone, accuracy of classification was 70.4 (ROC curve AUC: 0.69, sensitivity 57.5%, specificity 79.3%). When ADC was added to the analysis, the diagnostic accuracy increased to 85.7 (AUC 0.87, sensitivity 85.0%, specificity 86.2%).

RESOLVE in the imaging of optic neuritis

Acute optic neuritis (ON) is one the most common optic neuropathology in young adulthood. It is often associated with multiple sclerosis (MS) or neuromyelitis optica (NMO) but can also occur in isolation [9]. The diagnosis of ON is currently based solely on clinical and neuro-ophthalmological examination [10]. However, MRI is also used for the assessment of the inflammatory changes in the optic nerve as well as to rule out structural lesions and other compressive or inflammatory orbital lesions.

Diffusion-weighted imaging of the optic nerve in patients with ON have been shown to predict clinical outcome [11, 12]. However, these studies were based on SS-EPI diffusion which is more prone to susceptibility artifacts in the topic area compared to RESOLVE (Fig. 3). We thus sought to evaluate the role of RESOLVE in detecting acute ON relative to fat-suppressed contrast-enhanced T1w TSE imaging [13].

The final study population consisted of 42 patients with ophthalmological symptoms who have undergone an evaluation for ON by a neuro-ophthalmologist and an MRI within 4 weeks of their acute presentation. 8 patients had neither a clinical history nor positive findings of ON during the ophthalmological examination while the remaining 34 were diagnosed as having left, right, or bilateral ON. Out of the total of 84 optic nerves evaluated, 41 were considered clinically positive and 43 negative.

The MRI examination included RESOLVE (TR 4700 ms, TE 70 ms, slice thickness 2.9 mm, gap 10%, 25 slices, bandwidth 723 Hz/px, matrix 192, FOV 220 mm, averages 1 to 2, b-value 1000 s/mm^2, diffusion directions 3, TA 2.5–5.3 minutes) and post-contrast T1-weighted TSE (CE-T1) in 3 orientations: axial (TR 643 ms, TE 12 ms, slice 2 mm), oblique sagittal (TR 713 ms, TE 12 ms, slice 2 mm) and coronal (TR 568 ms, TE 11 ms, slice 3 mm). The RESOLVE and CE-T1 images were reviewed separately by two independent neuroradiologists who were blinded to the clinical history and diagnosis by the neuro-ophthalmologist. Each optic nerve was evaluated for optic neuritis and marked as 'positive' (+), 'negative' (-) or indeterminate.

This study found, as expected, that the accuracy of fat suppressed CE-T1 for acute optic neuritis was higher than diffusion ADC. For the two readers, the sensitivity, specificity and accuracy of CE-T1 for acute ON neuritis were 68.3/85.4%, 79.1/93.0% and 82.1/90.0%, respectively. For RESOLVE, they were 82.9/82.9%, 81.4/83.7% and 82.1/83.3%, respectively [13]. Nevertheless it should be noted that the sensitivity and specificity of RESOLVE were high and helped in the resolution of a number of patient cases. In our study, there were 3 cases of bilateral acute atypical ON with no obvious enhancement on CE-T1 but with high signal on DWI with decreased ADC values (Fig. 4). Moreover, for patients contraindicated for contrast injection, DWI can inform on molecular motion and thus play an important role in diagnosis and patient management.

Beyond diagnosis of acute ON, it is also important to be able to differentiate between different clinical types. Acute ON usually precedes the onset of MS or NMO. While NMO can be distinguished from MS at a biochemical level by the presence of the antibody to the astrocyte water channel protein aquaporin 4 (AQP4) [14], it can still commonly be misdiagnosed as MS. As the treatment and prognosis for NMO are distinct from MS [15], it is important to help clinically differentiate between them. We evaluated the possibility that diffusion MRI with RESOLVE may help differentiate between MS- and NMO-related acute ON. We also investigated if MR diffusion parameters may help predict findings on optical coherence tomography (OCT) at six months post the acute attack [16].

34 patients, 19 diagnosed with MS-ON and 15 with NMO-ON, and 16 normal controls were studied (see [16] for more information on patient selection criteria). RESOLVE was acquired on all participants with the following parameters (TR 4700 ms, TE 70 ms, slice thickness 2.9 mm, gap 10%, 25 slices, bandwidth 723 Hz/Px, matrix of 192, FOV 220 mm, voxel size of 1.1 x 1.1 x 2.9 mm^3, 2 averages, b-value of 0, 1000 s/mm^2, 3 diffusion directions, 7 readout segments, TA 5.3 minutes) (Fig. 5).

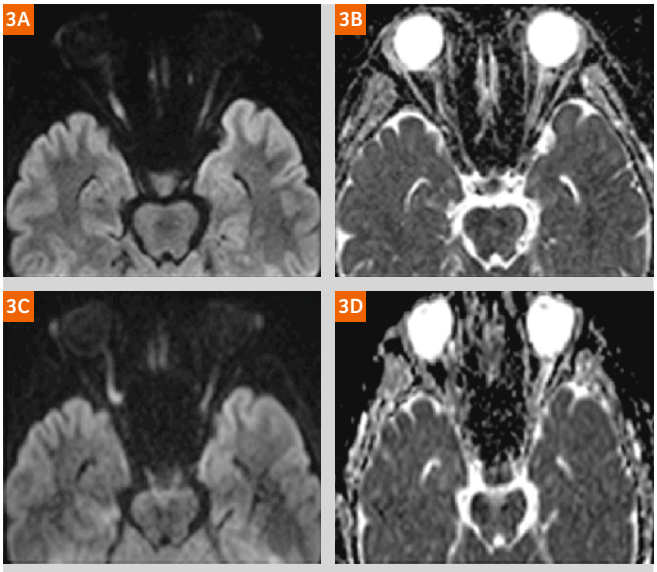

Figure 3: RESOLVE (**3A**: b1000, **3B**: ADC) shows reduced distortion and greater anatomical detail of the optic area compared to SS-EPI (**3C**: b1000, **3D**: ADC) [13].

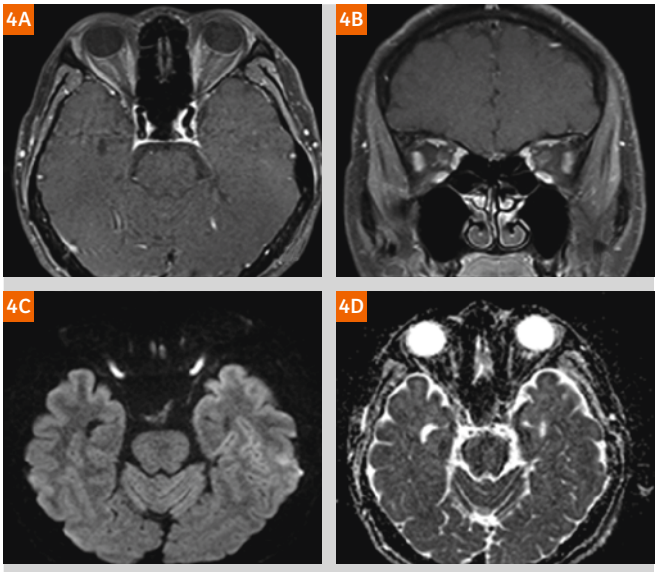

Figure 4: 21-year-old male with bilateral optic neuritis and no light perception. CE-T1 axial and coronal **(4A, B)** showed no obvious contrast enhancement while RESOLVE b1000 and ADC **(4C, D)** showed apparent diffusion restriction, bilaterally.

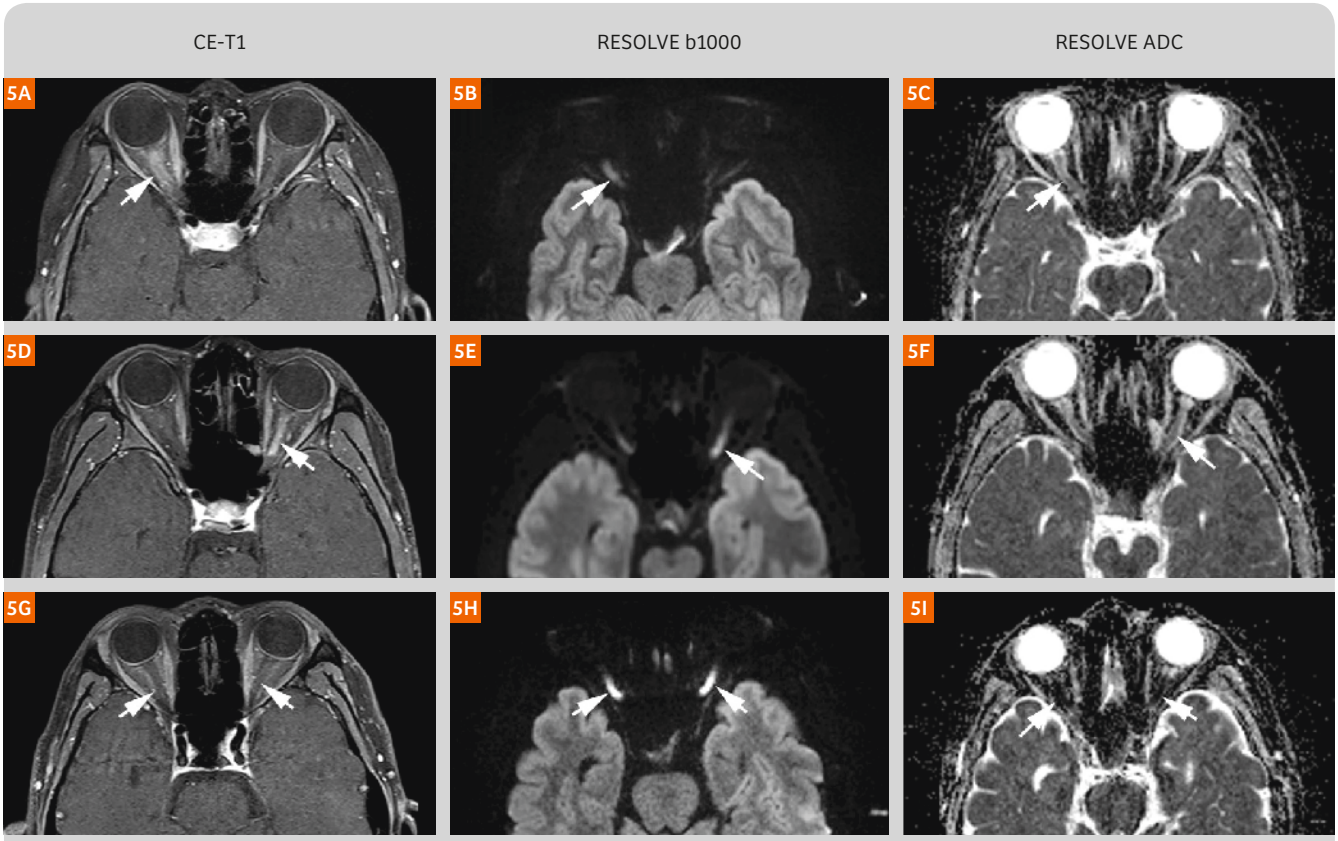

Figure 5: CE-T1, RESOLVE b1000 and ADC maps of three patients. **5A–C**: Patient with MS-ON with acute visual decrease in the right eye. **5D–F**: NMO-ON patient with affected left eye and positive serum AQP4-IgG. **5G–I**: Bilateral NMO-ON patient with negative serum AQP4-IgG [16]. Mean ADC values were significantly higher for the controls ((1.025 ± .067) x 10^{-3} mm^2/s) compared to the two patient groups ($p < .0001$); with significantly higher mean ADC for the MS-ON patients ((.879 ± .144) x 10^{-3} mm^2/s) compared to the NMO-ON patients ((.691 ± .195) x 10^{-3} mm^2/s) ($p = .013$). ROC curve analysis to differentiate between MS-ON and NMO-ON patients indicated an AUC of 0.785. A threshold value of 0.830 x 10^{-3} mm^2/s had the best result with sensitivity 75%, specificity 78.3% and accuracy 76.7%. Significant correlations were found between ADC values and optic nerve peripapillary retinal nerve fiber layer (RNFL) thickness ($r = .44$, $p = .006$) as well as the macular ganglion complex (GCC; $r = .526$, $p < .0001$). These findings support the idea of different pathophysiology of MS and NMO and that, unlike the acute demyelination of MS-ON, the infiltration and necrosis generated by the AQP4 antibodies may result in more severe axonal damage.

Summary and conclusions

We reviewed four recent papers from our institution which evaluated the role of RESOLVE in the imaging of lesions within the sinonasal and optic regions. Compared to conventional SS-EPI, RESOLVE is a breakthrough in terms of achieving high-resolution, low distortion diffusion-weighted imaging of these challenging regions. With RESOLVE, small anatomical structures can be better visualized without the marked susceptibility distortion typically present for conventional diffusion in these areas [6].

With the improvement to diffusion imaging quality provided by RESOLVE, this opens up opportunities to quantitatively assess the role of diffusion in the clinical diagnoses of orbital and sinonasal lesions. We have shown that RESOLVE ADC values can improve the accuracy to differentiate between malignant and benign sinonasal lesions over and above CE-T1 [8]. For optic neuritis, the most common optic neuropathology in young adults, RESOLVE ADCs have a high accuracy in differentiating between normal and affected optic nerves and complements T1-CE in the diagnostic process. RESOLVE ADCs may also help differentiate between multiple sclerosis related optic neuritis and neuromyelitis optica related optic neuritis as well as predict optic nerve atrophy [16]. This can help support better diagnosis of these diseases and also help predict the prognosis of these patients.

References

1 Moritani T, Ekholm S, Westesson PL (eds.). Diffusion-weighted MR imaging of the brain. 2005. Springer-Verlag: Berlin.
2 Koh DM, Thoeny HC (eds.). Diffusion-weighted MR imaging: Applications in the body. Springer-Verlag: Berlin.

3 Porter DA, Heidemann RM. High resolution diffusion-weighted imaging using readout-segmented echo-planar imaging, parallel imaging and a two-dimensional navigator-based reacquisition. Magn Reson Med 2009;62(2):468–75.
4 Hayes LL, Porter DA, Jones RA, Palasis S, Grattan-Smith D. RESOLVE: A powerful tool for imaging the pediatric spine. MAGNETOM Flash 2014; 57: 38-45.
5 Griswold MA, Jakob PM, Heidemann RM, Nittka M, Jellus V, Wang J, et al. GeneRalized Autocalibrating Partially Parallel Acquisitions (GRAPPA). Magn Reson Med 2002;47:1202-1210.
6 Zhao ML, Liu Z, Sha Y, Wang SJ, Ye XP, Pan YC, et al. Readout-segmented echo-planar imaging in the evaluation of sinonasal lesions: A comprehensive comparison of image quality in single-shot echo-planar imaging. Magn Reson Imaging 2016; 34: 166-172.
7 Bogner W, Pinker-Domenig K, Bickel H, Chmelik M, Weber M, Helbich TH, et al. Readout-segmented echo-planar imaging improves the diagnostic performance of diffusion-weighted MR breast examinations at 3.0 T. Radiology 2012; 263(1):64–76.
8 Wang F, Sha Y, Zhao ML, Wan HL, Zhang F, Cheng YS, et al. High-resolution diffusion-weighted imaging improves the diagnostic accuracy of dynamic contrast-enhanced sinonasal magnetic resonance imaging. Comput Assist Tomogr 2016. Published ahead of print.
9 Beck RW. Optic neuritis: Clinical considerations and the relationship to multiple sclerosis. Neuro-ophthalmology 1998; 20:1-20.
10 Hickman SJ, Dalton CM, Miller DH, Plant GT. Management of acute optic neuritis. Lancet 2002;360:1953–1962.
11 Naismith RT, Xu J, Tutlam NT, et al. Radial diffusivity in remote optic neuritis discriminates visual outcomes. Neurology 2010;74:1702–1710.
12 van der Walt A, Kolbe SC, Wang YE, et al. Optic nerve diffusion tensor imaging after acute optic neuritis predicts axonal and visual outcomes. PLoS ONE 2013; 8(12):e83825.
13 Wan HL, Sha Y, Zhang F, Hong RJ, Tian GH, Fan H. Diffusion-weighted imaging using readout-segmented echo-planar imaging, parallel imaging, and two-dimensional navigator-based reacquisition in detecting acute optic neuritis. J Magn Reson Imaging 2016; 43(3): 655-660.
14 Lennon VA, Wingerchuk DM, Kryzer TJ, Pittock SJ, Lucchinetti CF, Fujihara K, et al. A serum autoantibody marker of neuromyelitis optica: distinction from multiple sclerosis. Lancet 2004; 364:2106–2112.
15 Vodopivec I, Matiello M, Prasad S. Treatment of neuromyelitis optica. Curr Opin Ophthalmol 2015;26:476–483.
16 Wan HL, He HJ, Zhang F, Sha Y, Tian GH. Diffusion-weighted imaging helps differentiate multiple sclerosis and neuromyelitis optica-related acute optic neuritis. J Magn Reson Imaging 2016. Published ahead of print.

Contact

Professor Yan Sha
Department of Radiology
Eye, Ear, Nose and Throat Hospital
Fudan University

No. 83 Fenyang Road
Xuhui District, Shanghai 200031
China
cjr.shayan@vip.163.com

Experiences with Robot Assisted MR-guided Inbore Prostate Biopsies

Jeroen Reijnen; Jon Bache Marthinsen

Radiology Department, Sørlandet Hospital Kristiansand, Kristiansand, Norway

Background

Clinical management of prostate cancer is strongly challenged by the triangle of very high prevalence [1], heterogeneous and poorly understood tumor biology, and significant side effects of established treatments [2]. In order to contain the harms of therapy, we have to put great effort into the difficult task of identifying, from a huge pool of indolent prostate cancers, the patients that actually benefit from treatment.

In recent years, multiparametric MR imaging of the prostate (mpMRI) has evolved into a useful tool in the pursuit of better prognostic stratification. On the one hand, quality assured mpMRI has great potential for triage of patients for biopsies [3], i.e. omitting unnecessary biopsies [4]. On the other hand, mpMRI targeted biopsies, instead of or in addition to systematic biopsies, escalate the detection rate of cancer that might need treatment [5] and increase the likelihood and confidence of attaining optimally representative biopsies, i.e. sampling tumor tissue that can be expected to drive prognosis.

Diagnostic pathway

In the assessment for possible prostate cancer at our prostate center, mpMRI is the first test for all patients. For interpretation of the mpMRI we apply PI-RADS v2, but in some cases deviate from the scoring guidelines. Based on recent literature [4] and internal results (Table 1), our group refrains from biopsy in most patients with a negative mpMRI (PI-RADS 1–2). Systematic biopsies despite negative mpMRI are performed in selected patients on the basis of certain clinical alarm signals, since it is clear that prostate cancers can have growth patterns that make them more or less MR-invisible. Patients with a positive mpMRI (PI-RADS 3–5) are scheduled for either MR-guided inbore biopsy or TRUS-biopsy, the preferred method depending on the targets defined on the mpMRI, in the following manner: Lesions considered potentially deterministic for prognosis and treatment choice are defined as biopsy targets, with a maximum of three targets for practical reasons. In case of heterogeneous intratumoral signal characteristics on diffusion-weighted images (DWI) or dynamic contrast-enhanced images (DCE), the area that is suspected to correlate to highest tumor aggressiveness is defined as a separate biopsy target. Only in the case of a high probability of hitting all the defined targets is TRUS-biopsies considered the preferred method. At our institute this currently generates approximately 6 MR-guided biopsies weekly.

	PI-RADS 1+2	PI-RADS 3	PI-RADS 4+5
Group size	**43%**	**8%**	**49%**
% cancer	**1%**	**27%**	**91%**
Gleason score 6	1%	20%	33%
Gleason score 7a	0	7%	30%
Gleason score 7b or higher	0	0	28%

Table 1: Performance of diagnostic mpMRI at our institute. Retrospective data collected for quality assurance purposes (189 patients). Numbers represent highest Gleason score found during completed diagnostic workup or in prostatectomy specimens.

System and workflow

For the MR-guided biopsies we use a MAGNETOM Skyra 3T system and Soteria's Remote Controlled Manipulator (RCM)[1], a pneumatically driven robotic device that allows for precise needle guide steering from the operator room (Fig. 1).

Oral antibiotic prophylaxis and an enema are the only preparations for the biopsy procedure. For the procedure the patient is placed in the prone position on the MR table and a needle guide is inserted in the rectum and subsequently connected to the RCM (Fig. 2). Image guidance is done with TrueFISP, alternatively short T2w TSE, sequences and when deemed beneficial, diffusion-weighted imaging (Case 3). Images are send from the MR console to the RCM software, which then allows for quick and easy calibration and thereafter manipulation of the needle guide position (Fig. 3). When the images show satisfactory needle guide positioning, a biopsy needle is inserted into the needle guide at appropriate depth and the biopsy taken.

[1] The information shown herein refers to products of 3rd party manufacturers (Soteria) and thus are in their regulatory responsibility. Please contact Soteria for further information.

Figure 1: The RCM-system. **(1A)** MRI-compatible robotic device that holds and manipulates the position of the needle guide. **(1B)** Cart that is positioned outside of the MRI-room and connected to the robotic device by plastic tubing, containing a steering unit, compressor and vacuum pump. The system includes a portable laptop with the control and targeting software.

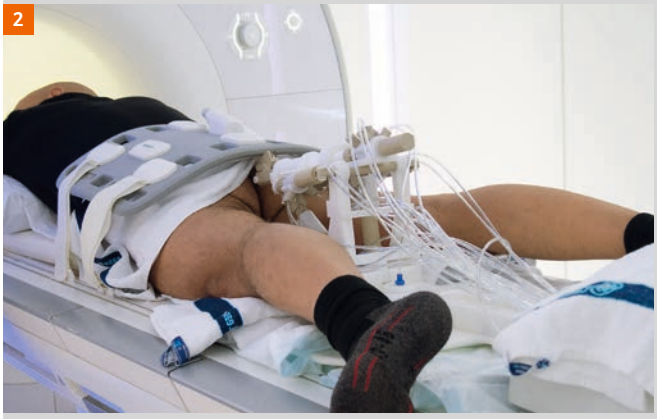

Figure 2: Patient and RCM positioning.

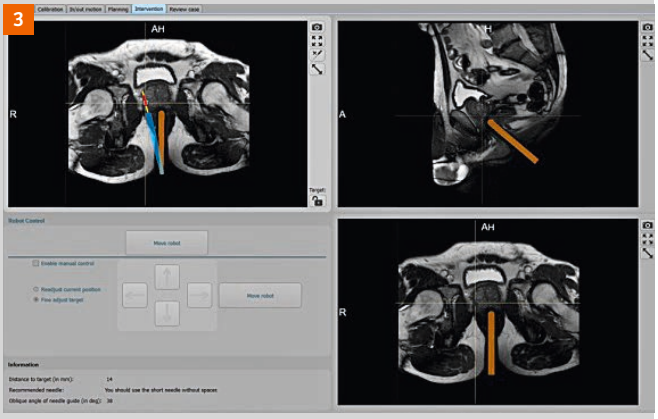

Figure 3: Software interface.

Usage of an MR-compatible biopsy needle permits for image documentation of the needle position. However, in our experience the procedure allows for such accurate needle positioning that this step is superfluous in most cases. By routinely using ordinary biopsy needles we save both time and money.

Procedure time varies with lesion size, location and especially number. In the majority of our cases a door-to-door time of 30 minutes is achieved, but since somewhat longer procedures do occur quite regularly, we currently schedule 40 minutes per patients.

Experiences

Patients generally tolerate the procedure very well. The prone position can become somewhat uncomfortable for the shoulders, but due to predominantly short procedure times this rarely creates significant problems.

Learning to use the RCM system has been quite easy and right from the start we have been able to perform accurate biopsies. Obtaining short procedure times required some experience for both radiologists and technologists, but was achieved rather quickly.

All our targets have been reachable with the system. Biopsy precision is logically dependent on the operator's ability to correctly identify the target and readiness to aim accurately, but the RCM enables the operator to achieve a very high level of precision. In our experience, even the smallest of targets, in all locations in the prostate, are consistently hit (e.g. Case 1).

In approximately 85% of our biopsy cases cancer is found. In the benign cases the mpMRI findings are usually equivocal and the confident needle positioning routinely allows for considering the benign histology to be representative.

In addition to high detection rates, we experience three further important advantages of the high accuracy. First, targeting of more than one lesion and precise targeting of the tumor center or intratumoral areas suspicious of higher-grade cancer regularly generates higher final Gleason scores (Case 2). Second, the technique clarifies mpMRI findings, which increases to total accuracy of the diagnostics. Third, concise learning feedback to the diagnostic imaging is generated, which is highly valuable given the evolving pivotal role of mpMRI in clinical management of probable prostate cancer.

Conclusions

The RCM facilitates targeted MR-guided biopsies of the prostate with very high precision and confidence in a time-efficient manner. Providing high-quality diagnostic mpMRI,

Case 1

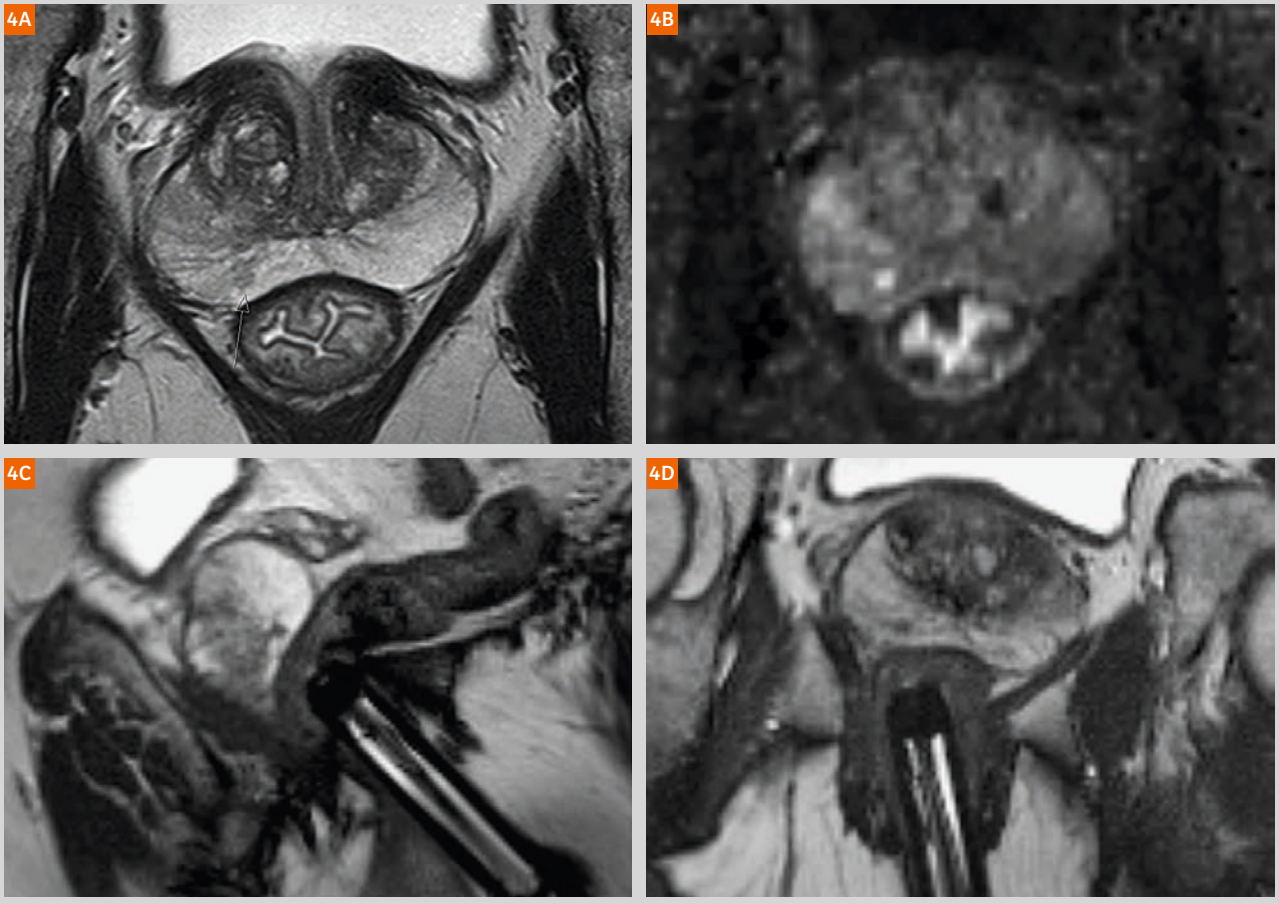

Figure 4: 65-year-old patient with PSA level 4.4.

Diagnostic mpMRI showed a 3 mm highly tumor suspicious lesion in the peripheral zone of the right midgland and additionally typical prostatitis changes anterolaterally mainly on the right side.

MR-guided biopsies revealed prostate cancer Gleason grade 4+3.

4A) Diagnostic mpMRI, transversal TSE T2w.
4B) Diagnostic mpMRI, transversal calculated b1500 images (RESOLVE diffusion).
4C) TrueFISP sagitally along the axis of the biopsy needle guide pointing at the target.
4D) TrueFISP transversally along the axis of the biopsy needle guide pointing at the target.

this allows for routine application of a one-stop, definitive biopsy strategy that aims at accurately mapping prostate cancer. Our center performs RCM-biopsies whenever they are expected to outperform TRUS-biopsies in the challenging task of detecting and delineating the clinical significance of prostate cancer, i.e. in the majority of our patients. With this, the system has revolutionized our practice and empowered us to improve and further develop stratification of our patients. A hope for the future is that improvements in histological grading and molecular testing of tumor tissue [6, 7], combined with optimized biopsies, will lead to further improvements in prognostication.

References

1 Bell, Katy J. L., Del Mar, Chris, Wright, Gordon, Dickinson, James & Glasziou, Paul. 2015. Prevalence of incidental prostate cancer: A systematic review of autopsy studies. International Journal of Cancer. Journal International du Cancer 137: 1749-1757.
2 Resnick, Matthew J., Koyama, Tatsuki, Fan, Kang-Hsien, Albertsen, Peter C., Goodman, Michael, Hamilton, Ann S., Hoffman, Richard M.,

Case 2

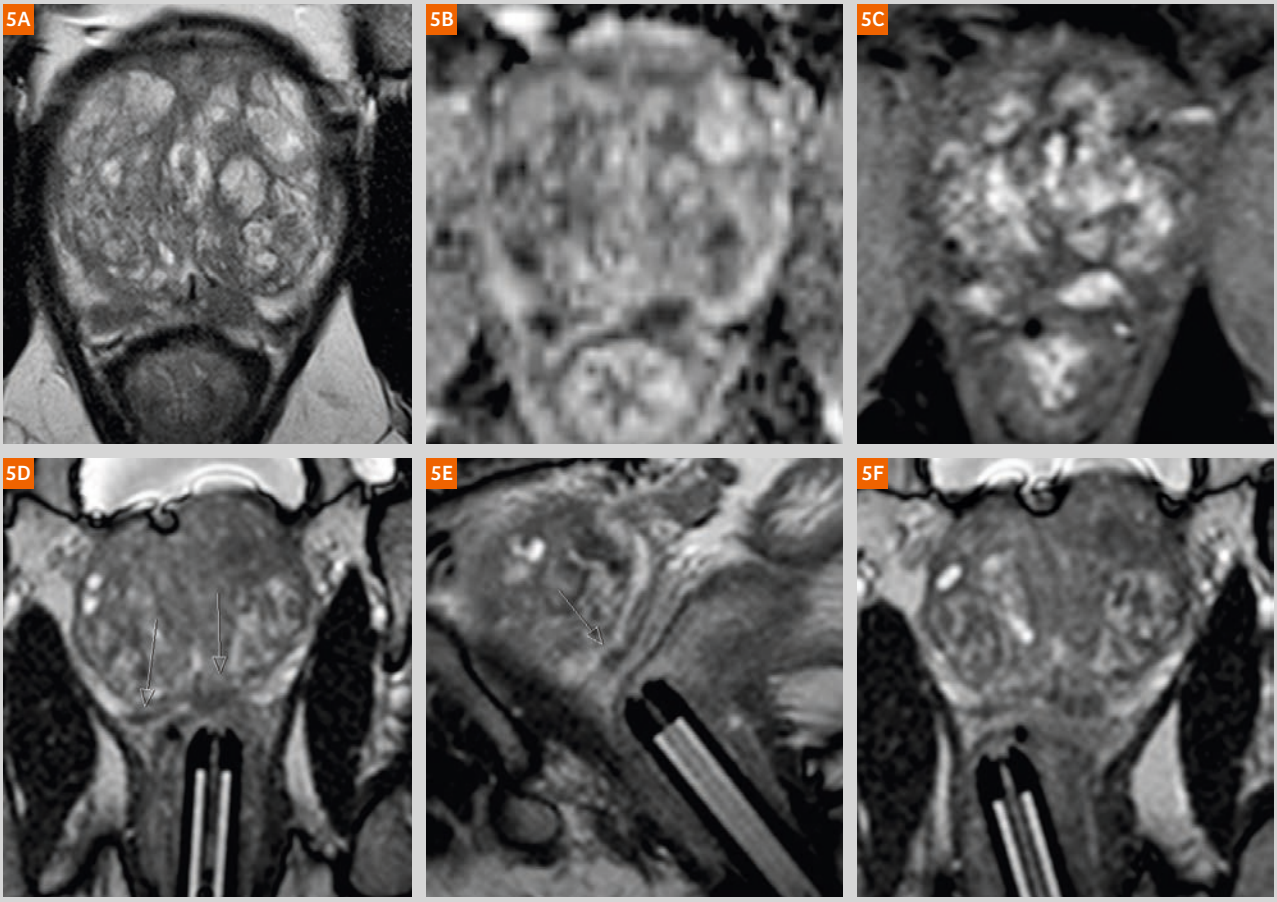

Figure 5: 63-year-old patient with PSA level 6.0, referred to our center for MR-guided biopsies after negative MR-US Fusion-guided biopsies at an external institute.

Diagnostic mpMRI showed a large prostate (estimated volume 128 ml) and apically bilateral relatively small, but highly tumor suspicious lesions.

Both lesions were targeted with MR-guided biopsies. Histology revealed prostate cancer Gleason grade 4+3 on the left side and Gleason grade 4+5 on the right side.

5A) Diagnostic mpMRI, transversal TSE T2w.
5B) Diagnostic mpMRI, transversal ADC map (RESOLVE diffusion).
5C) Diagnostic mpMRI, initial contrast uptake phase of transversal DCE (Twist VIBE).
5D) TrueFISP transversally along the axis of biopsy needle guide pointing at the target on the left side.
5E) TrueFISP sagittaly along the axis of the biopsy needle guide pointing at the target on the right side.
5F) TrueFISP transversally along the axis of the biopsy needle guide pointing at the target on the right side.

Potosky, Arnold L., Stanford, Janet L., Stroup, Antoinette M., Van Horn, R. Lawrence & Penson, David F.. 2013. Long-Term Functional Outcomes after Treatment for Localized Prostate Cancer. The New England journal of medicine 368: 436-445.

3 de Rooij, M., Hamoen, E. H., Futterer, J. J., Barentsz, J. O. & Rovers, M. M.. 2014. Accuracy of multiparametric MRI for prostate cancer detection: a meta-analysis. AJR Am J Roentgenol 202: 343-51.

4 Ahmed HU. The PROMIS study: a paired-cohort, blinded confirmatory study evaluating the accuracy of multi-parametric MRI and TRUS biopsy in men with an elevated PSA. J Clin Oncol 2016; 34: (suppl; abstr 5000).

5 Pokorny, M. R., de Rooij, M., Duncan, E., Schroder, F. H., Parkinson, R., Barentsz, J. O. & Thompson, L. C.. 2014. Prospective study of diagnostic accuracy comparing prostate cancer detection by transrectal ultrasound-guided biopsy versus magnetic resonance (MR) imaging with subsequent MR-guided biopsy in men without previous prostate biopsies. Eur Urol 66: 22-29.

6 McKenney, Jesse K., Wei, Wei, Hawley, Sarah, Auman, Heidi, Newcomb, Lisa F., Boyer, Hilary D., Fazli, Ladan, Simko, Jeff MD, Hurtado-Coll, Antonio, Troyer, Dean A., Tretiakova, Maria S., Vakar-Lopez, Funda, Carroll, Peter R., Cooperberg, Matthew R., Gleave, Martin E., Lance, Raymond S., Lin, Dan W., Nelson, Peter S.,

Case 3

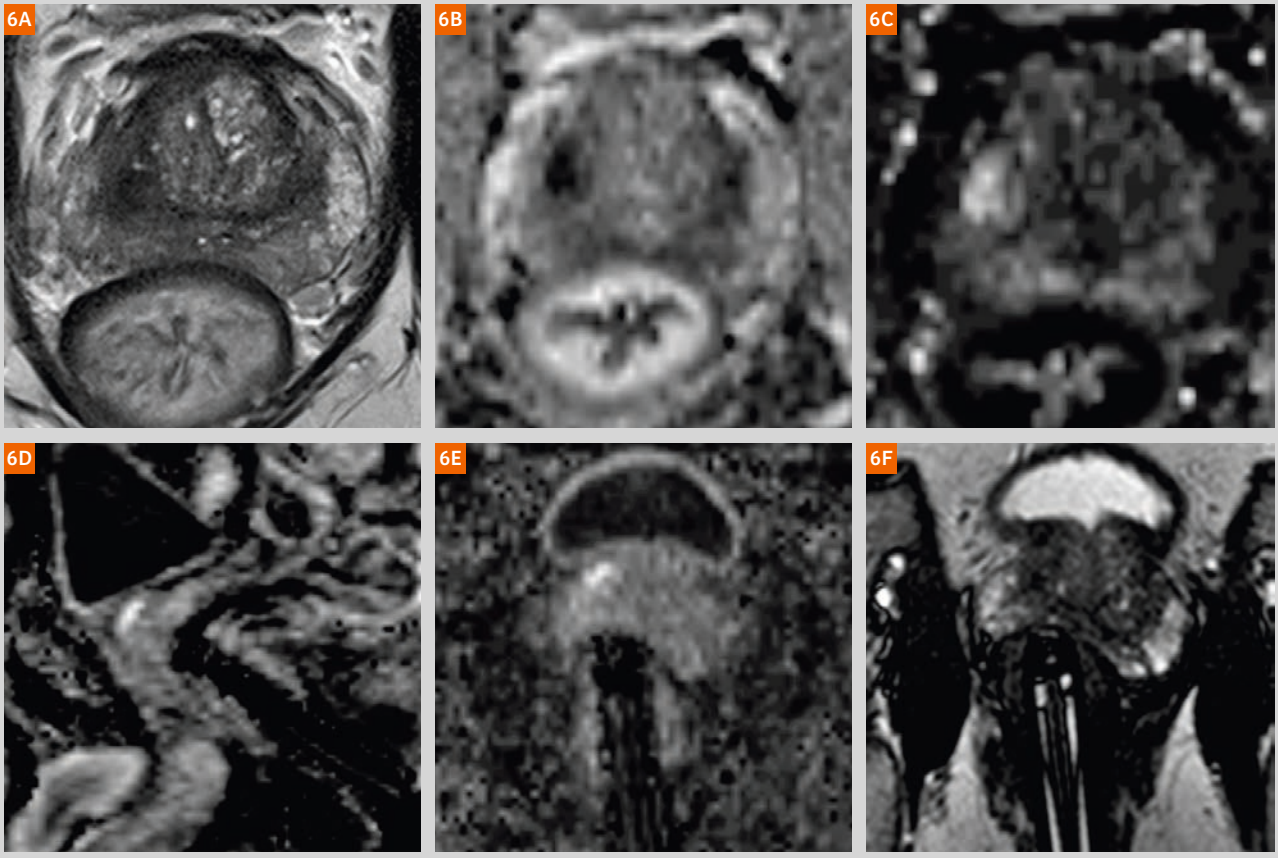

Figure 6: 63-year-old patient with PSA level 5.3.

Diagnostic mpMRI showed an 8 mm tumor suspicious lesion in the transitional zone of the right basal gland.

During the MR-guided biopsy procedure the lesion was hard to localize on TrueFISP and TSE T2 images, but possible to target confidently with the use of diffusion-weighted images.

Histology revealed prostate cancer Gleason grade 3+4.

6A) Diagnostic mpMRI, transversal TSE T2w.
6B) Diagnostic mpMRI, transversal ADC map (RESOLVE diffusion).
6C) Diagnostic mpMRI, transversal calculated b3000 images (RESOLVE diffusion).
6D) Calculated b1500 images (RESOLVE diffusion) sagittaly along the axis of the biopsy needle guide pointing at the target.
6E) Calculated b1500 images (RESOLVE diffusion) transversally along the axis of the biopsy needle guide pointing at the target.
6F) TrueFISP transversally along the axis of the biopsy needle guide pointing at the target.

Thompson, Ian M., True, Lawrence D., Feng, Ziding, Brooks, James D. 2016. Histologic Grading of Prostatic Adenocarcinoma Can Be Further Optimized: Analysis of the Relative Prognostic Strength of Individual Architectural Patterns in 1275 Patients From the Canary Retrospective Cohort. Am J Surg Pathol 2016 Nov;40(11):1439-1456.

7 Hoogland, A. Marije, Kweldam, Charlotte F. and Van Leenders, Geert J. L. H.. Prognostic Histopathological and Molecular Markers on Prostate Cancer Needle-Biopsies: A Review. BioMed Research International, vol. 2014, Article ID 341324.

Contact

Jeroen Reijnen
Radiology Department
Sørlandet Hospital Kristiansand

Egsveien 1000
Postboks 416
4604 Kristiansand
Norway
Phone: +47 97799733
Jeroen.Sebastiaan.Reijnen@sshf.no

Jon Bache Marthinsen, Jeroen Reijnen, Frank Gonzalez

PI-RADS 2
Standardized Prostate MRI Reporting

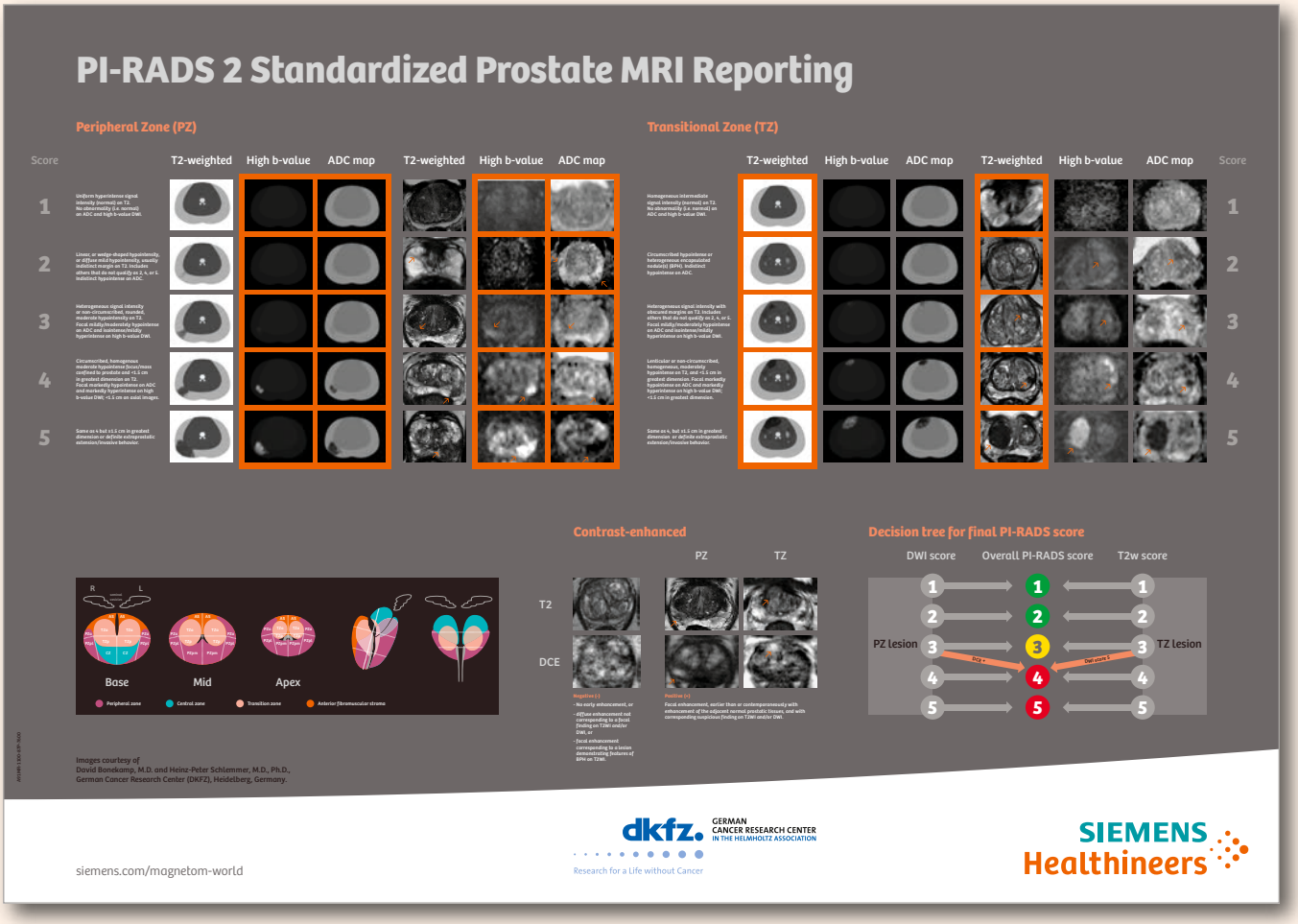

Visit us at **www.siemens.com/magnetom-world**

Go to > Publications > Subscriptions > **MRI Poster**

Get your free copy of the PI-RADS 2 poster

Metastatic Prostate Cancer in Practice – the MET-RADS-P Imaging Response System Using Whole-body MRI

Anwar R. Padhani[1]; Nina Tunariu[2]

[1] Paul Strickland Scanner Centre, Mount Vernon Hospital, Northwood, Middlesex, UK
[2] Royal Marsden NHS Foundation Trust & Institute of Cancer Research and Cancer Research UK Cancer Imaging Centre, Sutton, Surrey, UK

Introduction

Whole-body MRI (WB-MRI) is an increasingly used, radiation-free imaging method for assessing bone and soft tissue pathology, and for evaluating response to therapy [1]. WB-MRI has been developed to overcome the limitations of Bone Scintigraphy (BS) and Computed Tomography (CT) for detection and therapeutic response assessments in bone metastases [2]. Although increasingly used and recommended by international guidelines for multiple myeloma [3], WB-MRI usage has been confined mainly to expert centers, causing some concerns about its broader applicability. While WB-MRI can be performed on almost all modern MRI scanners, inconsistencies in WB-MRI acquisition protocols and reporting standards have prevented its widespread testing and implementation, beyond the indication for multiple myeloma.

Recently, a group of oncologic imaging specialists teamed with a leading urologist and oncologist, to develop recommendations on the minimum requirements for WB-MRI acquisition protocol as well as standardized reporting guidelines. They recognized that for this promising method to become mainstream it is vital to enforce some uniformity in acquisition, interpretation, and reporting. The authors have named their formulation for metastatic disease response and diagnostic system for prostate cancer as MET-RADS-P (METastasis Reporting And Data System for Prostate cancer) [4].

Why MET-RADS is needed

BS/CT scans are widely used and endorsed by international guidelines as the standard imaging investigations in the staging and follow-up of metastatic prostate cancer, thereby affecting patient management [5, 6]. However, it is increasing clear that currently used imaging methods are limited in their effectiveness in directing therapy and may no longer be relevant in the era of high-precision medicine, where an increasing number of cytostatic and novel therapies are becoming available [2]. For example, the accepted minimum lymph node diameter (10 mm – short axis) on CT scan as measure of involvement is only modestly correlated with the presence of malignant disease, and CT cannot accurately evaluate the presence or the therapeutic response in bone metastases, the commonest metastatic site in prostate cancer. Conversely, increased BS uptake in number and extent of lesions can equally occur with the osteoblastic healing (FLARE reaction) associated with tumor response and with the osteoblastic progression associated with tumor burden increase, thus creating confusion between response and progression, when response to therapy is being assessed. Next generation whole-body imaging tools such as PET with targeted tracers and WB-MRI with diffusion-weighted sequences are emerging as powerful alternatives; however, the challenge remains in validating these newer imaging approaches, so that their use can be justified in the clinical routine.

An important step in this process is to ensure uniformity in the acquisition, interpretation, and reporting of next generation whole-body imaging methods, so that multicenter trials leading to validation of these methods can be more easily performed and evaluated. An important step for WB-MRI is the new MET-RADS-P standard for use in patients with advanced prostate cancer [4]. The standard establishes minimum acceptable technical parameters for imaging acquisitions built with sequences already available on most modern scanners. Of the sequences recommended, it is acknowledged that whole-body diffusion-weighted sequences are the most challenging to implement across imaging platforms. These sequences have been grouped to enable fast, high-quality examinations for tumor detection and response assessments (core and comprehensive protocols respectively). Image quality control and quality assurance procedures are also detailed by the standard. The MET-RADS-P standard is designed to offer day-to-day reporting guidance, paired with a detailed reporting tool that describes the disease phenotype based on anatomic patterns of metastatic spread thus, enabling systematic collection of analyzable data for research purposes.

Comprehensive response criteria for bone and soft tissue metastases and local disease have been proposed, with the ability to summarize the likelihood of a response to treatment, using a Likert-like 1–5 scale. It is important to note that the summarized likelihood of response in bone, uses newly developed MET-RADS criteria, but the response in soft-tissues continues to be based on long established

Figure 1: Updated MET-RADS-P template form and response criteria for bone and soft tissue disease.

1A

Physician | Exam date current | Exam date comparator

Soft tissues RECIST	MET-RADS Prostate Report	Bones MET-RADS
Primary Involved Y N RAC 1+ 2+ Comment	Primary lesion; Soft tissue metastasis; Bone metastasis	Skull Involved Y N RAC 1+ 2+ Comment
Pelvic nodes Involved Y N RAC 1+ 2+ Comment		Cervical spine Involved Y N RAC 1+ 2+ Comment
Retroperitoneal Involved Y N RAC 1+ 2+ Comment		Dorsal spine Involved Y N RAC 1+ 2+ Comment
Other nodes Involved Y N RAC 1+ 2+ Comment		Lumbosacral spine Involved Y N RAC 1+ 2+ Comment
Liver Involved Y N RAC 1+ 2+ Comment		Pelvis Involved Y N RAC 1+ 2+ Comment
Lungs Involved Y N RAC 1+ 2+ Comment		Thorax Involved Y N RAC 1+ 2+ Comment
Other sites Involved Y N RAC 1+ 2+ Comment		Limbs Involved Y N RAC 1+ 2+ Comment

Lung; Other lymph nodes; Liver; Retroperitoneal lymph nodes; Other; Pelvic lymph nodes; Skull; Cervical spine; Clavicle; Sternum; Scapula; Rib; Dorsal spine; Extremities; Lumbosacral spine; Pelvis; Thorax

OVERALL ASSESSMENT

	No dis	CR	PR	SD	PD	DISCORD
Primary						
Nodes						No/minor/major only for PR/SD categories
Viscera						
Bones			RAC 1/2	RAC 3	RAC 4/5	

Comments

Response assessment categories (RAC): 1 Highly likely to be responding; 2 Likely to be responding; 3 No change; 4 Likely to be progressing; 5 Highly likely to be progressing. Single lesion 1° RAC only; ≥2 lesions/diffuse disease use both RACs

METastasis Reporting and Data System for Prostate Cancer: Practical Guidelines for Acquisition, Interpretation, and Reporting (MET-RADS-P) of Whole-body MRI Evaluations of Multiorgan Involvement in Advanced Prostate Cancer. Eur Urol. 2017 Jan;71(1):81-92.

Radiologist | Date

Figure 1A: Updated MET-RADS-P template form allocates the presence of unequivocal identified disease to 14 predefined regions of the body (primary disease, seven skeletal and three nodal regions, lung, liver and other soft tissue sites) at baseline and on follow-up assessments. At each anatomical location, the presence of disease is indicated (yes/no) together with the response assessment categories (primary/secondary). The overall response of the primary tumor, nodal and visceral disease are categorical (no disease (ND), complete response (CR), partial response (PR), stable disease (SD) and progressive disease (PD)). However, the overall response of bone disease is on a scale of 1–5 indicating the likely overall response category: (1) highly likely to be responding, (2) likely to be responding, (3) stable, (4) likely to be progressing and (5) highly likely to be progressing.

1B

RAC	Region	MET-RADS-P Description
	Local, nodal and visceral	Consistent with RECIST v1.1/PCWG criteria for unequivocal response (partial/complete).
1 Highly likely to be responding	Bone	Return of normal marrow in areas previously infiltrated by focal/diffuse metastatic infiltration Decrease in number/size of focal lesions Evolution diffuse neoplastic pattern to focal lesions Decreasing soft tissue associated with bone disease Dense lesion sclerosis (edge to edge), sharply defined, very thin/disappearance of hyperintense rim on T2W-FS images The emergence of intra/peri-tumoural fat within/around lesions (fat dot/halo signs) Previously evident lesion shows increase in ADC from ≤1400 µm²/s to >1400 µm²/s ≥40% increase in ADC from baseline with corresponding decrease in high b-value SI; and morphological findings consistent with stable or responding disease
	Local, nodal and visceral	Changes depicting tumour response that do not meet RECIST v1.1/PCWG criteria for partial or complete response (see below)
2 Likely to be responding	Bone	Evidence of improvement, but not enough to fulfil criteria for RAC 1. For example: Previously evident lesions showing increases in ADC from ≤1000 µm²/s to <1400 µm²/s >25% but <40% increase in ADC from baseline with corresponding decrease in high b-value SI; and morphological findings consistent with stable or responding disease
3 No change	All	No observable change
	Local, nodal and visceral	Changes depicting tumour progression that do not meet RECIST v1.1/PCWG criteria for progression
4 Likely to be progressing	Bone	Evidence of worsening disease, but not enough to fulfil criteria for RAC 5. Equivocal appearance of new lesion(s) No change in size but increasing SI on high b-value images (with ADC values <1400 µm²/s) consistent with possible disease progression Relapse disease: re-emergence of lesion(s) that previously disappeared or enlargement of lesion(s) lesions that had partially regressed/stabilized with prior treatments Imaging depicted bone lesions that might be clinically significant (therefore excludes asymptomatic fractures in non-critical bones) Soft tissue in spinal canal causing narrowing not associated with neurological findings and not requiring radiotherapy
	Local, nodal and visceral	Tumour progression that meet RECIST v1.1/PCWG criteria for unequivocal progression
5 Highly likely to be progressing	Bone	New critical fracture(s)/cord compression requiring radiotherapy/surgical intervention → only if confirmed as malignant by MRI signal characteristics Unequivocal new focal/diffuse area(s) of metastatic infiltration in regions of prior normal marrow Unequivocal increase in number/size of focal lesions Evolution of focal lesions to diffuse neoplastic pattern Appearance/increasing soft tissue associated with bone disease New lesions/regions of high signal intensity on high b-value images with ADC value between 600-1000 µm²/s

Response Assessment Category (RAC) allocation rules – compare to relevant baseline scan

The primary RAC value is based on the dominant response of more than half of the disease within the region; The secondary RAC value is for the second most frequent pattern of response.
For a single lesion in a region only the primary number category is assessed. Regions with multiple lesions/diffuse disease, all with the same RAC, both the primary and secondary have the same values
When equal numbers of lesions are of higher and lower RACs then the primary pattern allocation is reserved for the higher RAC

RECIST v1.1 categories

- Complete Response (CR): Disappearance of all target lesions
- Partial Response (PR): At least a 30% decrease in the sum of the longest diameter (LD) of target lesions, taking as reference the baseline sum LD
- Stable Disease (SD): Neither sufficient shrinkage to qualify for PR nor sufficient increase to qualify for PD, taking as reference the smallest sum LD since the treatment started
- Progressive Disease (PD): At least a 20% increase in the sum of the LD of target lesions, taking as reference the smallest sum LD recorded since the treatment started or the appearance of one or more new lesions

Progression of local prostate disease: Use RECIST v1.1 for progression criteria above applied to local disease
Progression of nodes (short axis)

- <1.0 cm nodes have to have grown by at least 5mm in from baseline or treatment nadir and be ≥1 cm to be considered to have progressed
- For nodes that are 1.0-1.5 cm that have grown by at least 5 mm from baseline or treatment nadir and are ≥1.5 cm in short axis can be considered to have progressed
- For nodes ≥1.5cm short axis use RECIST v1.1 progression criteria

Progression of visceral disease: Use RECIST v1.1 progression criteria above applied to visceral disease

Figure 1B: Criteria for regional response assessment categories (RACs) that summarize likelihood of response in bone disease employ the newly developed MET-RADS criteria, but RACs for response in soft-tissues uses established standards already prescribed by RECIST v1.1 and PCWG guidance [7, 8]. Response assessment is indicated on a 1–5 scale indicating the likely RAC for each location, comparing to the baseline study (RAC-1, indicates highly likely to be responding, up to RAC-5, indicating highly likely to be progressing).

Figure 2: Primary resistance to hormonal therapy
67-year-old male with metastatic castrate resistant prostate cancer (mCRPC).
WB-MRI examinations before and on androgen deprivation therapy (Abiraterone and Goserelin).

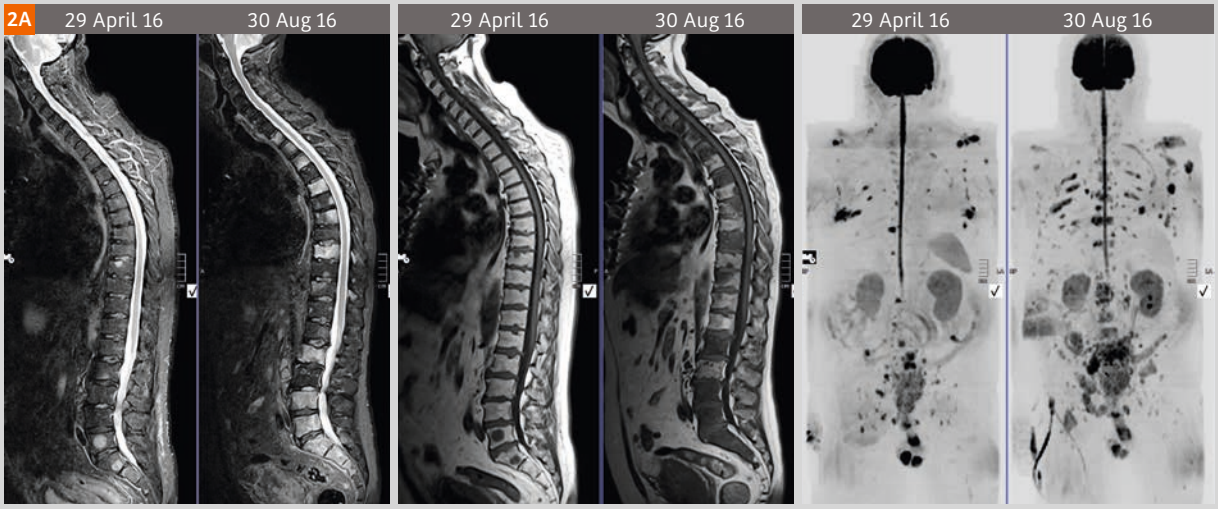

Figure 2A: Marked disease progression can be seen on morphology T1-weighted and STIR sequences and on WB b900 MIP images and confirmed by ADC measurements (see Fig. 2D also). Disease progression is seen in the prostate gland with extensive bladder invasion together with rectal invasion. There is disease progression in pelvic and retroperitoneal lymph nodes with nodal enlargement in the left axilla also. There is bone disease progression throughout the spine with extra-osseous soft tissue disease with new and enlarging deposits. No liver or lung disease is seen. The spinal stenosis at L3/l4 is degenerative in nature.

2B

30/08/2016 MRI Whole body

Clinical details: mCRPC. Restaging post urinary diversion. On Abiraterone and zoladez.

Technique: A whole-body MRI scan with whole body diffusion sequences. Comparison is made to the previous whole-body MRI scan dated 29/04/2016.

Findings:

Cervical and dorsal spine:

The intervertebral bony alignment is normal. Regrettably, there is marked disease progression. New metastases are seen throughout the cervical and dorsal spine with multifocal lesions. No interval loss of vertebral height. The craniocervical junction is normal. The cervical and dorsal cord outline normally.

Lumbosacral spine:

The intervertebral bony alignment remains normal with no interval loss of vertebral height. Degenerative spinal stenosis at L3/L4 as noted on the previous occasion. Regrettably, there is marked disease progression in the lumbosacral spine since the previous study.

Body scan:

No skull vault deposits have emerged. Normal sinonasal airways.

No supraclavicular fossa lymphadenopathy. Progressive left axillary lymphadenopathy also.

There is marked disease progression left scapula bone with extra osseous soft tissue disease now visible. Marked disease progression the ribs bilaterally also. There are artefacts are sternotomy wires.

The central mediastinal and hilar regions are normal. No lung abnormalities are detected.

The liver and spleen are homogeneous. Normal pancreas and adrenal glands. Both kidneys are unobstructed with bilateral renal stents in situ. Small retroperitoneal lymph nodes are also detected.

Extensive metastatic bone disease is present in the sacrum predominantly on the left side, right and left hemipelvis bone disease also.

Nodal disease in the common iliac regions bilaterally. Right obturator region with extra nodal tumour spread.

There is large locally advanced prostate carcinoma with bladder and ureteric involvement. No tumour involvement of the rectum or rectosigmoid junction.

Metastatic disease in the right proximal femur also.

Impression:

There is marked disease progression since 29/04/2016. Disease progression is seen locally the prostate gland with extensive bladder invasion. There is disease progression within pelvic and retroperitoneal lymph nodes with extra nodal tumour spread. There is disease progression in the left axilla also. Bone disease progression additionally throughout the spine with extra-osseous soft tissue disease also visible. No new visceral relapse of disease.

Please see graphical MET-RADS-P report also.

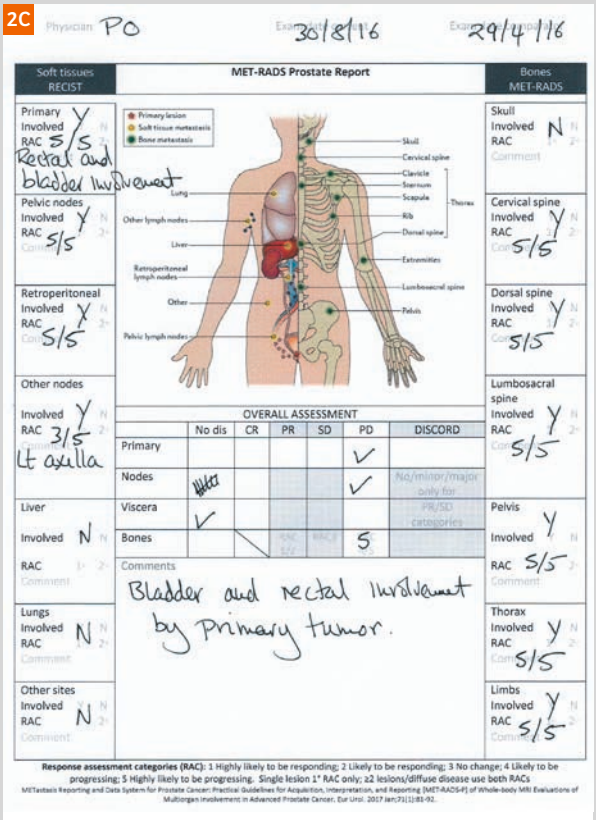

Figure 2B: Original text report for the follow-up examination that accompanies the MET-RADS-P template report.

Figure 2C: Completed MET-RADS-P template report indicating sites of disease and RACs at each anatomical location compared to the baseline study. The presence of unequivocal identified disease is indicated together with primary and secondary RACs at each site using the criteria set out in Figure 1B. Short relevant comments are included for clarification purposes where needed.

Figure 2D: WB-tumor load segmentation undertaken on *syngo*.via Frontier MR Total Tumor Load software (Siemens Healthcare; released research prototype – not part of the MET-RADS-P standard) for illustrative purposes only.

The whole-body b900 images are segmented using computed high b-value images of 1200 s/mm² and signal intensity threshold of approximately 100 AU. Extraneous signals (such as the brain, kidneys, bowel, gonads) are removed to leave only recognizable disease sites. The color the b900 MIP images are overlaid with ADC value classes using the thresholds indicated. The green voxels are values ≥1500 µm²/s (representing voxels that are 'highly likely' to be responding). The yellow voxels are set to lie between the 95th centile ADC value of the pre-treatment histogram (1295 µm²/s) and 1500 µm²/s thus representing voxels 'likely' to be responding. Red-voxels represent mostly untreated disease.

43 mL of tumor are segmented before therapy and 472 mL on therapy. Note that there is no significant global increase in ADC values (859 µm²/s and 885 µm²/s) on the corresponding absolute frequency histograms. There is also no increase in the standard deviation of the histogram (247 and 249 µm²/s). Note increased extent and volume of red-voxels consistent with disease progression (95% before therapy and 94% after therapy).

standards, prescribed by RECIST v1.1 and PCWG, the Prostate Cancer Working Group [7, 8) for clinical research. Discordant responses in which progressing and responding lesions are seen at same time point, are increasing seen with the use of targeted therapies and are a recognized manifestation of tumor heterogeneity. MET-RADS-P proposes methods to record the presence, location and extent of discordant responses between and within body parts. The use of MET-RADS-P enables for the first time to categorize bone disease response into 3 categories (progressive disease, stable disease and response), rather than the clinically recommended categories (progression/no progression) when using BS/CT scans [8], thus mirroring response assessments in soft tissues disease.

The benefits of using a standardized approach include enhanced data collection for outcomes monitoring in clinical trials and from patient registries, enhancing the education of radiologists to reduce variability in imaging interpretations, and for improving communication with referring clinicians. The MET-RADS-P authors state that the new way of response categorization from 2 categories used currently, to 3 categories when assessing bone disease response, could lead to a paradigm shift from the current concept of treating patients to documentable progression (when tumor volume could be substantially greater than baseline), to being guided by the presence or absence of benefit to therapy thus introducing more nuanced delivery of patient care.

MET-RADS-P template form

Response assessment categories (RACs)
An updated MET-RADS-P template form can be found in Figure 1 and is available as a pdf document at: www.siemens.com/magnetom-world.

The use of MET-RADS-P system starts by allocating the presence of unequivocal identified disease based on morphology and signal characteristics on all acquired images to 14 predefined regions of the body (primary disease, seven skeletal and three nodal regions, lung, liver and other soft tissue sites) at baseline and on follow-up assessments (see page 1 of the MET-RADS-P template form Figure 1A).

For follow-up studies, a response assessment on a scale of 1–5 indicating the likely response assessment category (RAC) for each location is recorded, comparing to the baseline study (RAC-1, indicating highly likely to be responding, up to RAC-5, indicating highly likely to be progressing).

The reporting guideline provides detailed explanations of the imaging criteria to be used to classify the likelihood of response in bones. Thus, RACs that summarize likelihood

of response in bone disease employ the newly developed MET-RADS criteria (Fig. 1B), but RACs for response in soft-tissues continues to use established standards already prescribed by RECIST v1.1 and PCWG guidance [7, 8].

For each region, only 2 RACs are needed to account for heterogeneity of responses that may occur in different anatomic areas. The primary RAC value (1–5) is based on dominant pattern of response within the region (that is, the response shown by more than half of the lesions within the region). A secondary RAC value (1–5) is assigned to the second most frequent pattern of response seen within the region.

A tertiary RAC value (4–5) maybe assigned to the region to illustrate progressing disease (i.e. RAC 4–5), if not already captured by the primary or secondary RAC values but this is not usually necessary in clinical practice.

When assessing a single lesion in a region, only the primary number category is used. Regions with multiple lesions all with the same pattern of response will have the same RAC value assigned as both the primary and secondary RACs. When equal numbers of lesions are category RAC 4/5 (progressing) as RAC 1/2/3 (responding & stable), then the primary pattern allocation is reserved for RAC 4/5 (the higher category). Similarly, when equal numbers of lesions are category RAC 1/2 as RAC 3, then the primary pattern allocation is reserved for RAC 3 (the higher category).

Overall response
The final response assessment consists of separately assessing the status of the primary disease, bones, nodes, and viscera without an overall patient response result. The overall patient assessment should be summarized in the text report which should accompany the MET-RADS-P template report (Figs. 2B, C).

Unlike regional response assessments which allocate RACs, the overall response for the primary tumor, nodal and visceral disease should be categorical, thus following established guidelines [7, 8], to improve communication with clinicians who are already familiar with this format. The following categories should be assigned: no disease (ND), complete response (CR), partial response (PR), stable disease (SD) and progressive disease (PD).

In contradistinction, the overall response of bone disease should be categorized on a scale of 1–5 indicating the likely overall response category: (1) highly likely to be responding, (2) likely to be responding, (3) stable, (4) likely to be progressing and (5) highly likely to be progressing.

Discordance or mixed response indicates the presence of progressing bone/soft tissue disease, not meeting definite progression criteria in the primary category, that is, when the majority of disease is stable or responding.

Discordant response should also be separately reported for primary, nodal, viscera and bone; evaluation of regional responses will enable the specific identification of the anatomic sites of mixed responses.

When discordant response is observed, the degree of discordance should be indicated major or minor to indicate in the evaluators opinion on whether alternative therapy options should be considered.

ADC value measurements should be made using a region-of-interest (ROI) technique on ADC images. Due to the lower spatial resolution of WB-MRI compared to CT scans, a 1.5 cm diameter threshold for bone lesions ROI is recommended for ADC measurements.

ADC measurements in bone disease should only be obtained from lesions that have sufficient signal intensity detected on all b-value images (including b0); otherwise the ADC values will be erroneous, reflecting only the noise in the images. Note that the absence of tissue signal on highest b-value images does not exclude tissues from ADC measurements because signal maybe present at lower b-values (thus, low or intermediate b-value images should be chosen instead for ROI placements).

Research components
Because of the need to unequivocally identify disease and to cope with the lower spatial resolution of WB-MRI compared to CT scans, a 1.5 cm diameter threshold for lesion size assessments is advised. Lesion size should be measured on anatomic T1-weighted images where possible.

Note that progression assignments for soft tissues, if based on measurements should be from baseline or the treatment induced summed measurement nadir, whichever is lower as per the RECIST v1.1 guidelines [7].

The type of progression (new disease versus growth of existing lesions) should be separately recorded; the location of progression can be accessible from the regional response assessments.

RACs at each time point should be compared to the baseline (pre-treatment) study for clinical use, but maybe referenced to the immediate prior study for research purposes if needed.

Whole-body tumor segmentations and histogram analysis are not part of the MET-RADS-P standard but can be used as ancillary tools if available (and are used in this paper for illustrative purposes only).

Worked up examples

An updated MET-RADS-P template form and detailed bone response assessment criteria can be found in Figure 1 and is available as a pdf document at www.siemens.com/magnetom-world.

Figures 2–4 illustrate the use of the MET-RADS-P standard in advanced, metastatic prostate cancer illustrated with examples of disease progression, responding and discordant responses.

The figures also demonstrate the utility of the WB-tumor load segmentation which is undertaken with the MR Total Tumor Load prototype, a released research software tool available on *syngo*.via Frontier (Siemens Healthcare,

Figure 3: Excellent response to chemotherapy
65-year-old male with metastatic castrate naive prostate cancer (mCNPC).
WB-MRI examinations before and after 4 cycles of docetaxel, goserelin and prednisolone therapy.

Figure 3A: There is improvement in the spinal canal narrowing in the mid-dorsal and lumbar spine on the T2W-FS images. The T1-weighted images are essentially unchanged or possibly minimally worse. There is also marked improved appearances of the bone and nodal disease on the paired WB b900 MIP images (inverted scale) and confirmed by significant increase in ADC values (see Figure 3C) of the bone lesions and reduction in size of the nodes.

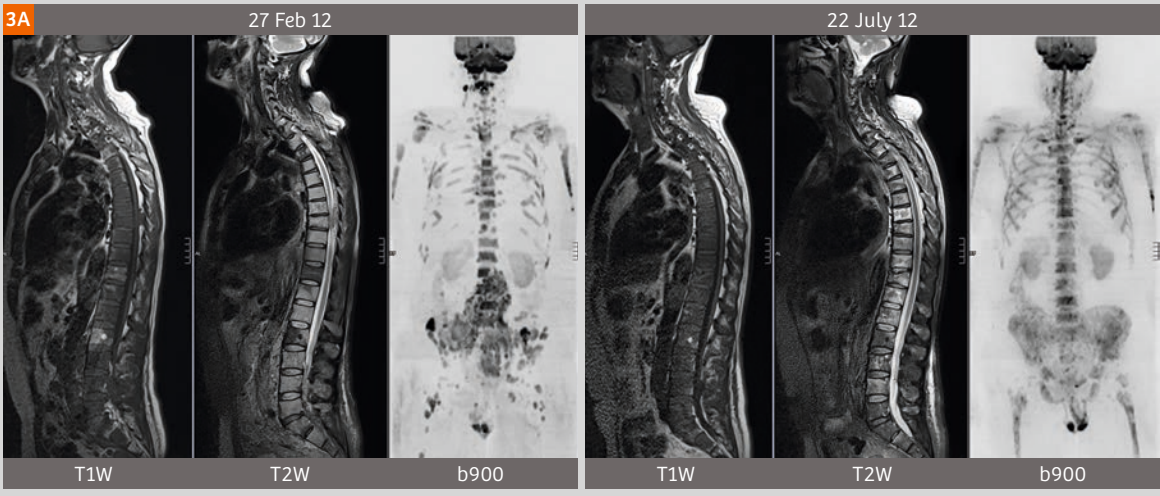

Figure 3B: Completed MET-RADS-P template report indicating sites of disease and RACs at each anatomical location compared to the baseline study. Note how the overall response at the primary tumor is indicated as no disease (previous radiotherapy). The overall pelvic nodal and retroperitoneal disease is excellent indicated as partial response (PR). The bone disease response is indicated by category 1 (highly likely to be responding).

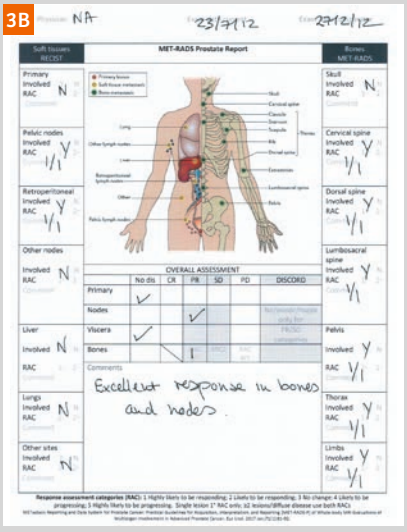

Figure 3C: WB-tumor load segmentation undertaken on *syngo*.via Frontier MR Total Tumor Load software (Siemens Healthcare; released research prototype – not part of the MET-RADS-P standard) for illustrative purposes only.

The whole-body b900 images are segmented using computed high b-value images of 1000 s/mm² and signal intensity threshold of approximately 30 AU. Extraneous signals (such as the brain, kidneys, bowel, gonads) are removed to leave only recognizable disease sites. The thresholded mask is overlaid with ADC value classes using the thresholds indicated and superimposed onto the b900 MIP images. The green voxels are values ≥1500 µm²/s (representing voxels that are 'highly likely' to be responding). The yellow voxels are set to lie between the 95th centile ADC value of the pre-treatment histogram (1067 µm²/s) and 1500 µm²/s thus representing voxels 'likely' to be responding. Red-voxels represent mostly untreated disease.

1281 mL of bone marrow and retroperitoneal nodal disease were segmented before therapy and 430 mL on therapy. Note that there is marked global increase in ADC values (705 µm²/s and 1635 µm²/s) on the corresponding relative frequency histograms. There is a marked decrease in excess kurtosis of the histograms (9.0 and -0.60). Note decreased extent and volume of red-voxels consistent with disease response (95% before therapy and 17% after therapy). The residual red regions on the post therapy scan are presumed to represent residual disease with low ADC values in the lower lumbar spine and in the left proximal femur.

Figure 4: Discordant response to Radium-223 therapy
55-year-old male with metastatic castrate resistant prostate cancer (mCRPC). Previously failed treatments include docetaxel chemotherapy and abiraterone. Previously lumbar spinal radiotherapy. WB-MRI scans were obtained before and after Radium-223 treatment. Symptomatically the patient is worse with increasing bone pain and has become blood transfusion dependent; however PSA values are improved from 792 ng/mL to 167 ng/mL thus creating diagnostic confusion on the effectiveness of Radium-223 therapy.

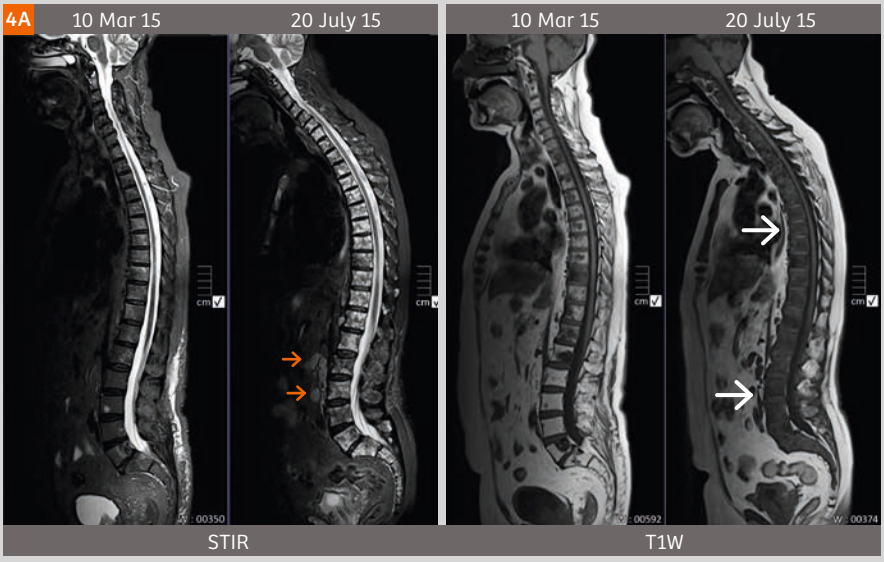

Figure 4A: T1-weighted spine images show increased abnormal signal in the cervical, dorsal and lumbosacral spine suggestive of disease progression using the criteria in Figure 1B. However, the STIR sequence shows higher signal intensities in the cervical and dorsal spine indicating increased tissue water. Note increase in size of retro-peritoneal nodes (orange arrows).

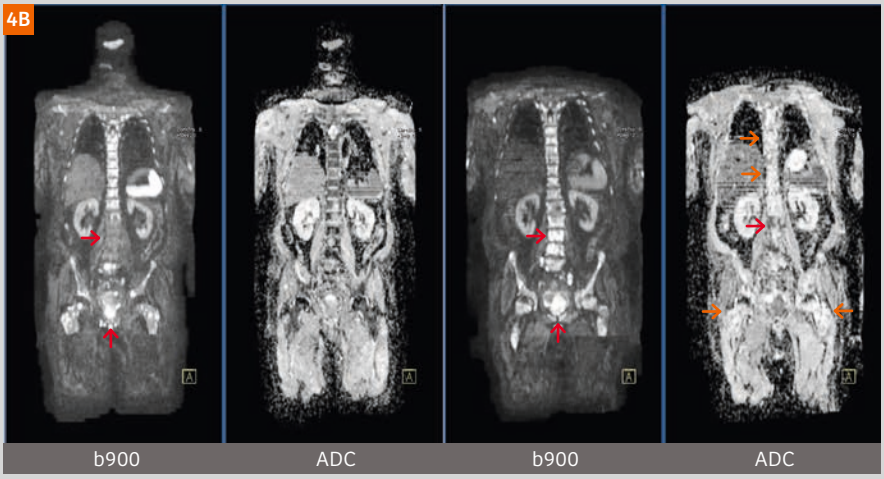

Figure 4B: Responding disease in femora & dorsal spine, new disease in lumbar spine
Coronal b900 and ADC maps show decreased b900 signal intensities and increased ADC values in the dorsal spine and proximal femora (orange arrows) indicating responding disease (T1w-pseudo-progression in the dorsal spine). However, the opposite is seen in the lumbar spine where b900 signal intensity is increased (red arrows) and with low ADC values indicating new disease (true progression). Note some enlargement of the primary prostate tumor also (vertical red arrows).

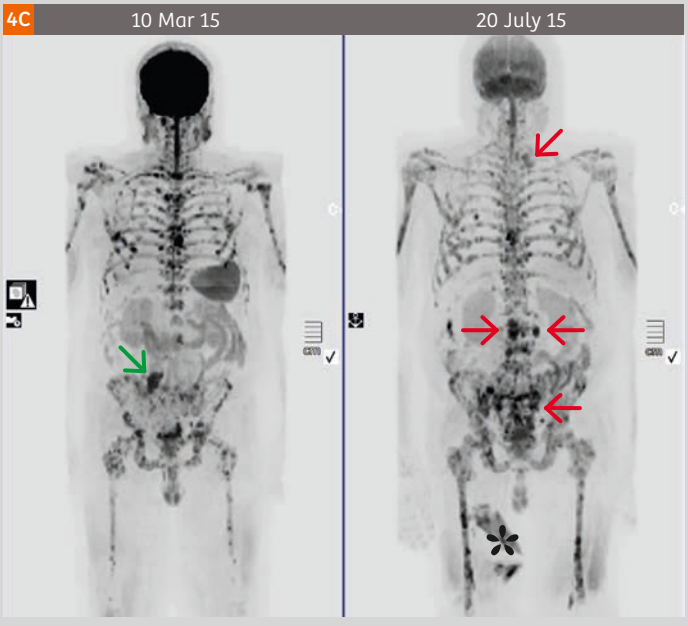

Figure 4C: Paired b900 MIP images (inverted scale) showing new nodal disease in the left hemipelvis, retroperitoneum and in the left supraclavicular fossa (red arrows). On the other hand, the enlarged lymph nodes in the right common iliac region is improved (green arrow). There seems to be an increase in extent of bone marrow signal intensity. The high signal geographic lesion over the right thigh on the follow-up examination is a dipper pad (*). Note lower signal intensity of the brain on follow-up examination due to the absence of the head coil.

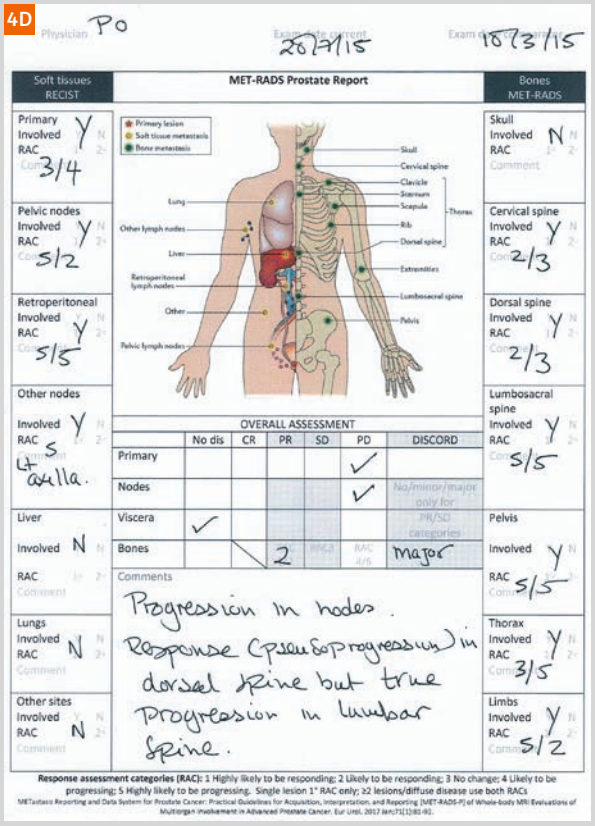

Figure 4D: Completed MET-RADS-P template report indicating sites of disease and RACs at each anatomical location compared to the baseline study. Note how the RAC of response at the primary tumor is mostly stable with some progression (RAC 3/4). The RAC of the pelvic nodes is indicated as 5/2 meaning that there is progression in the majority of the nodes although a single lymph node has responded (see also Figure 4E). Overall the bone disease is scored as 2 (likely to be responding in the majority of regions) with major discordance due to progression in lumbo-sacral spine and pelvis (both with RAC scores of 5/5).

Figure 4E: WB-tumor load segmentation undertaken on *syngo*.via Frontier MR Total Tumor Load software (Siemens Healthineers; released research prototype – not part of the MET-RADS-P standard) for illustrative purposes only.

The whole-body b900 images are segmented using computed high b-value images of 1000 s/mm² and signal intensity threshold of approximately 100 AU. Extraneous signals (such as the brain, kidneys, bowel, gonads) are removed to leave only recognizable disease sites. The color the b900 MIP images are overlaid with ADC value classes using the thresholds indicated. The green voxels are values ≥1500 µm²/s (representing voxels that are 'highly likely' to be responding). The yellow voxels are set to lie between the 95th centile ADC value of the pre-treatment histogram (1208 µm²/s) and 1500 µm²/s thus representing voxels 'likely' to be responding. Red-voxels represent mostly untreated disease.

570 mL of bone marrow and nodal disease are segmented before therapy and 538 mL on therapy. Note that there is moderate global increase in ADC values (670 µm²/s and 920 µm²/s) on the corresponding relative frequency histograms. There is a decrease in excess kurtosis of the histograms (2.2 and -0.05). Note decrease extent and volume of red-voxels consistent with disease response (95% before therapy and 76% after therapy). Heterogeneity of response in the spine (more red voxels in the lumbar spine and more green voxels in the dorsal spine) and in the pelvis is appreciable on these color projected images. This heterogeneity of response emphasizes the need to evaluate all the relevant WB-MRI images and to apply regional responses using the MET-RADS-P criteria.

Erlangen, Germany; released research prototype). Note that tumor load and ADC histogram analysis is not part of the MET-RADS-P standard, and is included for illustrative and cross-correlations purposes only. Detailed working of the *syngo*.via Frontier MR Total Tumor Load software is described in an accompanying article by Robert Grimm and Anwar R. Padhani in this issue of MAGNETOM Flash.

Conclusions and future developments

The MET-RADS-P system provides the minimum standards for whole-body MR with DWI image acquisition, interpretation, and reporting of both baseline and follow-up monitoring examinations of men with advanced, metastatic prostate cancer. MET-RADS-P is suitable for guiding patient care in practice (using the regional and overall assessment criteria), but can also be incorporated into clinical trials when accurate lesion size and ADC measurements become more important (thus, recording of measurements is not mandated for clinical practice). MET-RADS-P enables the evaluation of the benefits of continuing therapy to be assessed, when there are signs that the disease is progressing (discordant responses).

MET-RAD-P requires validation within clinical trials initially in studies that assess the effects of known efficacious treatments, such as those targeting the androgen axis, cytotoxic chemotherapy, Radium-223 and PARP inhibitors. METRADS-P measures should be correlated to other tumor response biomarkers delineated by PCWG (such as PSA declines), quality of life measures, rates of skeletal events, radiographic progression free survival and overall survival. The latter will be needed for the introduction of WB-MRI into longer term follow-up studies that will allow objective assessments of whether WB-MRI is effective in supporting patient care. Thus, we recommend that MET-RADS-P is now evaluated in clinical care and trials, to assess its impact on the clinical practice of advanced prostate cancer.

References

1 Lecouvet FE. Whole-Body MR Imaging: Musculoskeletal Applications. Radiology. 2016;279:345–365.
2 Padhani AR, Lecouvet FE, Tunariu N, et al. Rationale for Modernising Imaging in Advanced Prostate Cancer. Eur Urol Focus. European Association of Urology; 2016;44:198–205.
3 Dimopoulos M a., Hillengass J, Usmani S, et al. Role of magnetic resonance imaging in the management of patients with multiple myeloma: a consensus statement. J Clin Oncol. 2015;33:657–664.
4 Padhani AR, Lecouvet FE, Tunariu N, et al. METastasis Reporting and Data System for Prostate Cancer : Practical Guidelines for Acquisition , Interpretation , and Reporting of Whole-body Magnetic Resonance Imaging-based Evaluations of Multiorgan Involvement in Advanced Prostate Cancer. Eur Urol. European Association of Urology; 2017;71:81–92.
5 Mottet N, Bellmunt J, Bolla M, et al. EAU-ESTRO-SIOG Guidelines on Prostate Cancer. Part 1: Screening, Diagnosis, and Local Treatment with Curative Intent. Eur Urol. 2016;1–12.
6 Cornford P, Bellmunt J, Bolla M, et al. EAU-ESTRO-SIOG Guidelines on Prostate Cancer. Part II: Treatment of Relapsing, Metastatic, and Castration-Resistant Prostate Cancer. Eur Urol. 2016;1–13.
7 Eisenhauer EA, Therasse P, Bogaerts J, et al. New response evaluation criteria in solid tumours: revised RECIST guideline (version 1.1). Eur J Cancer. 2008/12/23. 2009;45:228–247.
8 Scher HI, Morris MJ, Stadler WM, et al. Trial Design and Objectives for Castration-Resistant Prostate Cancer: Updated Recommendations From the Prostate Cancer Clinical Trials Working Group 3. J Clin Oncol. 2016;34:1402–1418.

Contact

Professor Anwar R. Padhani
MB, BS, FRCP, FRCR
Paul Strickland Scanner Centre
Mount Vernon Hospital

Rickmansworth Road
Northwood, Middlesex HA6 2RN
United Kingdom
anwar.padhani@stricklandscanner.org.uk

Contact

Nina Tunariu
MD MRCP FRCR MDR
Royal Marsden NHS Foundation Trust &
Institute of Cancer Research
Cancer Research UK Cancer Imaging Centre

Downs Road, Sutton, Surrey, SM2 5PT
United Kingdom
Nina.Tunariu@icr.ac.uk

Visit us at

www.siemens.com/magnetom-world

to download the MET-RADS-P template form.

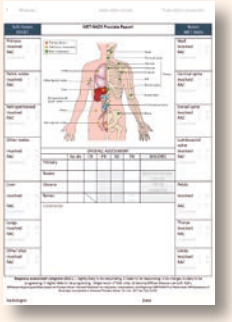

Whole-body Diffusion-weighted MR Image Analysis with *syngo*.via Frontier MR Total Tumor Load

Robert Grimm[1], Anwar R. Padhani[2]

[1] Siemens Healthineers, Erlangen, Germany
[2] Paul Strickland Scanner Centre, Mount Vernon Hospital, Northwood, Middlesex, UK

Whole-body diffusion-weighted MRI has recently gained a lot of attention as a promising technique for the assessment of multifocal bone disease such as multiple myeloma and bone metastases from breast and prostate cancer [1–3]. Compared to other imaging techniques, diffusion-weighted MRI has a high sensitivity and specificity for disease detection, without exposing the patient to ionizing radiation. Uniquely, diffusion imaging also enables therapy response to be evaluated, with particular application for bone disease. However, one challenge is the relatively large effort in response interpretation, due to the number of images that are generated and the lack of tools for efficient evaluation for multifocal disease.

This limitation was addressed by an efficient analysis approach that has been proposed by Blackledge et al. [4], using a threshold-based segmentation on diffusion-weighted images to identify regions of disease. Based on this segmentation, the overall tumor volume as well as histogram metrics of the corresponding apparent diffusion coefficient (ADC) maps are analyzed. Excellent inter- and intra-observer agreement of this computed approach was demonstrated recently in a pilot study [5].

1A

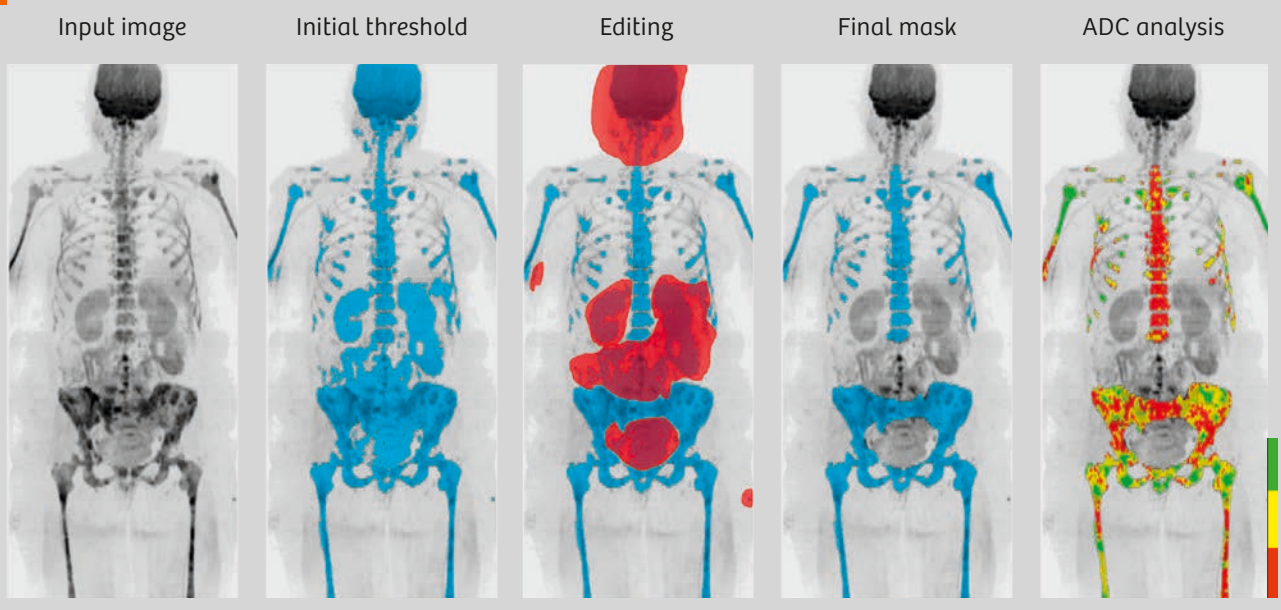

Figure 1: Application workflow. A computed high b-value image (b = 800 s/mm²) serves as input. An initial segmentation of the multiple myeloma lesions is obtained by thresholding and then edited to manually exclude regions from the analysis. In this case the brain, neck nodes, salivary glands, kidneys, spleen, and pelvic bowel were removed. Furthermore, the lower lumbar spine was removed, because of artifacts from a spine stabilization. Finally, back-mapping analysis reveals the ADC associated with each voxel, and provides detailed ADC histogram metrics (see also Figure 2).

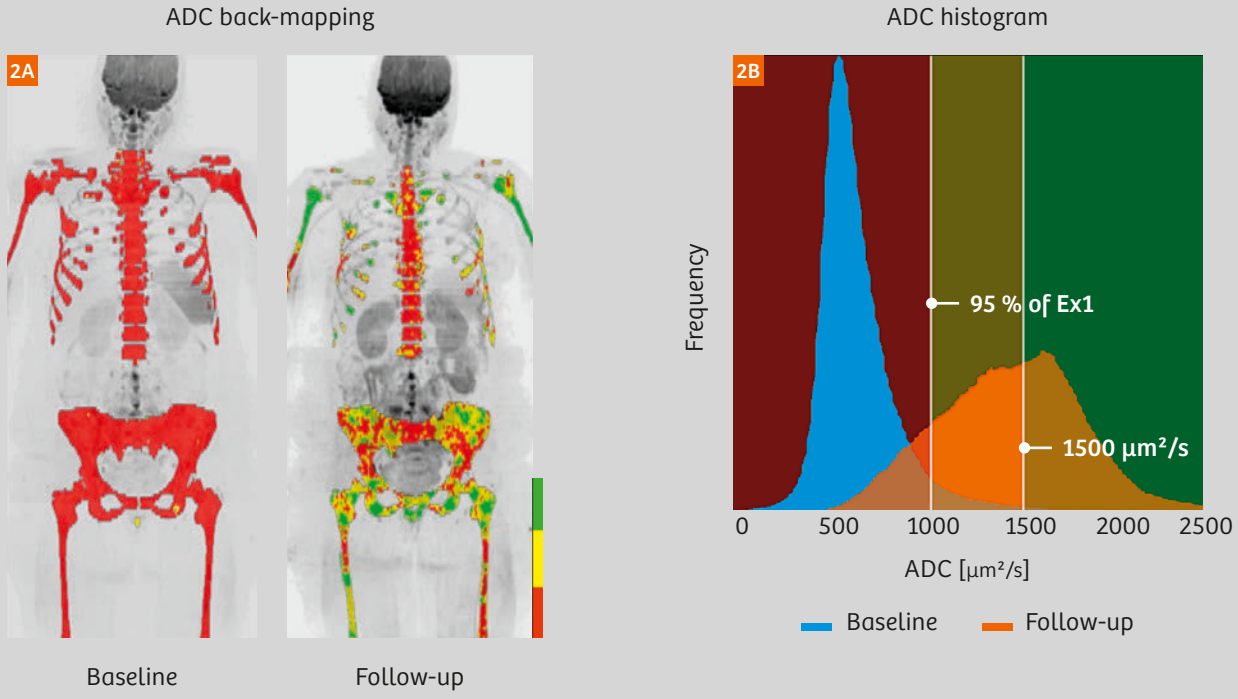

Figure 2: Example result for a multiple myeloma patient before and after one cycle of ESHAP (etoposide, methylprednisolone, cytarabine and cisplatin) therapy. The ADC back-mapping **(2A)** indicates reduced tumor burden and region based responses by yellow and green overlays. The ADC histograms **(2B)** show a significant change due to the treatment. The ADC statistics show reduced active tumor volume, increased mean and median ADC, and decreased ADC skewness and kurtosis. While 94.5% of the segmented volume were in the ADC range associated with active tumor at baseline, only 13.8% of the volume at follow-up were in the same range (ADC < 1000 µm²/s). Conversely, the fraction of the data in the ADC range associated with tumor cell kill (ADC > 1500 µm²/s) has increased from 0.9% at baseline to 44.7% on the follow-up study.

Quantitative whole-body diffusion MRI is implemented in the *syngo*.via Frontier MR Total Tumor Load[1] released research prototype: It uses diffusion-weighted images as input and allows creation of a 3D mask on diffusion images, for the analysis of the corresponding ADC maps. The prototype supports evaluation of up to two time-points, side-by-side and utilizes maximum intensity projections (MIPs) to facilitate efficient visual assessment of the intermediate result at each step. The workflow is structured in three steps, as depicted in Figure 1. The example illustrates the processing steps for a patient with multiple myeloma:

1. **Initial segmentation:** An initial mask is defined interactively by applying a threshold to a computed high b-value image (for example, b = 800 s/mm²). An automatic outlier removal can be performed to reduce false positive voxels due to artifacts or T2 shine-through.
2. **Mask editing:** The initial mask is edited by the user. The user can perform volume punching in order to exclude artifact regions and normal hyperintense organs such as brain, kidneys, spleen, testes, salivary glands etc, or users can choose to retain only a selected volume of interest. Furthermore, a volumetric, semi-automatic segmentation tool is available for manually adding false negative regions to the mask if not already captured.

[1] *syngo*.via Frontier is for research only, not a medical device.

Metric	Baseline	Follow-up
Volume [cm³]	1298	978
ADC mean [µm²/s]	653	1432
ADC median [µm²/s]	609	1437
ADC skewness	2.11	0.12
ADC e. kurtosis	8.21	0.07
% Low	94.5	13.8
% High	0.9	44.7

Table 1: Segmentation statistics. The tumor volume as well as several histogram metrics have changed significantly during treatment.

3. **Analysis:** The ADC histogram and corresponding statistics are computed for the edited masked volume. Histogram metrics include mask volume, mean, median, standard deviation, skewness, excess kurtosis, and customizable percentiles.

   Regions of low, intermediate and high ADC values can be inspected interactively by adjusting slider positions on the histogram. Depending on the ADC chosen, the colored back-mapping ADC overlays allow the visual discrimination of regions with untreated disease (typically associated with lower ADC values) compared to disease regions that have been treated effectively (high ADC values).

In the example shown in Figure 2, the 95th percentile of the baseline examination, approximately 1000 µm²/s, was used as lower ADC threshold and 1500 µm²/s was used as upper threshold. The ADC back-mapping in Figure 2A shows a red overlay for voxels with an ADC below 1000 µm²/s, a yellow overlay for voxels in the intermediate range, and a green overlay for voxels above 1500 µm²/s. The corresponding histograms and limits are shown in Figure 2B. The patient shows changes consistent with a significant response to the therapy, indicated by the emergence of mixed yellow and green regions in the humeri, pelvis, and femur. However, red regions continue to be seen indicating the continued presence of untreated disease.

The histogram statistics, listed in Table 1, show a reduction of the total diffusion volume, from 1298 cm³ at baseline to 978 cm³ at follow-up, and a radical change in the histogram shape. The mean and median values have increased from 653 (609) µm²/s at baseline to 1432 (1437) µm²/s in the follow-up examination. The skewness decreased from 2.11 to 0.12, while the excess kurtosis decreased from 8.21 to 0.07.

Further examples obtained with the *syngo*.via Frontier MR Total Tumor Load[1] released research prototype software can be found in the article *"Metastatic Prostate Cancer in Practice – the MET-RADS-P Imaging Response System Using Whole-body MRI"* on page 64 and in the case study *"Observing Endocrine Therapy Resistance in Metastatic Breast Cancer with Whole-body MRI"* on page 80 of this issue of MAGNETOM Flash.

To summarize, the *syngo*.via Frontier MR Total Tumor Load released research prototype provides an efficient and reproducible workflow with quantitative results for the processing and analysis of whole-body diffusion-weighted images in the response assessment setting. It is a promising tool to support the standardization of whole-body MRI for treatment response monitoring of bone disease in particular. Extensions like a fully automatic bone segmentation (as described in *"Whole-body MRI Reading and Bone Assessment with syngo.via Frontier MR Bone Scan"* on page 76 in this issue), simultaneous consideration of other MR parameters such as the normalized signal intensity, fat fraction, or Gadolinium enhancement fraction [6, 7], and integrated classification techniques to detect and separate regions of discordant response [7], may further add to the potential of the technique to promote high-precision medicine.

References

1 Pawlyn C, Fowkes L, Otero S, et al. Whole-body diffusion-weighted MRI: a new gold standard for assessing disease burden in patients with multiple myeloma? Leukemia. 2016;30(6):1446-1448. doi:10.1038/leu.2015.338.
2 Padhani AR, Lecouvet FE, Tunariu N, Koh DM, De Keyzer F, et al. (2016) Rationale for Modernising Imaging in Advanced Prostate Cancer. European Urology Focus, Available online. doi:10.1016/j.euf.2016.06.018.
3 Padhani AR and Tunariu N, Metastatic response system in using whole body MRI for prostate cancer in practice. See also page 76 in this issue of MAGNETOM Flash.
4 Blackledge MD, Collins DJ, Tunariu N, Orton MR, Padhani AR, et al. (2014) Assessment of Treatment Response by Total Tumor Volume and Global Apparent Diffusion Coefficient Using Diffusion-Weighted MRI in Patients with Metastatic Bone Disease: A Feasibility Study. PLOS ONE 9(4): e91779. doi: 10.1371/journal.pone.0091779.
5 Blackledge MD, Tunariu N, Orton MR, Padhani AR, Collins DJ, et al. (2016) Inter- and Intra-Observer Repeatability of Quantitative Whole-Body, Diffusion-Weighted Imaging (WBDWI) in Metastatic Bone Disease. PLOS ONE 11(4): e0153840. doi: 10.1371/journal.pone.0153840
6 Amlani A, Ghosh-Ray S, van Ree K, Makris A, D'Sa S, Ostler P, Anyamene N, Padhani AR. Relationships Between Diffusion Weighted Signal Intensity, ADC and Water/fat Content of Malignant Bone Marrow. Program Number: 3447. Proceedings of the International Society of Magnetic Resonance in Medicine. 20th Scientific Meeting and Exhibition, Salt Lake City, May 2013.
7 Blackledge MD, Leach M, Rata M, Tunariu N, Koh DM, et al. (2016) Visualizing whole-body treatment response heterogeneity using multi-parametric magnetic resonance imaging. Journal of Algorithms & Computation Technology, in press. doi: 10.1177/1748301816668024.

Contact

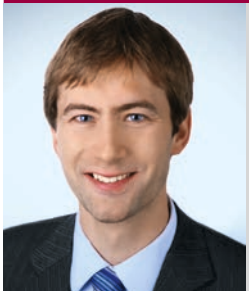

Robert Grimm, Ph.D.
Siemens Healthcare GmbH
HC DI MR PI TIO ONCO

Postbox 32 60
91050 Erlangen
Germany
Phone: +49 (0) 9131 84-2717
robertgrimm@siemens.com

Whole-body MR Image Reading and Bone Assessment with *syngo*.via Frontier MR Bone Scan

Matthias Fenchel[1]; Anwar R. Padhani[2]

[1] Siemens Healthineers, Erlangen, Germany
[2] Paul Strickland Scanner Centre, Mount Vernon Hospital, Northwood, Middlesex, UK

Whole-body MRI with diffusion imaging has gained a lot of attention as a promising technique for the assessment of multifocal bone disease, such as multiple myeloma and bone metastases from breast and prostate cancer [1–3]. Diffusion-weighted MRI in combination with other MRI contrasts has a high sensitivity and specificity for disease detection [4], without exposing patients to ionizing radiation. However, one challenge is the relatively large effort in image interpretation, due to the number of images that are generated, and the lack of available tools for efficient evaluation.

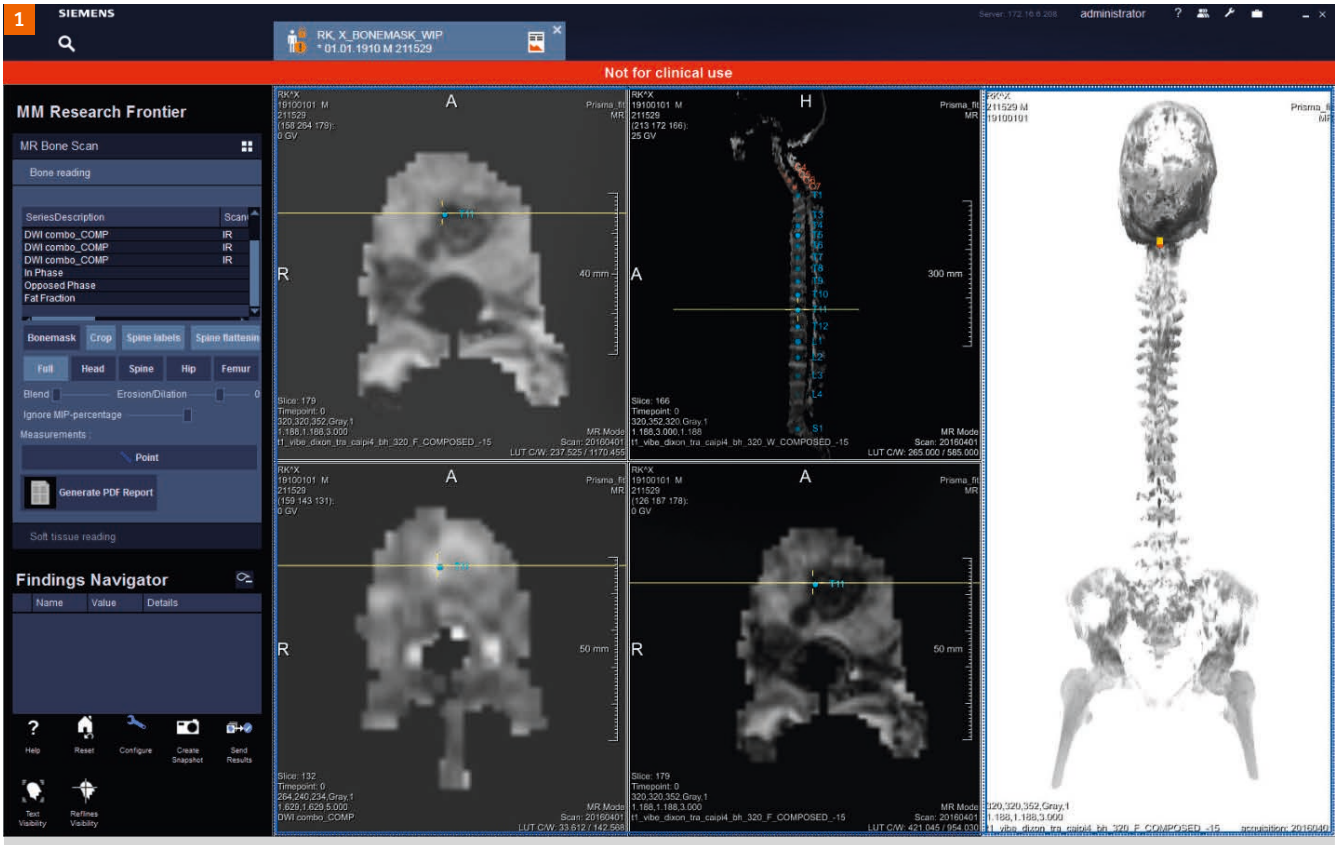

Figure 1: The figure shows a snapshot of the bone reading step of the application with the cropping and the spine unrolling/flattening and spine labeling features activated. The cursor is centered at the T11 vertebral body.

Siemens has implemented a novel MR whole-body image reading prototype with a specific focus on metastatic bone disease. The vision behind this *syngo*.via Frontier MR Bone Scan[1] is to leverage MR and MR-PET bone reading and make it as efficient as in the *syngo*.CT Bone Reading application. As a central feature, the application computes segmentations of the axial skeleton based on Dixon input images, using an atlas based algorithm [5].

The bone segmentations can be used in several ways:

1) Bone segmentations can be applied to remove all other tissues on any given image contrast, thus directing the reader's attention directly to the bone and the bone marrow. When this is done with high b-value images, rotating maximum intensity projections (MIPs) can be generated that provided a focused overview of the state of the disease in the skeleton. This enables assessments of abnormalities within the bones at a single glance. The ability to automatically remove soft tissues and other extraneous signals increases metastatic conspicuity on inverted MIPs on the segmented volume. This is of advantage in metastatic prostate cancer where lesion conspicuity may be obscured by surrounding tissue signal.

   The ability to isolate bones on multiple, registered image sequences such as DWI, ADC maps, in- and opposed phase Dixon, Fat Fraction and T1- and T2-weighted images with combined MIP images, enables focused, efficient multiparametric evaluations of the bones without signals and artefacts from surrounding soft tissues.

2) Bone segmentations can help to support visualizations like unrolling bones into a plane to simplify the geometric complexity for complete and easy assessment with few scroll moves through a reduced number of slices. In particular, the *syngo*.via Frontier MR Bone Scan allows for projecting the spine to a plane, displaying all vertebra at a single glance as a straightened flattened spine. All other image contrasts can also be warped accordingly in the unrolled spine mode.

3) Bone segmentations provide useful additional anatomic orientations, which helps to facilitate reporting. The vertebra of the segmented spine can be labelled, with labels presented to the user as overlays.

4) Bone segmentations from DWI independent image contrasts could support unbiased, quantitative multiparametric evaluation of the bone marrow also. Co-registered bone segmentations of image contrasts such as fat fraction, ADC, high b-value signals can enable the separation of normal yellow marrow, mixed marrow, viable tumor regions, microscopic necrosis, macroscopic necrosis voxels. Co-registered voxels can be evaluated in *syngo*.via Frontier Total Tumor Load and Scatter Plot software for these purposes.

5) In addition, separate evaluations of the different bones are supported. For instance, the pelvic bone and its voxels can be isolated and evaluated. Quantitative values could be evaluated independently thus enabling therapy response assessment and evaluation of spatial heterogeneity if required.

syngo.via Frontier MR Bone Scan supports standard tools for reading and reporting such as automatic configuration of hangings, automatic scrolling and synching of the segments as well as measurement tools.

The workflow of the application is structured into two steps.

1) Bone reading step: Layout, hangings and tool configuration are set up for the assessment of bone metastases. The bone segmentation runs in the background and yields the bone mask that allows for the usage of the advanced visualization tools mentioned above to support the reading process.

2) Soft tissue reading: Layout, hangings and tool configuration are set up to assess the status of soft tissues including primary tumors, lymph node and visceral organs.

3) In a final step, results and findings can be exported in a report pdf sheet.

4) The computed bone mask can be stored back to the patient image database and be made available for secondary (quantitative) evaluation tools like *syngo*.via Frontier Total Tumor Load as an independent bone mask.

Figure 1 shows a snapshot of *syngo*.via Frontier MR Bone Scan.

The clinical case in Figure 2 shows a 70-year-old man with castrate resistant prostate cancer who has failed hormonal therapy and docetaxel chemotherapy, and is now undergoing a novel therapy that targets the prostate specific membrane antigen (PSMA) receptor. Pre- and post-therapy assessments were undertaken on a 3T MAGNETOM Prisma scanner. Note that assessments of the bone status on the whole-body inverted b800 MIP images is impaired due to signals from soft tissues, including the swollen right leg (new hip fracture on the post therapy), kidneys and bowel on both studies. After automated cropping and removal of the soft tissue signals, the response of the disease becomes easier to evaluate.

[1] *syngo*.via Frontier is for research only, not a medical device.

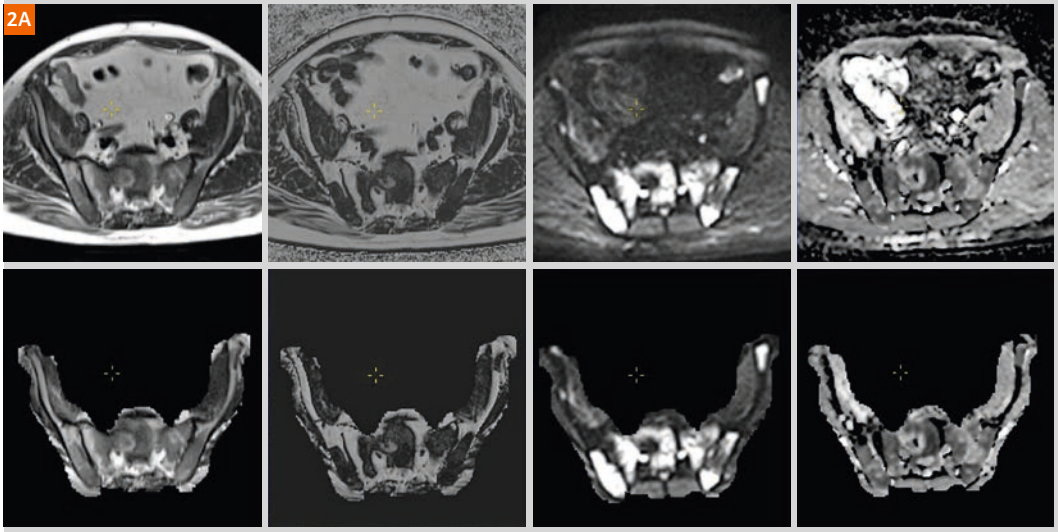

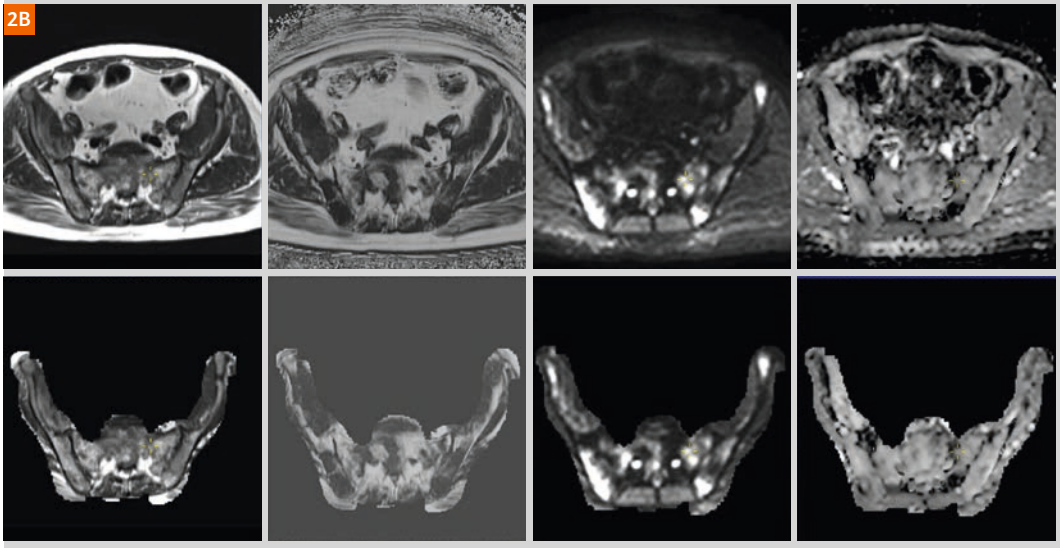

Figure 2:
2A: From left to right axial T2-weighted, fat fraction, b-value 800 mm²/s, ADC images through the sacrum before therapy. Top row before cropping and bottom row after cropping. After cropping, focused evaluations of the bones can be undertaken.

2B: From left to right axial T2-weighted, fat fraction, b-value 800 mm²/s, ADC images through the sacrum after therapy. Top row is before cropping and bottom row after cropping. Note increased artifacts in the anterior abdomen on the b800 images related to bowel motion. These artifacts are removed by cropping, thus allowing focused evaluations of bone response. Note decreases in b800 signal intensity and extent, with increasing ADC values are consistent with therapy response.

2C: Whole-body b800 MIP images (inverted scale) of the same patient as in 2A, B before and after cropping – frontal projection. Columns 1 and 2 are pre-treatment. Columns 3 and 4 after treatment. Note improved depiction of metastatic bone disease status at both time points when signals from overlying soft tissues are automatically removed. The increased soft tissue signal over the right hip after therapy is due to a new impacted hip fracture.

In summary, *syngo*.via Frontier MR Bone Scan is a promising application for whole-body reading enabling unbiased qualitative and quantitative assessments of bone marrow and bone lesions, with potential applications in therapy monitoring. However, it should be noted that it is still an evolving application, requiring optimizing the reading workflow for therapy response assessment in metastatic bone disease. Future developments will include layouts and tools for parallel evaluation of several time points. It is also planned to include features for direct quantitative evaluation as described in the Total Tumor Load (see article by Grimm and Padhani in this issues of MAGNETOM Flash) and seamless interactions with other *syngo*.via Frontier oncology prototypes.

References

1 Pawlyn C, Fowkes L, Otero S, et al. Whole-body diffusion-weighted MRI: a new gold standard for assessing disease burden in patients with multiple myeloma? Leukemia. 2016;30(6):1446-1448. doi:10.1038/leu.2015.338.
2 Padhani AR, Lecouvet FE, Tunariu N, Koh DM, De Keyzer F, et al. (2016) Rationale for Modernising Imaging in Advanced Prostate Cancer. European Urology Focus, Available online. doi:10.1016/j.euf.2016.06.018.
3 Padhani AR and Tunariu N, Metastatic response system in using whole body MRI for prostate cancer in practice – also in this issue of MAGNETOM Flash.
4 Li B, Li Q, Nie W, Liu S. Diagnostic value of whole-body diffusion-weighted magnetic resonance imaging for detection of primary and metastatic malignancies: a meta-analysis. European Journal of Radiology 2014; 83(2): 338-344.
5 Paulus DH, Quick HH, Geppert C, Fenchel M, Zhan Y, Hermosillo G, Faul D, Boada F, Friedman KP, Koesters T. Whole-Body PET/MR Imaging: Quantitative Evaluation of a Novel Model-Based MR Attenuation Correction Method Including Bone. J Nucl Med. 2015 Jul;56(7):1061-6.

Contact

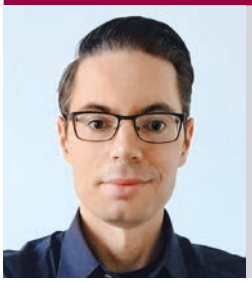

Matthias Fenchel, Ph.D.
Siemens Healthcare GmbH
HC DI MR PI TIO ONCO

Postbox 32 60
91050 Erlangen
Germany
Phone: +49 (0) 9131 84-2113
matthias.fenchel@siemens.com

Watch Cancer Develop Multidrug Resistance

In this video Professor Padhani shows how quantitative whole-body MRI is used to monitor therapy response in metastatic breast cancer. Watch the video at

www.siemens.com/magnetom-world

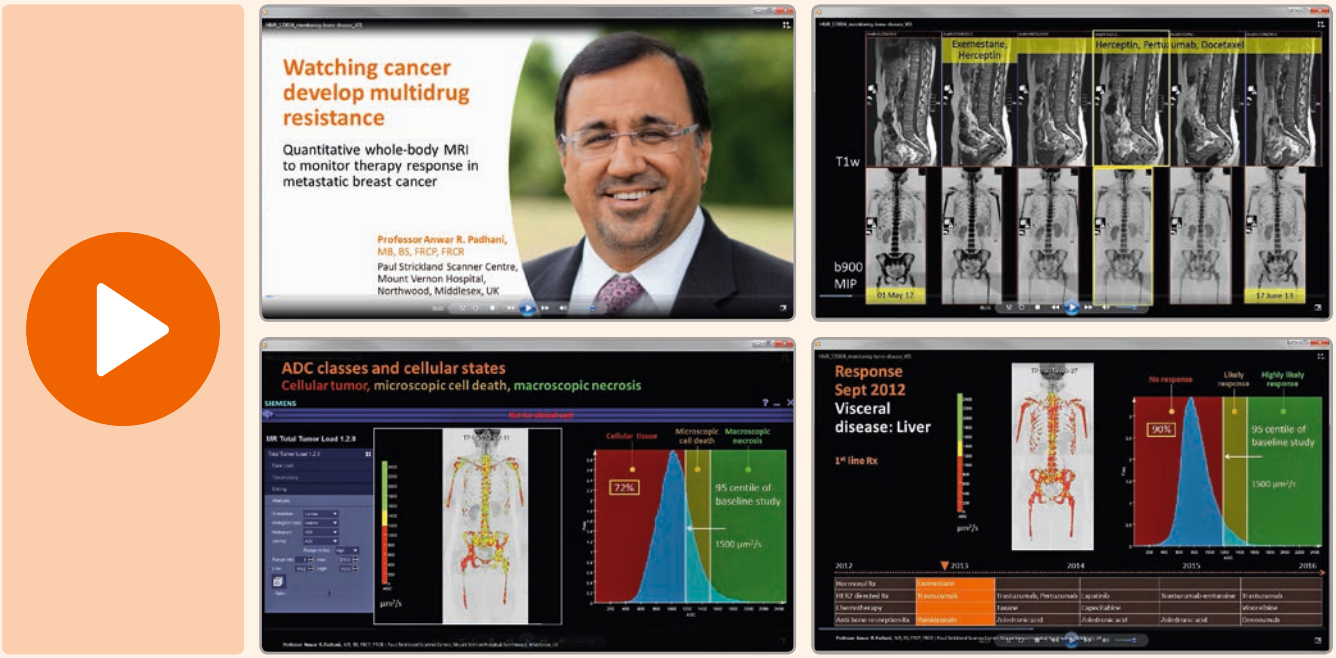

Observing Endocrine Therapy Resistance in Metastatic Breast Cancer with Whole-body MRI

Anwar R. Padhani

Paul Strickland Scanner Centre, Mount Vernon Hospital, Northwood, Middlesex, UK

Introduction

Approximately 70% of breast cancers are estrogen receptor (ER) positive, and are, therefore, treated with endocrine therapies. However, about 25% of patients with primary disease and almost all patients with metastases will present with or eventually develop endocrine resistance [1]. The mechanisms underlying the development of resistance remain largely unknown but in the last 2 years, several studies have shown ER independent gain-of-function mutations in ESR1, the gene that encodes the ER, in approximately 20–30% of patients with metastatic ER-positive disease who received endocrine therapies, such as tamoxifen and aromatase inhibitors. These mutations lead to ligand-independent ER activity that promotes tumor growth, promoting resistance to endocrine therapy, and potentially enhancing metastatic ability. The emergence of endocrine therapy resistance via this mechanism suggests that, under selective treatment pressure, clonal expansion of rare mutant clones occurs, thus contributing to resistance. Rationale-based novel therapeutic strategies that target these ESR1 mutants have the potential to improve treatment outcomes for patients. Fulvestrant is a hormonal therapy that specifically targets the ESR1 mutation, that seems to work well in metastatic breast cancer patients with endocrine resistance. Multiple studies suggest greater therapy efficacy in those with bone disease.

In this case study, we demonstrate the potential of quantitative whole-body MR imaging (WB-MRI) to monitor response of breast cancer to hormonal therapy, showing that (1) morphological response does not work as well as diffusion MRI for monitoring response to therapy, (2) that ADC histogram analyses can depict the emergence of treatment resistance, and (3) that spatially discordant response to targeted therapy can emerge when bone disease is effectively treated.

Patient history

50-year-old woman with metastatic invasive breast cancer, ER positive and HER-2 neu negative disease was initially treated with first line hormonal therapy (Exemestane, Goserelin) and bisphosphonates (Zoledronic acid) for bone only metastatic disease. She was switched to 2nd line hormonal therapy with Fulvestrant and Zoledronic on bone disease progression, with good response in her bone disease

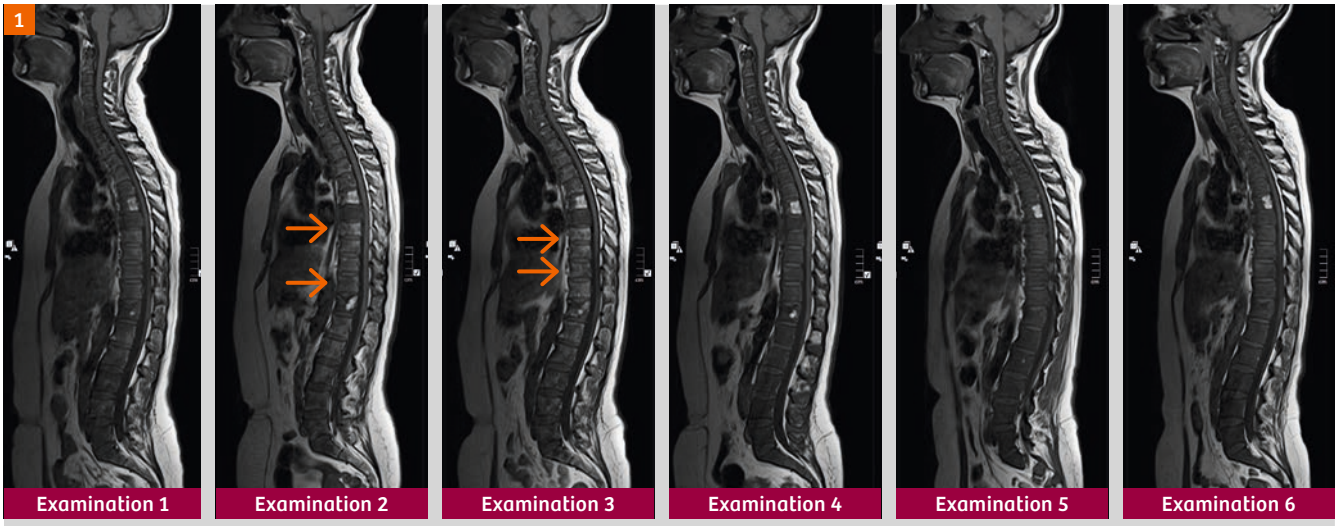

Figure 1: Whole-spine T1-weighted images show diffuse bone marrow infiltration with some return of bone marrow fat on examinations 2 and 3 (arrows) with first-line hormonal therapy. The bone marrow fat disappears at therapy relapse on examination 4 and no further T1w changes are detected after therapy change to second-line on examinations 5 and 6. There is a hemangioma in T6.

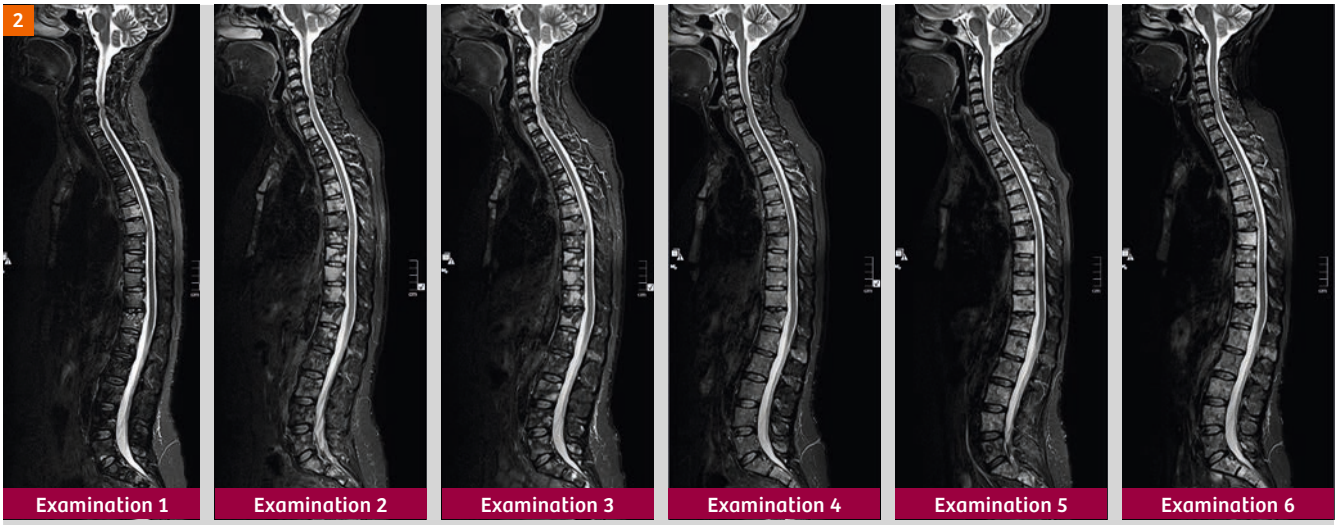

Figure 2: Whole-spine STIR show diffuse bone marrow infiltration with subtle increases in signal intensity with first-line therapy on examinations 2 and 4, but signal intensity lowers by examination 4 at the time of disease relapse (relapse). The bone marrow signal increases again after change to second-line hormonal therapy on examinations 5 and 6. These increases in bone marrow signal intensity are consistent with alternations in tissue water associated with the cell kill mechanism of hormonal treatment (apoptosis).

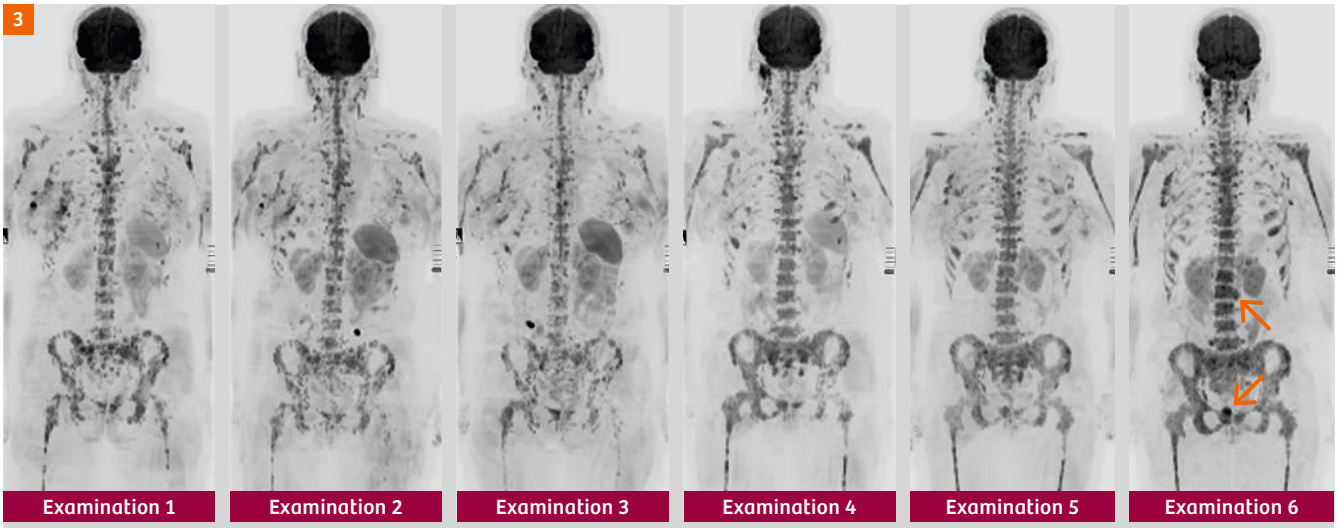

Figure 3: Whole-body b900 3D MIP (inverted scale). The bone marrow is diffusely involved with multiple small focal and confluent regions of high-signal intensity in the axial skeleton and in the proximal limb bones. The primary right-sided breast cancer is *in-situ* with axillary nodal disease visible also. Decreases in the signal intensity of bone marrow with first-line therapy can be seen to occur slowly, but there are focal areas of persistent hyperintensities indicating the likely presence of active disease (examination 3). On examination 4, full-blown relapse can be seen, indicated by increases in signal intensity extent in the bones (see article by Padhani & Tunariu on page 64 in this MAGNETOM Flash for progression criteria for bone disease). On changing to second-line hormonal therapy, no response can be confidently identified but there is increasing disease in the anterior ribs, on the left side of L2 and pubic symphysis (arrows).

only shown on quantitative diffusion imaging. Unfortunately, she also developed liver and pancreas metastases needing further therapy change to chemotherapy. No regional radiotherapy has been administered.

Serial examinations with whole-body diffusion MRI were undertaken using published protocols [2]. Whole-body diffusion sequences using b-values of b50, b600 and 900 s/mm^2 were undertaken together with spinal T1-weighted and STIR sequences, to monitor response to treatment. Six examinations were performed in total. Following the baseline examination, three further examinations were done while on first-line hormonal therapy and two examinations while on second-line hormonal therapy.

Figure 4: WB-tumor load segmentations were undertaken on *syngo*.via Frontier MR Total Tumor Load software (Siemens Healthcare, Erlangen, Germany; released research prototype). The whole-body b900 images are segmented using computed high b-value images of 1000–1200 s/mm², setting a signal intensity threshold of approximately 100 AU. Extraneous signals (such as the brain, kidneys and bowel) are removed, to leave only recognizable bone disease sites including the right breast and axilla. The color the b900 MIP images are overlaid with ADC value classes using the following thresholds. The green voxels are values ≥1500 µm²/s (representing voxels that are 'highly likely' to be responding). The yellow voxels are set to lie between the 95th centile ADC value of the pre-treatment (examination 1 or examination 4) histograms (1256 and 1127 µm²/s respectively) and 1500 µm²/s. Thus, yellow voxels represent regions 'likely' to be responding. Red voxels represent mostly areas that are untreated disease or have no detected response.

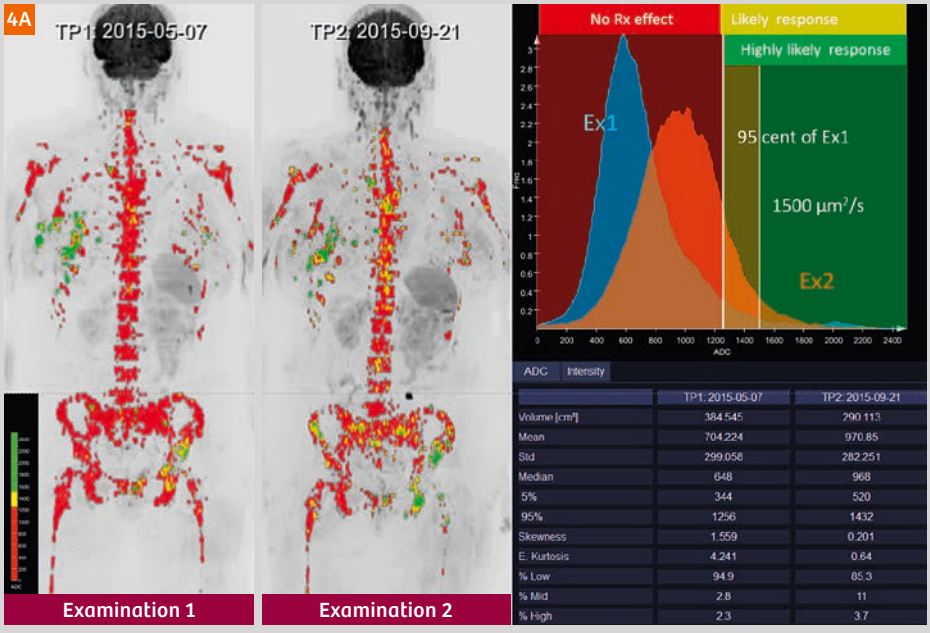

Figure 4A: Histogram analysis of examination 1 and 2.
384 ml of tumor was segmented before therapy and 290 ml on therapy. Note that there is a significant global increase in ADC values (704 µm²/s and 971 µm²/s) and a decrease in kurtosis (4.2 and 0.6) on the corresponding relative frequency histograms indicating some response on a whole-body basis. Note increasing numbers of yellow and green voxels occurring in patches (for example the left hip – note no radiotherapy has been given). These appearances taken with morphologic assessments indicate a favourable response overall with no evidence of progression.

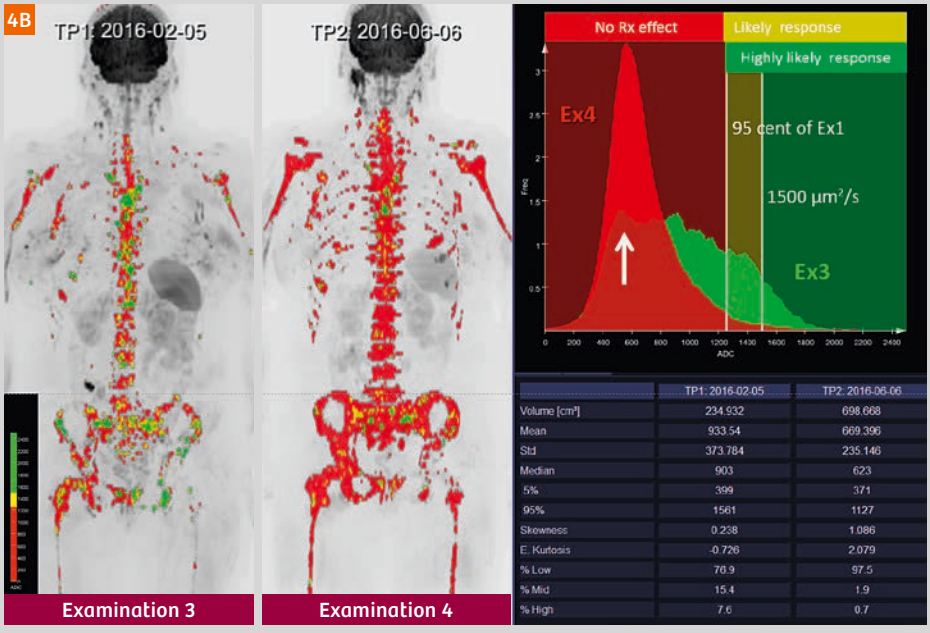

Figure 4B: Histogram analysis of examination 3 and 4.
235 ml of tumor was segmented on examination 3 and 698 ml on examination 4 at disease relapse. Note that on examination 3 there is a flattened histogram (green histogram) with a significant global increase in ADC values (933 µm²/s) compared to baseline and a marked decreased kurtosis (-0.7) on the relative frequency histograms, indicating a good response to first-line hormonal therapy. Note increasing numbers of yellow and green voxels. These appearances taken with morphologic assessments indicate a good response overall. However, note persistent red voxels on examination 3 and a corresponding peak on the examination 3 histogram, indicating areas of therapy resistance (vertical white arrow). On examination 4, the patient has relapsed with a histogram that is identical to the baseline pretherapy study (examination 1).

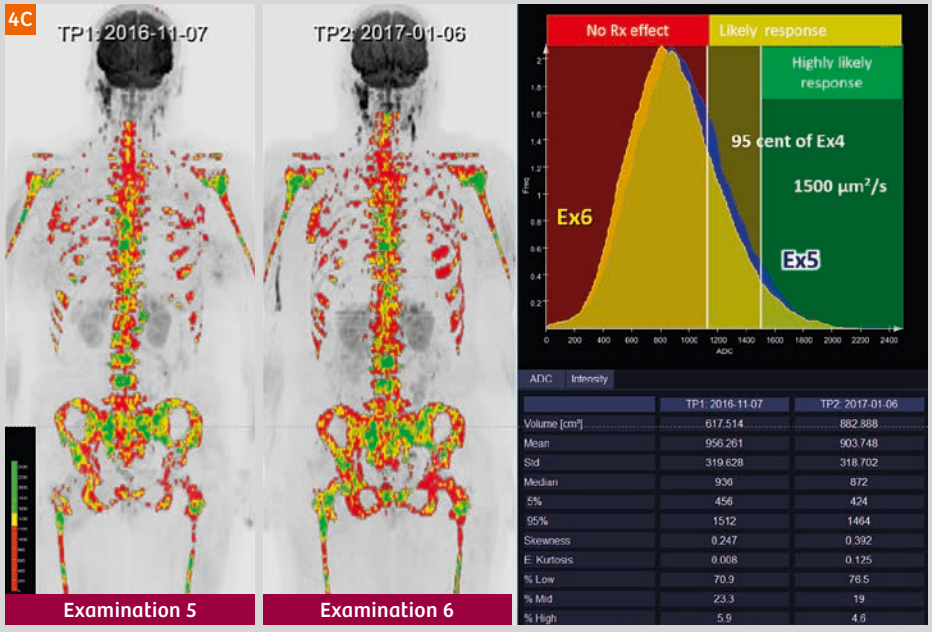

	TP1: 2016-11-07	TP2: 2017-01-06
Volume [cm³]	617.514	882.888
Mean	956.261	903.748
Std	319.628	318.702
Median	936	872
5%	456	424
95%	1512	1464
Skewness	0.247	0.392
E. Kurtosis	0.008	0.125
% Low	70.9	76.5
% Mid	23.3	19
% High	5.9	4.6

Figure 4C: Histogram analysis of examination 5 and 6.
617 ml of tumor was segmented on examination 5 and 883 ml on examination 6. Note that on both examinations, the histograms show significant global increases in ADC values (956 and 904 µm²/s) compared to examination 4 (pre-second-line treatment baseline) indicting a good response to second-line hormonal therapy. The diffusion imaging appearances indicate a good response overall not observable on the T1w spine images. However, note that there are persistent red voxels on both examinations 5 and 6, indicating persistent areas of therapy resistance in the bones. Note also increased volume of right axillary nodal disease. Therapy was changed because of new liver and pancreatic metastases.

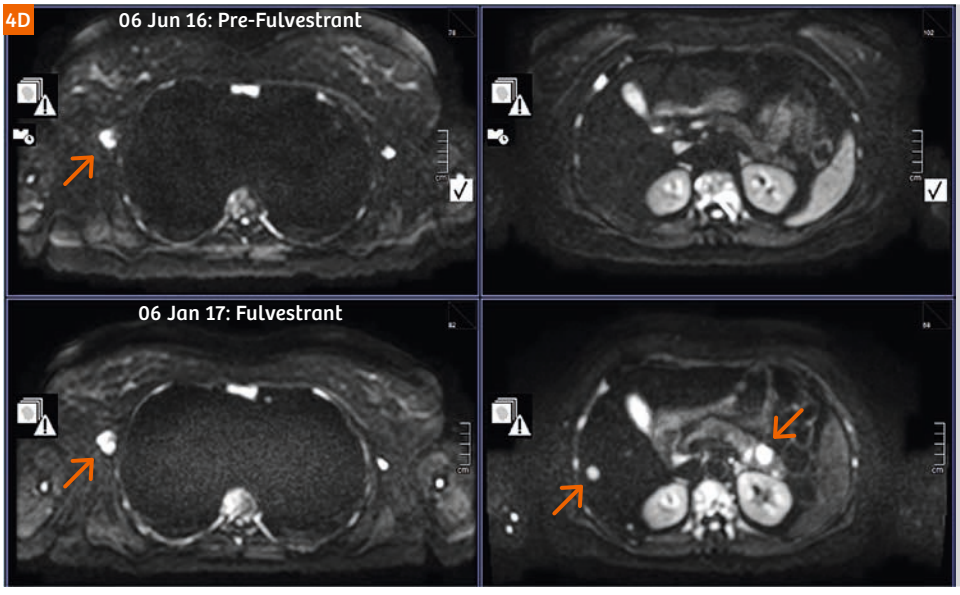

Figure 4D: Axial b900 images of the upper abdomen for examinations 4 (pre-second-line hormonal therapy) and 6 show the emergence of new disease in liver and pancreas (arrows), resulting in a change to chemo-therapy therapy. Right axillary nodes are also enlarging.

References

1 Jeselsohn R, Buchwalter G, De Angelis C, Brown M, Schiff R. ESR1 mutations – a mechanism for acquired endocrine resistance in breast cancer. Nat Rev Clin Oncol. 2015;12:573–583.
2 Padhani AR, Lecouvet FE, Tunariu N, et al. METastasis Reporting and Data System for Prostate Cancer : Practical Guidelines for Acquisition , Interpretation , and Reporting of Whole-body Magnetic Resonance Imaging-based Evaluations of Multiorgan Involvement in Advanced Prostate Cancer. Eur Urol. European Association of Urology; 2017;71:81–92.

Contact

Professor Anwar R. Padhani
MB, BS, FRCP, FRCR
Paul Strickland Scanner Centre
Mount Vernon Hospital

Rickmansworth Road
Northwood, Middlesex HA6 2RN
United Kingdom
anwar.padhani@
stricklandscanner.org.uk

CS-VIBE – a Breakthrough in Ultrafast Dynamic Breast MRI

Ritse M. Mann; Suzan Vreemann

Radboud University Medical Centre, Department of Radiology, Nijmegen, the Netherlands

Abstract

In this article we present a compressed sensing (CS) – volume-interpolated breath-hold examination (VIBE) sequence[1] as a new approach for ultrafast dynamic breast MRI. Opposed to more common viewsharing techniques such as time resolved angiography with stochastic trajectories (TWIST), timepoints in CS-VIBE are independently obtained and therefore resolve the temporal blurring that is inherent to viewsharing techniques. The smart *k*-space filling of the CS-VIBE sequence allows for creation of high spatial resolution images from heavily undersampled data at an excellent temporal resolution of less than 5 seconds per volume obtained. As published previously [1] CS-VIBE allows acquisition of images at a similar quality as those obtained with TWIST at identical temporal resolution, but with a spatial resolution of 0.8 x 0.8 x 1.6 mm, thus more than halving the voxel size when compared to TWIST. This implies that CS-VIBE allows multiplanar reconstruction and assessment of morphologic lesion characteristics in multiple planes, which was so far not possible with viewsharing techniques.

Key points

- CS-VIBE allows ultrafast dynamic breast MRI at unprecedented spatial resolution
- CS-VIBE overcomes temporal blurring in ultrafast breast MRI
- Morphological lesion evaluation on CS-VIBE images is virtually identical to morphological lesion evaluation using conventional T1-weighted VIBE Dixon images

Background

Lately, interest in ultrafast dynamic breast MRI has surged. This is mainly due to the large improvements of MRI hardware and software that enabled the creation of high quality images at very high temporal resolution [2–5]. Already from studies in the early nineties it was evident that dynamic analysis of the inflow phase was more informative than late phase wash-out features [6]. However, initial approaches were single slice techniques and could therefore only be used to classify already known lesions at known locations. Around the shift of the century whole-breast acquisitions had become possible, albeit at spatial resolutions that still prevented most radiologists from actually looking at these images [7, 8]. Instead, the generated data was used for pharmacokinetic modeling using simple or more advanced iterations of the Tofts model [9, 10]. The thus obtained quantitative parameters were once again shown to yield more diagnostic information than wash-out features, and were complementary to morphologic assessment of lesion characteristics using the Breast Imaging Reporting and Data System (BIRADS) lexicon, or similar classification systems [7, 8, 11]. Especially K^{trans}, the transfer constant from the intravascular to the extravascular extracellular space proved to be a robust predictor of malignancy, being much higher in malignant than in benign lesions, which can be explained by the increased vascularization and the immaturity of these new-formed vessels in which the endothelial lining is often incomplete and sometimes even the basement membrane is lacking [12].

Nonetheless, the so-called 'quantitative' parameters still suffered from huge variation within patients and from site to site, mainly due to difficulties with the determination of a realistic arterial input function [13]. This is difficult due to the simple fact that in breast MRI no representative vessels that are large enough for measurements are present within the field-of-view. The common solution is to use a population based arterial input function, thus reducing the variation, but also the true quantitative aspect of the measurements. Alternative approaches make use of reference tissues, such as the pectoral muscle, but are likewise hampered by huge variations in the reference tissue due to the physical properties of the patients imaged [13, 14].

A further difficulty is that due to the limited spatial resolution maps of these pharmacokinetic parameters were not really sufficient for lesion detection, and use is therefore

[1] WIP. Cartesian CS-VIBE is currently under development and is not for sale in the US and in other countries. Its future availability cannot be ensured. CS GRASP-VIBE is 510(k) pending and may be used for the same purpose.

still limited to classification of otherwise detected lesions (and possible evaluation of the effects of primary systemic therapies), although the prerequisite of knowledge of lesion location is lifted by the whole-breast approach [7, 8, 11].

This largely shifted when modern viewsharing sequences became available that improved spatial and temporal resolution well beyond the borders of what was obtainable with keyhole based techniques [2–5]. In fact, it became possible to generate images within 5 seconds that met the international standards for diagnostic breast MRI, with a spatial resolution in plane of 1 x 1 mm, and a slice thickness of only 2.5 mm [5]. Suddenly it thus became possible to actually detect lesions on ultrafast dynamic breast MRI and perform classification based upon dynamic and morphologic features using the same images. By generating temporal maximum intensity projections (MIP), it has become possible to create an actual movie of contrast inflow; in general first highlighting the most suspicious finding in the breast ('the light bulb effect'), as these tend to enhance fastest.

In addition, a strong simplification of the interpretation of the dynamic data obtained, abandoning the pharmacokinetic model, but just looking at the slope of the enhancement curve, allows for much broader use of the ultrafast dynamic data, hardly without loss of its classifying properties [5, 15]. The rule of thumb is simple; the steeper the curve, the more likely that a lesion is malignant. Hence the maximum slope (MS) is an excellent tool for lesion classification. Furthermore, in analogy to the previously mentioned light bulb effect, the earlier a lesion enhances relative to the enhancement of the descending aorta, the more likely that it is malignant. This is captured in the 'time to enhancement' (TTE) [16]. In general most malignant lesions enhance within 15 seconds after aortic enhancement, whereas benign lesions enhance commonly later.

The excellent classifying properties of these simple inflow dynamics have since been confirmed by several studies using both radiologists and machine learning techniques. In one of the largest series to date, comparing 217 cancers to 172 benign lesions, Dalmis et al. reported that the overall classifying property of the inflow enhancement curve was 0.84, which compares favorably to most morphologic characteristics [17]. Moreover, this was robust over all types of malignant breast lesions, with only a slightly lower performance in ductal carcinoma in situ (DCIS) (Table 1).

Cancer type	n	Classifying property of dynamic features
DCIS	38	0.7690 (0.6728–0.8469)
IDC	141	0.8459 (0.7969–0.8893)
ILC	38	0.8673 (0.8018–0.9161)

Table 1: Classifying capacity of inflow dynamics for different types of malignant lesions. *Adapted from Dalmis et al. [17].*

Screening and abbreviated MRI

In the era of preventive and personalized medicine, screening for disease that is better treatable in its asymptomatic form is becoming more and more important. This is particularly true for breast cancer, which has an excellent prognosis when detected early [18].

Due to the excellent sensitivity of breast MRI for cancer screening trials already commenced in the late nineties, mainly in women at increased risk. Recent studies repeatedly report a sensitivity of MRI of approximately 90%, more or less doubling the sensitivity of mammography in the same populations [19, 20]. Also a stage shift of detected breast cancers is observed, making them smaller and thus easier to treat when detected by MRI [21].

Nonetheless, MRI screening, although internationally supported for all women with a lifetime risk of more than 20–25% [22], is in many countries reserved for women with hereditary breast cancer susceptibility genes or a history of chest radiation during puberty. This is mainly due to the inherent high costs of breast MRI, that have even increased over recent years by our aim to improve the specificity of the technique by adding sequences such as T2, diffusion and even spectroscopy on top of the conventional T1-weighted dynamic contrast-enhanced series.

This has led to the recent introduction of abbreviated scan protocols, that are aimed at lesion detection only, and are not specifically tailored to obtaining the best possible classification of eventual lesions. In screening this seems more than acceptable, as by far most of the scans are normal.

The simplest form of an abbreviated protocol was presented by Kuhl et al. in 2011 and suggested acquisition of only two T1-weighted acquisitions; one before, and one after contrast administration [23]. This acquisition protocol takes about 3 minutes and hence largely reduces the scan time needed for breast MRI that is in most practices at least a quarter of an hour. Subsequent generation of subtraction images and MIPs allowed for fast and accurate evaluation of the MRI acquisitions and did not reduce either sensitivity or specificity when compared to a full diagnostic protocol.

However, especially in screening women at somewhat increased risk morphological features of cancers can sometimes be deceptively benign. Hence abandoning all dynamic information on top of the lack of T2 and diffusion-weighted imaging (DWI) is unwanted if it is not really necessary.

Ultrafast breast MRI performed during and shortly after contrast examination might be used to overcome this issue. In women without lesions it is obviously unnecessary, but since it can be obtained without lengthening the protocol, it provides additional classification tools in women with breast lesions at no penalty in terms of acquisition time. In fact, when only ultrafast breast MRI is performed the acquisition time might be even further reduced to

approximately 2 minutes [5]. In a study presented by van Zelst et al. seven readers read 200 cases containing 31 MRI screen detected breast lesions and 54 biopsied benign lesions using only ultrafast breast MRI (TWIST) and using a full diagnostic protocol (FDP) consisting of high-resolution T1-weighted acquisitions before and after contrast administration, T2, and DWI [24]. Overall, sensitivity between the two techniques was equal (84%, vs 86%, ns.), whereas specificity was in fact higher using only TWIST than the FDP (81% vs 76%, p<0.001). This unambiguously shows that ultrafast breast MRI has high potential as screening technique.

Still, rather than choosing either the simple abbreviated approach or the ultrafast approach it is possible to combine the techniques in a short hybrid protocol, interleaving a number of ultrafast acquisitions in between the two high-resolution T1-weighted series during contrast administration, without lengthening the acquisition time of the simple approach. Such a hybrid protocol allows for very fast and simple evaluation in women without breast lesions, but enables both morphologic assessment and dynamic analysis of the contrast inflow in women with abnormalities.

Compressed sensing VIBE

The rationale for a hybrid protocol implies that there are still shortcomings of the current ultrafast techniques available. These are present both in the spatial and the temporal domain. In terms of spatial resolution TWIST might achieve a diagnostic level according to international standards; but the slice thickness of 2.5 mm still limits the possibility of multiplanar reconstruction, and thus assessment of morphological features and lesion extent in other planes than the axial slices usually obtained. In terms of temporal resolution viewsharing inherently causes some temporal blurring and thus less reliable dynamic information, despite the successes that have been achieved so far.

	CS-VIBE
TR (ms)	4.47
TE (ms)	2.06
FA (°)	15
Field-of-view (mm²)	358.4 x 358.4
Matrix size	448 x 381
TWIST central region A (%) / Sampling density B (%)	-
Slice thickness (mm)	1.6
Voxel volume (mm³)	1.024
Phase resolution (%)	85
Slice resolution (%)	70
Acceleration factor	20
Acceleration mode	CS
Time resolution per volume (s)	4.55
Total acquisition time (min)	1:40

Table 2: Parameters of the prototype CS-VIBE sequence.[1]

By shifting the acquisition from a viewsharing approach to compressed sensing several of these limitations are overcome. CS VIBE incoherently subsamples the phase-encoding plane with variable density, obeying a Gaussian distribution in which the density is higher in the center of *k*-space than at its borders. Despite the sparsity of the sampling technique adequate images can be reconstructed by optimization of a cost-function. Since volumes are independently obtained per time point no temporal blurring is present. Furthermore, a spatial resolution is achieved of 0.8 x 0.8 x 1.6 mm. Parameters of the prototype CS-VIBE sequence are presented in Table 2.

In a reader study by Vreemann et al. presented at this years ISMRM [25], it was shown that image quality of the CS-VIBE is equal to that of TWIST, despite the fact that the voxel volumes are more than halved. Artifacts between sequences are somewhat different. TWIST is particularly known for infolding and ghosting artifacts, likely directly caused by the viewsharing; CS-VIBE seems somewhat more prone to pulsation artifacts from the heart, which are particularly seen in the axillary region. The image quality of CS-VIBE almost approaches that of the conventional VIBE Dixon acquisitions with a spatial resolution of 0.9 x 0.9 x 1 mm, acquired in 91 seconds (Fig. 1).

Morphological lesion evaluation based on the CS-VIBE was compared to evaluation of lesion morphology on VIBE Dixon and results were virtually identical, showing the excellent capability of morphological assessment on CS-VIBE acquisitions alone, which is enabled by the possibility to create multiplanar reconstructions of the acquired volume. In addition it becomes possible to create rotating MIPs; although these might not be very essential for diagnostic practice, they certainly improve the clarity of the scan when explaining the findings to treating physicians, in particular surgeons (Fig. 2).

Currently, the implementation of CS-VIBE in clinical practice is still somewhat limited by the required reconstruction time of approximately 45 minutes on the scanner. This implies that images cannot be generated during the daily program, but instead image generation has to be performed over night. While for screening this might not be a real problem, in the sense that there is in general no reason why scans could not be read one day after acquisition. However, it still prevents the technologists from controlling the quality of their work. Future advances in the calculating capacity of work-stations used for image generation will however likely resolve this issue.

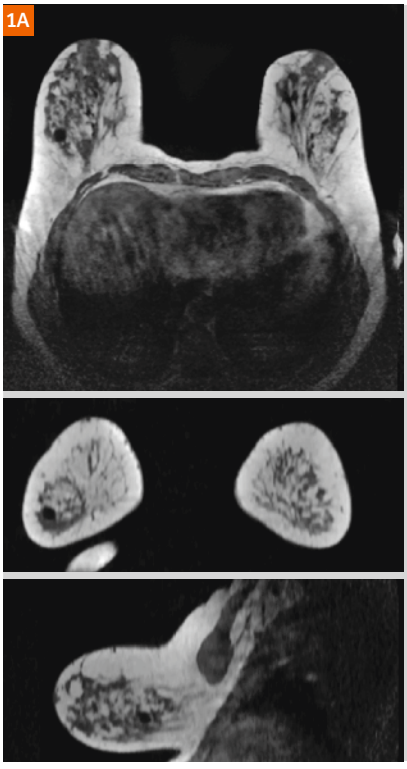

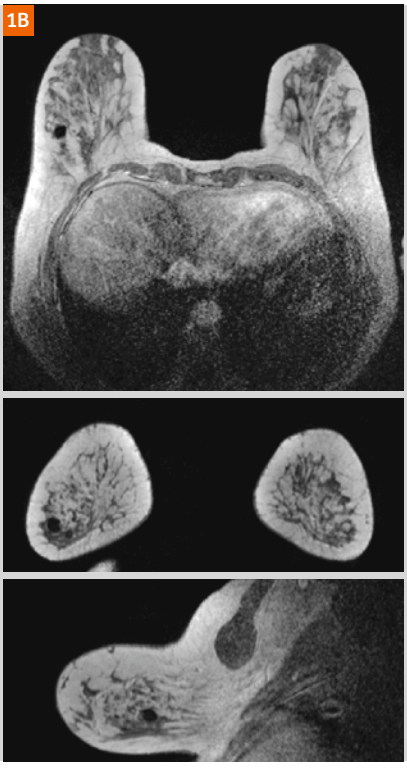

Figure 1: A comparison of image quality between the CS-VIBE **(1A)** and VIBE Dixon **(1B)** in multiple planes. Even though the VIBE Dixon acquisition is still somewhat sharper, morphological evaluation of structures within the breast is almost identical in all directions.

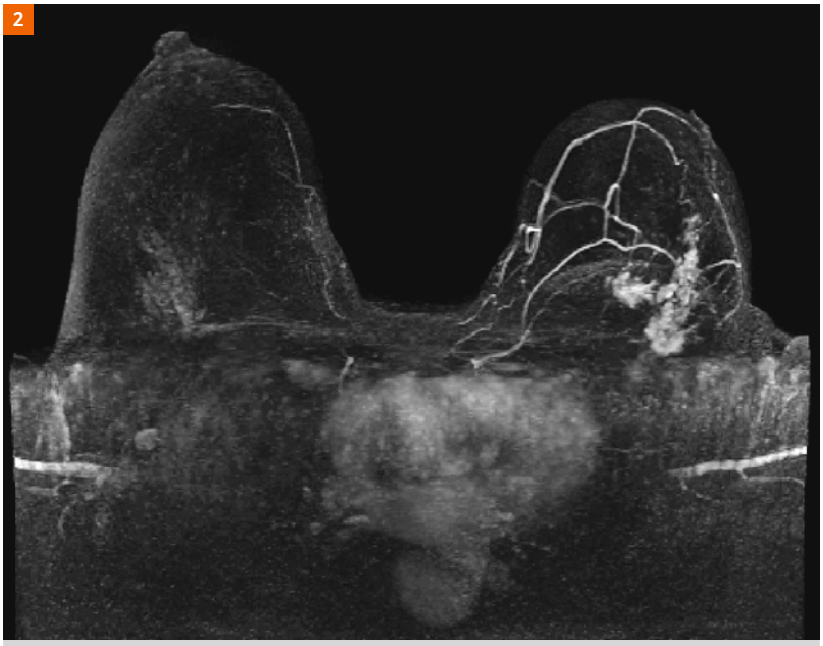

Figure 2: A maximum intensity projection image obtained from the first and last CS-VIBE acquisition, showing with high morphological detail a multifocal cancer in the left breast with marked vascular asymmetry.

In conclusion, CS-VIBE is a major step forward in ultrafast breast MRI; for the first time allowing high quality image generation at a spatial resolution that enables multiplanar reformatting, without temporal blurring and within 5 seconds. CS-VIBE therefore brings screening with ultrafast breast MRI alone one step closer.

References

1 Vreemann S, Rodriguez-Ruiz A, Nickel D, Maas M, Karssemeijer N, Weiland E, Kiefer B, Mann R. Advanced Ultrafast Dynamic Contrast Enhanced Breast MRI with Compressed Sensing VIBE. Proceedings of the 25th Annual Meeting of ISMRM, p. 2670, Honolulu, HI, USA, April 2017.

2 Herrmann KH, Baltzer PA, Dietzel M, Krumbein I, Geppert C, Kaiser WA, Reichenbach JR. Resolving arterial phase and temporal enhancement characteristics in DCE MRM at high spatial resolution with TWIST acquisition. J Magn Reson Imaging. 2011 Oct;34(4):973-82.

3 Tudorica LA, Oh KY, Roy N, Kettler MD, Chen Y, Hemmingson SL, Afzal A, Grinstead JW, Laub G, Li X, Huang W. A feasible high spatiotemporal resolution breast DCE-MRI protocol for clinical settings. Magn Reson Imaging. 2012 Nov;30(9):1257-67.

4 Le Y, Kipfer H, Majidi S, Holz S, Dale B, Geppert C, Kroeker R, Lin C. Application of time-resolved angiography with stochastic trajectories (TWIST)-Dixon in dynamic contrast-enhanced (DCE) breast MRI. J Magn Reson Imaging. 2013 Nov;38(5):1033-42.

5 Mann RM, Mus RD, van Zelst J, Geppert C, Karssemeijer N, Platel B. A novel approach to contrast-enhanced breast magnetic resonance imaging for screening: high-resolution ultrafast dynamic imaging. Invest Radiol. 2014 Sep;49(9):579-85.

6 Boetes C, Barentsz JO, Mus RD, van der Sluis RF, van Erning LJ, Hendriks JH, Holland R, Ruys SH. MR characterization of suspicious breast lesions with a gadolinium-enhanced TurboFLASH subtraction technique. Radiology. 1994 Dec;193(3):777-81.

7 Veltman J, Stoutjesdijk M, Mann R, Huisman HJ, Barentsz JO, Blickman JG, Boetes C. Contrast-enhanced magnetic resonance imaging of the breast: the value of pharmacokinetic parameters derived from fast dynamic imaging during initial enhancement in classifying lesions. Eur Radiol. 2008 Jun;18(6):1123-33.

8 Pinker K, Grabner G, Bogner W, Gruber S, Szomolanyi P, Trattnig S, Heinz-Peer G, Weber M, Fitzal F, Pluschnig U, Rudas M, Helbich T. A combined high temporal and high spatial resolution 3 Tesla MR imaging protocol for the assessment of breast lesions: initial results. Invest Radiol. 2009 Sep;44(9):553-8.

9 Tofts PS, Berkowitz B, Schnall MD. Quantitative analysis of dynamic Gd-DTPA enhancement in breast tumors using a permeability model. Magn Reson Med. 1995 Apr;33(4):564-8.

10 Brix G, Kiessling F, Lucht R, Darai S, Wasser K, Delorme S, Griebel J.Microcirculation and microvasculature in breast tumors: pharmacokinetic analysis of dynamic MR image series. Magn Reson Med. 2004 Aug;52(2):420-9.

11 Huang W, Tudorica LA, Li X, Thakur SB, Chen Y, Morris EA, Tagge IJ, Korenblit ME, Rooney WD, Koutcher JA, Springer CS Jr. Discrimination of benign and malignant breast lesions by using shutter-speed dynamic contrast-enhanced MR imaging. Radiology. 2011 Nov;261(2):394-403.

12 Saaristo A, Karpanen T, Alitalo K. Mechanisms of angiogenesis and their use in the inhibition of tumor growth and metastasis. Oncogene. 2000 Dec 11;19(53):6122-9.

13 Heisen M, Fan X, Buurman J, van Riel NA, Karczmar GS, ter Haar Romeny BM. The use of a reference tissue arterial input function with low-temporal-resolution DCE-MRI data. Phys Med Biol. 2010 Aug 21;55(16):4871-83.

14 Stoutjesdijk MJ, Zijp M, Boetes C, Karssemeijer N, Barentsz JO, Huisman H. Computer aided analysis of breast MRI enhancement kinetics using mean shift clustering and multifeature iterative region of interest selection. J Magn Reson Imaging. 2012 Nov;36(5):1104-12.

15 Platel B, Mus R, Welte T, Karssemeijer N, Mann R. Automated characterization of breast lesions imaged with an ultrafast DCE-MR protocol. IEEE Trans Med Imaging. 2014 Feb;33(2):225-32.

16 Mus RD, Borelli C, Bult P, Weiland E, Karssemeijer N, Barentsz JO, Gubern-Mérida A, Platel R, Mann RM. Time to enhancement derived from ultrafast breast MRI as a novel parameter to discriminate benign from malignant breast lesions. European Journal of Radiology, Vol. 89, p90–96

17 Dalmış MU, Gubern-Mérida A, Vreemann S, Karssemeijer N, Mann R, Platel B. A computer-aided diagnosis system for breast DCE-MRI at high spatiotemporal resolution. Med Phys. 2016 Jan;43(1):84.

18 Saadatmand S, Bretveld R, Siesling S, Tilanus-Linthorst MM. Influence of tumour stage at breast cancer detection on survival in modern times: population based study in 173,797 patients. BMJ. 2015 Oct 6;351:h4901.

19 Kuhl C, Weigel S, Schrading S, Arand B, Bieling H, König R, Tombach B, Leutner C, Rieber-Brambs A, Nordhoff D, Heindel W, Reiser M, Schild HH. Prospective multicenter cohort study to refine management recommendations for women at elevated familial risk of breast cancer: the EVA trial. J Clin Oncol. 2010 Mar 20;28(9):1450-7.

20 Sardanelli F, Podo F, Santoro F, Manoukian S, Bergonzi S, Trecate G, Vergnaghi D, Federico M, Cortesi L, Corcione S, Morassut S, Di Maggio C, Cilotti A, Martincich L, Calabrese M, Zuiani C, Preda L, Bonanni B, Carbonaro LA, Contegiacomo A, Panizza P, Di Cesare E, Savarese A, Crecco M, Turchetti D, Tonutti M, Belli P, Maschio AD; High Breast Cancer Risk Italian 1 (HIBCRIT-1) Study.. Multicenter surveillance of women at high genetic breast cancer risk using mammography, ultrasonography, and contrast-enhanced magnetic resonance imaging (the high breast cancer risk italian 1 study): final results. Invest Radiol. 2011 Feb;46(2):94-105.

21 Rijnsburger AJ, Obdeijn IM, Kaas R, Tilanus-Linthorst MM, Boetes C, Loo CE, Wasser MN, Bergers E, Kok T, Muller SH, Peterse H, Tollenaar RA, Hoogerbrugge N, Meijer S, Bartels CC, Seynaeve C, Hooning MJ, Kriege M, Schmitz PI, Oosterwijk JC, de Koning HJ, Rutgers EJ, Klijn JG. BRCA1-associated breast cancers present differently from BRCA2-associated and familial cases: long-term follow-up of the Dutch MRISC Screening Study. J Clin Oncol. 2010 Dec 20;28(36):5265-73.

22 Mann RM, Kuhl CK, Kinkel K, Boetes C. Breast MRI: guidelines from the European Society of Breast Imaging. Eur Radiol. 2008 Jul;18(7):1307-18.

23 Kuhl CK, Schrading S, Strobel K, Schild HH, Hilgers RD, Bieling HB. Abbreviated breast magnetic resonance imaging (MRI): first postcontrast subtracted images and maximum-intensity projection-a novel approach to breast cancer screening with MRI. J Clin Oncol. 2014 Aug 1;32(22):2304-10.

24 Van Zelst J, Gubern-Merida A, Vreemann S, Veltman J, Dorrius M, Loo C, Duvivier-van Hoof K, Karssemeijer N, Mann RM, High Risk Breast Cancer Screening with an Ultrafast High Spatiotemporal Resolution MRI Sequence; Less Costly and as Reliable as a Full Diagnostic MRI Protocol. Radiological Society of North America 2016 Scientific Assembly and Annual Meeting, November 27 - December 2, 2016, Chicago IL. archive.rsna.org/2016/16014917.html

25 Vreemann S, Rodriguez-Ruiz A, Nickel D, Maas MC, Karssemeijer N, Weiland E, Kiefer B, Mann RM. Advanced Ultrafast Dynamic Contrast Enhanced Breast MRI with Compressed Sensing VIBE. ISMRM 2017, abstract number 445

Contact

Ritse Mann
Radboud University Medical Centre
Department of Radiology

huispost 766
P.O. Box 9101
6500 HB
Nijmegen
the Netherlands
ritse.mann@radboudumc.nl

Suzan Vreemann
Radboud University Medical Centre
Department of Radiology

huispost 766
P.O. Box 9101
6500 HB
Nijmegen
the Netherlands
suzan.vreemann@radboudumc.nl

Try them on your system

Trial licenses for many of the applications featured in this issue of MAGNETOM Flash are available free of charge for a period of 90 days.

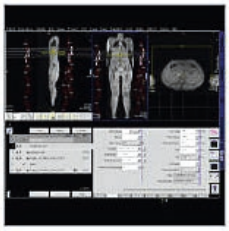

Tim Planning Suite
Allows planning of several stations at once, e.g. on composed localizer images. >

Tim Planning Suite

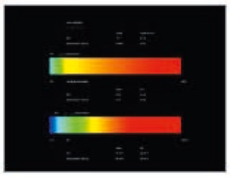

LiverLab
Evaluating the iron and fat content of the liver is an important step in monitoring early stages of liver diseases. >

LiverLab

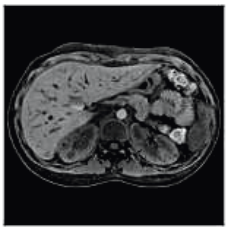

FREEZEit
Embrace motion in liver imaging. >

FREEZEit

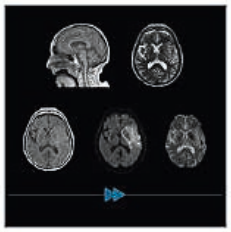

GOBrain
Push-button brain exam in 5 minutes.* >

GOBrain

Brain Dot Engine
The Brain Dot Engine increaes productivity and standardization with guided and automated workflows. >

Brain Dot Engine

Abdomen Dot Engine
The Abdomen Dot Engine is customized for dynamic liver examinations and cosistent contrast timing. >

Abdomen Dot Engine

Spine Dot Engine
The Spine Dot Engine optimizes cervical, thoracic, and lumbar spine imaging for a wide range of patients and conditions. >

Spine Dot Engine

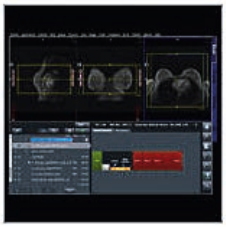

Breast Dot Engine
The Breast Dot Engine supports consistent frequency selection for fat, water, saline or silicone. >

Breast Dot Engine

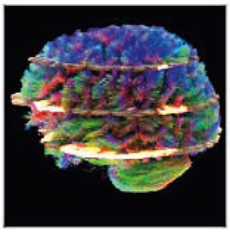

Simultaneous Multi-Slice
Accelerate advanced neuro applications for clinical routine. >

Simultaneous Multi-Slice

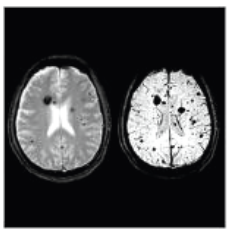

SWI
SWI is a new type of contrast technique in MRI that detects blood and iron deposits better than conventinal methods. >

Susceptibility-Weighted Imaging

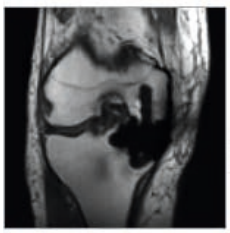

Advanced WARP
Advanced WARP corrects in- and through-plane distortions for more accurate diagnosis of tissue surrounding orthopedic implants. >

Advanced WARP

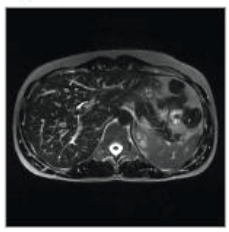

SPACE
SPACE enables the acquisition of high resolution 3D datasets. >

SPACE

For further details, product overviews, image galleries, step-by-step videos and general requirements visit us at:

www.siemens.com/mri-options-overview

Whole-Body MRI Including DWI

David Hillier

MR Application Specialist, Siemens Healthineers Great Britain and Ireland (GB&I)

Background

National Institute for Health and Care Excellence (NICE) guidance (NG35) published in February 2016 [1] recommends to consider whole-body MRI (wbmri) as first-line imaging for patients with suspected or newly diagnosed Myeloma. The burden on the clinical MRI service is significant as these examinations can take approximately one hour and require special attention in order for favorable image quality to be achieved. It is therefore important to optimize the workflow for maximum efficiency. Before embarking on wbmri, it is advisable to be familiar with articles such as Padhani et al. [2] and Koh et al. [3] in order to understand the aim of wbmri. The purpose of this article is to explain the technique of performing wbmri using particular features of the MR system and how to build a robust program rather than discuss clinical opinions or even to prescribe sequence parameters as these can be agreed locally.

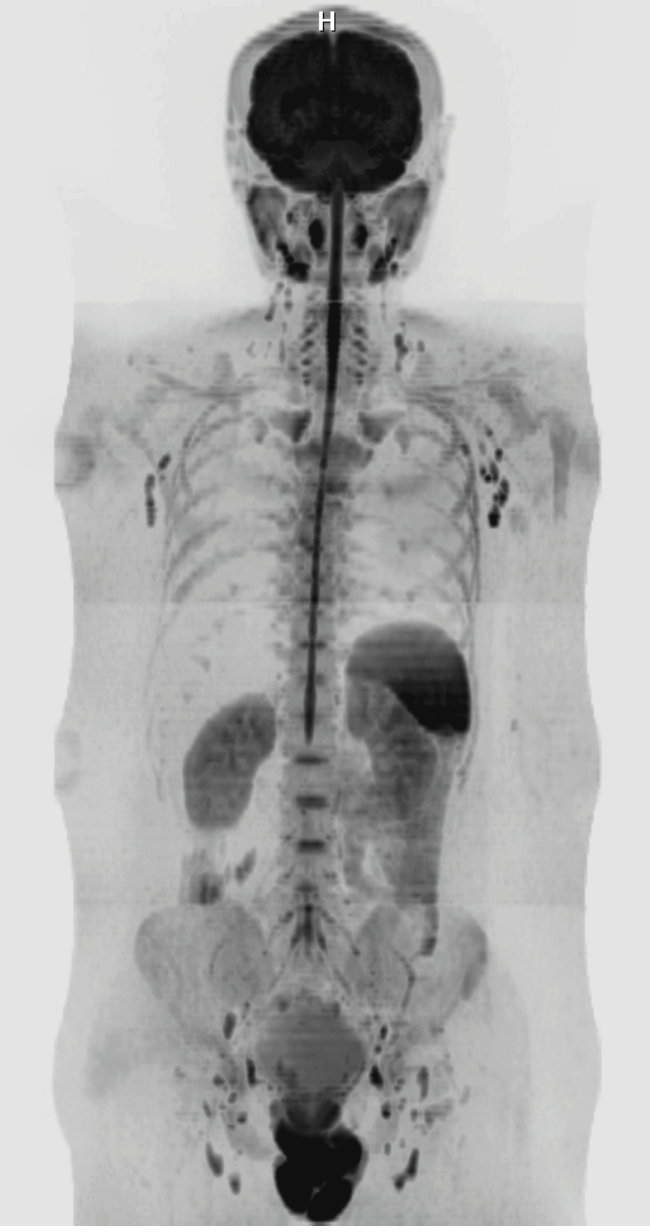

Equipment

This article is based on using a MAGNETOM Aera / Skyra system with *syngo* MR E11 software. The following licenses are not mandatory, but do make the workflow more efficient: Tim Whole Body Suite (205 cm table movement), Tim Planning Suite (Set-n-Go) and Inline Composing.

Preparation

The referring clinician should be aware that the patients they send for this examination will be required to lie supine for approximately one hour and they will be covered from head to toe with receiver coils. It is not well tolerated by patients who will feel uncomfortable lying for this length of time or who may feel claustrophobic. It is also advisable that the patient empties their bladder prior to the examination.

Examination

The patient is positioned head first supine. If available, Head/Neck 20, Spine 32, Body 18 (x2) and peripheral angio 36 coils are arranged on the patient. Centre to the chin and move to isocentre.

It is helpful to use the Tim Planning User Interface (UI) (Top menu: *View > Tim Planning UI*), coupled graphics and Auto Coil Select (ACS). To ensure ACS is used, save each sequence with this switched on in local settings (*System > Miscellaneous > Coil Select Mode 'On-AutoCoilSelect'*). The imaging protocol will vary according to local agreements, but typically consists of:

Localizer		Whole body	
Sagittal	t2	Whole spine – 2 stations	Fig. 7A
Sagittal	t1	Whole spine – 2 stations	Fig. 7B
Coronal	tirm	Vertex to below knee joints	Fig. 7D
Coronal	t1	Vertex to below knee joints	Fig. 7E–G
Transverse	DWI	Vertex to mid femur	Fig. 7C

Localizer: *Siemens > TimCT oncology > TimCT oncology > standard > FastView*

FastView is preferred over multi step trufi as it has a shorter acquisition time and image quality is adequate to plan subsequent steps in the program. In *Geometry > Tim CT* (Fig. 1) the 'Range start' value of H 250 mm ensures the acquisition starts above the vertex when centred to the chin.

It is recommended to save this step before starting the examination with sufficient table movement in order to cover the required anatomy on the majority of patients. Suggested value for 'Total FoV H>>F' is 1700 mm. Allow the sequence to complete rather than stopping manually, otherwise it will re-acquire in the F>>H direction.

1

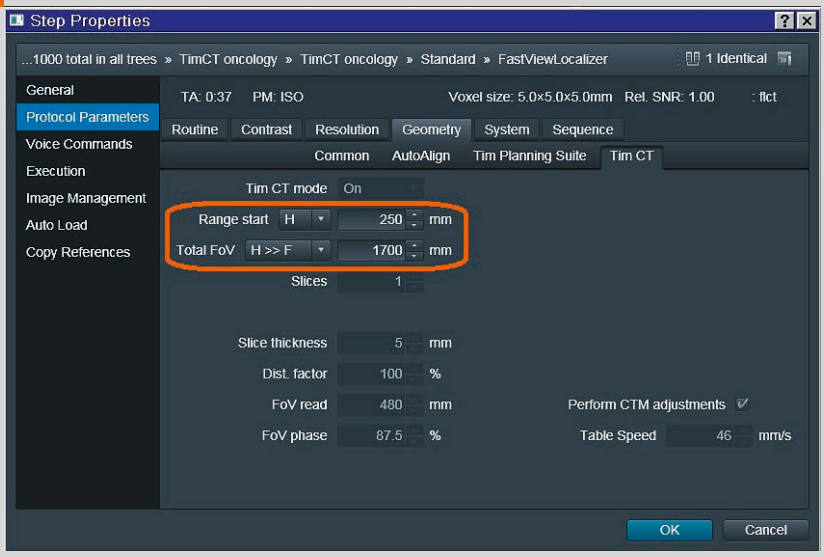

Figure 1: FastView parameter card: *Geometry > Tim CT*

Sagittal t2 whole spine: *Siemens > c-spine > library > t2_tse_sag*

These are acquired as a 2 subprotocol set-n-go protocol. Begin by opening a sagittal t2 and plan the cervical and upper thoracic spine off the Multi Planar Reconstruction (MPR) FastView localizer images. A field-of-view (FOV) of 400–420 mm for each subprotocol is suggested as this allows coverage of the whole spine, sacrum and coccyx in most patients. The use of integrated Parallel Acquisition Technique (iPAT) in order to achieve a short scan time is advisable. Once the upper sub-protocol has been planned, add the second subprotocol by either the 'add sub-protocol' button in the Tim Planning UI (Fig. 2), or go to *Geometry > Tim Planning Suite* and tick 'Set-n-Go Protocol' (Fig. 3). Also tick 'Inline composing' at this stage. Select composing function 'adaptive'. Go to *Inline > composing* and type 'sag_t2' in series description for the composed series to be more obvious in the patient browser.

2

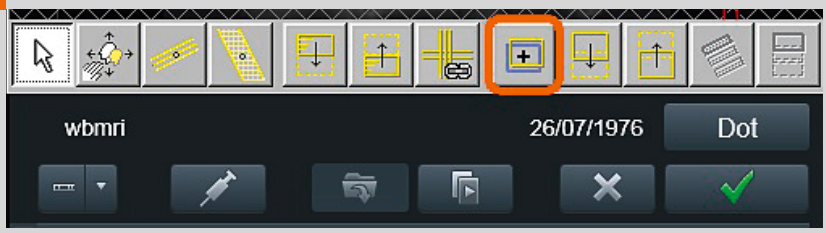

Figure 2: Tim Planning UI: 'Add Subprotocol'*CT*

3

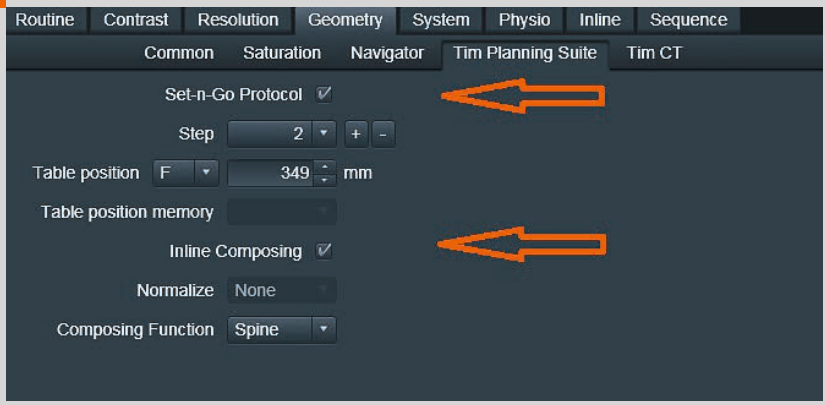

Figure 3: *Geometry > Tim Planning Suite*

Sagittal t1 whole spine:
Siemens > c-spine > library > t1_tse_sag

Ensure the FOV is 400 to 420 mm (as per sagittal t2). Create a copy reference to the t2_tse_sag of 'slices and saturation regions', and tick the boxes 'copy phase encoding direction' and 'steps'. Go to *Geometry > Tim Planning Suite* and tick 'Inline composing' Select composing function 'adaptive'. Go to *Inline > composing* and type 'sag_t1' in series description.

Coronal tirm:
Siemens > whole body oncology > head to pelvis > standard > headneck_t2_tirm_cor

(Or you can select a cor_tirm from the soft tissue neck program in the user tree as this is likely to contain local preferred parameters for tirm.)

Delete 'headneck' from the series description. Change FOV to 500 mm in order to visualize as much anatomy as possible in the X direction.

Prescribe as many slices as required in order to cover the patient's anatomy in the Y direction. It is accepted that the maximum FOV in the Z direction on MAGNETOM Aera and Skyra systems is 450 mm [5]. To avoid distortions being evident at the superior and inferior margins of the FOV (Fig. 4) degrading the original and composed images, it is suggested that the phase encoding direction is F>>H and to use 68.8% FOV phase. Subsequent subprotocols will then be acquired with a smaller table movement. Use 70% phase oversampling to avoid wrap. Position the first subprotocol so that the superior margin of the FOV is above the vertex. Add further subprotocols by using the 'add subprotocol'

4

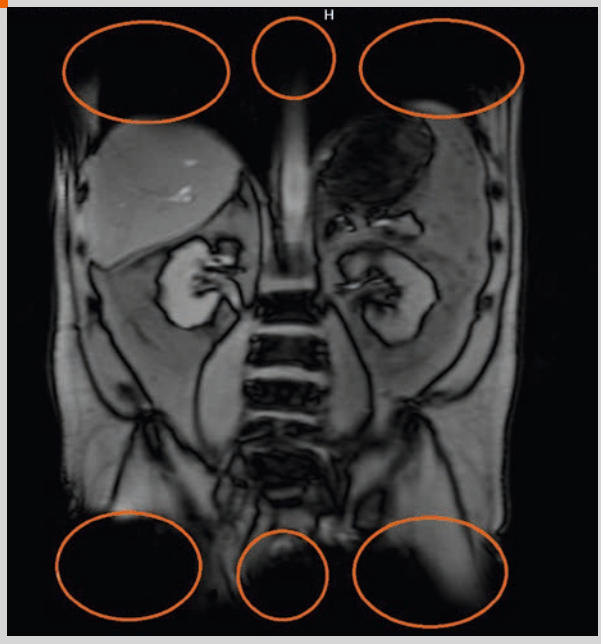

Figure 4: Z axis distortions represented by orange circles on a 500 mm FOV image

button in the Tim Planning UI. This will position the next subprotocol displaced inferiorly by a distance of the FOV -50 mm i.e. 450 mm. With a 100% FOV phase, there would be adequate overlap, but using 68.8% means that there is a gap between the rectangular FOV's. After adding sufficient subprotocols to cover the anatomy, click on the first sub-protocol in the Graphic Slice Position (GSP). It will appear yellow. Click 'Align FOV' (Fig. 5). This will result in all subprotocols being aligned and overlapping sufficiently. Tick 'Inline composing' at this stage. Select composing function 'adaptive'. Go to *Inline > composing* and type 'cor_tirm' in series description.

5

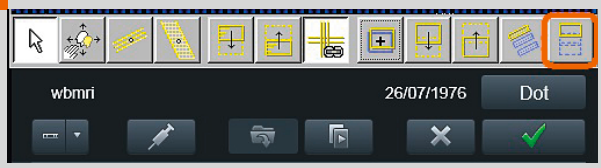

Figure 5: Tim Planning UI: 'Align FOV'

Coronal t1:
Siemens > abdomen > library > 3D > t1_vibe_dixon_cor

A turbo spin echo (TSE) pulse sequence could be considered for this acquisition, however volume interpolated breath-hold acquisition (VIBE) has some advantages. VIBE is faster and this is important in an examination that is already lengthy. It is possible to acquire on breath-hold (Dot Cockpit: double click on sequence, or in the queue: right mouse button > Edit Properties > Voice Commands) which results in less movement artifact particularly on the thorax and abdominal sub-protocols. The use of auto voice commands results in a more efficient workflow. It is also possible to re-construct up to 4 contrasts. Go to *Contrast > Common* and click on the 3 dots next to Dixon. Ensure in phase, out of phase, fat and water images boxes are ticked.

Change FOV to 500 mm and phase encoding direction F>>H. 68.8% FOV phase and 70% phase oversampling. Manipulate slice thickness and number of slices to ensure adequate coverage in the A-P direction. Create a copy reference to the cor tirm of 'centre of slice groups and saturation regions', and tick the boxes 'copy phase encoding direction' and 'steps'. Go to *Geometry > Tim Planning Suite* and tick 'Inline composing'. Select composing function 'adaptive'. Go to *Inline > composing* and type 'cor_t1' in series description.

Transverse DWI:
Siemens > whole body diffusion > general > standard > ep2d_diff_stir

For robust nulling of fat signal over a large FOV, a short tau inversion recovery (STIR) pulse is preferred over spectral adiabatic inversion recovery (SPAIR). As there are multiple

modifications to make, it is more efficient to do this to step 1 first and then add subprotocols rather than modifying every subprotocol. Therefore, go to *Geometry > Tim Planning Suite* and un-tick 'Set-n-Go Protocol' in order to reduce the number of steps to 1. Change FOV to 500 mm. It is optional to reduce the number of slices from 50 to 40. This results in a 200 mm (assuming 5 mm slice thickness with 0% distance factor) scan range in the Z direction per subprotocol resulting in the first and last slices being less distorted. Naturally, more subprotocols will be required to cover the same range in the slice direction, but this is offset by each subprotocol containing fewer slices and a lower minimum TR possible which reduces the acquisition time of each subprotocol. Crucially, the Maximum Intensity Projection (MIP) of the composed high b-value inverted window series will contain less step artefact. A bipolar double refocused spin echo diffusion encoding can be used rather than monopolar. Although bipolar will lead to a higher minimum TE and therefore lower signal-to-noise ratio (SNR) and longer TR (therefore increased acquisition time) distortions will be reduced [6].

6

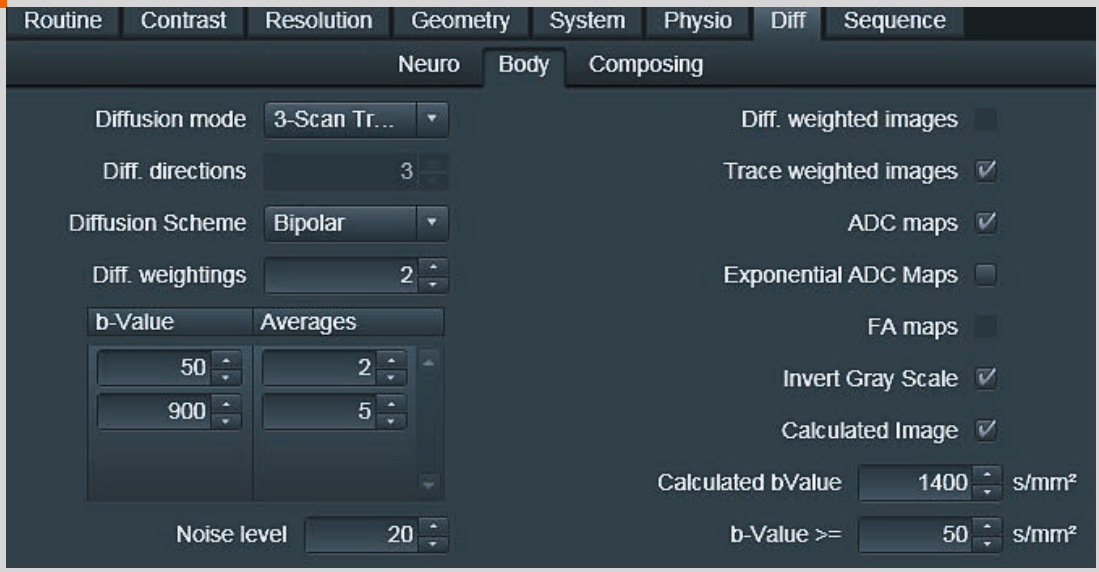

Figure 6: *Diff>Body*

In the *Diff>Body card* (Fig. 6), it is possible to define the required number of diffusion weightings and b-values. This is to be decided locally, but typically 2 diffusion weightings are acquired, for example b=50 and b=900 [7]. As the b-value increases, SNR is reduced. It is therefore advantageous to employ more averages on higher b-value images than lower b-value images. Ensure the boxes 'Trace-weighted images' and 'ADC Maps' are ticked. If a calculated b-value is required, tick the 'Calculated Image' box. The default calculated b-value is 1400 s/mm² but up to 1600 s/mm² can be calculated inline. Ensure 'Invert Gray Scale' is ticked. This will allow you to produce inverted MIP radial ranges from the composed high b-value images.

In resolution>filter image there is an option: dynamic field correction. This can be selected using 'direct' mode (click on the 3 dots next to the parameter option) in order to reduce eddy current induced distortions in diffusion-weighted images. There will be a small time penalty if this feature is used.

After modifying the sequence parameters, position the first subprotocol either above the vertex or at the level of the eyes. Click 'Add Subprotocol'. The subsequent subprotocol is positioned with an inferior offset which corresponds to the slice range -50 mm which ensures adequate overlap in the slice direction. Continue to 'Add Subprotocols' until the desired coverage has been achieved. Go to *Geometry > Tim Planning Suite* and ensure that 'Inline composing' is ticked and composing function is set to 'Diffusion'. Go to *Inline > composing* and type 'tra_DWI' in series description.

A wbmri Dot program can then be saved in the user tree by dragging and dropping the steps from the queue into a new program in the Dot Cockpit. In the patient view go to *Dot Add-In Configurator > GSP* and ensure GSP layout is set to Tim Planning UI and coupled graphics are on. This results in these settings being default every time the wbmri Dot program is used. The sequences should contain the required number of subprotocols and 'copy references' applied where appropriate. Although the initial program building can be intensive, the workflow for future examinations should be straightforward.

Figure 7: Example images (images are not all from the same patient):

- **(7A)** Sagittal T2
- **(7B)** Sagittal T1
- **(7C)** MIP of composed high b-value inverted transverse DWI
- **(7D)** Coronal TIRM
- **(7E)** Coronal VIBE 'in phase' image
- **(7F)** Coronal VIBE 'water' image
- **(7G)** Coronal VIBE 'out of phase' image

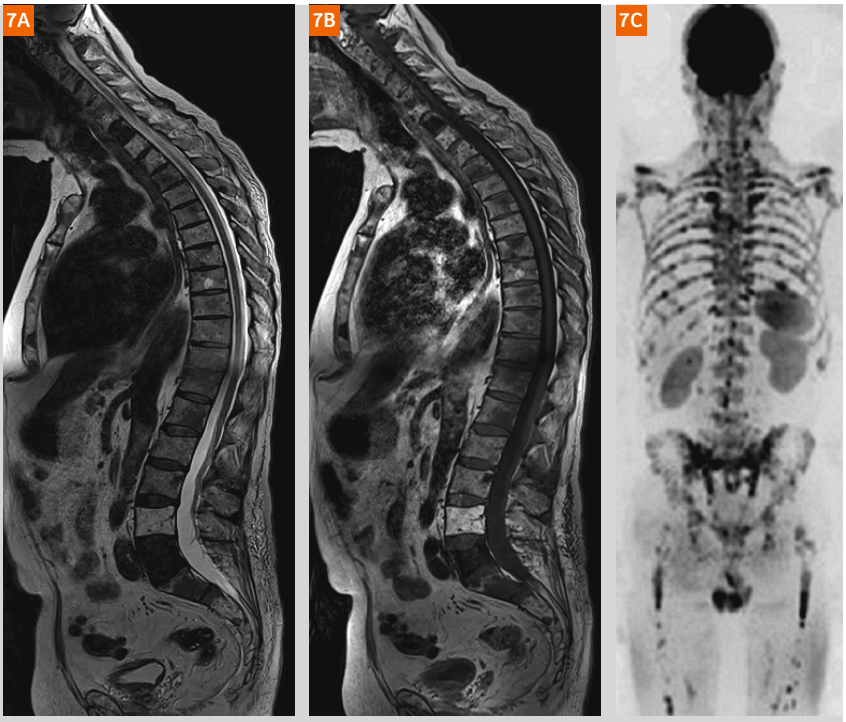

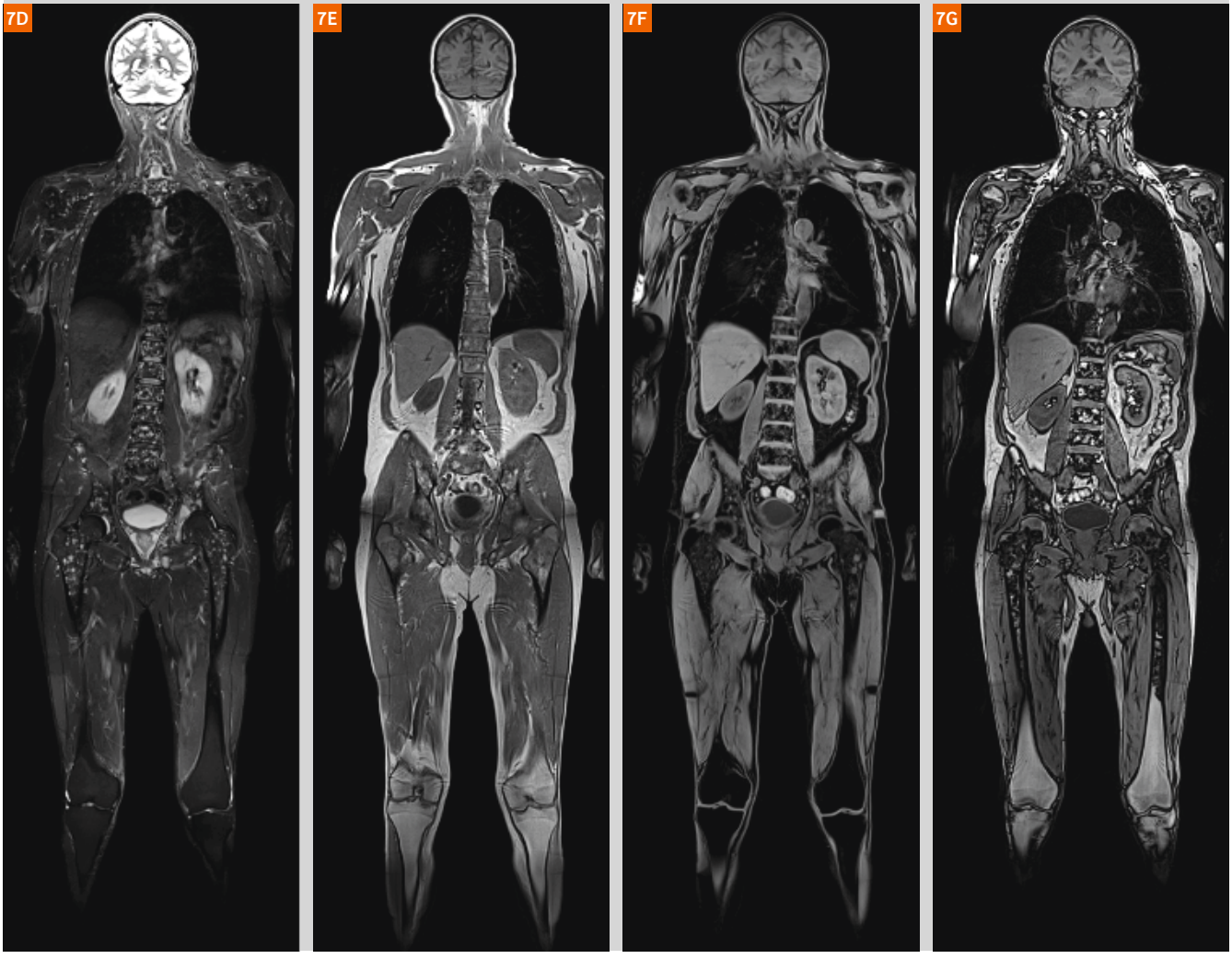

Results and post processing

The source images as well as the Inline composed images for all series must be available to the radiologist for reporting.

Select the composed transverse high b-value images from the patient browser or the viewing card. Load to 3D MIP and select the transverse image. Use 'radial ranges' to reconstruct a MIP series of images rotating around the Z axis. See Fig. 7C for example images.

The *syngo*.MR OncoCare package offers a histogram tool. It is possible to define a region-of-interest (ROI) around the spine. Then right click on the ROI and create the histogram. A threshold can then be set of what is accepted as pathology and what is accepted as normal tissue in order to predict metastatic load. This can then be mapped as a color overlay onto the tissue. This process can also be performed with the gray-scale images from the morphology scans and the ADC levels from the whole-body images.

Limitations

Some patients will be excluded on safety grounds e.g. implanted devices.

A proportion of patients will be unable to tolerate the procedure due to claustrophobia or discomfort.

It can be challenging to achieve adequate quality images of the humeri due to these structures being situated outside of the maximum 500 mm range in the X axis when the patient is positioned. It is possible to position the patient's arms anterior to the chest so they are not out of range in the X axis or to use an immobilisation device (e.g. velcro strap) to ensure that the patient's arms are as central as possible. However, patient comfort must also be considered and most examinations are performed with the patient in a comfortable position that they can maintain for the duration of the examination.

Conclusion

Inevitably whole-body MRI requests to the clinical MRI department will increase and therefore so will the pressure with regards to throughput. By building a wbmri program which employs Tim Whole Body Suite, Tim Planning Suite, Inline Composing and utilizing *syngo*.via for image reading it is possible to create an effective workflow for every step of the patient journey in order to maximize efficiency.

References

1 https://www.nice.org.uk/guidance/ng35/chapter/recommendations
2 Padhani, A.R., Douis, H. and Gall, P. (2012), Whole-Body Diffusion-Weighted MRI of the Bone Marrow in Health and Disease, MAGNETOM Flash, Vol 50, Issue 2 RSNA Edition, pp60-65.
3 Koh, D-M., Blackledge, M., Padhani, A.R., Takahara, T., Kwee, T.C., Leach, M.D. and Collins, S.J. (2012), Whole-Body Diffusion-Weighted MRI: Tips, Tricks and Pitfalls, American Journal of Roentgenology, Vol 199, pp252-262.
4 Smith, G. (2015), Using Remote Assist to Expand Your Expertise, MAGNETOM Flash, Vol 63, Issue 3 RSNA Edition, pp 87-89.
5 https://w5.siemens.com/web/ua/ru/medecine/detection_diagnosis/magnetic_resonans/035-15-MRI-scaners/MAGNETOM-Aera/Documents/mri_magnetom-aera_productbrochure_en-00044418.pdf
6 Furuta, A., Isoda, H., Yamashita, R., Ohno, T., Kawahara, S., Shimizu, H., Shibata, T. and Togashi, K. (2014), Comparison of Monoploar and Bipolar Diffusion Weighted Imaging Sequences for Detection of Small Hepatic Metastases, European Journal of Radiology, Vol 83 Issue 9, pp1626-1630.
7 Giles, S.L., deSouza, N.M., Collins, D.J., Morgan, V.A., West, S., Davies, F.E., Morgan, G.J. and Messiou, C. (2015), Assessing Myeloma Bone Disease With Whole-Body Diffusion-Weighted Imaging: Camparison With X-Ray Skeletal Survey by Region and Relationship With Laboratory Estimates of Disease Burden, Clinical Radiology, Vol 70, Issue 6, pp614-621.

Contact

David Hillier
Siemens Healthineers
Great Britain and Ireland (GB&I
HC WEA GBR SV CS BD AM MR

Mobile: +44 7808 828554
david.hillier@siemens.com

Simultaneous Multi-Slice – a Concise Review Covering Major Applications in Clinical Practice

Val M. Runge, M.D.; Johannes K. Richter, M.D.; Johannes T. Heverhagen, M.D., Ph.D.

Department of Diagnostic, Interventional and Pediatric Radiology, University Hospital of Bern, Inselspital, Bern, Switzerland

Introduction

When MR was originally introduced clinically, only single slice acquisition was possible. Rapidly thereafter, 2D multislice imaging was developed. This has remained a clinical standard for the last 30 years, being used in almost every patient exam. The term multislice however is somewhat misleading, since data for the individual slices is actually acquired sequentially during each TR. True simultaneous multislice (SMS) imaging was only recently introduced [1–3], and can be and is often combined with conventional 2D multislice imaging. SMS is likely the most significant technical development for clinical MR imaging in the current decade, enabling in its current implementation scan time to be reduced by a factor of two to three.

The technique was originally introduced for echo-planar imaging, but has subsequently been expanded as well to turbo spin echo (TSE) imaging. From a scientific point-of-view, higher order acceleration is also possible, with research currently focused in this area. As with many such developments in MR over the past decades, the application of the technique should be viewed more generally, for example in terms of providing higher SNR/time, as opposed to simply enabling scan time to be reduced. The higher SNR per unit time can be used to either shorten scan time (Fig. 1), acquire more slices in situations where these are limited by TR (Fig. 2), and/or to acquire high-resolution images (with complete anatomic coverage) in a reasonable scan time (Fig. 3).

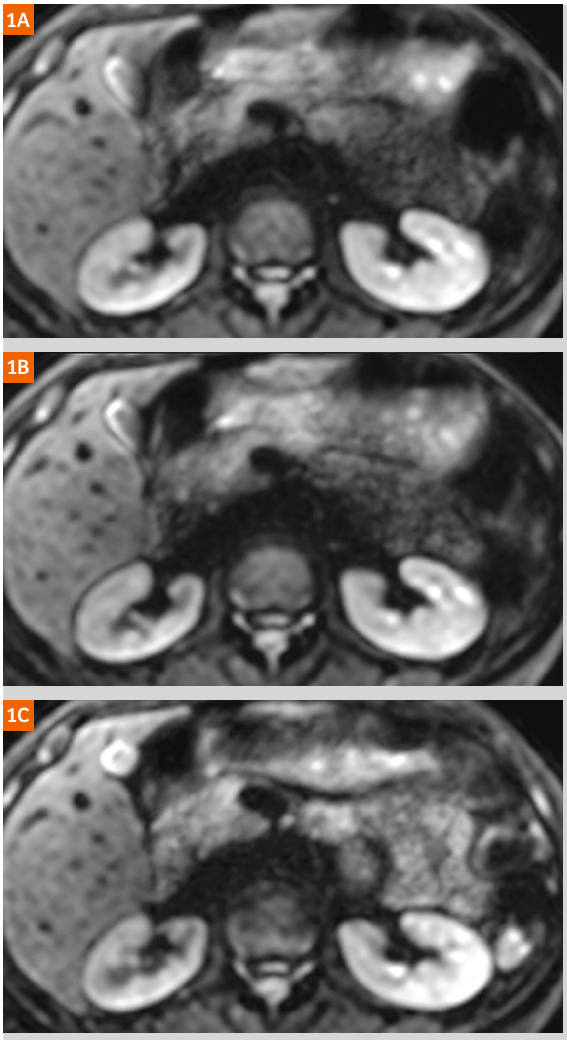

Figure 1: SMS in liver diffusion imaging, general principles. As illustrated, SMS in this instance can be used either to decrease scan time or to provide thinner sections with near equivalent image quality in a similar scan time.

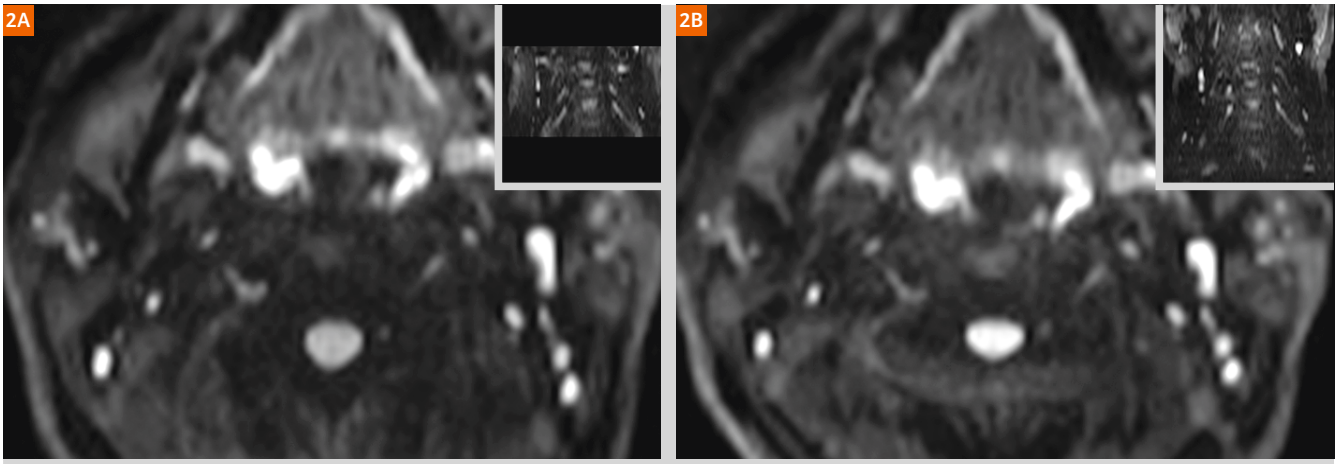

ss-EPI, b800, 3T, 1:45 min

SMS2 with increased cc coverage, 1:54 min

Figure 2: Application of SMS in head and neck diffusion-weighted imaging to provide complete anatomic coverage.

Figure 3: For brain thin section diffusion-weighted imaging, SMS can make complete anatomic coverage possible in a reasonable scan time. 2D ss-EPI DWI thin section scans are illustrated, with the sagittal reformats (inserts) revealing the anatomic coverage achieved without and with SMS.

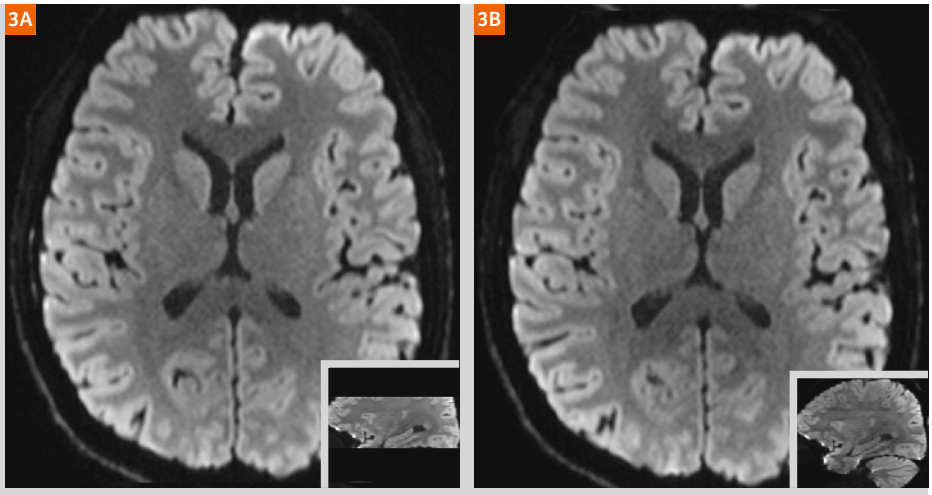

no SMS, 0.6 x 0.6 x 0.8 mm^3, 5:03 vs

SMS2, 5:15 (TA)

SMS would not have been possible without prior important technological advances in both MR hardware and software, including specifically multicoil arrays, CAIPIRINHA and slice-GRAPPA reconstruction. It also can be, and typically is, implemented clinically in combination with more conventional parallel imaging. Its implementation in 2D echo-planar imaging (EPI) sequences is possible because diffusion encoding, which requires a significant portion of the acquisition time, is performed for the whole imaging volume with each single slice excitation. Because fewer total slice excitations (with the simultaneous excitation of two or three slices each time) are needed to cover the anatomic area of interest, TR can be reduced and thus the scan accelerated. SMS has been implemented for both single shot (ss) EPI and readout segmented (rs) EPI [4]. The latter implementation is particularly important because of the longer scan time required for rs-EPI when compared to ss-EPI. Subsequent to its implementation for EPI, SMS was extended to turbo spin echo sequences. Here, like with EPI, if TR can be shortened, SMS can be implemented in this way to accelerate the scan. However, another perhaps more important application is for TSE scans in which two or more concatenations are required to obtain the necessary number of slices. In this instance, SMS can be used to acquire the desired number slices in a single concatenation, and thus a reduction in scan time.

Several important advances in pulse sequence design were necessary to make SMS a clinical reality. Improved unaliasing of the simultaneously acquired yet closely spaced slices was required. This was made possible, for example for single shot sequences, by the use of a blipped CAIPIRINHA approach [5] which avoids the high g-factor (SNR) penalty

and blurring associated with previous techniques. Specialized reconstruction techniques are also used to reduce signal contamination between the simultaneously acquired slices. The multiband RF pulses, which allow for simultaneous excitation and refocusing of multiple slices, also increase specific absorption rate (SAR). Implementation with low SAR variable-rate selective excitation (VERSE) pulses provides adequate SAR reduction.

The applicability of SMS to routine clinical practice is broad and includes almost every anatomic region [6, 7]. The scans in this article were all acquired at 3T. In the head, SMS can increase throughput by reducing scan times, at the same time decreasing the impact of inadvertent patient motion (Fig. 4). If the thin sections are desired through the entire brain, whether with diffusion-weighted or T2-weighted scans, SMS makes this clinically feasible, with reasonable scan times (Fig. 5). In breast imaging, SMS reduces the scan time needed for diffusion imaging, which is required today in evaluations for breast cancer (Fig. 6) [8]. In body imaging the acquisition of axial diffusion-weighted scans is now routine, for example in the liver, with SMS enabling a decrease in scan time [9]. However, depending on the area of interest and the required coverage in the z-dimension, both the application of SMS to reduce slice thickness (yet maintain coverage and image quality) as well as the application to cover larger regions in the z-dimension are important (Fig. 7). Not yet mentioned in regard to diffusion-weighted imaging, the image quality of ADC maps is maintained with SMS, being largely a reflection of SNR and potential artifacts (Fig. 8). For musculoskeletal imaging, in many instances high-resolution images are desired, with SMS permitting their acquisition in a more reasonable scan time (Figs. 9, 10). However, often there are time pressures, due to either the condition of the patient or throughput needs, with the application of SMS in this situation geared to making scans faster (Fig. 11).

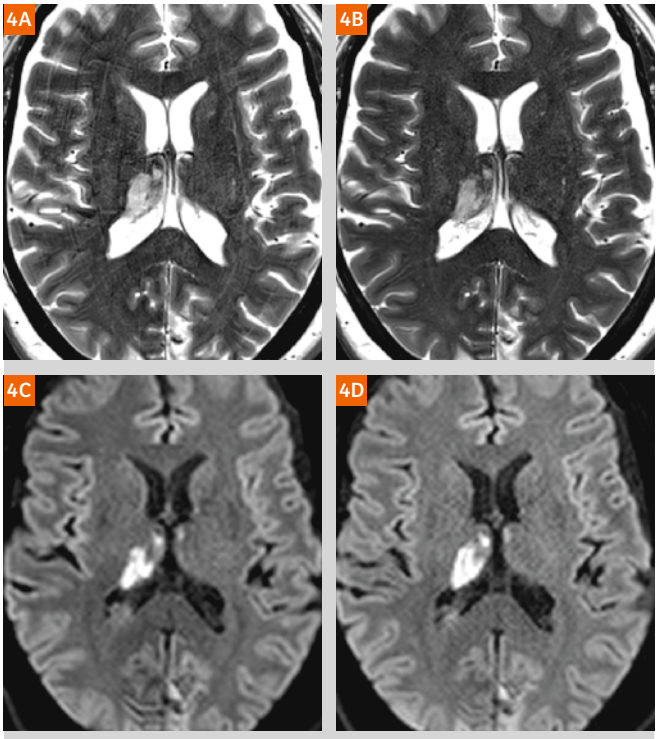

Figure 4: Thalamic infarct, **(4A, B)** T2-weighted TSE and **(4C, D)** diffusion-weighted ss-EPI scans. **(4A, C)** Conventional acquisition compared to **(4B, D)** SMS, the T2-weighted scan with an acceleration factor of three and the DWI with a factor of two. Note the ghosting and image degradation on the conventional T2-weighted scan due to the longer acquisition time. The SMS T2-weighted scan in this instance is superior and the SMS DWI scan equivalent in terms of image quality to the scans acquired in a conventional fashion.

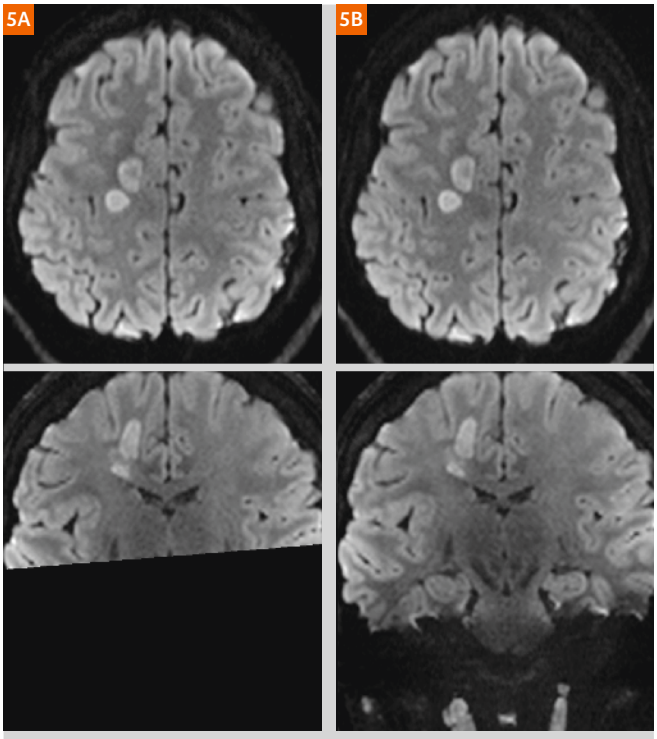

Figure 5: Multiple sclerosis, thin section high resolution 2D ss-EPI DWI without **(5A)** and with SMS **(5B)**. The specific techniques used and scan times are similar to that of Figure 3. Note that SMS permits complete coverage of the brain, as illustrated by the reformatted coronal sections.

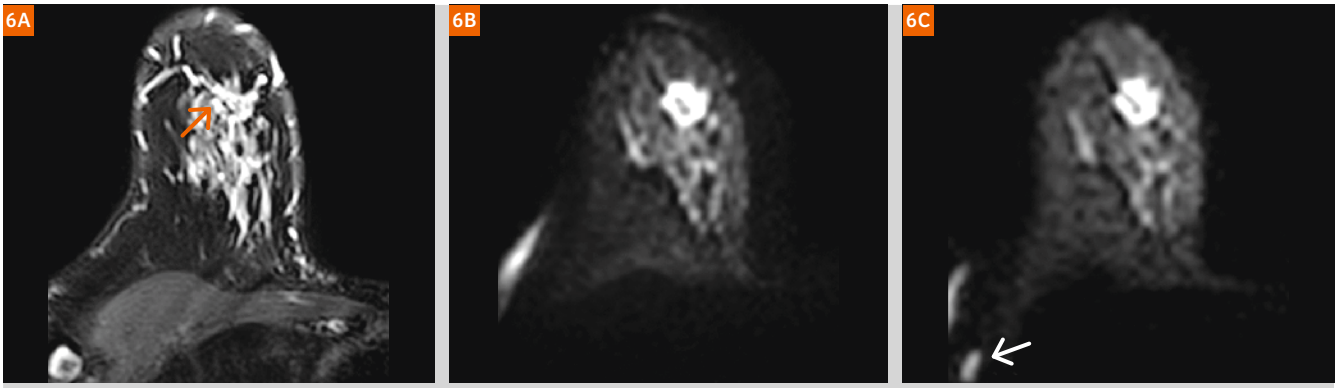

Figure 6: Breast imaging, utilizing SMS for decreased scan time in the acquisition of diffusion-weighted images. A spiculated, hyperintense lesion **(6A**, orange arrow) highly suspicious for malignancy is noted on the T2-weighted scan in the right breast. **6B**, The conventional single-shot DWI sequence acquired with a selective field-of-view (zoomed), for faster speed and decreased susceptibility artifacts as well as geometric distortion, is compared with **(6C)** the SMS (acceleration factor of 2) rs-EPI diffusion-weighted scan. The tumor, with restricted diffusion (high signal intensity) is similarly depicted, with scan time decreasing from 5:52 to 3:17 min. On the rs-EPI scan, the metastatic lymph node in the right axilla (white arrow) can also be visualized, which is not depicted in 6B due to residual susceptibility issues/ geometric distortion.

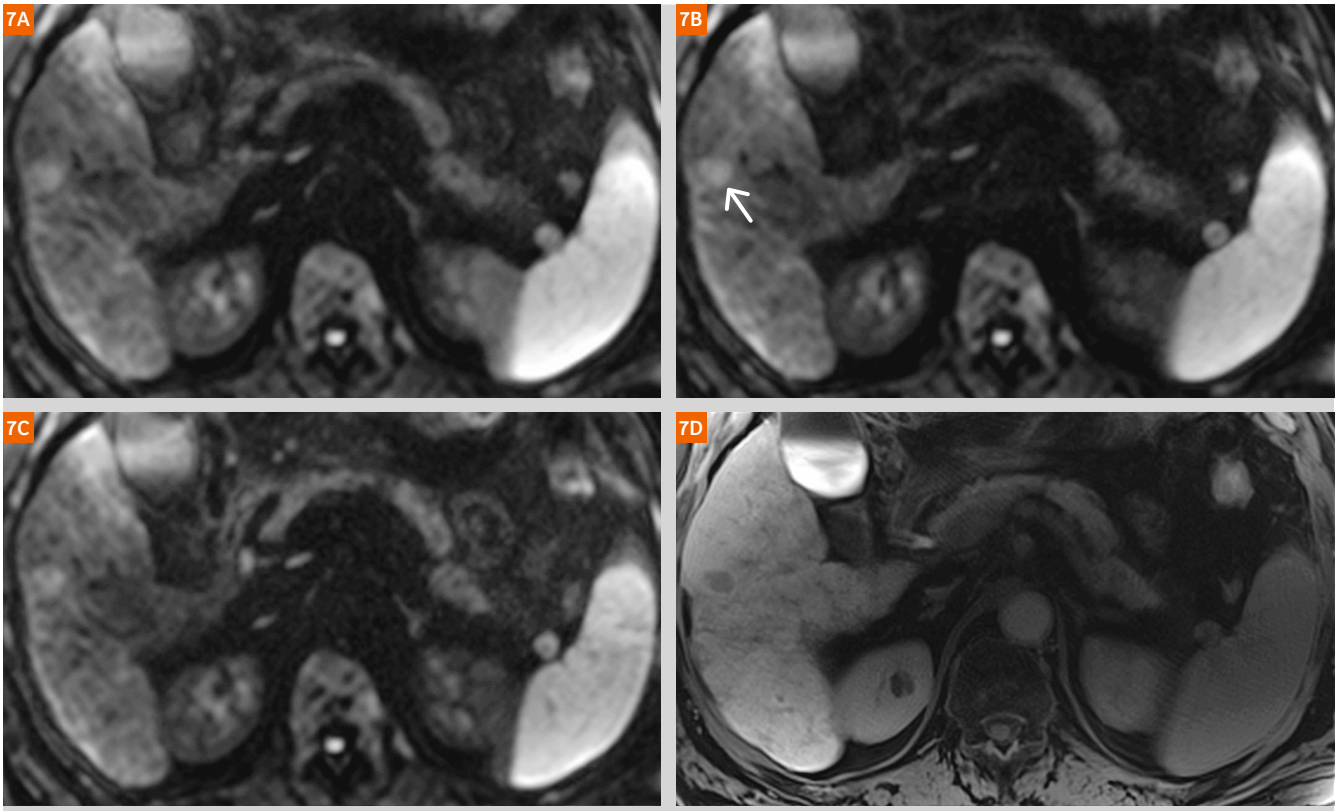

Figure 7: 2D ss-EPI DWI SMS in the liver for shorter scan acquisition or alternatively thinner sections. DWI scan times were **(7A)** 2:41 min (non-SMS), **(7B)** 1:38 min, and **(7C)** 2:54 min (both SMS with a 2 fold acceleration). The slice thickness in 7A and B was equivalent (5 mm), with 7C performed using a thinner slice (3 mm), and complete liver coverage with all scans. A small HCC with restricted diffusion (arrow) is noted. The lesion is also well seen on delayed imaging after gadoxetic acid administration, in **(7D)** a non-breath-hold 2-minute acquisition radial VIBE scan.

SMS can be applied today to both DWI and TSE techniques, with great utility. Immediate applications include brain, axial spine, breast, abdomen, whole body and musculoskeletal imaging. An important decision tree in terms of its specific use in any patient is whether to employ the technique to decrease scan time, or to provide high-resolution images without significantly prolonging scan time, or to enable a larger number of slices to be acquired.

Acknowledgment

Portions of this article are excerpted with permission from "The Physics of Clinical MR Taught Through Images", 4th edition, 2018, Thieme. Figures 6–7 and 9–10 are reprinted with permission, together with some excerpted text, from Runge VM, Richter JK, Heverhagen JT. Speed in Clinical Magnetic Resonance. Invest Radiol. 2017;52(1):1–17.

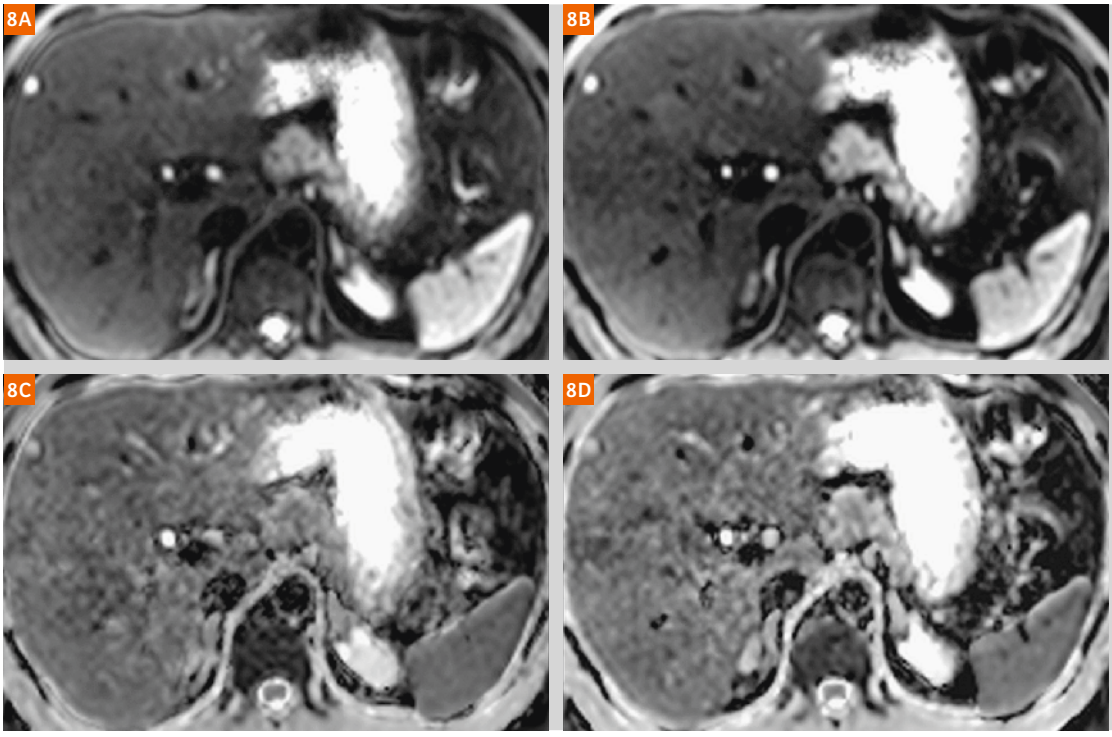

Figure 8: Small hepatic cysts. Liver DWI, **(8A, C)** no SMS in comparison to **(8B, D)** SMS 2, b-value 800 s/mm² top, ADC bottom. Scan times were 4:14 vs 2:31 min, with the same anatomic coverage (number of slices) for both scans and complete liver coverage (using a 4 mm slice thickness).

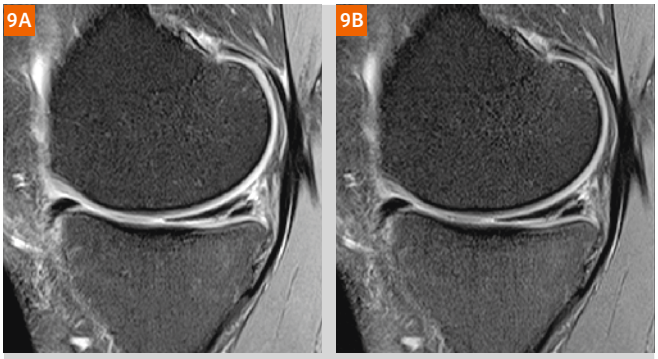

Figure 9: Sagittal proton density-weighted images of the knee demonstrate a horizontal tear of the posterior horn of the medial meniscus on high resolution images **(9A)** without and **(9B)** with SMS (2 fold acceleration). Image quality and SNR are essentially equivalent, with a reduction in scan time from 6:36 to 3:27 min.

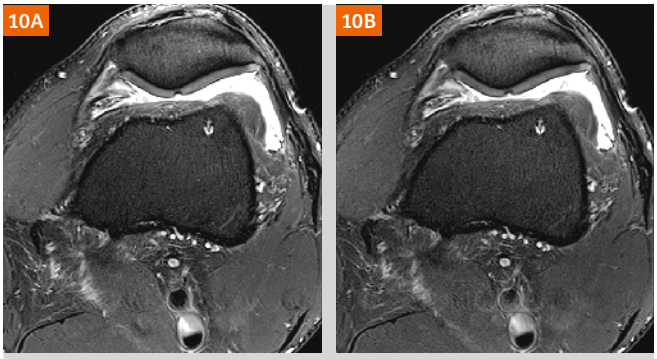

Figure 10: Axial TSE T2-weighted scans of the knee at 3T depicting patellar cartilage damage, in a patient with prior medial collateral ligament and anterior cruciate ligament surgery, on images **(10A)** without and **(10B)** with SMS (2 acceleration). Image quality is equivalent, with SMS allowing a reduction in scan time from 7:14 to 3:48 min. In plane resolution is 0.4 x 0.4 mm².

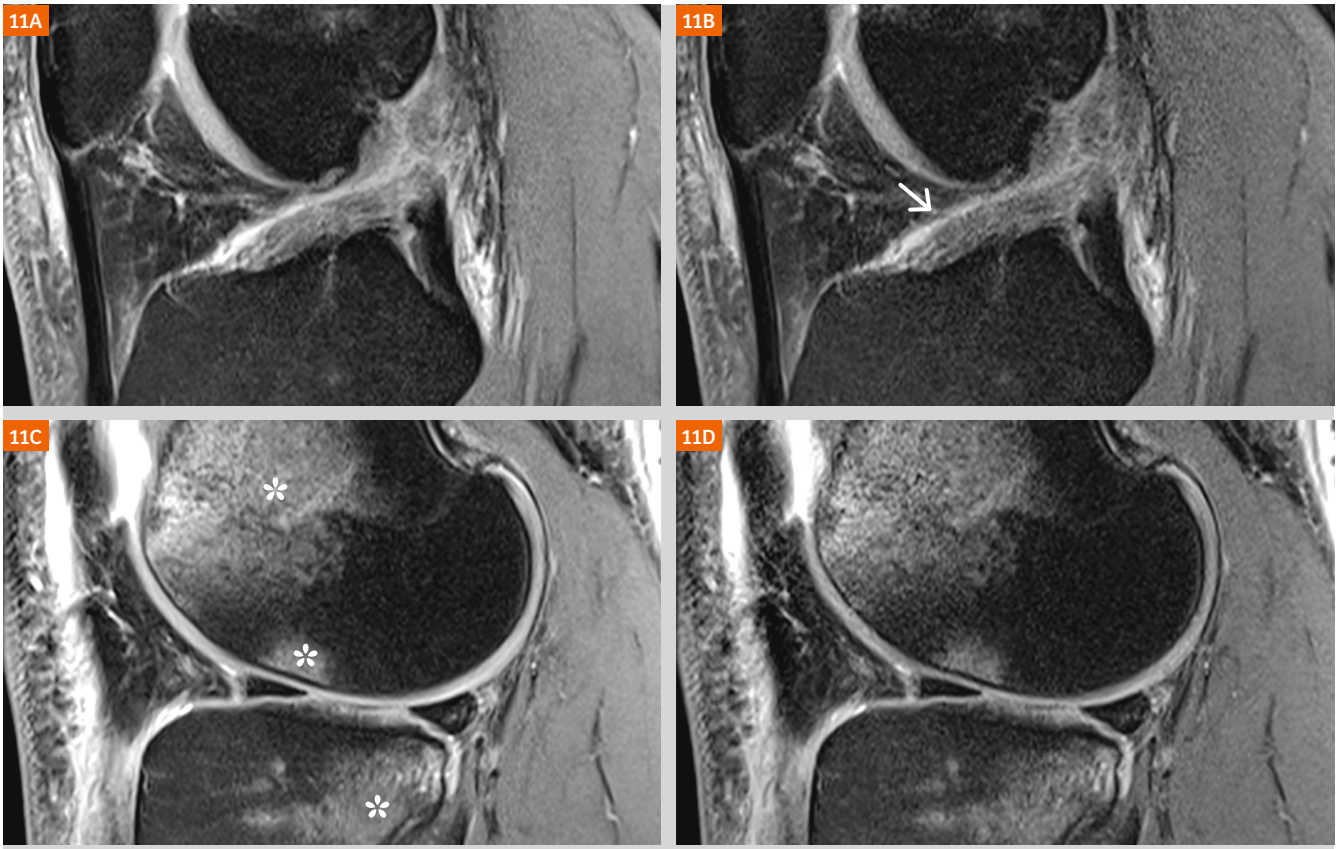

Figure 11: The use of SMS for short scan times in a trauma patient. A ruptured anterior cruciate ligament (arrow) is seen on **(11A and B)** sagittal proton density-weighted images acquired at 3T, together with **(11C and D)** bone marrow edema (asterisks) of the distal femur, lateral femoral condyle, and posterolateral tibial plateau. Depiction is essentially equivalent on the scans **(11A and C)** without and **(11B and D)** with SMS. The SMS scan, due to use of 2 accelerations, required only 1:34 min for acquisition, approximately half that for the non-SMS scan.

References

1 Breuer FA, Blaimer M, Heidemann RM, Mueller MF, Griswold MA, Jakob PM. Controlled aliasing in parallel imaging results in higher acceleration (CAIPIRINHA) for multi-slice imaging. Magn Reson Med. 2005;53(3):684-91.
2 Setsompop K, Cohen-Adad J, Gagoski BA, et al. Improving diffusion MRI using simultaneous multi-slice echo planar imaging. Neuroimage. 2012;63(1):569-80.
3 Feinberg DA, Setsompop K. Ultra-fast MRI of the human brain with simultaneous multi-slice imaging. J Magn Reson. 2013;229:90-100.
4 Frost R, Jezzard P, Douaud G, Clare S, Porter DA, Miller KL. Scan time reduction for readout-segmented EPI using simultaneous multislice acceleration: Diffusion-weighted imaging at 3 and 7 Tesla. Magn Reson Med. 2014;74(1):136-49.
5 Setsompop K, Gagoski BA, Polimeni JR, Witzel T, Wedeen VJ, Wald LL. Blipped-controlled aliasing in parallel imaging for simultaneous multislice echo planar imaging with reduced g-factor penalty. Magn Reson Med. 2012;67(5):1210-24.
6 Barth M, Breuer F, Koopmans PJ, Norris DG, Poser BA. Simultaneous multislice (SMS) imaging techniques. Magn Reson Med. 2016;75(1):63-81.
7 Runge VM, Richter JK, Heverhagen JT. Speed in Clinical Magnetic Resonance. Invest Radiol. 2017;52(1):1-17.
8 Taviani V, Alley MT, Banerjee S, et al. High-resolution diffusion-weighted imaging of the breast with multiband 2D radiofrequency pulses and a generalized parallel imaging reconstruction. Magn Reson Med. 2017;77(1):209-20.
9 Taron J, Martirosian P, Erb M, et al. Simultaneous multislice diffusion-weighted MRI of the liver: Analysis of different breathing schemes in comparison to standard sequences. J Magn Reson Imaging. 2016;44(4):865-79.

Contact

Val M. Runge, M.D.
Editor-in-Chief, Investigative Radiology
Department of Diagnostic, Interventional and Pediatric Radiology
University Hospital of Bern, Inselspital

Freiburgstrasse 10
3010 Bern
Switzerland
ValMurray.Runge@insel.ch

Chest MRI: Morphological Imaging and Beyond

Pierluigi Ciet[1,2,3]; Harm A W M Tiddens[1,2]; Giovanni Morana[3]

[1] Department of Radiology and Nuclear Medicine, Erasmus Medical Center, Rotterdam, The Netherlands
[2] Department of Pediatrics, Respiratory Medicine and Allergology, Sophia Children's Hospital, Erasmus Medical Center, Rotterdam, The Netherlands
[3] Department of Radiology, Ca' Foncello Regional Hospital, Treviso, Italy

Chest MRI for morphological imaging in cystic fibrosis

Chest MRI is intrinsically limited by several technical factors which affect image quality [1]. These limitations make comparison with computed tomography (CT) regarding morphological imaging somewhat biased. CT has undoubtedly higher spatial resolution than MRI and shorter acquisition times, which makes it the first choice for thoracic imaging [2]. In addition the long track record of chest CT has made it the current gold standard in clinical practice both as diagnostic and monitoring tool [3–5].

Conversely, chest MRI has been in development for only two decades, after the introduction of new techniques, which have allowed to obtain reasonable image quality in acceptable scan time [6]. The major driving force to develop chest MRI is its application for lung diseases requiring repeated imaging and where cumulative radiation dose related to the use of chest CT is considered an important limitation [7, 8]. One of these lung diseases is cystic fibrosis (CF), the most common hereditary disorder in Caucasians [9]. Patients with CF suffer of chronic lung infection and inflammation that starts in early childhood [10]. Repeated imaging is needed to efficiently monitor and to direct therapy in CF lung disease [11]. Several studies have shown that CT is more sensitive than pulmonary function tests to detect disease progression in CF [12]. At the same time, it is clear that, although small, the risk related to repeated scans cannot be ignored [8]. Some studies in large cohort populations have shown an increased incidence of radiation-induced cancers related to the use of CT imaging [13]. Even though the range of radiation dose registered in these cohort studies is clearly higher than those used in chest CT imaging for CF, the risk cannot be totally eliminated by reducing the dose, due to the stochastic nature of the damage caused by ionizing radiation [8]. Moreover, this risk is even higher in young children[1], who have higher radiation sensitivity than adults [14].

For these reasons, almost ten years ago the first studies were conducted comparing image quality of chest MRI to CT. In a cross sectional study of Puderbach et al., an MRI protocol using Half-Fourier single-shot turbo spin-echo (HASTE, Siemens Healthcare, Erlangen, Germany) sequence showed good comparability with CT to detect specific CF lung disease related to morphological findings, such as bronchiectasis, mucus plugging, bullae/cysts, and collapse/consolidation [15]. However, HASTE showed lower ability to correctly classify the severity of bronchiectasis, bronchial wall thickening and trapped air [15]. In a second study conducted by Failo et al. using a steady state free precession (SSFP, General Electric, Boston, MA, USA) MRI protocol, similar results were shown [16]. In particular it became clear that there was a systematic underestimation of the severity of lung damage by MRI relative to CT due to poor visualization of peripheral bronchiectasis [16]. Similarly MRI was less sensitive to detect trapped air relative to CT [16]. Rajaram et al. showed that SSFP MRI was inferior to CT in imaging parenchymal lung disease [17]. One limitation of these studies was the conventional Cartesian *k*-space acquisition scheme used [18]. The Cartesian geometry is inherently prone to motion-induced phase distortions, thus is more sensitive to breathing and cardiac artifacts than non-Cartesian (i.e. helicoidal, radial, etc.) acquisition [19]. Non-Cartesian *k*-space sequences, such as radial (StarVIBE, Siemens Healthcare) and helical (BLADE, Siemens Healthcare) are characterized by greatly reduced sensitivity to motion compared to previous fast spin-echo and gradient-echo sequences [20].

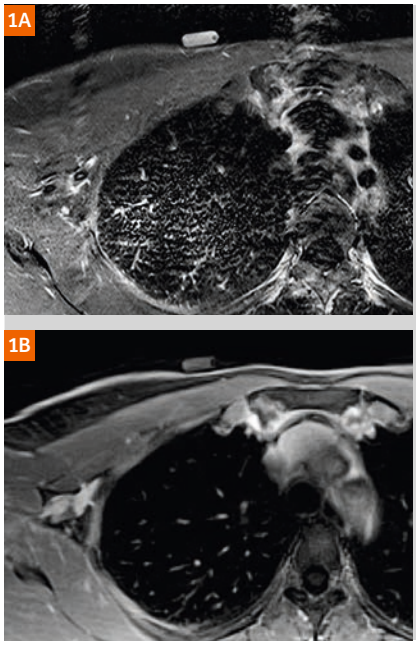

Figure 1: Normal lung: comparison of conventional contrast-enhanced TSE **(1A)** and StarVIBE **(1B).** The radial acquisition of *k*-space is able to greatly reduce the respiratory artifacts even in a free-breathing acquisition. *(Images courtesy of H. Chandarana, NYU)*

[1] MR scanning has not been established as safe for imaging fetuses and infants under two years of age. The responsible physician must evaluate the benefit of the MRI examination over other imaging procedures.

To test if this new type of sequences are superior to conventional MRI sequences, we conducted a study where we compared the PROPELLER (Periodically Rotated Overlapping ParallEL Lines with Enhanced Reconstruction, General Electric; BLADE, Siemens Healthcare) sequence to CT [21]. PROPELLER is a free-breathing Turbo Spin-Echo sequence with non-Cartesian *k*-space acquisition scheme (radial) [22]. The main finding of our study was that despite this lower sensitivity to motion, PROPELLER MRI was still inferior to CT [23]. In particular, we found that compared to CT, PROPELLR MRI tended to underestimate CF findings for mild CF disease and to overestimate for severe CF disease [23]. A second important positive finding of our study was the high specificity of MRI for CF findings, which justifies its use for short or long term monitoring of specific CF lung disease alteration. [23] (Fig. 2).

Recently a study using a multi-sequence MRI protocol – including HASTE, BLADE, volumetric interpolated breath-hold examination (VIBE) and time-resolved angiography with stochastic trajectories (TWIST) – showed good agreement with CT, although scoring was performed in consensus, and therefore intra- and inter-reader variability were not assessed [24].

To date all the sequences tested so far for CF lung imaging were limited by low signal-to-noise ratio (SNR) because of long echo times (TE) [1]. To overcome this limitation, ultra-short or zero-TE (UTE/ZTE) sequences (microseconds "µs" instead of milliseconds "ms") have been recently developed and tested in CF disease, showing better results compared to conventional sequences [25, 26]. Unfortunately, these UTE/ZTE sequences require long acquisitions times, because they are performed under free-breathing conditions; hence reproducibility is affected by patient performance.

It is important to note that, all the aforementioned studies were based on a single center experience. The primary and most obvious limitation of single-center studies is their potentially limited external validity. Especially the clinical value of MRI single center studies is limited as standardization across MRI vendors and centers is difficult [27]. This lack of standardization still remains the main limitation in the implementation of chest MRI as a tool for routine clinical care [28]. To date no multi-vendor studies have been published, mostly because of the large variability in MRI performance among vendors or even between similar scanners of the same vendor. In a recent study presented at the International Society of Magnetic Resonance in Medicine (ISMRM), variation up to 40% were registered in SNR for the same sequence (same scan parameters) performed in different scanners [29].

Beyond morphological imaging

One of the major advantages of MRI over CT is its multi-parametric imaging capability and superior tissue characterization. For instance T2-weighted sequences are important to identify fluid-containing structures, such as cysts or pleural effusions, while PD-weighted sequences are appropriate for airway imaging and trapped air assessment [1]. Moreover, while it is quite clear that MRI will not be able to obtain the same performance of CT in morphological imaging, MRI has high potential in functional imaging of the lung. Several MRI techniques can be used to obtain functional information about Ventilation, Inflammation, Perfusion, and Structure (VIPS) [21].

Assessment of inflammation in CF

In a cross-sectional study in patients with CF, we used diffusion-weighted MRI to assess inflammation [30]. Inflammation is a major component of CF lung disease

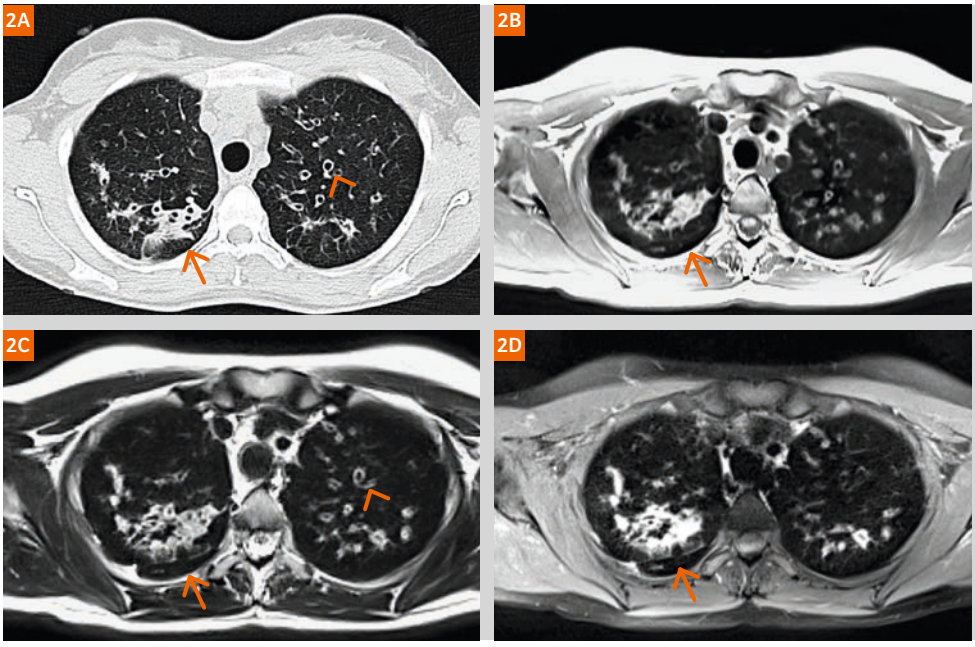

Figure 2:
CF patient. **(2A)** Axial end-inspiratory CT, **(2B)** axial end-expiratory navigator-triggered BLADE T1-weighted, **(2C)** axial end-expiratory navigator-triggered BLADE T2-weighted and **(2D)** axial end-expiratory navigator-triggered BLADE PD-weighted.

Please note the bronchiectasis with mucus plugging and peribronchial consolidation in RUL (arrow in 2A) clearly detected in all three MRI scans (arrows in 2B-D). Interestingly, bronchial wall thickening (arrowhead in 2A) is better depicted in the T2-weighted scan (arrowhead in 2C).

leading to progressive damage of lung structure [31]. The vicious cycle of infection, inflammation and damage determines those structural changes (i.e. bronchiectasis), which facilitate chronicity of infection [32]. CF patients face a state of chronic inflammation that increases during respiratory tract exacerbation (RTE). Different methods to assess lung inflammation have been evaluated so far. Several blood markers have been proposed, but they have shown low sensitivity and low clinical utility. Among pulmonary function tests, Lung Clearance Index (LCI) and Fractional exhaled Nitric Oxide (FeNO) have been used to assess inflammation [33, 34]. However both LCI and FeNO showed high variability and limited ability to provide regional information on inflammation [35, 36]. Regarding imaging, PET-CT has been also used to show persistent foci of inflammation in patients with CF, but its use is restricted by high radiation exposure [37]. Therefore, to date no radiation-free techniques were available to quantify and localize lung inflammation.

For the first time, we proposed DW-MRI as feasible technique to localize and quantify inflammation in patient with CF [30]. The major finding of this cross-sectional study performed in a group of stable patients with CF was that DW-MRI showed foci of high signal intensity ('hotspots') which only in part overlapped with structural lung changes on morphological CT or MRI [30]. We also observed that DW-MRI had a strong correlation with radiological and clinical parameters indicating CF lung disease severity [30]. In addition, there were significant differences in pulmonary function testing (PFT) parameters between patients with and without DW-MRI hotspots [30].

Based on these results, we decided to validate DW-MRI in a cohort of CF patients with and without respiratory tract exacerbations (RTE) (unpublished data). The most interesting observation of this study was that DW-MRI could track inflammatory changes over the course of RTE treatment. In patients with RTE, DWI signal at high b-values showed an overall significant reduction following antibiotic treatment (Fig. 3), while in the control group no significant differences in DWI signal between baseline and follow-up were observed. Interestingly, the morphological score (CF-MRI) was significantly different between the RTE and control groups both at baseline and follow-up. Therefore CF-MRI score was not able to detect patients with RTE. The other important finding was the fair to good accuracy of DW-MRI to differentiate patients with CF treated for a RTE. The final important finding of this study was the low intra- and inter-observer variability of DW-MRI, which supports the robustness of this method in clinical trials focused on RTE treatment.

Assessment of perfusion in CF

It is well known that structural changes affecting lung ventilation determine a reduction of lung perfusion according to the hypoxic-vasoconstriction reflex. This principle was demonstrated a decade ago by Eichinger et al., showing that areas of hypoperfusion (HP) matched areas of structural changes using contrast-enhanced MRI (CEMRI). Despite this study, CEMRI was not widely introduced in clinical practice. This likely happened because the technique at that time was not robust. Large variability between observers was a common problem, and only highly trained radiologists could provide reproducible results. Moreover no automated software tools for lung segmentation or perfusion quantification were available.

A recent study renewed interest on CEMRI. Wielpütz et al. showed that HP is a common entity in mild CF disease, and that it can be reversed after treatment for RTE exacerbation [38]. The findings of this study supported the use of CEMRI as an imaging biomarker in CF patients. Recently we conducted a study using CEMRI, where we aimed to study the relationship between HP and trapped air (TA). In addition we evaluated the relation between TA assessed by CEMRI and CT and PFT. The main finding of our study was that HP was more frequent and severe than TA in patients with early CF disease. We also confirmed that expiratory CT detects more TA than expiratory MRI. From our study it became clear that the term TA is a misnomer, and that hypodense regions on CT and hypo-intense regions on MRI would be better described by the terms low-density region (LDR) and low-intensity region (LIR) respectively [39].

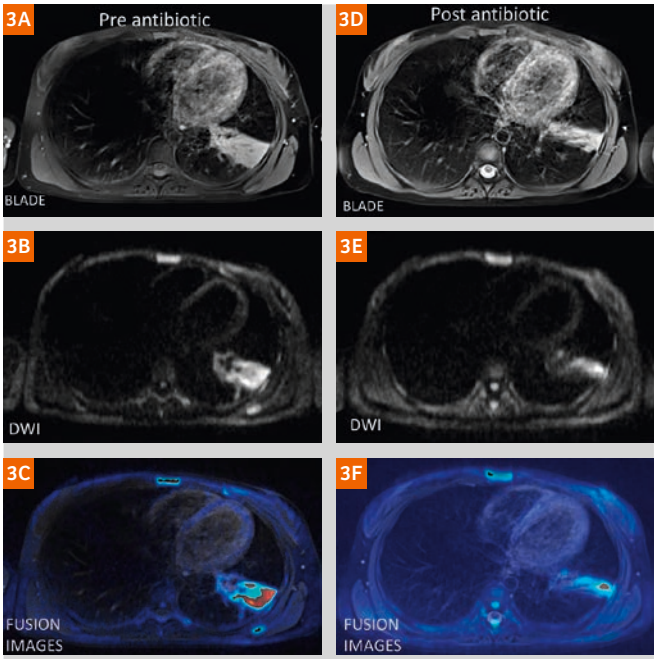

Figure 3: CF patient with pulmonary exacerbation, MRI pre (left column) and post (right column) intravenous antibiotic treatment. **(3A, D)** axial BLADE PD-weighted end-expiratory navigator triggered; **(3B, E)** axial DWI b=800 and **(3C, F)** FUSION image (DWI superimposed to BLADE). Note that between first and second MRI scan there is not only a reduction of the left lower lobe consolidation but also a consensual reduction of DWI signal (arrows in 3C, F).

The higher prevalence of HP compared to TA in CF patients suggests that other factors play a role in addition to the hypoxic-vasoconstriction reflex. One of these factors might be inflammation, as suggested by the findings of Wielpütz et al., that lung perfusion improved after RTE treatment [38]. It would be also interesting to investigate whether reversibility of TA/HP is restricted only to mild CF patients or it would occur in more advanced disease as well.

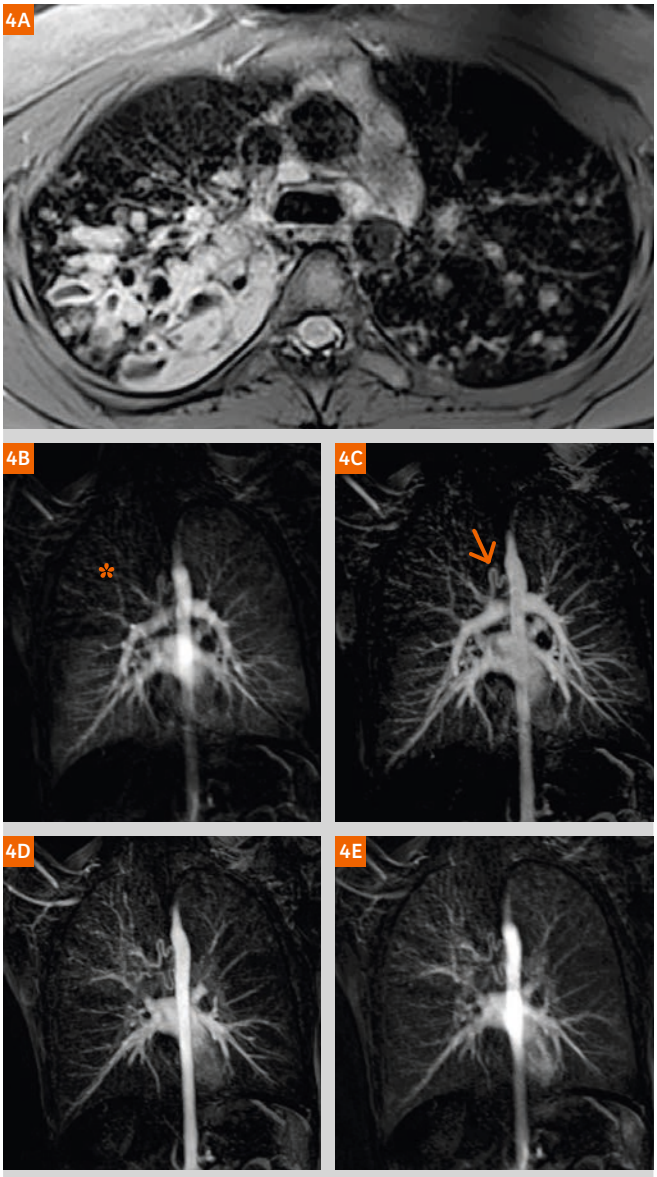

Figure 4: 17-year-old female CF patient. **(4A)** BLADE: a severe involvement of the upper right lobe is appreciable, with large bronchiectasis. With time-resolved MR Angiography (MRA) a large area of hypoperfusion (*) can be appreciated in the upper right lobe in the pulmonary phase **(4B),** where an hypertrophic bronchial artery can be appreciated, better in the maximum intensity projection (MIP) in the early **(4C)** and late **(4D)** arterial phase (arrow in 4C). With partial volume rendering reconstruction in the late arterial phase **(4E),** the upper right lobe shows a persistence of contrast medium from bronchial artery.

Moreover, in many chronic lung diseases, pulmonary circulation is reduced or occluded at the level of the pulmonary arterioles because of hypoxic vasoconstriction, intravascular thrombosis, and vasculitis [40]. As a result, bronchial arteries proliferate and enlarge to replace the pulmonary circulation. The enlarged bronchial vessels, which exist in an area of active or chronic inflammation, may be ruptured due to erosion by a bacterial agent or due to elevated regional blood pressure. The arterial blood under systemic arterial pressure subsequently leaks into the respiratory tree, resulting in massive hemoptysis. Thus, the ability of CEMRI to appreciate the hypertrophy of bronchial circulation in the affected lung, can significantly improve the management of these patients (Fig. 4).

Finally other non-contrast techniques such as Fourier Decomposition (FD)[2] or Arterial Spin Labeling (ASL) might be further developed in order to obtain information about perfusion without contrast administration [41, 42].

Assessment of ventilation

Ventilation imaging with MR can be performed with several techniques. The most studied technique for ventilation imaging is that with hyperpolarized gas MRI [43]. Hyperpolarized gas MRI uses gaseous contrasts based on helium (3He) and xenon (129Xe) to provide high resolution images of pulmonary ventilation, microstructure and gas exchange [43]. Despite the great potential of this technique, its high complexity and cost of the noble gasses and the need of dedicated hardware limits its application in clinical practice [44]. A more feasible and promising technique is oxygen-enhanced MRI, which uses the paramagnetic effect of oxygen to shorten T1 relaxation times obtaining maps of the oxygen distribution in the lung [45, 46]. Oxygen-enhanced MRI has been already used and tested in patients with asthma and chronic obstructive pulmonary disease [46, 47]. Even though the technique is cheaper and more available than hyperpolarized gases MRI, it has been not yet transferred in clinical practice because of its long acquisition times (5-30 min) [43]. The most promising technique for ventilation MRI is a non-contrast SSFP-based sequence that provides ventilation and perfusion maps [48]. This technique for ventilation MR imaging technique is FD, a free-breathing technique that does not use gaseous or intravenous contrast agents. FD has been already validated in healthy volunteers and patient with CF [41, 49] (Fig. 5).

MRI to assess central airways mechanics

We have developed an MRI protocol to assess central airways dynamics [52]. Central airways are routinely assessed with bronchoscopy, but this technique has some disadvantages [53]. Bronchoscopy in children usually requires anesthesia, therefore relevant breathing maneuvers

[2] WIP, the product is currently under development and is not for sale in the US and in other countries. Its future availability cannot be ensured.

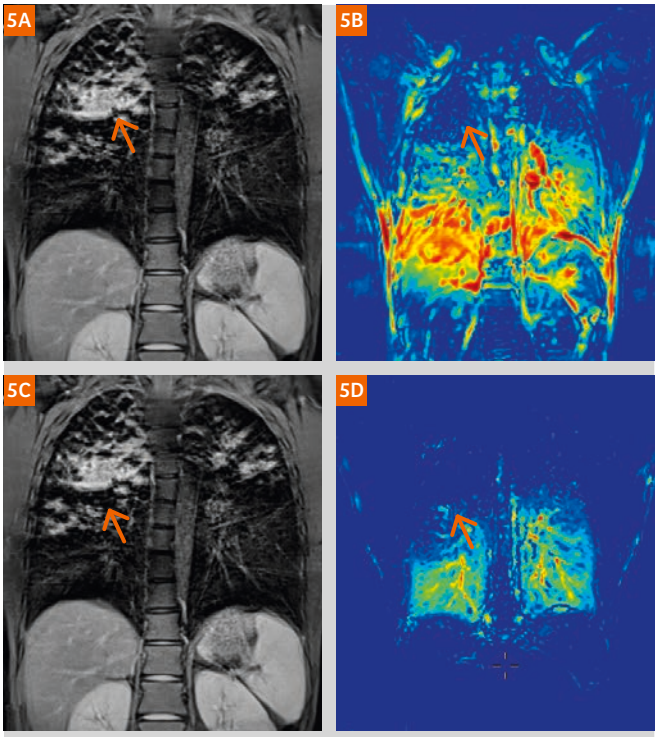

Figure 5: (5A, C) Coronal PD-weighted BLADE end-expiratory navigator-triggered, **(5B)** ventilation map Fourier Decomposition[2] and **(5D)** perfusion map Fourier Decomposition. Note large area of bronchiectasis, mucus plugging and consolidation in right upper lobe (arrows in 5A, C). This region also appears not properly ventilated (arrow in 5B) and perfused (arrow in 5D) in corresponding Fourier Decomposition ventilation and perfusion maps.

(i.e. forced expiration and coughing) cannot be performed and exact measurements of airway dimensions are difficult [53]. Dynamic evaluation can be performed using CT, but MRI has the advantage to avoid ionizing radiation, which is particularly important for pediatric[1] patients or for those patients who require repeated imaging studies [54].

In our study, we showed that cine-MRI is a feasible technique in pediatric patients [52]. By using an MRI compatible spirometer we were able to perform specific breathing maneuvers, such as peak flow or coughing that helped to diagnose tracheomalacia [52], thus giving to spirometer controlled cine-MRI a great potential to replace bronchoscopy or cine-CT.

MRI to assess diaphragm mechanics

Assessment of the function of the diaphragm is highly relevant for several diseases [55, 56]. Neurological diseases, such as muscular dystrophy or metabolic degenerative disease, can affect diaphragmatic function [56, 57] and can hence lead to respiratory insufficiency [57]. To date, the gold standard to assess diaphragmatic motion has been lung function tests, which – as previously mentioned – are limited by low sensitivity and high variability [58]. Regarding imaging, ultrasound (US) has been the most used technique to assess diaphragmatic motion [59]. In fact compared to MRI, US is cheaper and faster, although it lacks cross-sectional capabilities and it has large variability due to the operator dependency [56, 59]. MRI has a great potential to provide a sensitive imaging biomarker of diaphragm motility [60, 61].

In our study, we applied a spirometry controlled cine-MRI protocol to assess diaphragm motility in patients with Pompe disease and in a group of healthy volunteers [55]. Pompe disease is a hereditary genetic metabolic disorder, characterized by accumulation of glycogen in the muscles and nerves [62]. This results in progressive muscle weakness, hypotonia, recurrent chest infections and eventually respiratory insufficiency [62]. The enzyme replacement therapy for this disease costs approx. 23,000 € per month [63]. PFT can be indicative of diaphragmatic weakness by showing a difference between forced vital capacity (FVC) in sitting and supine position or by a decreased mean inspiratory pressure (MIP), but it provides only indirect information on diaphragm mechanics. In our study, we showed that MRI could be a sensitive tool to assess diaphragm mechanics [55]. We demonstrate that the diaphragmatic displacement can be severely impaired in patients with Pompe disease [55]. Moreover, Pompe patients could be stratified according the displacement of the diaphragm, which was extremely impaired in some of the patients, while in others some residual function of the diaphragm in supine position was measurable [55]. The main advantage of MRI compared to ultrasound is the superior detailed anatomical information in 3D that can be obtained in dynamic and static conditions as well as the repeatability of the technique. Our MRI protocol has also the advantage that it is combined with the use of the spirometer, enabling to correlate pulmonary function with MRI parameters related to the diaphragm. Combining these parameters may provide new insights in the disease process and on its response to therapy. This method has been recently improved by automated software tools analyzing the motion of the diaphragm and other respiratory muscles [64].

When validated, this technique is likely to become an important diagnostic tool for other diseases, such as congenital diaphragmatic hernia, diaphragm paralysis and other causes of limb-girdle weakness.

Other directions for future research

There are several opportunities to further improve the role of thoracic MRI as diagnostic and monitoring tool.

MRI protocol standardization

As discussed previously, the main reason of the limited use of chest MRI in the clinic is the lack of standardization

[1] MR scanning has not been established as safe for imaging fetuses and infants under two years of age. The responsible physician must evaluate the benefit of the MRI examination over other imaging procedures.

among MRI vendors and hospitals. Few centers have acquired sufficient experience to routinely introduce chest MRI in clinical practice [28]. Most pulmonologists are not aware of chest MRI capabilities, and they prefer to rely on CT. Even radiologists find chest MRI difficult and time consuming, mostly because they are not familiar with the technique.

However, with the technological advances achieved over the last decade, chest MRI is now mature to be translated in clinical practice [7, 65]. Through an international collaboration, we aim to develop a VIPS chest MRI protocol that will supply information about Ventilation, Inflammation, Perfusion and Structure in one session of maximal half an hour [21]. This protocol will be harmonized among the main MRI vendors (General Electric, Philips and Siemens Healthcare). This VIPS platform will be firstly tested for monitoring CF lung disease during a pulmonary exacerbation and later for other chronic lung diseases.

Other applications of lung MRI in pediatrics

Different chronic lung diseases are suitable to be assessed with thoracic MRI. Bronchopulmonary dysplasia (BPD) is a severe chronic lung condition associated with long-term respiratory sequelae [66]. Chest CT has been used to assess and monitor structural lung changes in BPD [67]. Despite low or ultra-low dose CT protocols developed for BPD, the young age of these patients and the need for repeated imaging are a matter of concern regarding the risk of radiation-induced cancer. MRI as radiation-free technique would allow repeated imaging in BPD patients [68]. Moreover MRI will allow to obtain information about structural lung changes, but also about ventilation and perfusion. This functional information might be relevant to understand pathophysiology of BPD and why some patients evolve to severe obstructive airways disease.

Other diseases that might be studied with MRI are Chronic Obstructive Pulmonary Disease (COPD) and asthma. For parenchymal visualization, ultrashort (UTE) and zero echo-time (ZTE) sequences showed better spatial resolution, signal-to-noise (SNR) and contrast-to-noise ratio (CNR) than conventional sequences [69, 70]. Using these sequences, patients with COPD can be differentiated from healthy subjects and classified according disease severity [70]. In fact, with increased COPD grade, the parenchymal signal intensity distribution shifts toward lower signal intensities, so UTE signal can be used to quantify parenchymal tissue destruction and inflammation [70]. These measurements are highly reproducible and usable for longitudinal studies.

Several studies have shown the utility of ventilation imaging with MRI for COPD and asthma [47, 71-73]. For example oxygen-enhanced MRI showed higher correlation to PFT and clinical parameters of COPD than CT, with higher potential for more accurate clinical stage classification [72]. Similar results were shown in patients with asthma [74]. Interestingly, to date Fourier Decomposition has not been tested in COPD patients. This technique would have the advantage to supply information about ventilation and perfusion in a single free-breathing scan without contrast administration. Perfusion biomarkers might become relevant for clinical trials and using Fourier Decomposition would avoid Gadolinium administration, which has been recently debated after evidence of brain Gd deposition [75].

Lung perfusion in COPD and asthma has been extensively investigated with MRI [76–82]. Multiple quantitative and semi quantitative perfusion-derived parameters have been described to classify COPD severity [76–78]. Interestingly MRI appears to be more sensitive than CT in identifying early perfusion abnormalities among controls and mild COPD subjects [78]. Full quantitative analysis of pulmonary microvascular perfusion seems time-consuming and not needed [76]. There is indeed a close correlation between quantitative and semi quantitative perfusion parameters, therefore semi quantitative values may be useful as surrogate markers for regional pulmonary blood flow (PBF) in clinical practice and for follow-up examinations [76].

Development of software tools for thoracic MRI

Another important limiting factor for the use of MRI in clinical practice has been the lack of dedicated software tools for automatic analysis of thoracic MRI. To date there is no commercially available automatic segmentation software for lung and airways on MR images. These tools are indispensable to move from qualitative to quantitative imaging. Physicians need to extract meaningful numbers out of the images that can help them to objectively determine disease progression, stability or improvement. Our group is aiming to develop scoring systems for several lung diseases that can be ultimately automated. The biomarkers derived from these software tools will be integrated in the report that accompanies the radiological examination.

Summary

In this essay we have shown the multiple capabilities of MRI for lung imaging. Chest MRI is ready to be converted in a unique single session imaging tool that can provide structural and functional information. Several chronic obstructive lung diseases might benefit from the development of the VIPS MRI platform, which will allow new clinical diagnostic scenarios and interventional clinical trials.

Contact

Giovanni Morana, M.D.
Radiology Department
General Hospital
Ca' Foncello

31100 Treviso
Italy
Phone: +39-0422-322253
Fax: +39-0422-322202
gmorana@ulss.tv.it

References

1 Ciet P, Tiddens HAWM, Wielopolski PA, Wild JM, Lee EY, Morana G, Lequin MH. Magnetic resonance imaging in children: common problems and possible solutions for lung and airways imaging. Pediatr. Radiol. [Internet] 2015. Available from: http://www.ncbi.nlm.nih.gov/pubmed/26342643.

2 Muller NL. Computed tomography and magnetic resonance imaging: past, present and future. Eur Respir J Suppl [Internet] 2002; 35: 3s–12s. Available from: http://www.ncbi.nlm.nih.gov/entrez/query.fcgi?cmd=Retrieve&db=PubMed&dopt=Citation&list_uids=12064679.

3 Goo HW. Advanced functional thoracic imaging in children: From basic concepts to clinical applications. Pediatr. Radiol. 2013; 43: 262–268.

4 Lobo L, Antunes D. Chest CT in infants and children. Eur. J. Radiol. [Internet] Elsevier Ireland Ltd; 2013; 82: 1108–1117. Available from: http://dx.doi.org/10.1016/j.ejrad.2011.12.006.

5 De Wever W, Verschakelen J, Coolen J. Role of imaging in diagnosis, staging and follow-up of lung cancer. Curr Opin Pulm Med [Internet] 2014; 20: 385–392. Available from: http://www.ncbi.nlm.nih.gov/pubmed/24837705.

6 Wild JM, Marshall H, Bock M, Schad LR, Jakob PM, Puderbach M, Molinari F, Van Beek EJR, Biederer J. MRI of the lung (1/3): methods. Insights Imaging [Internet] 2012 [cited 2014 Feb 1]; 3: 345–353. Available from: http://www.pubmedcentral.nih.gov/articlerender.fcgi?artid=3481083&tool=pmcentrez&rendertype=abstract.

7 Biederer J, Beer M, Hirsch W, Wild J, Fabel M, Puderbach M, Van Beek EJR. MRI of the lung (2/3). Why ... when ... how? Insights Imaging [Internet] 2012 [cited 2014 Jan 22]; 3: 355–371. Available from: http://www.pubmedcentral.nih.gov/articlerender.fcgi?artid=3481084&tool=pmcentrez&rendertype=abstract.

8 Kuo W, Ciet P, Tiddens H a WM, Zhang W, Guillerman RP, van Straten M. Monitoring cystic fibrosis lung disease by computed tomography. Radiation risk in perspective. Am. J. Respir. Crit. Care Med. [Internet] 2014 [cited 2014 Jun 6]; 189: 1328–1336. Available from: http://www.ncbi.nlm.nih.gov/pubmed/24697683.

9 Egan ME. Genetics of Cystic Fibrosis: Clinical Implications. Clin. Chest Med. [Internet] 2016; 37: 9–16. Available from: http://www.ncbi.nlm.nih.gov/pubmed/26857764.

10 Spoonhower KA, Davis PB. Epidemiology of Cystic Fibrosis. Clin. Chest Med. [Internet] 2016; 37: 1–8. Available from: http://www.ncbi.nlm.nih.gov/pubmed/26857763.

11 Tiddens HAWM, Rosenow T. What did we learn from two decades of chest computed tomography in cystic fibrosis ? Pediatr. Radiol. 2014; 44: 1490–1495.

12 de Jong P A, Lindblad A, Rubin L, Hop WCJ, de Jongste JC, Brink M, Tiddens HAWM. Progression of lung disease on computed tomography and pulmonary function tests in children and adults with cystic fibrosis. Thorax [Internet] 2006 [cited 2013 Dec 22]; 61: 80–85. Available from: http://www.pubmedcentral.nih.gov/articlerender.fcgi?artid=2080716&tool=pmcentrez&rendertype=abstract.

13 Pearce MS, Salotti J a, Little MP, McHugh K, Lee C, Kim KP, Howe NL, Ronckers CM, Rajaraman P, Sir Craft AW, Parker L, Berrington de González A. Radiation exposure from CT scans in childhood and subsequent risk of leukaemia and brain tumours: a retrospective cohort study. Lancet [Internet] Elsevier Ltd; 2012 [cited 2014 Jan 21]; 380: 499–505. Available from: http://www.pubmedcentral.nih.gov/articlerender.fcgi?artid=3418594&tool=pmcentrez&rendertype=abstract.

14 Miglioretti DL, Johnson E, Williams A, Greenlee RT, Weinmann S, Solberg LI, Feigelson HS, Roblin D, Flynn MJ, Vanneman N, Smith-Bindman R. The use of computed tomography in pediatrics and the associated radiation exposure and estimated cancer risk. JAMA Pediatr. [Internet] 2013 [cited 2013 Dec 14]; 167: 700–707. Available from: http://www.ncbi.nlm.nih.gov/pubmed/23754213.

15 Puderbach M, Eichinger M, Haeselbarth J, Ley S, Kopp-Schneider A, Tuengerthal S, Schmaehl A, Fink C, Plathow C, Wiebel M, Demirakca S, Müller F-M, Kauczor H-U. Assessment of morphological MRI for pulmonary changes in cystic fibrosis (CF) patients: comparison to thin-section CT and chest x-ray. Invest. Radiol. [Internet] 2007 [cited 2014 Feb 28]; 42: 715–725. Available from: http://www.ncbi.nlm.nih.gov/pubmed/17984769.

16 Failo R, Wielopolski PA, Tiddens HAWM, Hop WCJ, Mucelli RP, Lequin MH. Lung morphology assessment using MRI: a robust ultra-short TR/TE 2D steady state free precession sequence used in cystic fibrosis patients. Magn. Reson. Med. [Internet] 2009 [cited 2013 Dec 22]; 61: 299–306. Available from: http://www.ncbi.nlm.nih.gov/pubmed/19165879.

17 Rajaram S, Swift AJ, Capener D, Telfer A, Davies C, Hill C, Condliffe R, Elliot C, Hurdman J, Kiely DG, Wild JM. Lung morphology assessment with balanced steady-state free precession MR imaging compared with CT. Radiology [Internet] 2012 [cited 2014 Feb 4]; 263: 569–577. Available from: http://www.ncbi.nlm.nih.gov/pubmed/22371608.

18 Paschal CB, Morris HD. K-space in the clinic. J. Magn. Reson. Imaging [Internet] 2004 [cited 2014 Feb 1]; 19: 145–159. Available from: http://www.ncbi.nlm.nih.gov/pubmed/14745747.

19 Hennig J. K-space sampling strategies. Eur. Radiol. [Internet] 1999 [cited 2014 Jun 6]; 9: 1020–1031. Available from: http://www.ncbi.nlm.nih.gov/pubmed/10415232.

20 Wright KL, Hamilton JI, Griswold MA, Gulani V, Seiberlich N. Non-Cartesian parallel imaging reconstruction. J. Magn. Reson. Imaging 2014; 40: 1022–1040.

21 Tiddens HAWM, Stick SM, Wild JM, Ciet P, Parker GJM, Koch A, Vogel-Claussen J. Respiratory tract exacerbations revisited: Ventilation, inflammation, perfusion, and structure (VIPS) monitoring to redefine treatment. Pediatr. Pulmonol. [Internet] 2015; 50: S57–S65. Available from: http://doi.wiley.com/10.1002/ppul.23266.

22 Hirokawa Y, Isoda H, Maetani YS, Arizono S, Shimada K, Togashi K. Evaluation of motion correction effect and image quality with the periodically rotated overlapping parallel lines with enhanced reconstruction (PROPELLER) (BLADE) and parallel imaging acquisition technique in the upper abdomen. J. Magn. Reson. Imaging [Internet] 2008 [cited 2014 Feb 28]; 28: 957–962. Available from: http://www.ncbi.nlm.nih.gov/pubmed/18821630.

23 Ciet P, Serra G, Bertolo S, Spronk S, Ros M, Fraioli F, Quattrucci S, Assael MB, Catalano C, Pomerri F, Tiddens HAWM, Morana G. Assessment of CF lung disease using motion corrected PROPELLER MRI: a comparison with CT. Eur. Radiol. [Internet] 2015; 26: 780–787. Available from: http://www.ncbi.nlm.nih.gov/pubmed/26024847.

24 Renz DM, Scholz O, Böttcher J, Maurer MH, Denecke T, Schwarz C, Pfeil A, Streitparth F, Huppertz A, Mehl A, Poellinger A, Staab D, Hamm B, Mentzel H-J. Comparison Between Magnetic Resonance Imaging and Computed Tomography of the Lung in Patients With Cystic Fibrosis With Regard to Clinical, Laboratory, and Pulmonary Functional Parameters. Invest. Radiol. [Internet] 2015; 50: 21–24. Available from: http://www.ncbi.nlm.nih.gov/pubmed/26154442.

25 Dournes G, Menut F, Macey J, Fayon M, Chateil J-F, Salel M, Corneloup O, Montaudon M, Berger P, Laurent F. Lung morphology assessment of cystic fibrosis using MRI with ultra-short echo time at submillimeter spatial resolution. Eur. Radiol. [Internet] 2016. Available from: http://link.springer.com/10.1007/s00330-016-4218-5.

26 Dournes G, Grodzki D, Macey J, Girodet P-O, Fayon M, Chateil J-F, Montaudon M, Berger P, Laurent F. Quiet Submillimeter MR Imaging of the Lung Is Feasible with a PETRA Sequence at 1.5 T. Radiology

[Internet] 2015; 276: 258–265. Available from: http://www.ncbi.nlm.nih.gov/pubmed/25768672.
27 Ackman JB. A practical guide to nonvascular thoracic magnetic resonance imaging. J. Thorac. Imaging [Internet] 2014; 29: 17–29. Available from: http://eutils.ncbi.nlm.nih.gov/entrez/eutils/elink.fcgi?dbfrom=pubmed&id=24361974&retmode=ref&cmd=prlinks\npapers2://publication/doi/10.1097/RTI.0000000000000056.
28 Ackman JB. A practical guide to nonvascular thoracic magnetic resonance imaging. J. Thorac. Imaging 2014; 29: 17–29.
29 Keenan K, Stupic K, Boss M, Russek S, Chenevert T, Prasad P, Reddick W, Cecil K, Zheng J, Hu P, Jackson E. Multi-site, multi-vendor comparison of T1 measurement using ISMRM/NIST system phantom. Int. Soc. Magn. Reson. Med. 2016. p. #3290.
30 Ciet P, Serra G, Andrinopoulou ER, Bertolo S, Ros M, Catalano C, Colagrande S, Tiddens HAWM, Morana G. Diffusion weighted imaging in cystic fibrosis disease: beyond morphological imaging. Eur. Radiol. [Internet] 2016. Available from: http://link.springer.com/10.1007/s00330-016-4248-z.
31 Nichols DP, Chmiel JF. Inflammation and its genesis in cystic fibrosis. Pediatr. Pulmonol. [Internet] 2015; 50 Suppl 4: S39-56. Available from: http://doi.wiley.com/10.1002/ppul.23242.
32 Cohen-Cymberknoh M, Kerem E, Ferkol T, Elizur A. Airway inflammation in cystic fibrosis: molecular mechanisms and clinical implications. Thorax [Internet] 2013; 68: 1157–1162. Available from: http://www.ncbi.nlm.nih.gov/pubmed/23704228.
33 Belessis Y, Dixon B, Hawkins G, Pereira J, Peat J, MacDonald R, Field P, Numa A, Morton J, Lui K, Jaffe A. Early cystic fibrosis lung disease detected by bronchoalveolar lavage and lung clearance index. Am. J. Respir. Crit. Care Med. 2012; 185: 862–873.
34 Keen C, Gustafsson P, Lindblad A, Wennergren G, Olin A-C. Low levels of exhaled nitric oxide are associated with impaired lung function in cystic fibrosis. Pediatr. Pulmonol. 2010; 45: 241–248.
35 Wagener JS, Elkin EP, Pasta DJ, Schechter MS, Konstan MW, Morgan WJ, Investigators and Coordinators of the Epidemiologic Study of Cystic Fibrosis. Pulmonary function outcomes for assessing cystic fibrosis care. J. Cyst. Fibros. [Internet] European Cystic Fibrosis Society.; 2015; 14: 376–383. Available from: http://linkinghub.elsevier.com/retrieve/pii/S1569199314002690.
36 Horsley A, Wild JM. Ventilation heterogeneity and the benefits and challenges of multiple breath washout testing in patients with cystic fibrosis. Paediatr. Respir. Rev. [Internet] Elsevier Ltd; 2015; 16: 15–18. Available from: http://dx.doi.org/10.1016/j.prrv.2015.07.010.
37 Amin R, Charron M, Grinblat L, Shammas A, Grasemann H, Graniel K, Ciet P, Tiddens H, Ratjen F. Cystic Fibrosis: Detecting Changes in Airway Inflammation with FDG PET/CT. Radiology 2012. p. 868–875.
38 Wielpütz MO, Puderbach M, Kopp-Schneider A, Stahl M, Fritzsching E, Sommerburg O, Ley S, Sumkauskaite M, Biederer J, Kauczor H-U, Eichinger M, Mall M a. Magnetic Resonance Imaging Detects Changes in Structure and Perfusion, and Response to Therapy in Early Cystic Fibrosis Lung Disease. Am. J. Respir. Crit. Care Med. [Internet] 2014; : 1–49. Available from: http://www.ncbi.nlm.nih.gov/pubmed/24564281.
39 Ciet P, Bos A, Wielopolski P, Hernández-Tamames J, de Bruijne M, Tiddens HAWM, Perez-Rovira A. Three-dimensional Fourier Decomposition Ventilation Magnetic Resonance Lung Imaging Poster #4875, European Conference Radiology (ECR) 2017.
40 Deffebach M, Charan N, Lakshminarayan S, Butler J. The bronchial circulation. Small, but a vital attribute of the lung. Am Rev Respir Dis 1987; 135(2): 463–481.
41 Bauman G, Puderbach M, Heimann T, Kopp-Schneider A, Fritzsching E, Mall MA, Eichinger M. Validation of Fourier decomposition MRI with dynamic contrast-enhanced MRI using visual and automated scoring of pulmonary perfusion in young cystic fibrosis patients. Eur. J. Radiol. [Internet] Elsevier Ireland Ltd; 2013 [cited 2014 Feb 1]; 82: 2371–2377. Available from: http://www.ncbi.nlm.nih.gov/pubmed/24016829.
42 Schraml C, Schwenzer NF, Martirosian P, Boss A, Schick F, Schäfer S, Stern M, Claussen CD, Schäfer JF. Non-invasive pulmonary perfusion assessment in young patients with cystic fibrosis using an arterial spin labeling MR technique at 1.5 T. MAGMA [Internet] 2012 [cited 2013 Dec 22]; 25: 155–162. Available from: http://www.ncbi.nlm.nih.gov/pubmed/21786163.
43 Fain SB, Korosec FR, Holmes JH, O'Halloran R, Sorkness RL, Grist TM. Functional lung imaging using hyperpolarized gas MRI. J. Magn. Reson. Imaging [Internet] 2007 [cited 2013 Dec 22]; 25: 910–923. Available from: http://www.ncbi.nlm.nih.gov/pubmed/17410561.
44 Lilburn DML, Pavlovskaya GE, Meersmann T. Perspectives of hyperpolarized noble gas MRI beyond 3He. J. Magn. Reson. [Internet] 2013 [cited 2014 Feb 3]; 229: 173–186. Available from: http://www.pubmedcentral.nih.gov/articlerender.fcgi?artid=3611600&tool=pmcentrez&rendertype=abstract.
45 Jakob PM, Wang T, Schultz G, Hebestreit H, Hebestreit A, Hahn D. Assessment of human pulmonary function using oxygen-enhanced T(1) imaging in patients with cystic fibrosis. Magn. Reson. Med. [Internet] 2004; 51: 1009–1016. Available from: http://apps.webofknowledge.com/full_record.do?product=WOS&search_ralSearch&qid=3&SID=P1l8kGdSujUDf9X25m5&page=1&doc=8.
46 Stadler A, Stiebellehner L, Jakob PM, Arnold JFT, Eisenhuber E, von Katzler I, Bankier AA. Quantitative and O(2) enhanced MRI of the pathologic lung: findings in emphysema, fibrosis, and cystic fibrosis. Int. J. Biomed. Imaging [Internet] 2007; 2007: 23624. Available from: http://www.ncbi.nlm.nih.gov/pubmed/17710253.
47 Zhang W-J, Niven RM, Young SS, Liu Y-Z, Parker GJM, Naish JH. Dynamic oxygen-enhanced magnetic resonance imaging of the lung in asthma—Initial experience. Eur. J. Radiol. [Internet] Elsevier Ireland Ltd; 2015; 84: 318–326. Available from: http://linkinghub.elsevier.com/retrieve/pii/S0720048X14005051.
48 Bauman G, Puderbach M, Deimling M, Jellus V, Chefd'hotel C, Dinkel J, Hintze C, Kauczor H-U, Schad LR. Non-contrast-enhanced perfusion and ventilation assessment of the human lung by means of fourier decomposition in proton MRI. Magn. Reson. Med. [Internet] 2009 [cited 2014 Feb 6]; 62: 656–664. Available from: http://www.ncbi.nlm.nih.gov/pubmed/19585597.
49 Lederlin M, Bauman G, Eichinger M, Dinkel J, Brault M, Biederer J, Puderbach M. Functional MRI using Fourier decomposition of lung signal: reproducibility of ventilation- and perfusion-weighted imaging in healthy volunteers. Eur. J. Radiol. [Internet] Elsevier Ireland Ltd; 2013 [cited 2013 Dec 24]; 82: 1015–1022. Available from: http://www.ncbi.nlm.nih.gov/pubmed/23295084.
50 Saranathan M, Rettmann DW, Hargreaves BA, Clarke SE, Vasanawala SS. DIfferential subsampling with cartesian ordering (DISCO): A high spatio-temporal resolution dixon imaging sequence for multiphasic contrast enhanced abdominal imaging. J. Magn. Reson. Imaging 2012; 35: 1484–1492.
51 Ciet P, Wielopolski P, van der Wiel E, Krestin GP, Lequin MH, Morana G, Tiddens HAMW. Contrast-enhanced MRI (CE-MRI) is more sensitive to detect small airways disease than proton-MRI (MRI): a comparative study in cystic fibrosis (CF) lung disease (SS 604), B-0416, European Conference Radiology (ECR) 2012.
52 Ciet P, Wielopolski P, Manniesing R, Lever S, de Bruijne M, Morana G, Muzzio PC, Lequin MH, Tiddens HAWM. Spirometer-controlled cine magnetic resonance imaging used to diagnose tracheobronchomalacia in paediatric patients. Eur. Respir. J. [Internet] 2014 [cited 2014 Jan 29]; 43: 115–124. Available from: http://www.ncbi.nlm.nih.gov/pubmed/23598953.
53 Williamson JP, James AL, Phillips MJ, Sampson DD, Hillman DR, Eastwood PR. Quantifying tracheobronchial tree dimensions:

methods, limitations and emerging techniques. Eur. Respir. J. [Internet] 2009 [cited 2014 May 29]; 34: 42–55. Available from: http://www.ncbi.nlm.nih.gov/pubmed/19567601.

54 Boiselle PM, Ernst A. Recent advances in central airway imaging. Chest [Internet] 2002; 121: 1651–1660. Available from: <Go to ISI>://WOS:000175650500046.

55 Wens SC, Ciet P, Perez-Rovira A, Logie K, Salamon E, Wielopolski P, de Bruijne M, Kruijshaar ME, Tiddens HA, van Doorn PA, van der Ploeg AT. Lung MRI and impairment of diaphragmatic function in Pompe disease. BMC Pulm. Med. [Internet]; 2015; 15: 54. Available from: http://www.biomedcentral.com/1471-2466/15/54.

56 Kharma N. Dysfunction of the diaphragm: imaging as a diagnostic tool. Curr. Opin. Pulm. Med. [Internet] 2013; 19: 394–398. Available from: http://www.ncbi.nlm.nih.gov/pubmed/23715292.

57 Nason LK, Walker CM, McNeeley MF, Burivong W, Fligner CL, Godwin JD. Imaging of the diaphragm: anatomy and function. Radiographics [Internet] 2012 [cited 2014 Feb 1]; 32: E51-70. Available from: http://www.ncbi.nlm.nih.gov/pubmed/22411950.

58 Pacia EB, Aldrich TK. Assessment of diaphragm function. Chest Surg. Clin. N. Am. [Internet] 1998; 8: 225–236. Available from: http://www.ncbi.nlm.nih.gov/pubmed/9619303.

59 Chavhan GB, Babyn PS, Cohen R a, Langer JC. Multimodality imaging of the pediatric diaphragm: anatomy and pathologic conditions. Radiographics 2010; 30: 1797–1817.

60 Eichinger M, Tetzlaff R, Puderbach M, Woodhouse N, Kauczor H-U. Proton magnetic resonance imaging for assessment of lung function and respiratory dynamics. Eur. J. Radiol. [Internet] 2007 [cited 2013 Dec 22]; 64: 329–334. Available from: http://www.ncbi.nlm.nih.gov/pubmed/17889475.

61 Unal O, Arslan H, Uzun K, Ozbay B, Sakarya ME. Evaluation of diaphragmatic movement with MR fluoroscopy in chronic obstructive pulmonary disease. Clin. Imaging [Internet] 2001; 24: 347–350. Available from: http://www.ncbi.nlm.nih.gov/pubmed/11368935.

62 Pellegrini N, Laforet P, Orlikowski D, Pellegrini M, Caillaud C, Eymard B, Raphael JC, Lofaso F. Respiratory insufficiency and limb muscle weakness in adults with Pompe's disease. Eur. Respir. J. 2005; 26: 1024–1031.

63 Kanters T a, Hoogenboom-Plug I, Rutten-Van Mölken MPMH, Redekop WK, van der Ploeg AT, Hakkaart L. Cost-effectiveness of enzyme replacement therapy with alglucosidase alfa in classic-infantile patients with Pompe disease. Orphanet J. Rare Dis. [Internet] 2014; 9: 75. Available from: http://www.pubmedcentral.nih.gov/articlerender.fcgi?artid=4038090&tool=pmcentrez&rendertype=abstract.

64 Mogalle K, Perez-rovira A, Ciet P, Doorn PA Van, Tiddens HAWM, Ploeg AT Van Der, Bruijne M De, Mc E. Quantification of Diaphragm Mechanics in Pompe Disease using Dynamic 3D MRI. PLoS One 2016; (In Press): 1–23.

65 Biederer J, Mirsadraee S, Beer M, Molinari F, Hintze C, Bauman G, Both M, Van Beek EJR, Wild J, Puderbach M. MRI of the lung (3/3)-current applications and future perspectives. Insights Imaging [Internet] 2012 [cited 2013 Dec 14]; 3: 373–386. Available from: http://www.pubmedcentral.nih.gov/articlerender.fcgi?artid=3481076&tool=pmcentrez&rendertype=abstract.

66 Lal CV, Ambalavanan N. Biomarkers, Early Diagnosis, and Clinical Predictors of Bronchopulmonary Dysplasia. Clin. Perinatol. [Internet] 2015; 42: 739–754. Available from: http://www.ncbi.nlm.nih.gov/pubmed/26593076.

67 Walkup LL, Woods JC. Newer Imaging Techniques for Bronchopulmonary Dysplasia. Clin. Perinatol. [Internet] 2015; 42: 871–887. Available from: http://www.ncbi.nlm.nih.gov/pubmed/26593084.

68 Walkup LL, Woods JC. Newer Imaging Techniques for Bronchopulmonary Dysplasia. Clin. Perinatol. 2015; 42: 871–887.

69 Ohno Y, Nishio M, Koyama H, Yoshikawa T, Matsumoto S, Seki S, Obara M, van Cauteren M, Takahashi M, Sugimura K. Pulmonary 3 T MRI with ultrashort TEs: influence of ultrashort echo time interval on pulmonary functional and clinical stage assessments of smokers. J. Magn. Reson. Imaging [Internet] 2014; 39: 988–997. Available from: http://www.ncbi.nlm.nih.gov/pubmed/24123342.

70 Ma W, Sheikh K, Svenningsen S, Pike D, Guo F, Etemad-Rezai R, Leipsic J, Coxson HO, McCormack DG, Parraga G. Ultra-short echo-time pulmonary MRI: Evaluation and reproducibility in COPD subjects with and without bronchiectasis. J. Magn. Reson. Imaging [Internet] 2015; 41: 1465–1474. Available from: http://doi.wiley.com/10.1002/jmri.24680.

71 Ohno Y, Hatabu H, Takenaka D, Van Cauteren M, Fujii M, Sugimura K. Dynamic oxygen-enhanced MRI reflects diffusing capacity of the lung. Magn. Reson. Med. 2002; 47: 1139–1144.

72 Ohno Y, Iwasawa T, Seo JB, Koyama H, Takahashi H, Oh Y-M, Nishimura Y, Sugimura K. Oxygen-enhanced Magnetic Resonance Imaging versus Computed Tomography. Am. J. Respir. Crit. Care Med. [Internet] 2008; 177: 1095–1102. Available from: http://www.atsjournals.org/doi/abs/10.1164/rccm.200709-1322OC.

73 Kruger SJ, Nagle SK, Couch MJ, Ohno Y, Albert M, Fain SB. Functional imaging of the lungs with gas agents. J. Magn. Reson. Imaging [Internet] 2015. Available from: http://doi.wiley.com/10.1002/jmri.25002.

74 Ohno Y, Nishio M, Koyama H, Seki S, Yoshikawa T, Matsumoto S, Obara M, van Cauteren M, Sugimura K. Asthma: Comparison of Dynamic Oxygen-enhanced MR Imaging and Quantitative Thin-Section CT for Evaluation of Clinical Treatment. Radiology [Internet] 2014; 273: 132660. Available from: http://dx.doi.org/10.1148/radiol.14132660.

75 Murata N, Gonzalez-Cuyar LF, Murata K, Fligner C, Dills R, Hippe D, Maravilla KR. Macrocyclic and Other Non–Group 1 Gadolinium Contrast Agents Deposit Low Levels of Gadolinium in Brain and Bone Tissue. Invest. Radiol. [Internet] 2016; 0: 1. Available from: http://content.wkhealth.com/linkback/enurl?sid=WKPTLP:landingpage&an=00004424-900000000-99224.

76 Hueper K, Parikh MA, Prince MR, Schoenfeld C, Liu C, Bluemke DA, Dashnaw SM, Goldstein T a, Hoffman E a, Lima J a, Skrok J, Zheng J, Barr RG, Vogel-Claussen J. Quantitative and semiquantitative measures of regional pulmonary microvascular perfusion by magnetic resonance imaging and their relationships to global lung perfusion and lung diffusing capacity: the multiethnic study of atherosclerosis chronic obstructi. Invest. Radiol. [Internet] 2013; 48: 223–230. Available from: http://www.pubmedcentral.nih.gov/articlerender.fcgi?artid=3952075&tool=pmcentrez&rendertype=abstract.

77 Hueper K, Vogel-Claussen J, Parikh MA, Austin JHM, Bluemke DA, Carr J, Choi J, Goldstein TA, Gomes AS, Hoffman E a., Kawut SM, Lima J, Michos ED, Post WS, Po MJ, Prince MR, Liu K, Rabinowitz D, Skrok J, Smith BM, Watson K, Yin Y, Zambeli-Ljepovic AM, Barr RG. Pulmonary Microvascular Blood Flow in Mild Chronic Obstructive Pulmonary Disease and Emphysema. The MESA COPD Study. Am. J. Respir. Crit. Care Med. [Internet] 2015; 192: 570–580. Available from: http://www.atsjournals.org/doi/10.1164/rccm.201411-2120OC.

78 Fan L, Xia Y, Guan Y, Yu H, Zhang T, Liu S, Li B. Capability of differentiating smokers with normal pulmonary function from COPD patients: a comparison of CT pulmonary volume analysis and MR perfusion imaging. Eur. Radiol. [Internet] 2013; 23: 1234–1241. Available from: http://link.springer.com/10.1007/s00330-012-2729-2.

79 Xia Y, Guan Y, Fan L, Liu S-Y, Yu H, Zhao L-M, Li B. Dynamic Contrast Enhanced Magnetic Resonance Perfusion

Imaging in High-Risk Smokers and Smoking-Related COPD: Correlations with Pulmonary Function Tests and Quantitative Computed Tomography. COPD J. Chronic Obstr. Pulm. Dis. [Internet] 2014; 11: 510–520. Available from: http://www.tandfonline.com/doi/full/10.3109/15412555.2014.948990.

80 Sergiacomi G, Taglieri A, Chiaravalloti A, Calabria E, Arduini S, Tosti D, Citraro D, Pezzuto G, Puxeddu E, Simonetti G. Acute COPD exacerbation: 3 T MRI evaluation of pulmonary regional perfusion – Preliminary experience. Respir. Med. [Internet] Elsevier Ltd; 2014; 108: 875–882. Available from: http://linkinghub.elsevier.com/retrieve/pii/S0954611114001279.

81 Bryant M, Ley S, Eberhardt R, Menezes R, Herth F, Sedlaczek O, Kauczor H-U, Ley-Zaporozhan J. Assessment of the relationship between morphological emphysema phenotype and corresponding pulmonary perfusion pattern on a segmental level. Eur. Radiol. [Internet] 2015; 25: 72–80. Available from: http://link.springer.com/10.1007/s00330-014-3385-5.

82 Jobst BJ, Triphan SMF, Sedlaczek O, Anjorin A, Kauczor HU, Biederer J, Ley-Zaporozhan J, Ley S, Wielpütz MO. Functional Lung MRI in Chronic Obstructive Pulmonary Disease: Comparison of T1 Mapping, Oxygen-Enhanced T1 Mapping and Dynamic Contrast Enhanced Perfusion. PLoS One [Internet] 2015; 10: e0121520. Available from: http://dx.plos.org/10.1371/journal.pone.0121520.

www.siemens.com/lung-mri

The potential of MRI for scientific and clinical applications within the thorax is widely underestimated. Chest MRI has much untapped promise in providing structural and functional information. On this page you will find talks and articles, introducing MRI protocols and providing tips & tricks for routine thoracic MR imaging.

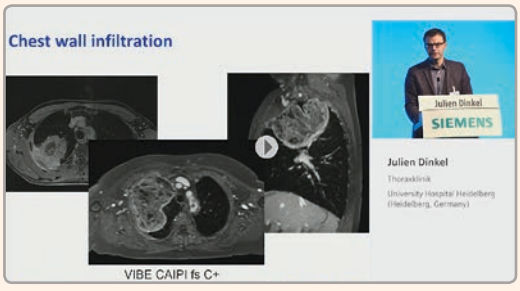

Don't miss the talks of international experts on all aspects of MR lung imaging.

Go to

Clinical Corner > Clinical Talks

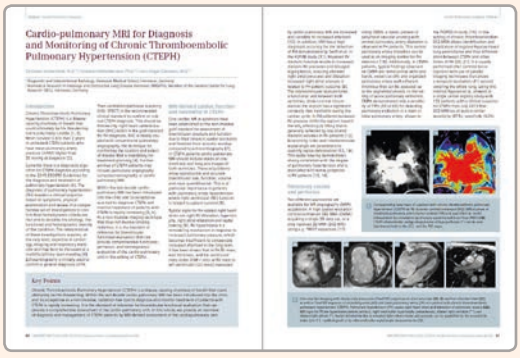

The centerpiece of the MAGNETOM World internet platform is MAGNETOM user's clinical results. Here you will find case reports and clinical methods on thoracic MRI.

Go to

Clinical Corner > Case Studies

Just a mouse click away you will find application videos and useful tips allowing you to optimize your daily MRI examinations.

Go to

Clinical Corner > Application Tips

On Microstructural Dynamics Underlying Myocardial Wall Thickening: Validation of *In Vivo* Diffusion Tensor CMR and Abnormalities in Hypertrophic and Dilated Cardiomyopathy

Sonia Nielles-Vallespin, Ph.D.[1,2,3,$]; Zohya Khalique, MB BS[2,3,4,$]; Pedro F. Ferreira, Ph.D.[2,3,4,$]; Ranil de Silva, MBBS Ph.D.[2,3,4]; Andrew D. Scott, Ph.D.[2,3,4]; Philip Kilner, M.D.[2,3,4]; Daniel Ennis, Ph.D.[5]; Peter Kellman, Ph.D.[1]; Robert S. Balaban, Ph.D.[1]; David N. Firmin, Ph.D.[2,3,4,#]; Andrew E. Arai, M.D.[1,#]; Dudley J. Pennell, M.D.[2,3,4,#]

[1] National Heart, Lung, and Blood Institute (NHLBI), National Institutes of Health (NIH), DHHS, Bethesda, MD, USA
[2] Cardiovascular MR Unit, Royal Brompton and Harefield NHS Foundation Trust, London, UK
[3] National Heart and Lung Institute, Imperial College London, UK
[4] NIHR Cardiovascular Biomedical Research Unit, Royal Brompton and Harefield NHS Foundation Trust, and Imperial College London, UK
[5] Department of Radiological Sciences, David Geffen School of Medicine, University of California, Los Angeles, Los Angeles, California, USA

[$] Joint first authors
[#] Joint senior authors

Abbreviations List

CMR	Cardiac Magnetic Resonance
DT	Diffusion Tensor
E1	Primary diffusion tensor eigenvector
E1A	E1 Angle
E1AR	E1 Angle Range
E2	Secondary diffusion tensor eigenvector
E2A	E2 Angle
SA	Sheetlet Angle
HA	Helix Angle
HAR	Helix Angle Range
LV	Left Ventricle
LAX	Long Axis
SAX	Short Axis

Introduction

Left ventricular contraction entails both longitudinal and circumferential shortening of the ventricle (~10–25%, depending on direction and depth) accompanied by radial wall thickening (>35%), together with twisting of the apex relative to the base [1]. The primary helical organisation of cardiomyocytes through the depth of the LV wall [2, 3] can be quantified by the helix angle (HA), [4, 5] (Fig. 1). However, cardiomyocytes only individually shorten by ~15% and thicken by ~8% during systole [1], meaning that the known conformational changes in cardiomyocytes in a helical arrangement alone are insufficient to explain the observed magnitude of systolic wall thickening [1]. The secondary arrangement of cardiomyocytes consists of laminar microstructures, 5–10 cardiomyocytes thick, termed sheetlets (Fig. 1) [4, 6]. Sheetlet reorientation [7, 8], quantified by changes in sheetlet angle (SA), is the predominant mechanism associated with macroscopic LV wall thickening *in vivo* [9–11].

Cardiomyopathies are disorders of myocardium affecting both structure and function in the absence of coronary artery disease or abnormal loading conditions [12]. Both hypertrophic and dilated cardiomyopathies (HCM, DCM) are relatively common with a prevalence of 1:500 and up to 1:250 respectively [13, 14] each being associated with a significant likelihood of cardiac events [15–17]. Phenotyping the myocardium is important for diagnosing and managing cardiomyopathies, particularly for identifying the sub-population at high risk of sudden cardiac death.

Diffusion tensor CMR (DT-CMR) potentially provides a novel approach for phenotyping through non-invasive interrogation of the 3D heart microarchitecture [18–36]. In previous work we implemented robust quantitative *in vivo* DT-CMR and confirmed its reproducibility in normals [37] and HCM [38].

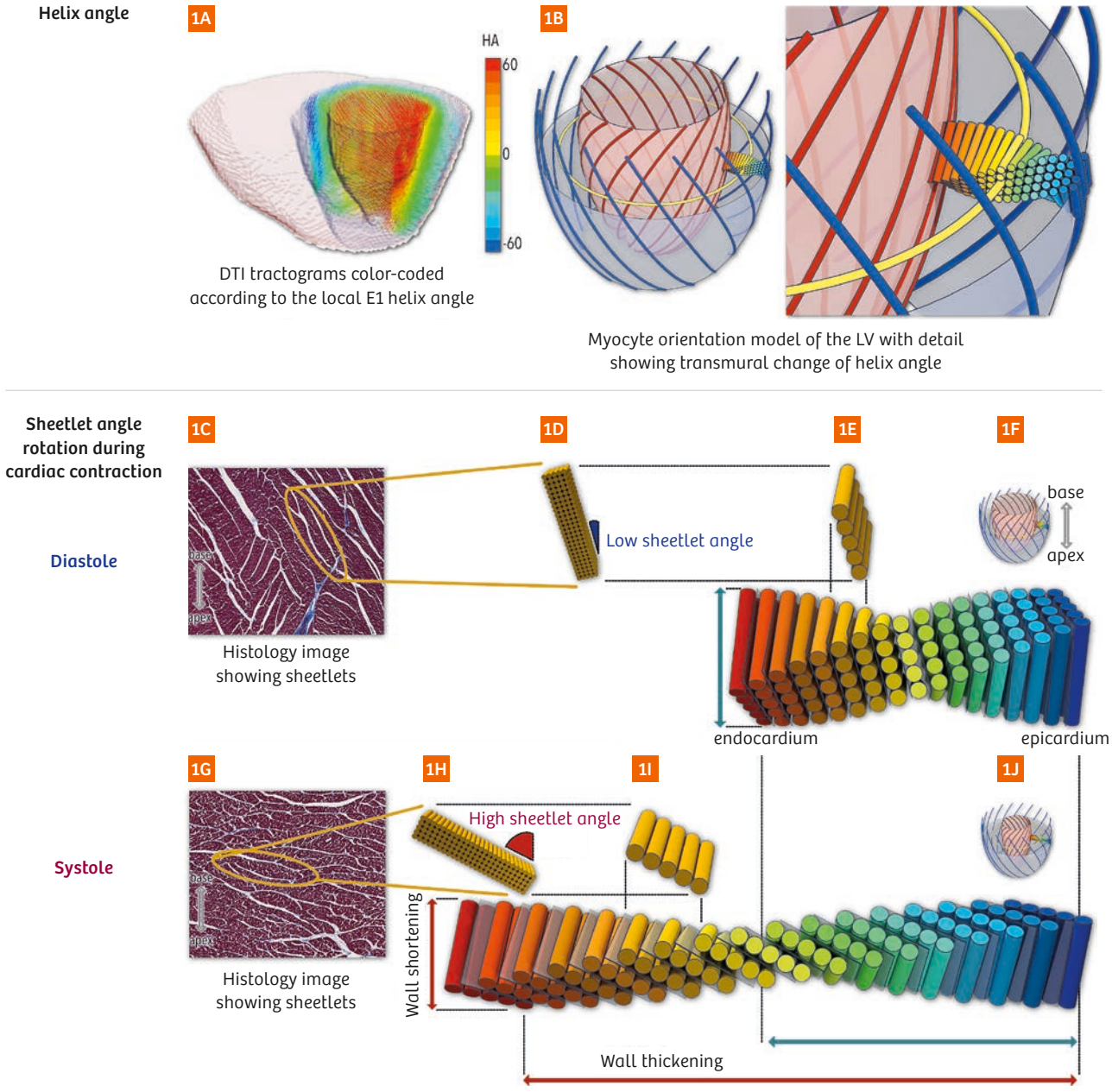

Figure 1: Illustration of the dynamics of myocardial helical and sheetlet microstructures of the left-ventricular (LV) myocardium during cardiac contraction. Multi-slice tractogram obtained from *ex vivo* DT-CMR, depicting the primary diffusion eigenvector (E1) direction color-coded according to the helix angle (HA) **(1A).** Schematic diagram of the helical structure of cardiomyocytes with zoom **(1B).** Left-handed helices in the epicardium are blue, circumferential alignments in the mid-myocardium are yellow, and right-handed helices in the endocardium are red. Schematic diagram of myocardial sheetlet microstructures in relaxed **(1F)** and contracted **(1J)** states. Mid-myocardial zooms of histology sections cut perpendicular to the local cardiomyocytes, acquired in this study from relaxed **(1C)** and contracted **(1G)** *ex vivo* heart samples. In them, the yellow ellipse surrounds a single sheetlet comprised of closely packed cardiomyocytes bounded by the pale cracks of shear layers. Its cardiomyocytes are represented in 3D by yellow cylinders in **(1D)** and **(1H)** which, for clarity, are then simplified to a single array in **(1E)** and **(1I),** and depicted together with more endocardial and epicardial sheetlets in their systolic **(1F)** and diastolic **(1J)** contractile states and orientations. The grey planes represent intervening cracks or shear layers. For clarity, no secondary, counter-oriented sheetlet populations have been represented although, like those illustrated, their orientations would also be expected to swivel towards more wall-perpendicular in systole or more wall-parallel in diastole. The sheetlet angle (SA) is also shown, and it is defined as the angle between the sheetlet and the local epicardial LV wall. In this illustration, SA varies from a low value (SA ~15°) in diastole **(1D)** to a high value (SA ~60°) in systole **(1H).** This represents the microstructural dynamic basis of the longitudinal and circumferential wall shortening that together deliver proportional wall thickening far greater than that of any single cardiomyocyte. *Figure from reference 40.*

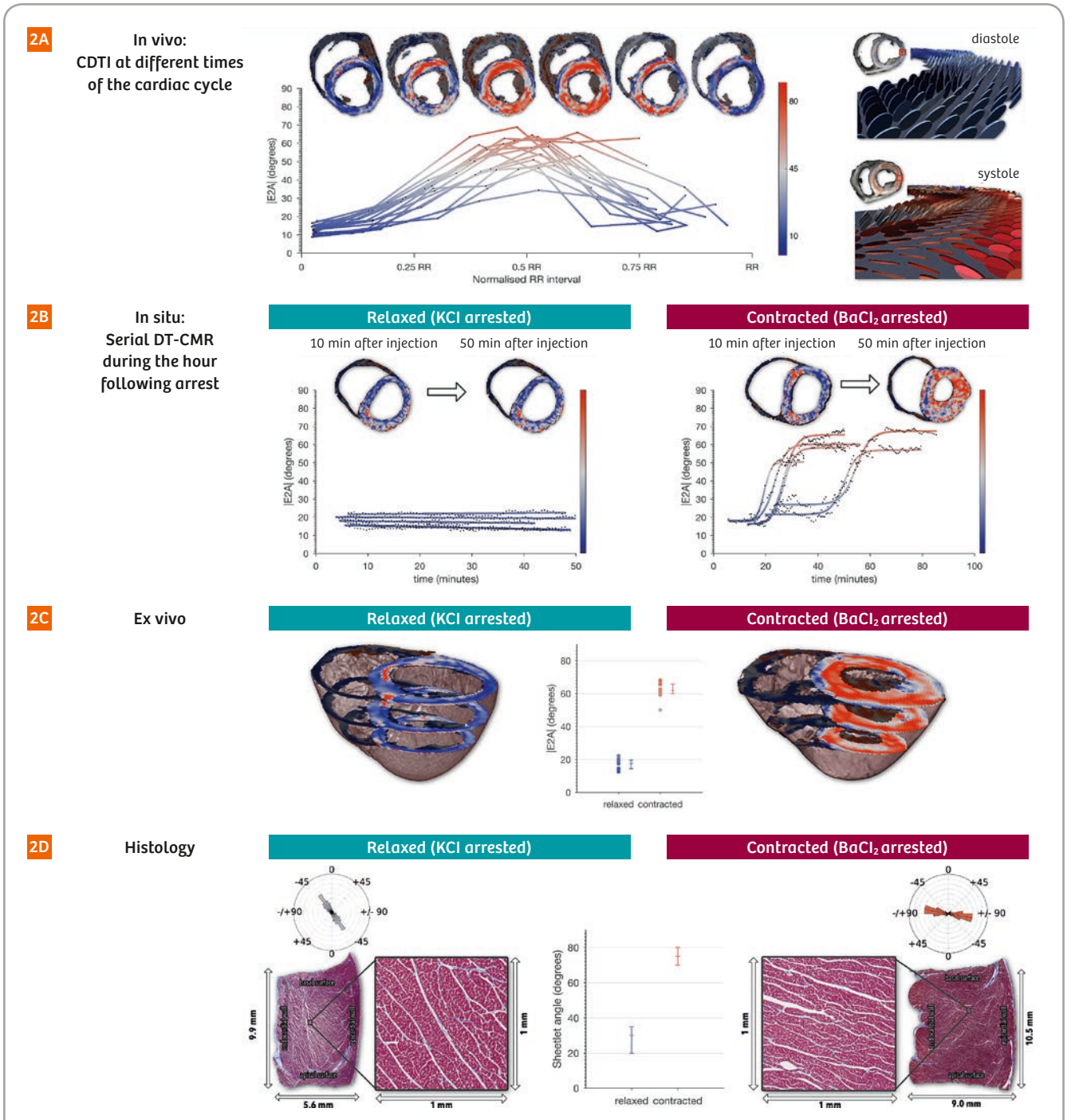

Figure 2: E2A changes substantially throughout the cardiac cycle; the increase in E2A from diastole to systole is consistently observed *in vivo, in situ, and ex vivo,* and corresponds well to changes in sheetlet angle (SA) in histology. Example *in vivo* E2A maps at multiple points of the cardiac cycle, together with a plot of E2A throughout the entire cardiac cycle for all *in vivo* experiments **(2A).** The inset in Figure 2A illustrates E2A changes from diastole to systole. Oblique views of *in vivo* short-axis images with detail views of the lateral wall, depicting the measured planes defined by E1 and E2, color-coded according to absolute E2A. As these planes swivel from diastole to systole, E2A increases and their color changes from blue to red. Example *in situ* E2A maps, ~10 minutes and ~50 minutes after injection, with plots of the E2A over a period of ~60 minutes after injection of KCl and $BaCl_2$ for all hearts **(2B).** Example *ex vivo* E2A maps at 3 mid-ventricular slices and plot of E2A in all *ex vivo* relaxed and contracted hearts **(2C).** Example long axis histological cuts with mesocardial layer details demonstrating sheetlets in relaxed and contracted heart tissue samples, with their corresponding angular histograms, demonstrating the sheetlet and cleavage plane reorientation **(2D).** Plots of absolute SA derived from the relaxed and contracted histological data **(2D).** *Figure from reference 40.*

We reported E2A changes from systole to diastole in HCM consistent with exaggerated systolic contraction and attenuated diastolic relaxation [24]. In this work we comprehensively validated *in vivo* DT-CMR measures[1] of cardiac microstructure against histology, analysed the influence of cyclic tissue deformation on the diffusion measurements [1, 24, 26, 39], characterized microstructural dynamics associated with myocardial wall thickening in the loaded beating heart *in vivo*, and characterized altered microstructural dynamics in HCM and DCM.

Methods

Detailed methods are described elsewhere [40]. Animal procedures[2] were approved by the NHLBI Animal Care and Use Committee. In brief, *in vivo* DT-CMR was acquired throughout the cardiac cycle in healthy swine, followed by *in situ* and *ex vivo* DT-CMR and validated against co-registered histology (Fig. 2). Cardiac arrest induced by $BaCl_2$ [30] slowed cardiac contraction by three orders of magnitude (from ~300 ms *in vivo* to ~5 minutes *in situ*) allowing DT-CMR during myocardial thickening in the absence of cyclical strain effects. The National Research Ethics Committee approved the clinical study. DCM and HCM were diagnosed in accordance with guidelines [41]. *In vivo* DT-CMR was performed both at late-diastole and end-systole in 19 healthy controls, 19 DCM patients, and 13 HCM patients.

Results and discussion

The results of the preclinical study demonstrate that both helical and sheetlet microstructural dynamics can be effectively interrogated *in vivo* in the beating heart with DT-CMR. Limited changes in helical microstructure, measured as E1A and HA by DT-CMR and histology, between different contractile states were observed. By contrast, E2A increased substantially over the cardiac cycle. Changes in E2A with contraction were consistently observed under all experimental conditions and closely agreed with SA changes measured histologically (Fig. 2). These data confirm *in vivo* E1A as an index of helix angle and E2A as an index of sheetlet angle and support the hypothesis that reorientations of secondary laminar microstructures underlie myocardial thickening, and can be measured by DT-CMR.

In healthy human controls, E2A was greater in systole (65°) than diastole (18°, $p < 0.001$), with an E2A mobility of 45°. HCM patients showed significantly greater E2A in diastole than controls (48°, $p < 0.001$) with impaired E2A mobility (23°, $p < 0.001$). In DCM, E2A was similar to controls in diastole (23°, $p = 1.0$), but systolic values were markedly lower (40°, $p < 0.001$) with impaired E2A mobility (20°, $p < 0.001$) (Figs. 3, 4). Thus we show for the first time, a unique pattern of sheetlet behavior in DCM patients with persistence of near-diastolic conformation of sheetlets in systole. The opposite pattern was observed in HCM, with persistence of near-systolic sheetlet orientation was observed in diastole. These observations provide new insight into aberrant dynamics of laminar microstructures in cardiomyopathies and identify distinct mechanisms underlying reduced strain development. These mechanistic findings have potential to be useful for assessment of effective new drug therapies.

We also compared *in vivo, in situ,* and *ex vivo* data to assess the influence of strain on *in vivo* DT-CMR data [1, 24, 26, 39, 42]. The correspondence between *in vivo, in situ,* and *ex vivo* E2A changes indicates that the *in vivo* E2A observations originate predominantly from phasic changes of micro-structural orientation. This is further supported by our model of slowed myocardial thickening over several minutes

[1] WIP, the product is currently under development and is not for sale in the US and in other countries. Its future availability cannot be ensured.
[2] Siemens MAGNETOM products have been designed and tested for use on humans only. None of these products are intended to be used for veterinary purposes.

3

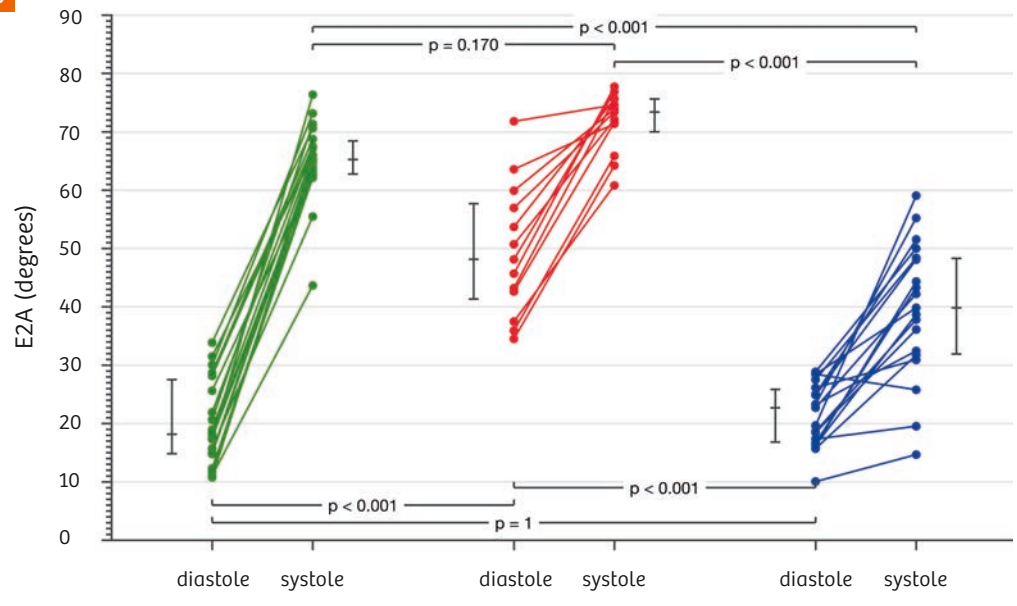

Figure 3: Plots of median E2A at diastole and systole in healthy volunteers, HCM and DCM patients. In all plots the median and IQR are also shown. In HCM, diastolic E2A is markedly higher than in controls, while systolic E2A values are similar. In DCM, diastolic E2A values are similar to controls, while systolic E2A values are markedly reduced. *Figure from reference 40.*

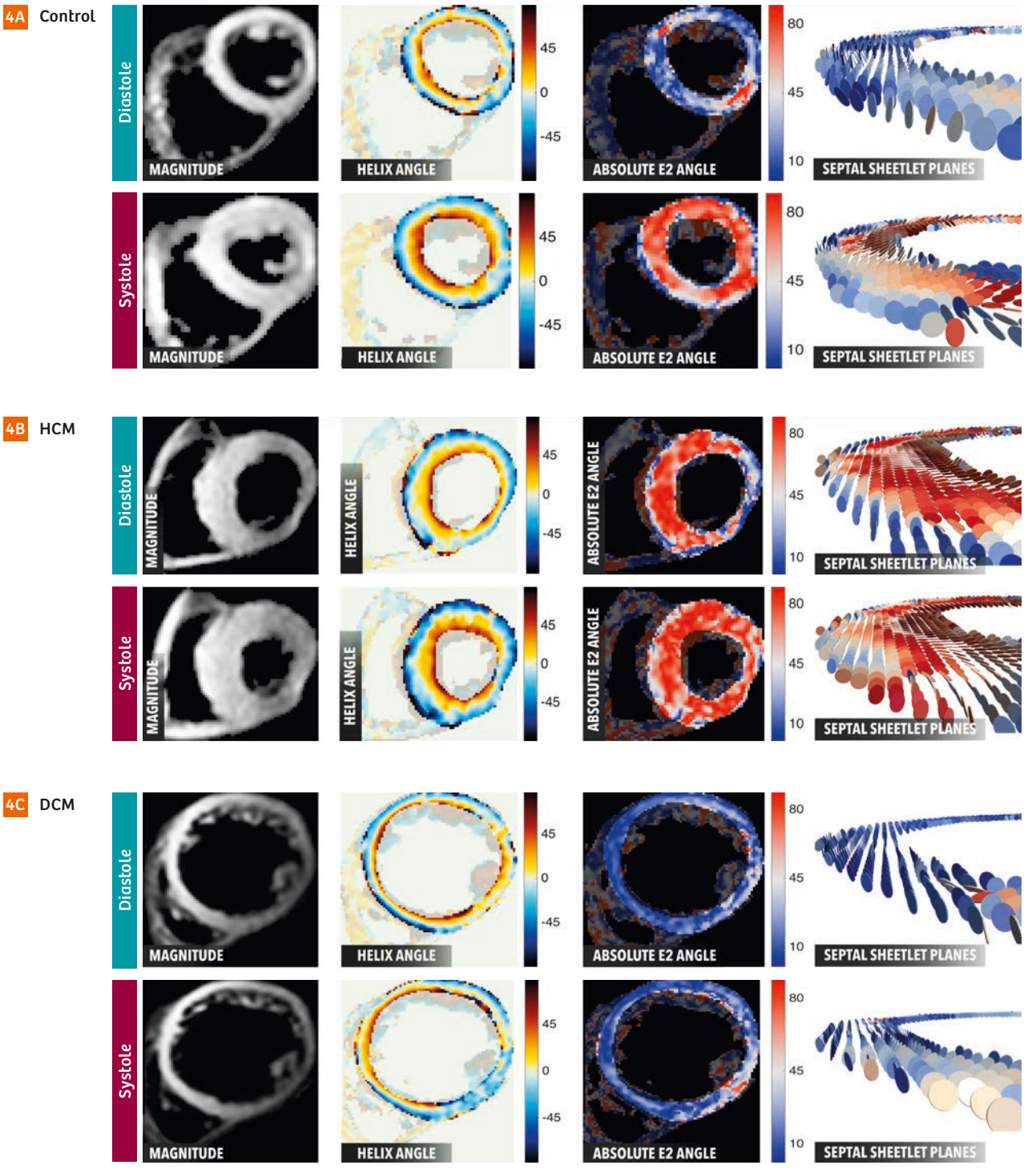

Figure 4: Example b-value = 0 images, E1A maps, E2A maps and E2A glyphs in controls, HCM and DCM. The E1A maps show similar E1A distributions in all populations and contractile states. The E2A maps and glyphs are color coded according to absolute E2 angle (low E2A in blue for wall parallel sheetlets; high E2A in red for wall perpendicular sheetlets). E2A changes are from blue in diastole to red in systole in healthy controls. The HCM example takes a healthy systolic conformation (wall perpendicular sheetlets) but an incomplete diastolic conformation (mix of wall parallel and wall perpendicular sheetlets). The DCM example takes a healthy diastolic conformation (wall parallel sheetlets) but an incomplete systolic conformation (mix of wall parallel and wall perpendicular sheetlets). *Figure from reference 40.*

induced by $BaCl_2$ administration [43, 44], which occurs in the absence of cyclical strain effects, and yet demonstrates remarkably similar behaviour of E1A and E2A to that observed during *in vivo* experiments. Comparisons of the relationships between ΔE2A and ΔWT *in vivo* and with $BaCl_2$ *in situ* provide an estimate of the maximum potential influence of cyclical strain to *in vivo* E2A of ~17%. This may be an overestimate, since the different loading conditions between *in vivo* and $BaCl_2$ *in situ* experiments might also account for some of the differences observed experimentally. The changes in E2A shown in DCM and HCM greatly exceed this potential confounder. Furthermore, the differences in the diastolic and systolic conformations of E2A in HCM and DCM occur in the context of similarly impaired strains, further supporting E2A mobility as a robust and clinically relevant measure.

In vivo DT-CMR may provide new mechanistic insights into altered ventricular mechanics, adverse remodeling and the substrate for arrhythmogenesis in a variety of clinical conditions including post-MI, valvular heart disease as well as inherited and congenital cardiac diseases. Other applications include identifying the potential for LV contractile recovery, reverse remodeling, and as a new monitoring marker for interventions to improve contractile function.

Conclusion

We show that myocardial sheetlet reorientation in the loaded and beating heart *in vivo* is the predominant mechanism associated with systolic LV wall thickening, and that primary and secondary microstructures in the myocardium and their dynamic reorientations during cardiac contraction can be studied non-invasively by *in vivo* DT-CMR. In DCM, DT-CMR shows reduced sheetlet mobility and a diastolic conformation, which contrasts with the reduced mobility and systolic conformation seen in HCM, despite similarly reduced systolic myocardial strain. In general terms at the microstructural level, this indicates a failure of systolic sheetlet rotation in DCM and a failure of relaxation of sheetlets in HCM. These results provide the rationale for further study of the microstructural dynamics of cardiac contraction and myocardial dysfunction using *in vivo* DT-CMR to provide new diagnostic and prognostic information in human cardiac disease.

Acknowledgements

The authors would like to thank Joni Taylor, Shawn Kozlov, Katherine Lucas for expert animal care and Rick Wage and Gill Smith for their expert CMR technical help. We would also like to thank Prof Fred Epstein and his team for their support with their *in vivo* strain measurement technique (DENSE). We would also like to thank Prof. Hewitt, Dr Candice Perry, and Dr Kris Ylaya for the use of the Nanozoomer.

This article is adapted from reference 40: Nielles-Vallespin S, Khalique Z, Ferreira PF et al. Assessment of Myocardial Microstructural Dynamics by In Vivo Diffusion Tensor Cardiac Magnetic Resonance. J Am Coll Cardiol 2017 ;69: 661-76.

References

1 Axel L, Wedeen V, Ennis D. Probing dynamic myocardial microstructure with cardiac magnetic resonance diffusion tensor imaging. Journal of Cardiovascular Magnetic Resonance 2014;16:89.
2 Streeter D, Bassett D. An engineering analysis of myocardial fiber orientation in pigs left ventricle in systole. Anat Rec 1966;155:503.
3 Streeter D, Spotnitz H, Patel D, Ross J, Sonnenbl E. Fiber Orientation in Canine Left Ventricle during Diastole and Systole. Circ Res 1969;24:339.
4 Sands G, Gerneke D, Hooks D, Green C, Smaill B, LeGrice I. Automated imaging of extended tissue volumes using confocal microscopy. Microsc Res Tech 2005;67:227-39.
5 Smerup M, Nielsen E, Agger P et al. The three-dimensional arrangement of the myocytes aggregated together within the mammalian ventricular myocardium. Anat Rec 2009;292:1-11.
6 Hales PW, Schneider JE, Burton RA, Wright BJ, Bollensdorff C, Kohl P. Histo-anatomical structure of the living isolated rat heart in two contraction states assessed by diffusion tensor MRI. Prog Biophys Mol Biol 2012;110:319-30.
7 Harrington K, Rodriguez F, Cheng A et al. Direct measurement of transmural laminar architecture in the anterolateral wall of the ovine left ventricle: new implications for wall thickening mechanics. Am J Physiol Heart Circ Physiol 2005;288:H1324-30.
8 Spotnitz H, Spotnitz W, Cottrell T, Spiro D, Sonnenbl E. Cellular basis for volume related wall thickness changes in Rat left-ventricle. J Mol Cell Cardiol 1974;6:317.
9 Costa KD, Takayama Y, McCulloch AD, Covell JW. Laminar fiber architecture and three-dimensional systolic mechanics in canine ventricular myocardium. Am J Physiol 1999;276:H595-607.
10 LeGrice I, Takayama Y, Covell J. Transverse shear along myocardial cleavage planes provides a mechanism for normal systolic wall thickening. Circ Res 1995;77:182-93.
11 Takayama Y, Costa KD, Covell JW. Contribution of laminar myofiber architecture to load-dependent changes in mechanics of LV myocardium. Am J Physiol Heart Circ Physiol 2002;282:H1510-20.
12 Elliott P, Andersson B, Arbustini E et al. Classification of the cardiomyopathies: a position statement from the European Society Of Cardiology Working Group on Myocardial and Pericardial Diseases. Eur Heart J 2008;29:270-6.
13 Gersh BJ, Maron BJ, Bonow RO et al. 2011 ACCF/AHA guideline for the diagnosis and treatment of hypertrophic cardiomyopathy: a report of the American College of Cardiology Foundation/American Heart Association Task Force on Practice Guidelines. Circulation 2011;124:e783-831.
14 Hershberger RE, Hedges DJ, Morales A. Dilated cardiomyopathy: the complexity of a diverse genetic architecture. Nat Rev Cardiol 2013;10:531-47.
15 Authors/Task Force m, Elliott PM, Anastasakis A et al. 2014 ESC Guidelines on diagnosis and management of hypertrophic cardiomyopathy: the Task Force for the Diagnosis and Management of Hypertrophic Cardiomyopathy of the European Society of Cardiology (ESC). Eur Heart J 2014;35:2733-79.
16 Felker GM, Thompson RE, Hare JM et al. Underlying causes and long-term survival in patients with initially unexplained cardiomyopathy. N Engl J Med 2000;342:1077-84.
17 Gulati A, Jabbour A, Ismail TF et al. Association of fibrosis with mortality and sudden cardiac death in patients with nonischemic dilated cardiomyopathy. JAMA 2013;309:896-908.
18 Basser P. Inferring microstructural features and the physiological state of tissues from diffusion- weighted images. NMR Biomed 1995;8:333-44.
19 Basser PJ, Mattiello J, LeBihan D. MR diffusion tensor spectroscopy and imaging. Biophys J 1994;66:259-67.

20 Edelman R, Gaa J, Wedeen V et al. In-vivo measurement of water diffusion in the human heart. Magn Reson Med 1994;32:423-8.
21 Reese TG, Weisskoff RM, Smith RN, Rosen BR, Dinsmore RE, Wedeen VJ. Imaging myocardial fiber architecture in vivo with magnetic resonance. Magn Reson Med 1995;34:786-91.
22 Garrido L, Wedeen VJ, Kwong KK, Spencer UM, Kantor HL. Anisotropy of water diffusion in the myocardium of the rat. Circ Res 1994;74:789-93.
23 Gamper U, Boesiger P, Kozerke S. Diffusion imaging of the in vivo heart using spin echoes--considerations on bulk motion sensitivity. Magn Reson Med 2007;57:331-7.
24 Ferreira PF K, McGill L, Nielles-Vallespin S et al. In vivo cardiovascular magnetic resonance diffusion tensor imaging shows evidence of abnormal myocardial laminar orientations and mobillity in hypertrophic cardiomyopathy. J Cardiovasc Magn Reson 2014;16:87.
25 Tseng W-Y, Dou J, Reese T, Wedeen V. Imaging myocardial fiber disarray and intramural strain hypokinesis in hypertrophic cardiomyopathy with MRI. J Magn Reson Imaging 2006;23:1-8.
26 Dou J, Reese T, Tseng W, Wedeen V. Cardiac diffusion MRI without motion effects. Magn Reson Med 2002;48:105-14.
27 Kung G, Nguyen T, Itoh A et al. The presence of two local myocardial sheet populations confirmed by diffusion tensor MRI and histological validation. J Magn Reson Imaging 2011;34:1080-91.
28 Scollan D, Holmes A, Winslow R, Forder J. Histological validation of myocardial microstructure obtained from diffusion tensor magnetic resonance imaging. Am J Physiol 1998;275:H2308-18.
29 Scollan D, Holmes A, Zhang J, Winslow R. Reconstruction of cardiac ventricular geometry and fiber orientation using magnetic resonance imaging. Ann Biomed Eng 2000;28:934-44.

Contact

Dr Sonia Nielles-Vallespin
National Heart, Lung, and Blood Institute
National Institutes of Health

Bldg 10, Rm B1D401
10 Center Drive
Bethesda, MD 20892-1061
USA
Phone: +1 301 451 0149
sonia.nielles-vallespin@nih.gov

30 Chen J, Liu W, Zhang H et al. Regional ventricular wall thickening reflects changes in cardiac fiber and sheet structure during contraction: quantification with diffusion tensor MRI. Am J Physiol Heart Circ Physiol 2005;289:H1898-907.
31 Hales P, Schneider J, Burton R, Wright B, Bollensdorff C, Kohl P. Histo-anatomical structure of the living isolated rat heart in two contraction states assessed by diffusion tensor MRI. Prog Biophys Mol Biol 2012;110:319-30.
32 Dou J, Tseng WY, Reese TG, Wedeen VJ. Combined diffusion and strain MRI reveals structure and function of human myocardial laminar sheets in vivo. Magn Reson Med 2003;50:107-13.
33 Stoeck CT, Kalinowska A, von Deuster C et al. Dual-phase cardiac diffusion tensor imaging with strain correction. PLoS One 2014;9:e107159.
34 Helm P, Younes L, Beg M et al. Evidence of structural remodeling in the dyssynchronous failing heart. Circ Res 2006;98:125-32.
35 Helm PA, Tseng HJ, Younes L, McVeigh ER, Winslow RL. Ex vivo 3D diffusion tensor imaging and quantification of cardiac laminar structure. Magn Reson Med 2005;54:850-9.
36 Cheng YJ, Lang D, Caruthers SD, Efimov IR, Chen J, Wickline SA. Focal but reversible diastolic sheet dysfunction reflects regional calcium mishandling in dystrophic mdx mouse hearts. Am J Physiol Heart Circ Physiol 2012;303:H559-68.
37 Nielles-Vallespin S, Mekkaoui C, Gatehouse P et al. In vivo diffusion tensor MRI of the human heart: reproducibility of breath-hold and navigator-based approaches. Magn Reson Med 2012;70:454-65.
38 McGill LA, Ismail TF, Nielles-Vallespin S et al. Reproducibility of in-vivo diffusion tensor cardiovascular magnetic resonance in hypertrophic cardiomyopathy. J Cardiovasc Magn Reson 2012;14:86.
39 Reese T, Wedeen V, Weisskoff R. Measuring diffusion in the presence of material strain. J Magn Reson B 1996;112:253-8.
40 Nielles-Vallespin S, Khalique Z, Ferreira PF et al. Assessment of Myocardial Microstructural Dynamics by In Vivo Diffusion Tensor Cardiac Magnetic Resonance. J Am Coll Cardiol 2017;69:661-676.
41 Richardson P, McKenna W, Bristow M et al. Report of the 1995 World Health Organization/International Society and Federation of Cardiology Task Force on the Definition and Classification of cardiomyopathies. Circulation 1996;93:841-2.
42 Tseng W, Reese T, Weisskoff R, Wedeen V. Cardiac diffusion tensor MRI in vivo without strain correction. Magn Reson Med 1999;42:393-403.
43 Munch DF, Comer HT, Downey JM. Barium contracture: a model for systole. Am J Physiol 1980;239:H438-42.
44 Saeki Y, Shibata T, Shiozawa K. Excitation-contraction coupling in mammalian cardiac muscle during Ba2+-induced contracture. Am J Physiol 1981;240:H216-21.

Recent Advances in In-bore Optical Prospective Motion Correction

Aditya Singh[1,2]; Will Alameida[1]; Maxim Zaitsev[3]; Jeffrey Yu[1,2]

[1] KinetiCor Inc., Honolulu, HI, USA
[2] Queen's Health Systems and University of Hawaii, Honolulu, HI, USA
[3] University Medical Center Freiburg, Department of Radiology, Medical Physics, Freiburg, Germany

Researchers have attempted to compensate for patient motion in the scanner for two decades. Several research studies have demonstrated the advantages of using an in-bore optical tracking system in conjunction with customized software interface to perform real-time motion correction [1–9].

Clinical adoption of prospective motion correction (PMC) will require seamless integration into the MR clinical workflow and acceptable patient comfort levels with fiduciary markers, as well as consistent and significant improvements in MR image quality. This article highlights efforts made by KinetiCor Inc. (Honolulu, HI, USA) and its world-wide scientific collaboration network to elevate in-bore optical tracking based PMC technology into clinical applications specific to neuroimaging.

Introduction

Motion artifacts caused by patient motion remain one of the last unsolved challenges to improving quality and reliability of MR imaging. As MR scanners reach higher levels of resolution, the need for motion correction becomes even more apparent. Unfortunately, those patient populations in the greatest need of a clear scan are often unable to obtain diagnostic quality images due to uncontrolled motion caused by pain, trauma, neurological disorders, or age. The costs of repeating scans, rescheduling appointments, and sedating patients are high. A recent study by Andre et al. [10] estimates the annual operational cost impact per scanner at $98,697.

	Motion Artifacts	Diagnostic Quality
MPRAGE	None	Diagnostic
FLAIR	None	Diagnostic

Table 1: Radiologist ratings.

How it works

KinetiCor motion correction technology[1] includes an in-bore retrofit motion tracking system (Fig. 1A) and software to update sequence parameters in real-time with actual head position. This allows the scanner to determine where the head precisely is at any given moment.

The motion tracking works by tracking a small fiducial marker that can be affixed to forehead, nose (Fig. 1B), or upper jaw. The translations and rotations of head are transmitted to the customized software, libXPACE, that resides on the real-time controller of the MR scanner.

[1] WIP, the product is currently under development and is not for sale in the US and in other countries. Its future availability cannot be ensured.

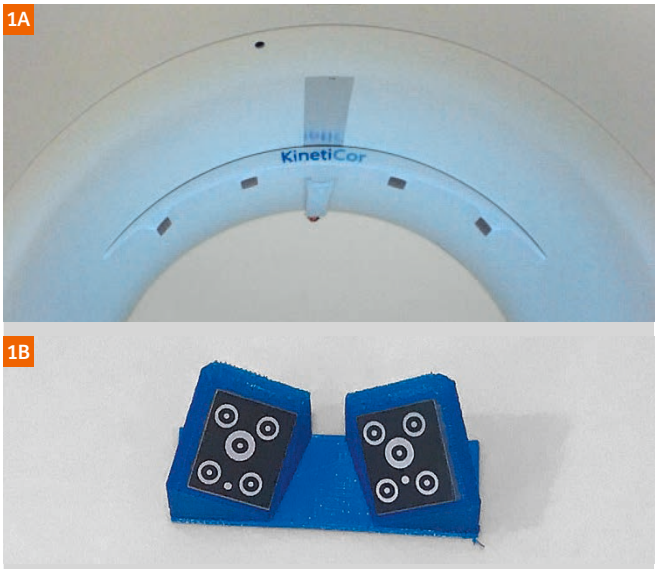

Figure 1: (1A) KinetiCor quad camera retrofit system mounted inside a MAGNETOM Skyra 3T MR scanner (Siemens Healthcare, Erlangen, Germany) and **(1B)** dual-marker nose bridge mount with markers.

Benefits of KinetiCor system

Some of the major challenges to in-bore optical tracking include marker visibility as head coils may vary from scanner to scanner. KinetiCor has solved this problem by designing a 4-camera system that is optimized for various head coil geometries. The system can simultaneously track 5 markers at the rate of 60 frames/s.

KinetiCor's prospective motion correction system does not consume any scanner bandwidth and therefore does not increase the scan time. This allows for clearer images and actually improves efficiency because time doesn't need to be wasted repeating sequences that were compromised by motion. The tracking information can be used to correct both in-plane and through-plane motion and it can be incorporated into pulse sequences easily.

In addition, KinetiCor and its academic partners at Freiburg are developing the ability to remove motion correction post-scanning to view uncorrected images [11]. The KinetiCor system and associated research sequences are currently for investigational use only.

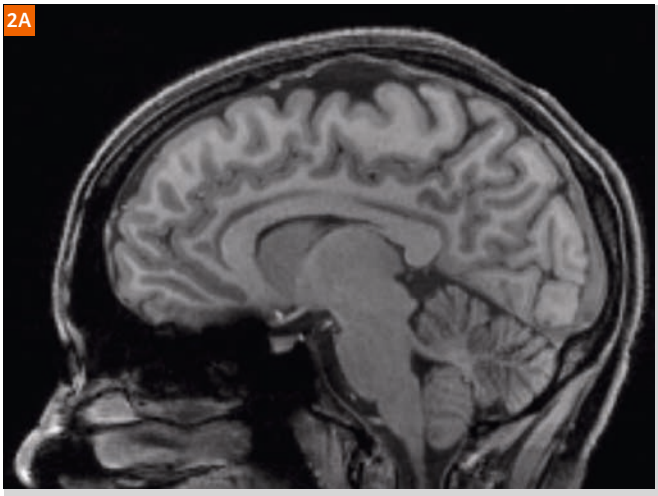

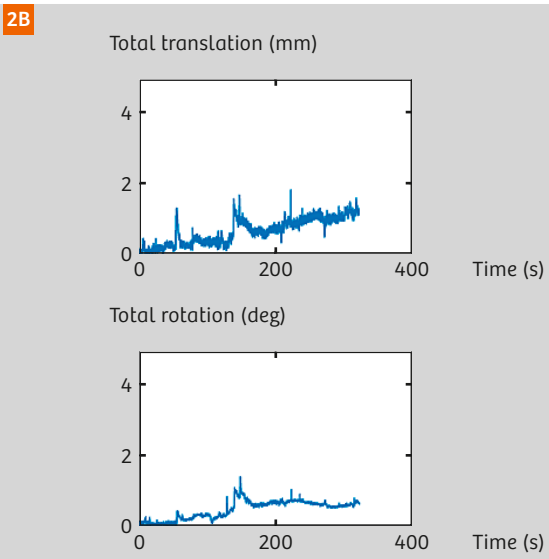

Figure 2: MPRAGE data from one of the study volunteers showing a slice from the MPRAGE **(2A)** and the motion traces **(2B)**.

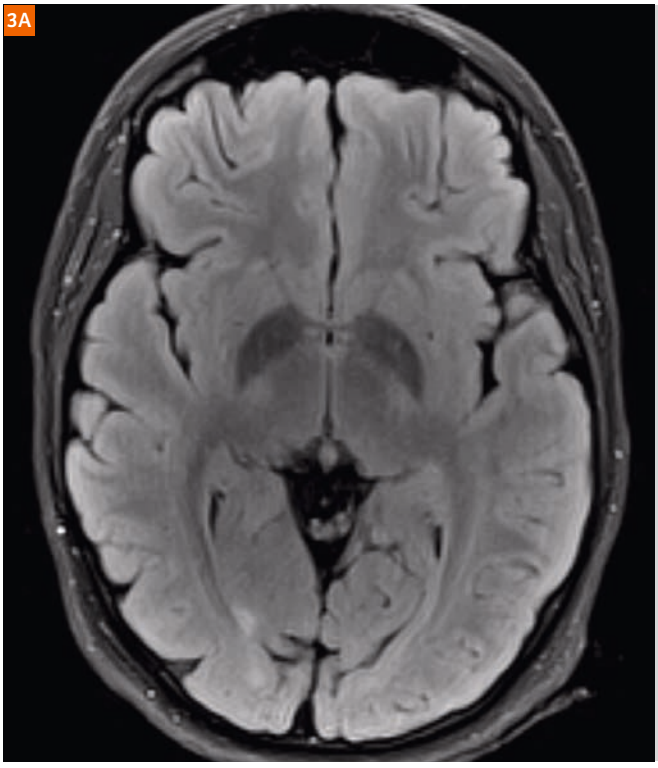

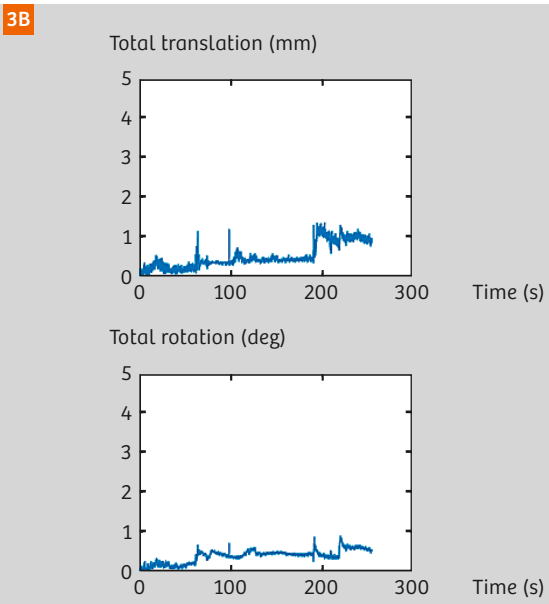

Figure 3: FLAIR data from one of the study volunteers showing a slice from the FLAIR images **(3A)**. The motion traces **(3B)** indicate that the participant shifted head position during the scan. The maximum rotation is approximately 1 degree.

Clinical study overview

To understand the impact of PMC technology in a clinical workflow, KinetiCor is currently running a multi-center clinical study. Two of the study centers are conducting the study on MAGNETOM Skyra scanners and one site is using a 3T MAGNETOM Prisma (Siemens Healthcare, Erlangen, Germany). The study is IRB (institutional review board) approved and informed consents were obtained from all the participants. The goals of the study are to:

1) Characterize the prevalence of motion in a clinical setting
2) Evaluate the use of KinetiCor PMC enabled research sequences (MPRAGE, FLAIR) that have been added to the clinical protocol.
3) Obtain feedback from MR technologists and patients on the time required to affix markers, as well as overall comfort levels for patients.

Two markers were mounted on the bridge of the nose through a 3D printed marker mount fabricated in-house. The marker mount with markers is shown in Figure 1B.

Preliminary evaluation outcomes

The images obtained in the study were evaluated by a board certified Radiologist who was blinded to the motion traces. Acquired motion data was processed to calculate the total translation (norm of translation) and total rotation.

Figures 2 and 3 show the results from one study participant. Figure 2 shows the motion traces and an image from motion corrected MPRAGE and Figure 3 shows the motion traces and an image from the FLAIR sequence. The comments from the Radiologist for the participant for both images are shown in Table 1. The images from both sequences were rated to be of diagnostic quality. Of the initial 15 datasets reviewed by the radiologist, none of the MPRAGE or FLAIR images were rated as non diagnostic.

MR technicians reported that markers were easily affixed in under one minute, including the time required to prepare the area with an alcohol wipe, for 29 of the 30 subjects studied (in the remaining case it took between one and two minutes). Of interest, it took less time to affix the tracking marker than it took to affix earplugs on the subjects.

Patient comfort levels with wearing and removing the marker were also studied. Initial study results revealed that 29 subjects indicated favorable comfort levels with the marker, with one subject not providing any input.

Conclusions and outlook

At present the technical issues related to the previous prototype implementations of the PMC technology are largely resolved: the current solution occupies very little bore space and is compatible with routine operations at the scanner. The handling of the marker and patient comfort has also improved substantially. In particular, the present solution addresses the hygiene aspects by introducing single-use markers and mounts as required for the future clinical use. The initial evaluation of the imaging outcomes reveals a favorable performance of the PMC system.

References

1 Maclaren J, Herbst M, Speck O, Zaitsev M. Prospective motion correction in brain imaging: a review. Magn Reson Med. 2012 May; 69(3):621–636. doi:10.1002/mrm.24314.
2 Speck O, Hennig J, Zaitsev M. Prospective real-time slice-by-slice motion correction for fMRI in freely moving subjects. Magn Reson Mater Phy 2006 May; 19(2):55–61. doi:10.1007/ s10334-006-0027-1.
3 Zaitsev M, Dold C, Sakas G, Hennig J, Speck O. Magnetic resonance imaging of freely moving objects: prospective real-time motion correction using an external optical motion tracking system. Neuroimage 2006 July; 31(3):1038–1050. doi:10.1016/j. neuroimage.2006.01.039.
4 Qin L, van Gelderen P, Derbyshire JA, Jin F, Lee J, de Zwart JA, Tao Y, Duyn JH. Prospective head-movement correction for high-resolution MRI using an in-bore optical tracking system. Magn Reson Med. 2009 Oct ;62(4):924–934. doi:10.1002/mrm.22076.
5 Andrews-Shigaki BC, Armstrong BS, Zaitsev M, Ernst T. Prospective motion correction for magnetic resonance spectroscopy using single camera Retro-Grate reflector optical tracking. J Magn Reson Imaging 2011 Jan 27; 33(2):498–504.
6 Schulz J, Siegert T, Reimer E, Labadie C, Maclaren J, Herbst M, Zaitsev M, Turner R. An embedded optical tracking system for motion-corrected magnetic resonance imaging at 7T. Magn Reson Mater Phy 2012 Dec; 25(6):443–453. doi:10.1007/ s10334-012-0320-0.
7 Lange T, Maclaren J, Herbst M, Lovell-Smith C, Izadpanah K, Zaitsev M. Knee cartilage MRI with in situ mechanical loading using prospective motion correction. Magn Reson Med. 2014 Feb; 71(2):516-523. doi:10.1002/mrm.24679.
8 Gummus K, Keating B, White N, Andrews-Shigaki B, Armstrong B, Maclaren J, Zaitsev M, Dale A, Ernst T. Comparison of optical and MR-based tracking. Magn Reson Med. 2014 Sept; 74(3):894-902.
9 Forman C, Aksoy M, Hornegger J, Bammer R. Self-encoded marker for optical prospective head motion correction in MRI. Med Image Anal. 2011 Oct;15(5):708-19. doi: 10.1016/j.media.2011.05.018.
10 Andre JB, Mossa-Basha, M, Bresnahan BW, Hoff MN, Smith CP, Anzai Y, Cohen WA. Toward Quantifying the Prevalence, Severity and Cost Estimates Associated With Patient Motion During Clinical MR Examinations. J Am Coll Radiol, 2015; 12(7):689-695.
11 Zahneisen B, Keating B, Singh A, Herbst M, Ernst T. Reverse Retrospective motion correction. Magn Reson Med. 2015 July 3; 75(6):2341-2349.

Contact

Aditya Singh
Kineticor

3465 Waialae Avenue
Suite 300A
Honolulu, HI 96816
USA
Phone: +1 (808) 380-1444
aditya.singh@kineticor.com

Pioneers of Connectome Gradients

Ralph Kimmlingen

Siemens Healthineers, HC DI MR TR R&D-PL, Erlangen, Germany

Abstract

A typical human brain contains 100 billion neurons which have about 10,000 individual connections with their neighbors. Being able to map structural and functional connectivity of an individual brain could be a first step on a new way of understanding and diagnosing mental illnesses. Continuous improvements on noninvasive magnetic resonance imaging (MRI) methods like functional MRI, resting-state MRI, and diffusion MRI enable this information (connectomics) to be obtained for the first time on a large human databasis. A key parameter is the available gradient field strength for diffusion-sensitive MRI sequences [1–3]. Siemens MR has developed two powerful prototype gradient systems for this purpose, which have been employed at five different locations in the US and Europe since 2011 (Fig. 1).

Up to today, the nervous system circuit diagram ('Connectome') of few creatures is known. Back in the early 1980s the little roundworm called *C. elegans* was discovered to have a nervous system of roughly 300 neurons showing a total of about 7,000 connections [4, 5]. Using invasive anatomical and neural-tracing techniques, mammalian brains like that of mice or primates are still under investigation. These methods are capable of an in-plane resolution of 40 µm [6, 7].

New non-invasive imaging methods which enable the study of brain connectivity of living humans have been developed since the beginning of this century. They are known as MR Imaging of anisotropic diffusion of water in the brain, and resting state fMRI [8–10]. The related advances in imaging technologies and data evaluation are empowering us today to study the human brain as an entire organ.

A group known as 'Blueprint for Neuroscience Research', a collaboration among 15 National Institutes of Health (NIH) in Bethesda, Maryland, USA, decided in 2009 to fund a five-year initiative for mapping the brain's long-distance communications network. The goal of the so called Human Connectome Project (HCP) was set to construct a map of the structural and functional neural connections *in vivo* within and across individuals. The HCP was funded with $40 million and comprised two research efforts: the first, a five-year project at the Center for Magnetic Resonance Research (CMRR) in Minneapolis, Minnesota, in collaboration with Washington University, St. Louis,

1

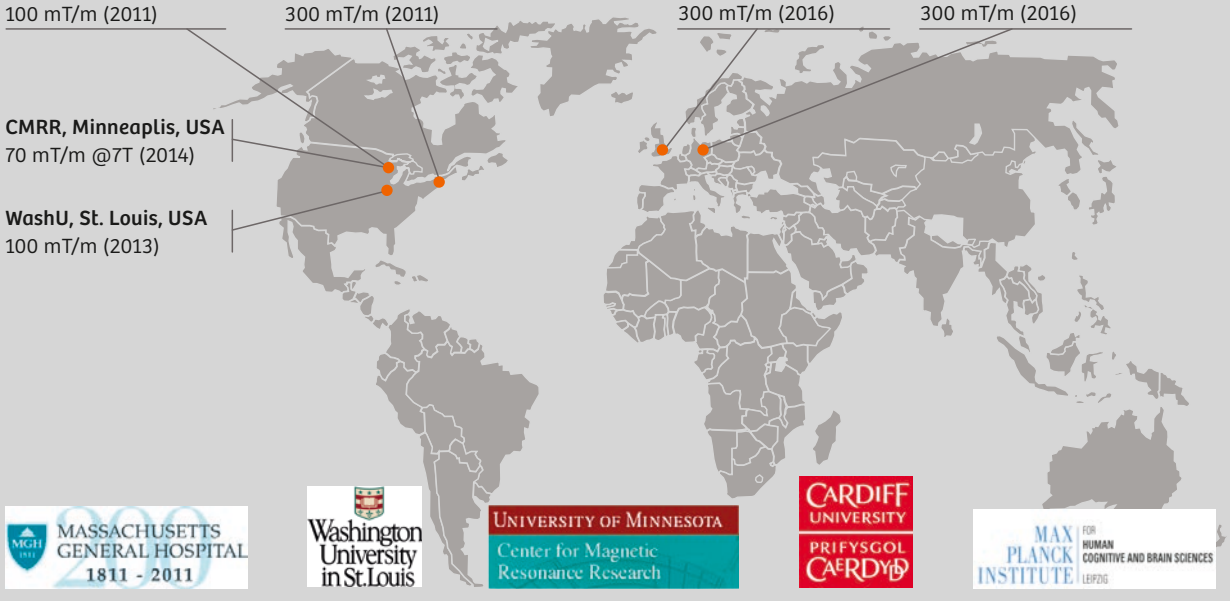

Figure 1: MAGNETOM Connectom scanners by Siemens Healthcare have been employed at five different locations since 2011.

2

Modern Gradient Design Introduced by R. Turner et al.

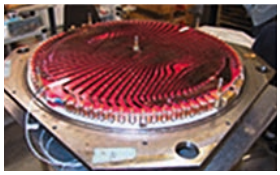

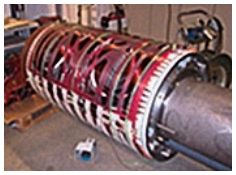

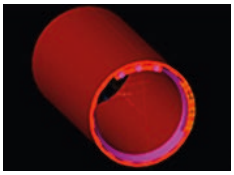

Shim Coils

Single Layer Gradient Coils
G ~3 mT/m
SR ~2 T/m/s

Actvly shielded gradients
G ~10 mT/m
SR ~10 T/m/s

(Asymmetric) head gradients, planar grds.
G ~20 mT/m
SR ~50 T/m/s

Dedicated systems: Head/Whole-body
G ~40 mT/m
SR ~200 T/m/s

Large bore / Hi G_{max} System[4)]
G 45–80 mT/m
SR ~200 T/m/s

1976 | 1984 | 1986 | 1991 | 2000 | 2017

U < 600 V, I < 200 A

U < 2.2 kV, I < 1 kA

Examples

First whole-body MRI
Aberdeen University, 1980
J. Mallard et al

20 mT/m SR 160 T/m/s
EPI enabling add-ons[1]

80 mT/m SR 700 T/m/s
Headgradient[3]

40 mT/m SR 200 T/m/s
Cardiac/EPI Gradients[2]

Figure 2: Gradient history of MRI systems.

[1] Cohen MS, Weisskoff RM. MRM. 1991; [2] Schmitt F, Eberlein E. et al. ISMRM, 1999; [3] Vom Endt A et al. ISMRM, 2006;
[4] Equals an increase of gradient power (slewrate x amplitude) of three magnitudes over 20 years.

Missouri, and the second a 3-year project at the Massachusetts General Hospital's (MGH) Martinos Center in cooperation with the University of California, Los Angeles. A comprehensive description for the HCP can be found in a 2012 *Nature* article [11].

In order to map the human connectomics, the Washington University & the University of Minnesota (WashU-Minn) consortium, utilized resting state fMRI and high angular resolution diffusion imaging (HARDI) – a special diffusion imaging technique. However, Diffusion Spectrum Imaging (DSI) – a general form of Diffusion Tensor Imaging that was pioneered in 2005 at the Massachusetts General Hospital (MGH) – was the method of choice for the MGH/University of California at Los Angeles (UCLA) consortium. To pursue this challenging task, both of these consortiums approached Siemens Healthineers to propose working together in hardware technology, more specifically in special gradient systems, which will enable the demanding diffusion imaging.

More recently, two European research centers have joined the exclusive club of Connectome gradient users. In 2016, the Cardiff University Brain Research Imaging Centre (CUBRIC), equipped with a 300 mT/m MAGNETOM Connectom, two 3T MAGNETOM Prisma and a MAGNETOM 7T system[1], was inaugurated by Queen Elizabeth II. At the end of 2016, the Max Planck Institute for Human Cognitive and Brain Sciences, Leipzig, Germany, also installed a MAGNETOM Connectom 3T MRI system[1].

Gradient technology

Siemens Healthcare introduced the first MAGNETOM 0.35T whole-body scanner in 1983 and has continuously extended the product portfolio with higher magnet and gradient field strengths. Starting with a peak amplitude (G_{max}) of 3 milli-Tesla per meter (mT/m) and a slew rate (SR) of 2 T/m/s in the early 1980s, today's (2017) clinical high-end 3T scanner MAGNETOM Prisma achieves a G_{max} of 80 mT/m and a SR of 200 T/m/s (see Fig. 2). Gradient system performance depends on many opposing factors including G_{max}, SR, linearity volume (LV) and available patient bore diameter. Highest performance demands are created by diffusion-weighted sequences which expect fast gradient switching for the readout pulses, highest peak amplitude / duty cycle for the diffusion pulses, and excellent shielding of eddy fields. As a consequence, gradient coils optimized for whole-body applications with a large linearity volume and inductance require high-voltage/-current power supplies. Starting with the first applications of the EPI imaging method in the early 1990s [12], especially gradient

[1] MAGNETOM Connectom and MAGNETOM 7T is ongoing research. All data shown are acquired using a non-commercial system under institutional review board permission. Siemens does not intend to commercialize the system.

3

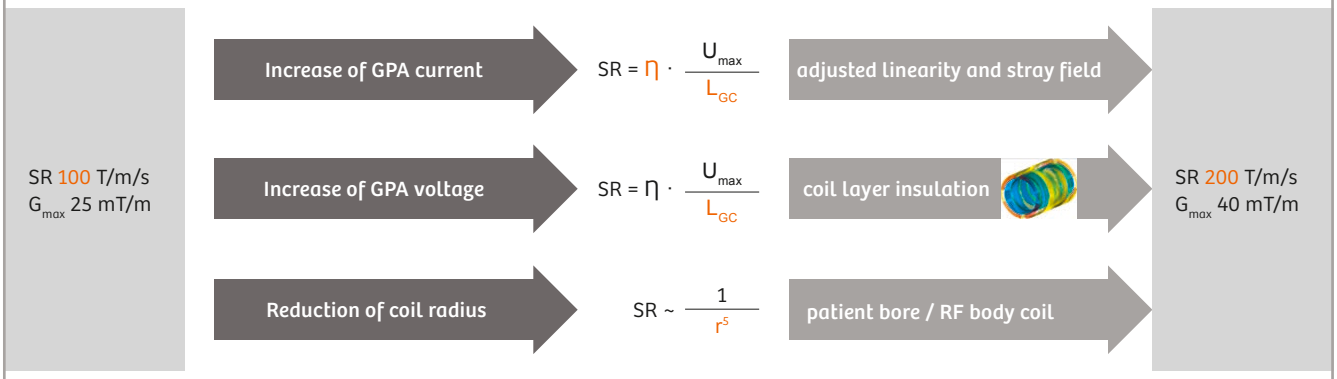

Figure 3: Improved gradient performance parameters (maximum gradient amplitude (G_{max}) or slew rate (SR)) can be achieved by either increasing gradient amplifier (GPA) power (via maximum voltage U_{max}) and adjusting the coil design (via field efficiency (Π) or inductance (L_{GC})) or by a reduction of the coil radius (r) and adjustments to the RF body coil and/or the patient bore diameter.

4

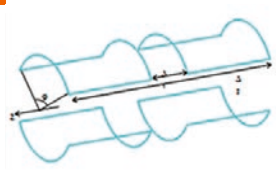

Biot Savart Methods
Maxwell / Golay design
analytical expressions
building blocks (still used)

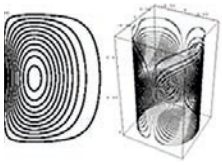

Current Density methods[2]
Target field / spherical harmonics
active screening / min. inductance
stream function discretization
(analytical & matrix based)

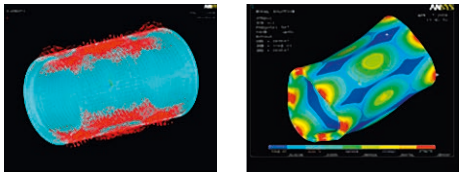

Additional methods
Lorentz force / moment compensation
stray field forming / eddy current reduction
heat & power minimization
geometry-specific (e.g. split/oval)

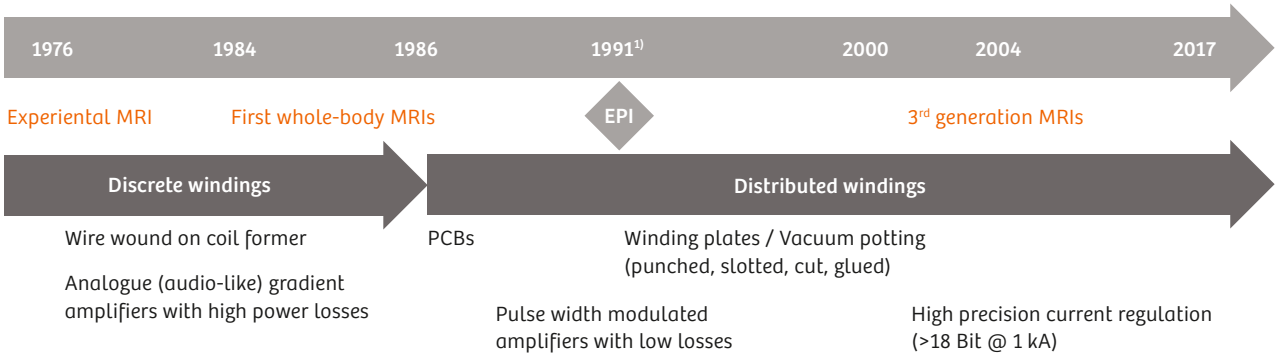

Figure 4: History of gradient coil design methods.

[1] In 1991, PNS (peripheral nerve stimulation) proves to limit gradient performance (predicted by T. Budinger 1979);
[2] R. Turner, Gradient Coil Design, A Review of Methods, MRM 11:903 (1993)

slew rate became a challenge for gradient system design. First attempts to reduce the rise time of EPI readout gradients involved additional resonant circuits, so-called 'EPI boosters' [13, 14].

With conventional gradient design methods [15, 16], SR increase (at otherwise constant parameters) can be achieved by either increasing the voltage of the power amplifier (GPA) or by reducing the inductance of the coil. Besides using more than a single amplifier and coil-set [17], the third alternative for higher SR is to reduce the inner radius of the coil system (Fig. 3). The strong (5^{th} order) dependence of the SR from the coil radius leads to about a factor of two increase when changing from 70 cm to 60 cm patient bore. Thus, this parameter is a crucial part of the MR system concept definition. It emphasizes the importance of efficient use

of radial space inside the magnet bore. The best gradient performance is achieved by using only the necessary number of windings driven by the highest available current. In practice, the maximum current is mainly limited by power amplifier technology, forces on gradient connectors, wire cross section, and cooling efficiency. Additional design targets like shielding efficiency, force/torque compensation, and acceptable nonlinearities of the linear gradient field tend to increase the required number of windings, making up the challenge to the coil designer (Fig. 4).

Cylindrical symmetry dominates today's gradient coils. Coil geometry mostly follows the boundary conditions set by the main magnet design. Insert gradients could be designed without following the basic symmetry of the main magnet, but hardly do so. Due to the non-ideal nature of magnet and gradient fields (e.g. concomitant fields, forces, and torques), it is always advantageous to keep as many symmetries as possible. Dedicated insert gradients for different body parts are known (for example spine or knee [18]), but have not been successful in replacing their big brothers. Electrical and mechanical design aspects of non-cylindrical geometries are not very different from the standard configurations. For example, the target field method could be applied to calculate the primary and the shields' current density on a circular plane. The wire pattern and axial connections are generated by extracting the contour lines of their stream function. The same method can be applied to generate the wire pattern for the electrical shim coils. The gradient system thus consists of a variety of complex subcomponents, each forming a subsystem of its own (Fig. 6). The coil system (Fig. 5) comprises the linear field coils (X, Y, Z) including their shielding coils, higher-order shim coils, cooling layers, temperature sensors, RF screen, current and water connectors, the coil support structure, and its suspension.

Magnetic field generation with high amplitudes and large volumes is a difficult task. Considering that the natural

5

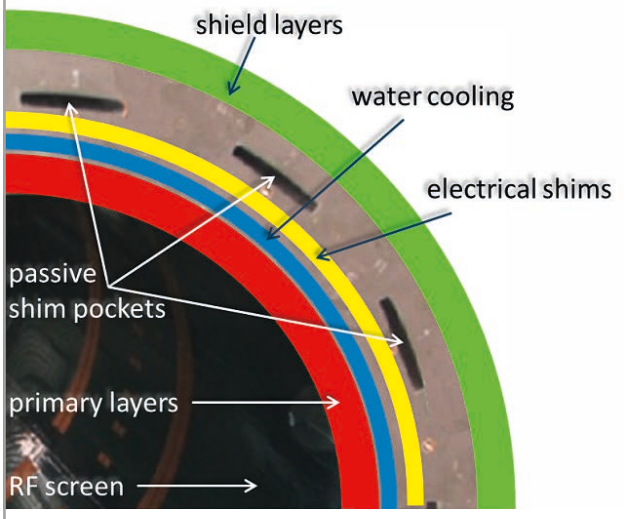

Figure 5: Layer breakdown of a cylindrical gradient coil system including passive iron shim.

6

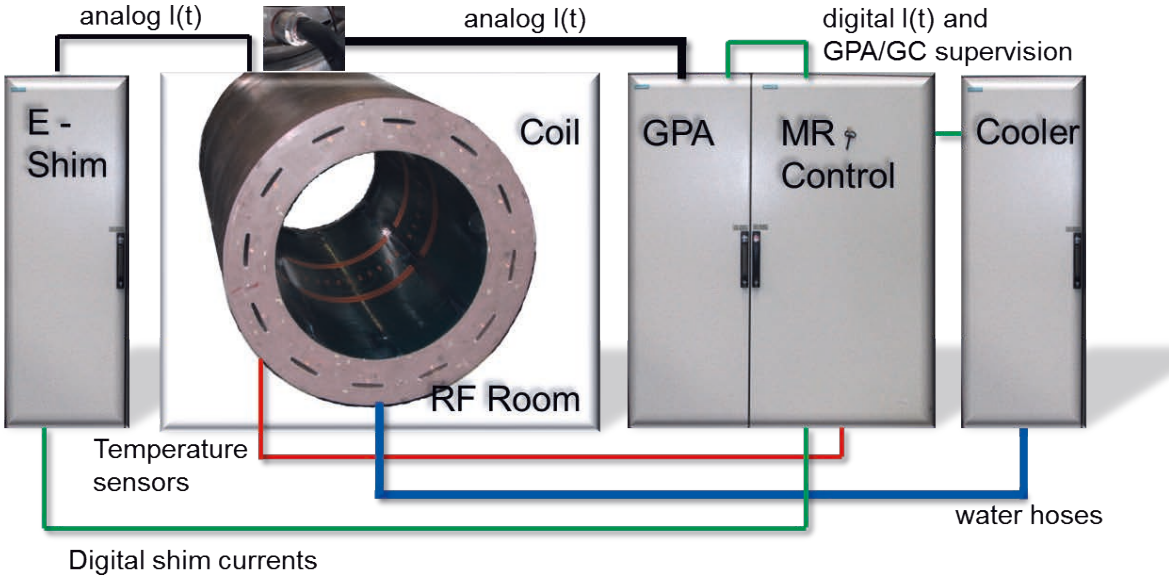

Figure 6: The gradient system consists of a coil system, a cooling system, a gradient power amplifier (GPA), a shim amplifier, and a gradient control system as part of the MR control system.

7

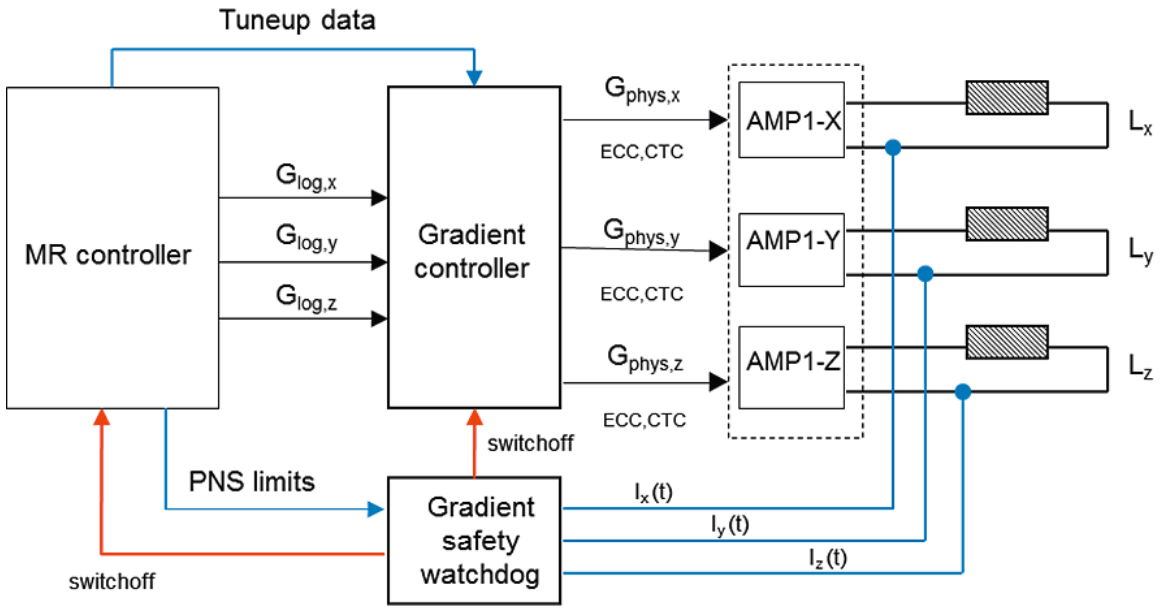

Figure 7: Control system of a typical MR scanner and its interface to the gradient controller. The gradient controller and the PNS safety watchdog are fed with logical gradient shapes (G_{log}) and gradient-coil-specific limits for peripheral nerve stimulation. The logical shapes are converted to physical shapes (G_{phys}) and modified by filter functions for eddy current and cross-term compensation (ECC and CTC) before being fed to the gradient amplifier's final stages (Amp X, Y, Z). The current in the gradient circuit with the coil impedance L is measured by high precision current probes and fed to the gradient safety watchdog unit. In case the PNS limit is exceeded, a safety switch-off signal is sent to the gradient and MR controller.

8

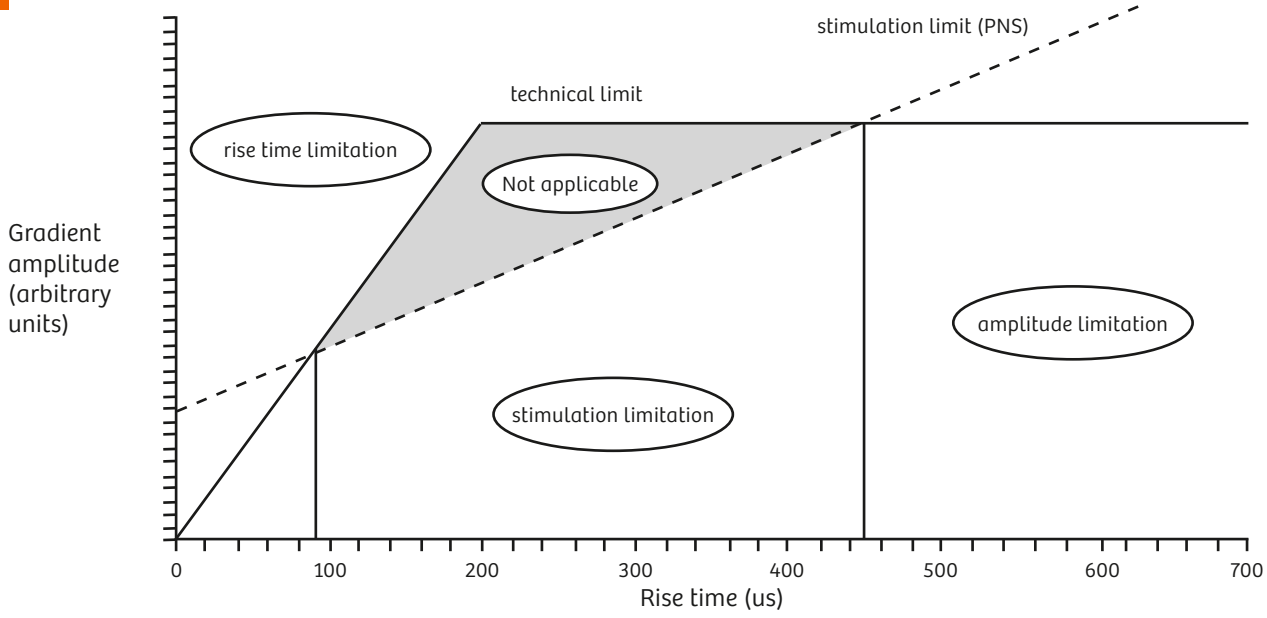

Figure 8: Limitations of gradient system performance for human use. The main limitation is given by the peripheral nerve stimulation threshold (PNS limit). If the technical performance of the gradient system is not adapted to this limit, a significant part of the parameter space is not applicable to human subjects.

(earth) magnetic field is about 50 uT in amplitude, the first whole-body gradient coils had to exceed this by two orders of magnitude. In one embodiment, wooden structures were used to support the race-track-like windings (Fig. 2). Furthermore, rapid gradient switching leads to strong vibrations due to the Lorentz forces of the conductors within the main magnetic field. This can be counteracted by increased stiffness of the support structures (e.g. with glass-fiber-reinforced plastic) and linking of all layers to a single body (e.g. with epoxy resin). In addition, dielectric strength of all gradient layers is required at minimal (<2 mm) radial distance of the conductors. Hence, today's gradient coils mainly consist of epoxy resin with excellent dielectric strength at low cost and high geometric flexibility. The challenge in the fabrication process is to ensure that all layers and subcomponents of the coil system are impregnated 100%. This can only be achieved with a complex vacuum potting procedure. Every step of this procedure needs to be defined and controlled thoroughly [19]. Process and material parameters like temperature profile, filling material, and filling percentage as well as curing time need to be adjusted to the geometry and inner structure of the gradient coil main body. A successful potting procedure is usually validated with a high voltage or electrical discharge test. This step ensures that the dielectric strength is good enough to withstand amplifier voltages of up to several kilovolts for an MR system's lifetime.

The control system of an MR scanner synchronizes and drives the activities of all hardware components (Fig. 7). The interface of the MR controller to a logical hardware component usually requires a sub control system of its own. The gradient controller and the Peripheral Nerve Stimulation (PNS [20]) safety watchdog are fed with logical gradient shapes (read, phase, slice) and gradient-coil-specific limits for PNS, respectively. Static correction data acquired during the first startup phase of the MR scanner ('Tune-up data') is transferred to the gradient controller and GPA before the start of the measurement sequence.

After the start of a gradient pulse sequence, the logical gradient shapes are converted into physical gradient shapes. In order to minimize eddy current effects, additional filters based on tune-up data may be applied to the gradient circuit current I(t) before transfer to the gradient amplifier component (e.g. eddy current pre-emphasis). The output of the gradient amplifier circuit is monitored by high-precision current sensors. Their signal is used for control and supervision of the gradient amplifier cabinet including PNS. The limits for human exposure to time-varying magnetic fields are defined by the IEC norm and need to be ensured based on calculations and measurements (Fig. 8).

Ultra-high gradient strength

The first decade of the new millennium brought the benefits of parallel imaging methods from research machines to clinical MRI scanners. Today (2017), most sequences make use of acquisition methods with measurement time reduction (or, in case of EPI, readout time reduction). Although the demand for high gradient amplitudes for diffusion imaging techniques is still unbowed, the advantage of ultra-high gradient slew rates now has a serious competitor.

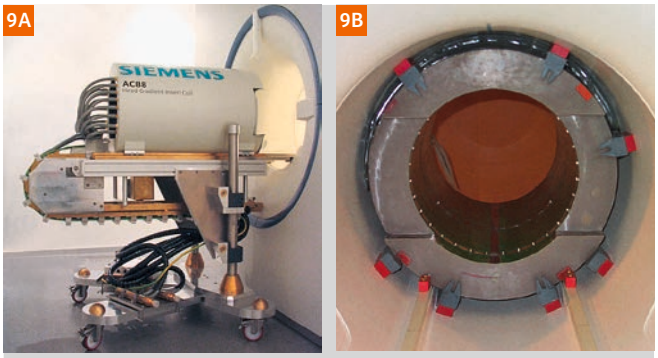

Figure 9: Gradient insert 'AC88'. **(9A)** Test of the handling device at a 3T scanner. **(9B)** Reduced size of patient bore after installation of the coil.

Implementation of ultra-high gradient amplitudes with head-sized gradients inside a whole-body magnet bore is one approach to tackle the problem [21]. The advantage of simultaneous ultra-high slew rate and gradient amplitude is counteracted by the limited space inside the coil (Fig. 9). It is difficult to design a combined transmit/receive RF coil with >8 receive channels, good intra-channel decoupling, and high SNR due to the close proximity to the copper windings of the gradient coil. Separating the transmit coil is even more challenging, as this requires additional radial space for the RF return flux. In addition, patient handling is difficult. It is not easy to find volunteers who are willing to expose themselves to the near-claustrophobic conditions of such an experimental device. Even with asymmetric gradient design, the limited size of the shoulder cutouts will exclude part of the normal population from being scanned.

In diffusion imaging of the brain, long-lasting diffusion weighting gradient lobes are applied. The highest possible gradient amplitude is applied in the shortest possible time, combined with an echo-planar imaging (EPI) pulse sequence to encode diffusion and minimize head motion at the shortest possible echo time (TE). Typical TEs for b = 1,000 s/mm^2 on a 3T whole-body scanner are around 70–80 ms when Stejskal-Tanner encoding is applied without additional parallel imaging techniques. Higher b-values can only be achieved with a penalty in SNR, as TE increases with the duration of the diffusion lobe. Studies on mammals have indicated that much higher gradient strength than 40 mT/m would be required to produce sharp diffusion images of an adult human brain's wiring patterns [22]. Typical small-bore (about 100 mm) NMR scanners can apply 150–300 mT/m. Owing to the nonlinear increase of gradient strength with reduction of the inner diameter, even 1,000 mT/m (at 60 mm bore) are not uncommon. This reopened the question whether ultra-high gradient strength (>100 mT/m) may be achievable with a whole-body gradient design.

10

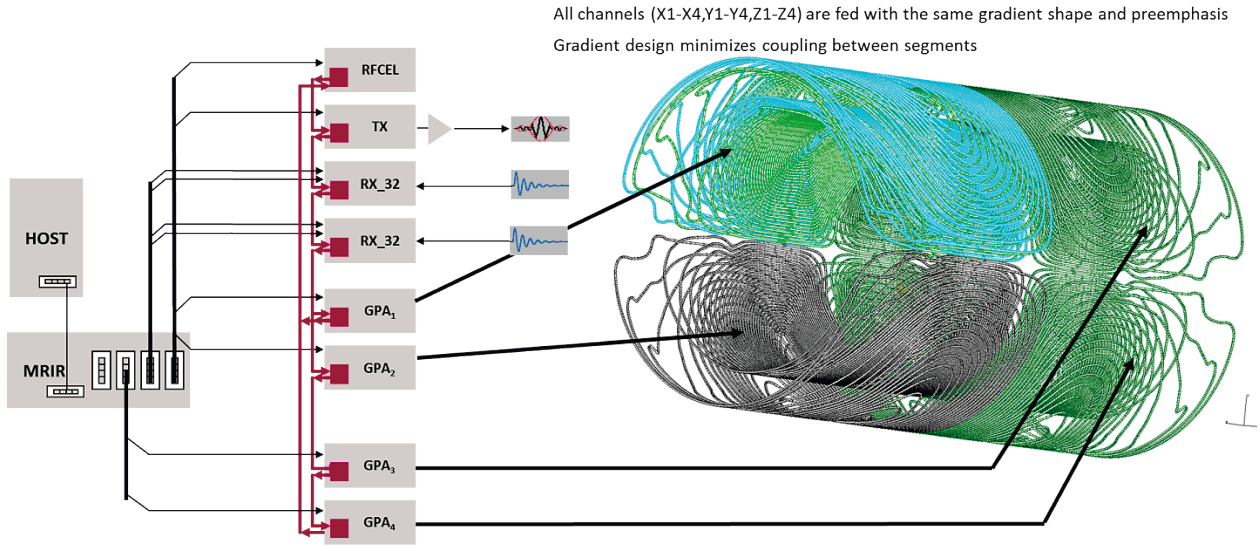

Figure 10: Control system concept for the 300 mT/m gradient. The MR control system (host computer HOST, image reconstruction computer MRIR) was extended to drive four sets of gradient amplifiers independently. The new architecture allows storing the calibration data for each of the 12 final stages driving the gradient coil segments.

The design target for a whole-body gradient was set to high gradient amplitudes with the linearity volume (LV) being limited to the brain volume (thus achieving less restrictive PNS thresholds). Two versions of this gradient design were designed and built. Version 1 (SC72) supports a G_{max} of 100 mT/m at SR 200 T/m/s with a single GPA cabinet (2 kV, 1 kA). It was designed to match forces and stray field of a 3T magnet and provide space for passive iron shims. It has a length of 158 cm, and an inner diameter of 64 cm. This yielded a robust, easy-to-use diffusion engine [23].

Version 2 (AS302) represents a quantum leap in whole-body gradient performance, i.e. G_{max} of 300 mT/m at SR 200 T/m/s. Design studies with reduced linearity constraints showed that up to 150 mT/m could be reached with a single gradient power amplifier. A further increase of gradient strength within conventional design constraints would have imposed duty cycle limitations, which are not favorable for diffusion applications. Due to the large volume of the coil body, the number of current density layers and thus the gradient strength could be doubled to 300 mT/m. As a consequence of the mutual coupling of the four primary and secondary layers per axis, coil inductance increased by more than a factor of two. To drive this high inductance at the SR 200 T/m/s needed for EPI readout, a new gradient system concept involving multiple gradient amplifiers was developed. In order to achieve the target slew rate, each of the three axes X, Y, Z was split into four independently driven segments (Fig. 10). Stray field and forces were matched to the 3T magnet used. The MR control system was extended to drive four sets of gradient amplifiers independently. The new architecture allows storing the calibration data for each of the 12 final stages driving the gradient coil segments. The gradient waveform is logically split and fed to four individual gradient controllers. This architecture also allows generating arbitrary field characteristics for each gradient coil axis, used to optimize eddy current compensation.

The GPA regulator architecture was extended to account for the dynamic differential control (D) of the driving signal. This allows counteracting the induced voltages in each segment coil due to mutual coupling. A new RF body coil was developed (capable of TrueForm excitation) which allows the use of the existing clinical patient table with minor

11

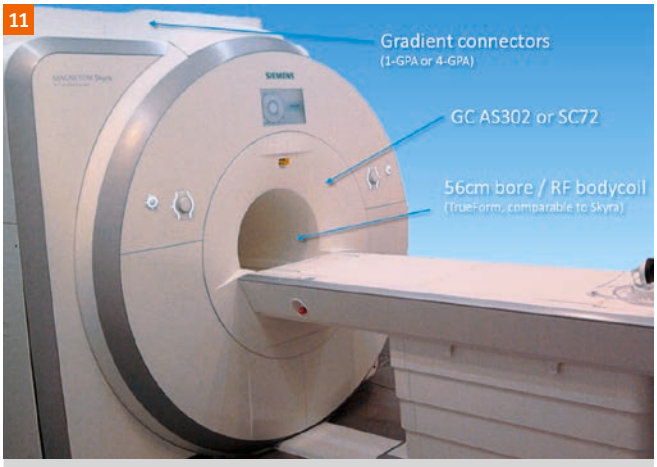

Figure 11: Modified MAGNETOM Skyra system. Dimensions of the RF body coil, patient table and cover were adjusted to the size requirements of both Connectom gradient coils.

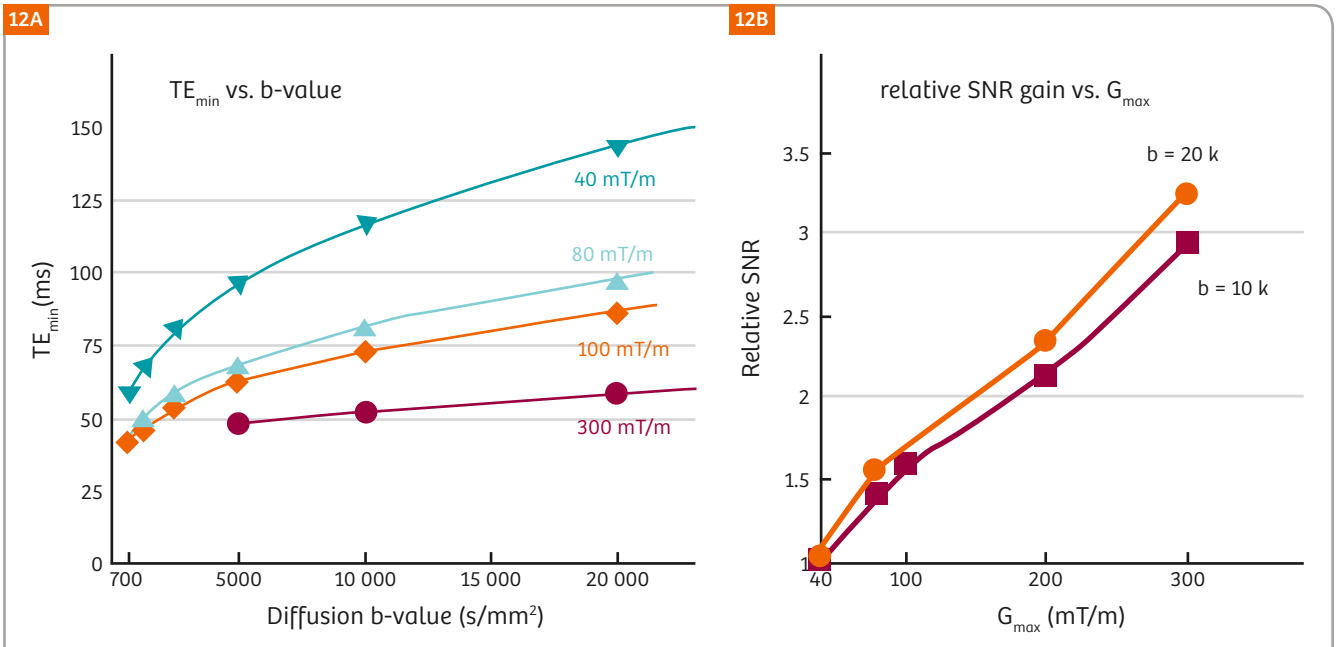

Figure 12: (12A) Minimum TE for a Skeskjal Tanner diffusion sequence (2 mm isotropic, FOV 200 mm). **(12B)** Measured SNR of the brightest sections of *in vivo* human white matter with 64-channel brain array coil (b = 10,000 s/mm² and 20,000 s/mm²).

mechanical modifications. The covers were modified accordingly (Fig. 11). Three cooling cabinets, four GPAs and a second filter panel were installed in the equipment room, before the first phantom images could be acquired in May 2011. Measurements of acoustic noise and vibrations showed lower amplitudes than typical 3T scanners, which is in line with the larger mass of the gradient coil body and the related higher net precision of torque and force balancing methods. The PNS studies performed on the AS302 and SC72 coils confirmed that it is possible to use high EPI readout amplitudes without PNS effects. Long rise times at high-amplitude pulses are limited by the regulatory-required cardiac monitor which was implemented in hardware.

Research in the US

Achieving the current state of connectomics has required a huge increase in MRI sensitivity, as well as much higher processing speeds to cope with the large amount of spatial data from water molecules. Unlike the BOLD effect which experiences enhanced contrast as field strength is increased, the diffusion contrast is set only by the displacement of the water and the applied field gradient and is thus independent of B_0. On the other hand, a more than two-fold sensitivity increase at 7T field strength would offer the opportunity to increase resolution for whole-brain studies towards one-millimeter isotropic voxel size. As the available methodologies in 2011 were not up to routinely coping with shorter T2 and T2* relaxation times, increased B_1(+) inhomogeneity and increased power deposition (SAR) at >7T field strength, both WU-Minn and MGH-UCLA teams set their main focus on 3T.

The MGH-UCLA consortium decided to re-engineer their scanner from the ground up to optimize diffusion imaging. Their efforts went into ultra-high gradient strength, sequence design and reconstruction, and high-channel receive coils. The gradient system with 300 mT/m was a major focus since gradient amplitude is central for the parameters diffusion contrast, T2 signal loss, and probability density function (PDF) of water. A field-of-view (FOV) shifting approach to Simultaneous Multi-Slice (SMS) EPI [25–27] was chosen to enable whole-brain coverage with low TR and TE. The group developed a 64-channel brain array coil showing a relative SNR gain of at least 40% compared to a sized-matched 32-channel brain array within the peripheral brain ROI [28]. The achieved efficiency gain is more than a factor of eight for high-b-value diffusion (3.5 x from shorter TE, 1.7 x from the slice acceleration factor of 3 from SMS, and 1.4 x from the RF coil) [29]. Average scan time for whole-brain diffusion was shown to be reduced from about one hour to 15 minutes (combined with compressed sensing, scan time was <5 minutes).

Increasing the gradient strength to the highest value ever attempted for human imaging also has significant impact on the concomitant field terms. In comparison to a conventional 45 mT/m scanner at 3T, the maximum field pertubation increases by a factor of ~$(300/45)^2$ = 44. The MGH-UCLA group successfully tackled this problem with the implementation of a fully refocusing Stejskal-Tanner scheme [1] and accompanying pre-processing eddy current correction. An unanticipated finding was that the increased gradient strength could induce magneto-phosphenes in the subjects' eye retina. Lowering the head coil vertically and

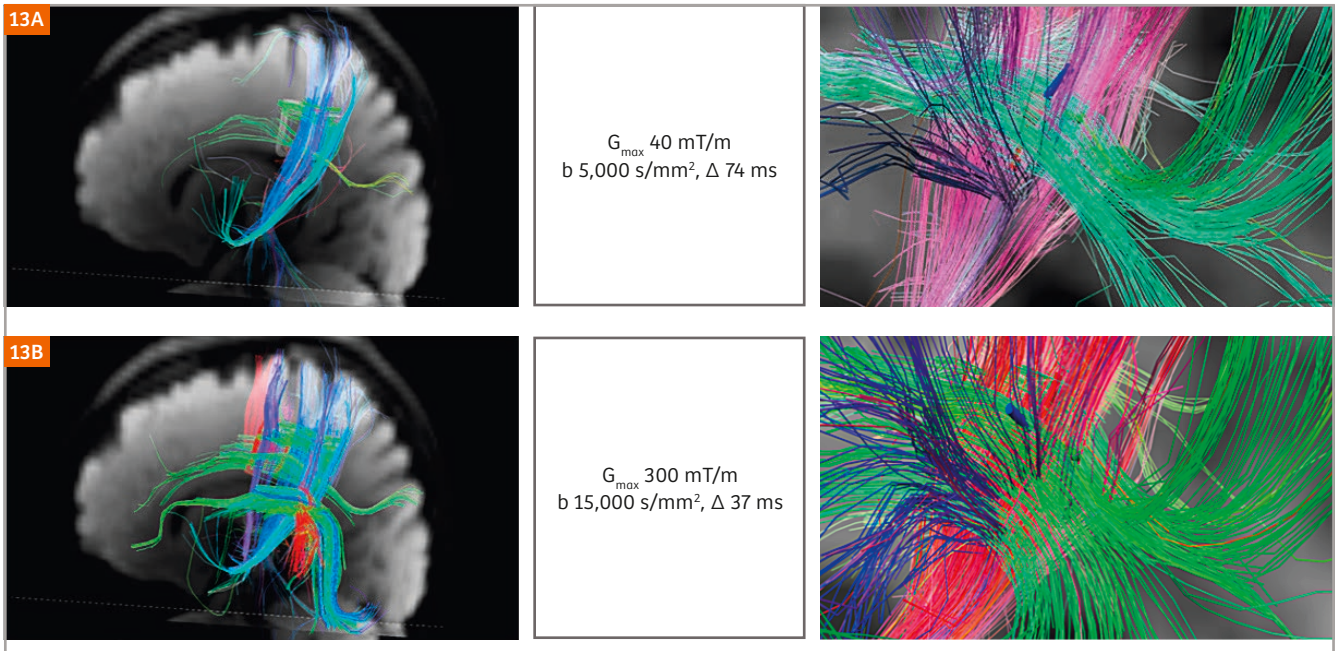

Figure 13: Micro-structural resolution with 40 mT/m **(13A)** and 300 mT/m **(13B)** gradients. dMRI data was aquired with a b-value of 5,000 s/mm² and 15,000 s/mm² respectively. Fiber pathways were computed with deterministic streamline integration and show a higher level of detail with a b-value of 15,000 s/mm². *Images courtesy of MGH, Boston, USA.*

positioning the eyes at isocenter in z was found to eliminate the induction of magneto-phosphenes within volunteer studies.

The ultra-high gradients yielded substantial and immediate gains in the sensitivity through reduction of TE while improved signal detection (Fig. 12) and increased efficiency of the DSI or HARDI acquisition, accuracy and resolution of diffusion tractography were illustrated (Fig. 13). Comparisons were performed across b-values based on q-ball orientation distribution function (ODF) metrics to investigate whether high-b-value dMRI (up to 10 k s/mm²) can improve resolving complex white-matter structures. The q-ball ODF features became sharper as the b-value increased. Crossing structures were detected in an increasingly larger fraction of white-matter voxels, and the spatial distribution of two-way and three-way crossing structures was found largely consistent with known anatomy (Fig. 14). Results indicate that dMRI with high diffusion encoding is a promising tool to characterize and understand the underlying structural organization and topological paths (motifs) in the human brain [30].

Relationships of adjacency and crossing between cerebral fiber pathways in humans and in nonhuman primate species are a major focus of the Connectomics department at the MGH. Whole-brain diffusion spectrum MRI was acquired with the 300 mT/m scanner *in vivo* in subjects (515 directions; pathways were computed with deterministic streamline integration, see Figs. 15–17) and *ex vivo*.

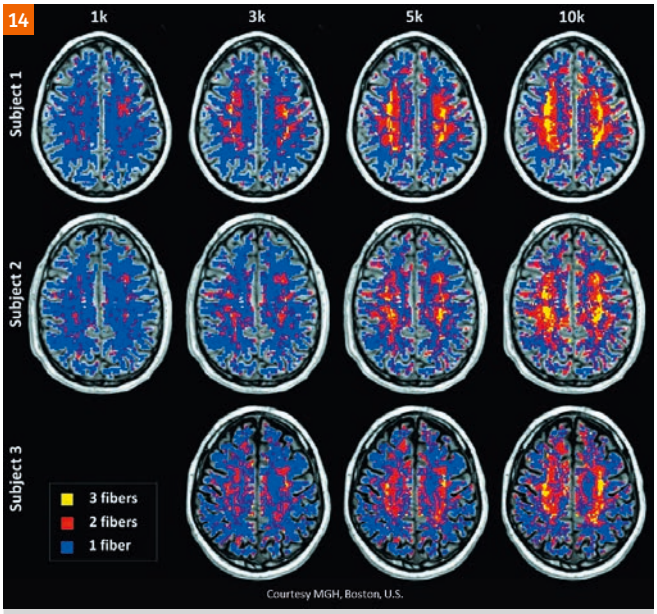

Figure 14: Spatial distribution of the number of fibers per voxel within the brain of three subjects (blue = 1, red = 2, yellow = 3 or more fibers). The orientation distribution function (ODF) peak threshold was selected to be two times the standard deviation above the mean of the noise peaks. A higher percentage of white matter voxels was identified as containing crossing fibers as b-value increased from 1,000 to 10,000 s/mm².

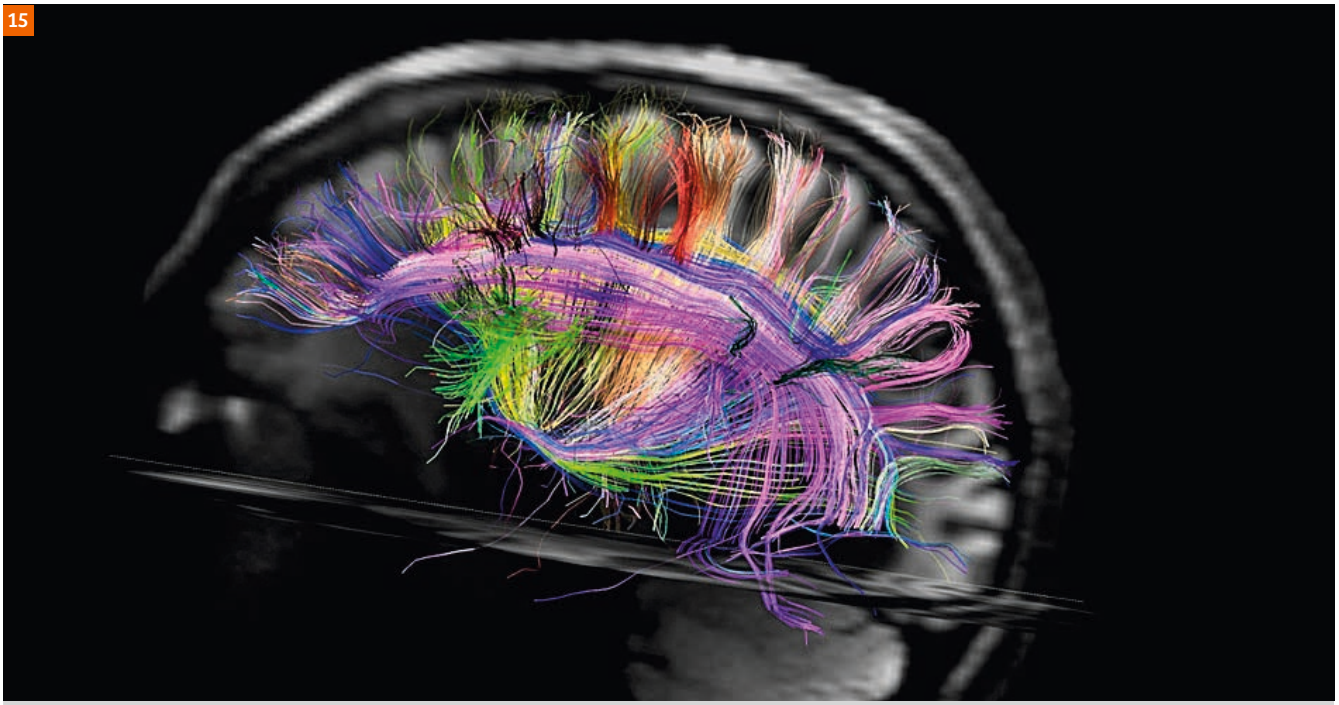

Figure 15: *In vivo* diffusion spectrum imaging (DSI) of the human brain. Reconstructed nerve fibers show the grid of corona radiata and SLF. Resolution 1.5 mm^3, max b-value 15,000 s/mm^2, TA 20 min. *Image courtesy of V. Wedeen, MGH, Boston, USA.*

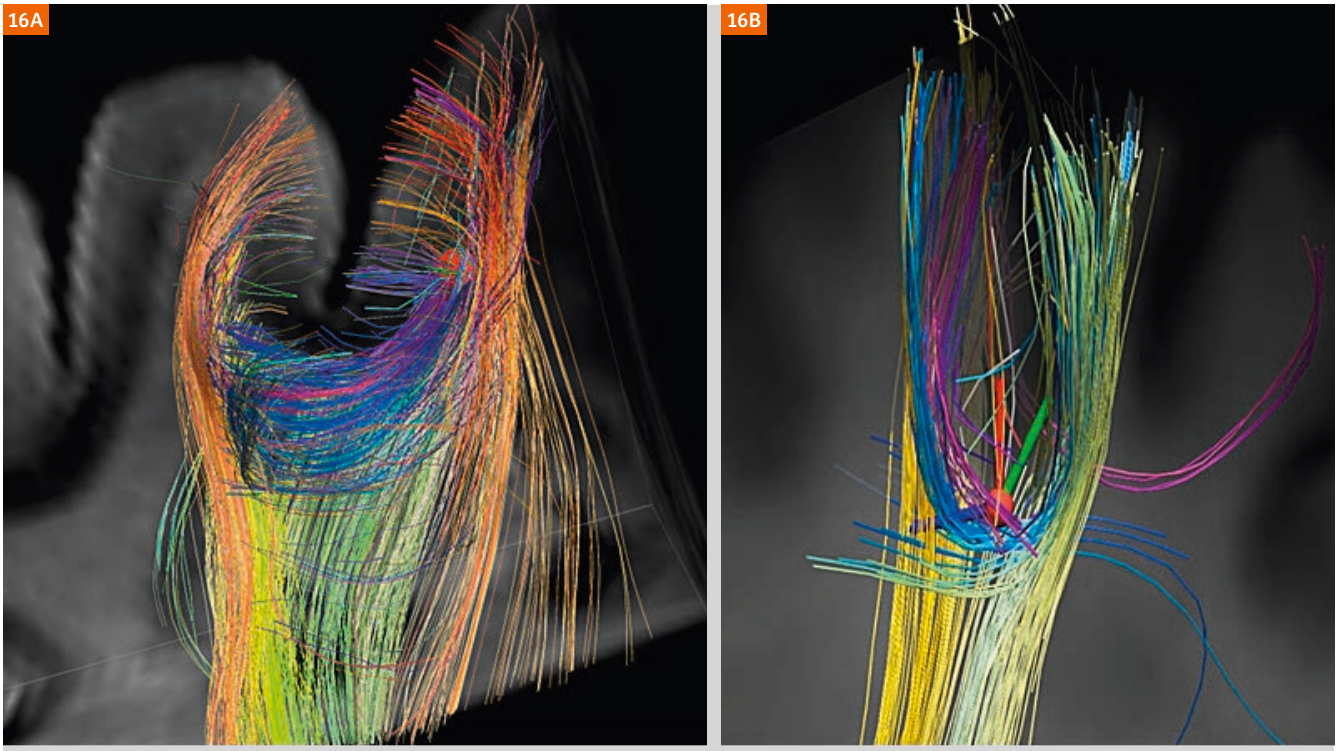

Figure 16: Diffusion spectrum imaging (DSI) of the human central sulcus U-fibers. **(16A)** *Ex vivo* data (b-value 40,000 s/mm^2, voxel size 0.5 mm^3 isotropic, TA 12 h). **(16B)** *In vivo* data (b-value 15,000 s/mm^2, voxel size 2 mm^3 isotropic, TA 20 min). *Images courtesy of V. Wedeen, MGH, Boston, USA.*

The cerebral fiber pathways were seen to form a rectilinear three-dimensional grid continuous with the three principal axes of early development. Cortico-cortical pathways were observed to form parallel sheets of interwoven paths in the longitudinal and medio-lateral axes, in which major pathways were local condensations. Details are covered by a *Science* publication from 2012 [31].

Beyond the immediate scope of the HCP, further applications like brain recovery after traumatic coma, axon diameter distributions [32, 33], and post-mortem diffusion tractography were explored. It could be shown that ultra-strong gradients enable human applications of techniques that were previously possible only in small-bore scanners. Detailed research results were published by Neuroimage

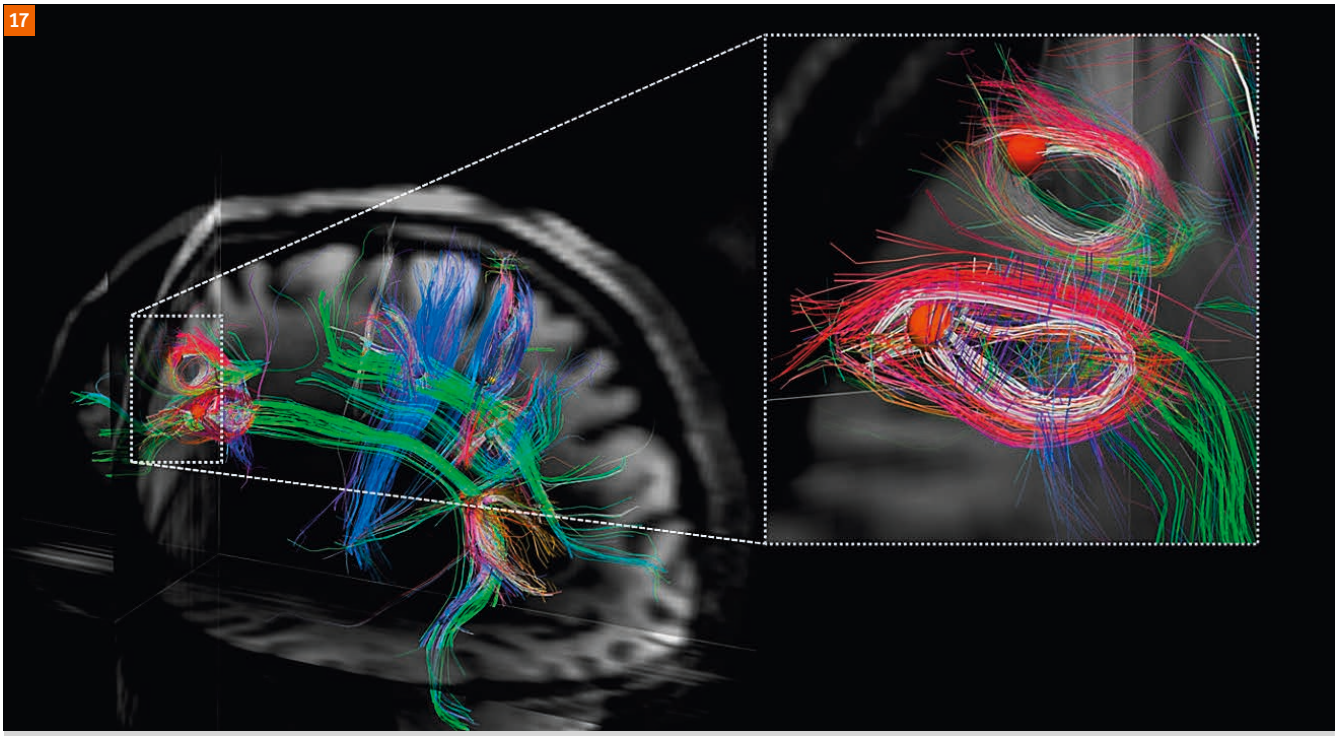

Figure 17: *In vivo* diffusion spectrum imaging (DSI) of the human gyri, and its continuity with deep white matter. (b-value 15,000 s/mm^2, voxel size 1.5 mm^3 isotropic, TA 20 min). *Image courtesy of V. Wedeen, MGH, Boston, USA.*

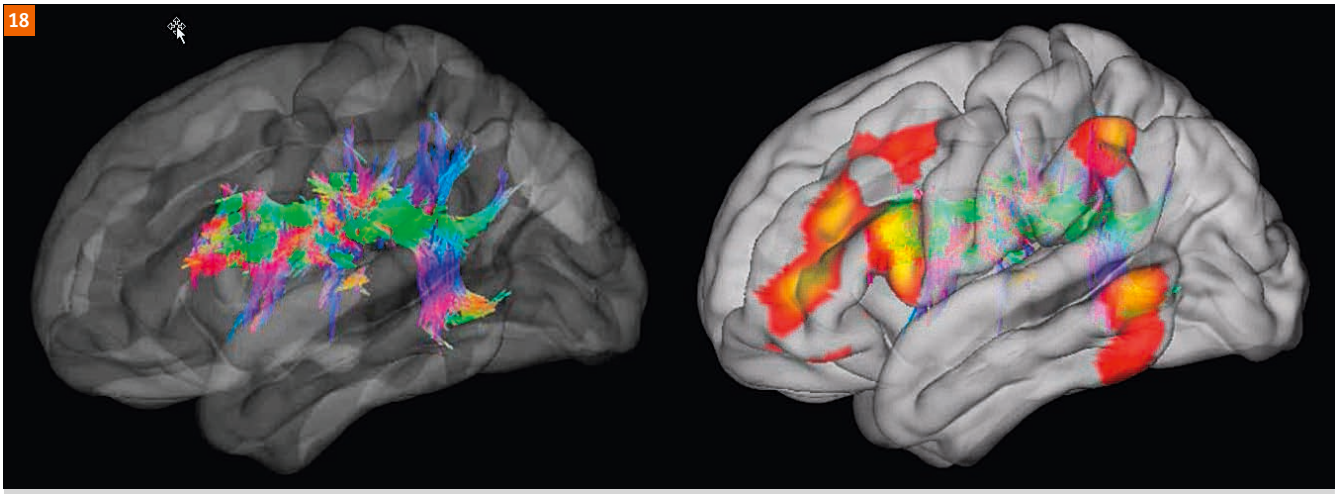

Figure 18: Interactive composite dataset of the human brain (180 areas per hemisphere). Red and yellow sections are based on data from resting state functional MRI, whereas the multicolored fibers were generated using probabilistic streamline tractography based on diffusion MRI. *Images courtesy of Washington University – University of Minnesota – Oxford University Human Connectome Project.*

[34] in 2013. More than 60 subjects were scanned with the 300 mT/m system by the MGH-UCLA consortium. The resulting reference data base was made publically available on the HCP internet homepage in 2016 [35].

The WU-Minn consortium focused on mapping long-distance brain connections [36] and their variability within healthy adults (twins and their non-twin siblings [37]). Three complementary methods were used, namely resting state functional MRI (rfMRI) which uses correlations in the temporal fluctuations in an fMRI time series to derive 'functional connectivity'; diffusion imaging (dMRI), which provides the input for axonal fiber tractography; and task-based fMRI (tfMRI), which is used together with T1- and T2-weighted imaging to identify functional parcellation in the human brain [38]. Improvements and optimization of these methods (Multiband/Simultaneous Multi-Slice Imaging) resulted in a whole-brain coverage with 2 mm isotropic resolution in 0.7 seconds for fMRI, yielding a data acquisition speed-up factor of up to nine. Applied to 1.25 mm isotropic dMRI data, a three-fold reduction in total data acquisition time was achieved. Using the HARDI [10] approach, diffusion encoding was performed with 270 q-points distributed over three shells of b = 1,000, 2,000, and 3,000 s/mm^2 (Fig. 20). Due to the targeted high number of subjects, the robust and easy-to-handle 100 mT/m gradient system was chosen.

The first half of the 5-year project focused on refining methods for data acquisition and processing [39] and resulted in robust fast pulse sequences and pre-processing pipelines providing substantial improvements for each of the MRI modalities [40]. The first pipeline provides correction algorithms for MRI raw data (e.g. eddy current and spatial distortion correction, reduction of temporal artifacts. The second pipeline involves mapping the data to cortical surfaces and subcortical gray-matter domains (Fig. 18), as understanding the human cerebral cortex requires a map (or parcellation) of its major subdivisions. Based on a pilot study of 10 healthy adults, an interactive composite dataset of the left and right cerebral hemispheres was created (Fig. 19). Red and yellow sections are strongly related to the seed location (black dot). The correlation factor is based on data from resting state functional MRI. This methodology could take research to a different level, considering that mental illnesses like autism might be related to abnormal brain circuits showing up a reduced functional connectivity in rsMRI scans.

Using multi-modal MRI images, 180 areas per hemisphere were delineated, bound by changes in cortical architecture, function, connectivity, and/or topography in a group average of 210 healthy adults. It has been possible to characterize 97 new areas and 83 previously reported areas. Automated delineation and identification of these areas was supported by a machine-learning classifier. This classifier detected the presence of >95% of the cortical areas in new subjects, replicated the group parcellation, and could correctly locate areas in individuals with atypical parcellations. These tools and datasets are part of the *'Connectome Workbench'* and *'ConnectomeDB'* database and were made available to the public [41].

After finalizing the HCP protocols in 2012, data was acquired using multiple imaging modalities, including customized 3T MRI (1,200 subjects) and 7T MRI (200 subjects) plus combined magneto- and electro-encephalography (MEG-248-channel/EEG-64-channel, 100 subjects). Technical optimizations in 7T image acquisitions for the HCP allowed to obtain high-quality, high-resolution whole-brain *in-vivo* dMRI data (Fig. 20). This data shows spatial details typically seen in *ex-vivo* studies and complement already very high-quality 3T HCP data in the same subjects [42]. More recently [43], it could

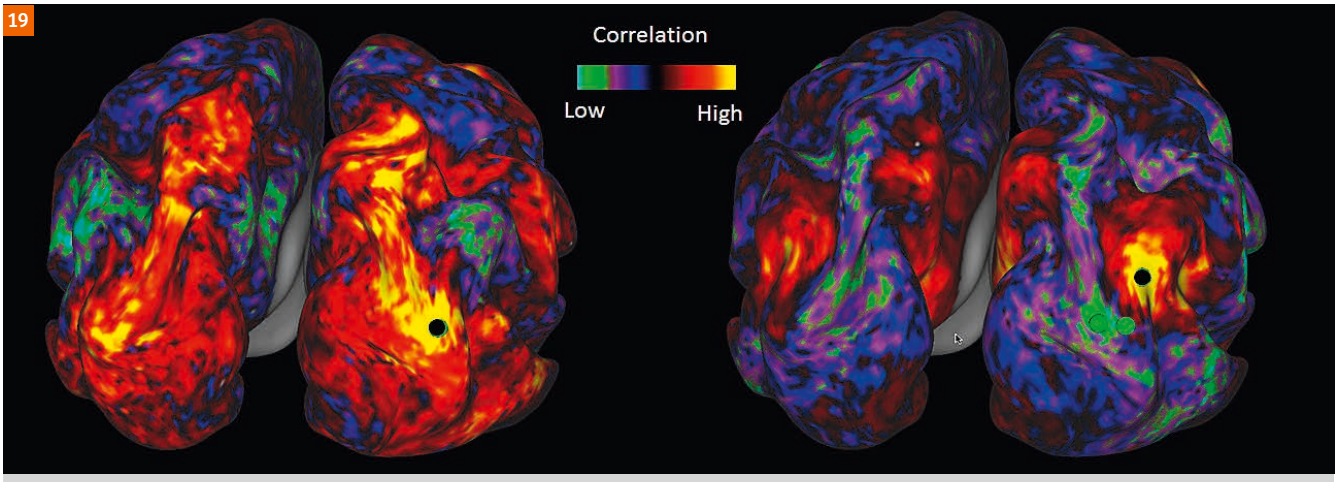

Group average, HCP Pilot-1 dataset (10 subjects, 14 scans), MB = 4, TR = 1.4 s, 2 mm voxels

Figure 19: Interactive composite dataset of the left and right cerebral hemispheres of the human brain (group average of 10 subjects). Red and yellow sections are strongly related to the seed location (black dot). The correlation factor is based on data from resting state functional MRI. *Images courtesy of Washington University – University of Minnesota – Oxford University Human Connectome Project.*

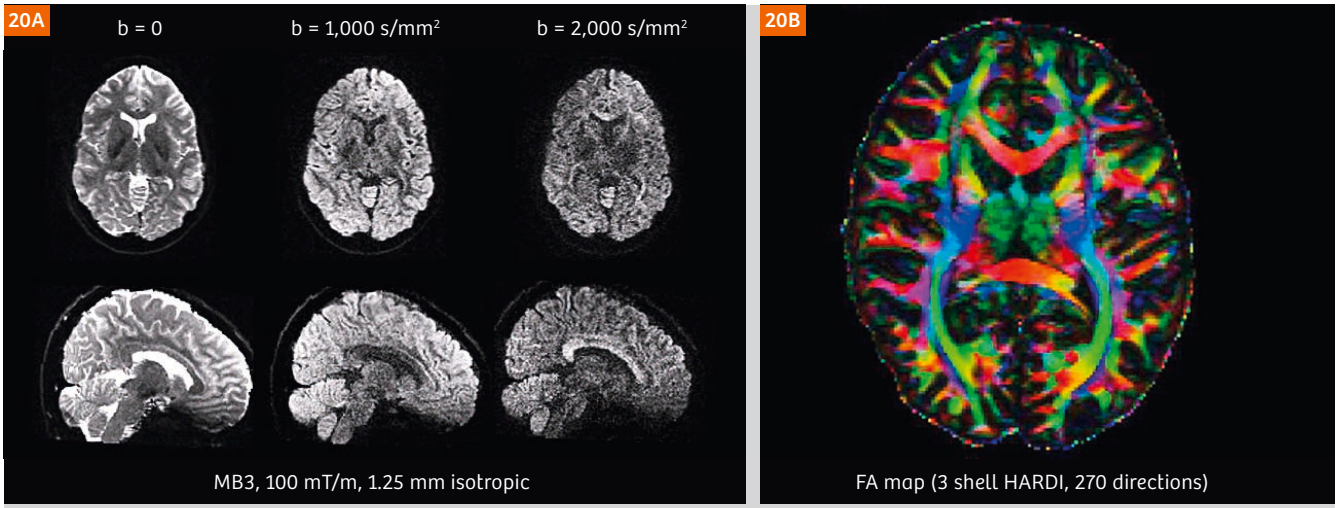

Figure 20: Representative examples of diffusion MRI with the finalized 3T HCP protocol (100 mT/m, MB3, 1.25 mm³ isotropic). Anatomical detail in comparison to a conventional 3T protocol (2 mm³ isotropic, not shown here) is significantly improved. **(20A)** Image intensities are presented in arbitrary units after distortion correction and averaging across paired phase encoding directions. **(20B)** Color fractional anisotropy (FA) maps. Colors depict the principal fiber orientation and gray scale intensities are defined by FA.
Images courtesy of Washington University – University of Minnesota – Oxford University Human Connectome Project.

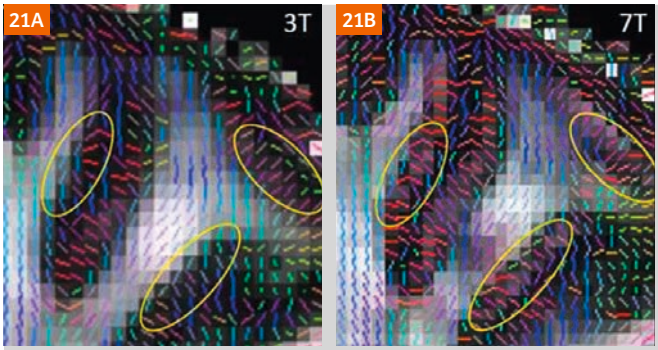

Figure 21: Zoomed-in coronal view of DTI principal direction of diffusion (PDD) maps overlaid on corresponding fractional anisotropy (FA) maps. HCP 3T **(21A)**. 7T **(21B)**. Due to the higher resolution and reduced partial volume effects, the 7T data recovers gray matter regions of low FA (yellow circles).
Images courtesy of Washington University – University of Minnesota – Oxford University Human Connectome Project.

be demonstrated that high-resolution images acquired at 7T provide increased functional contrast-to-noise ratios with significantly less partial-volume effects and more distinct spatial features (Figs. 21, 22). Studies of structural and functional brain connectivity were paired with behavioral and heritability measures. A detailed summary of the 5-year project result was published in *Nature Neuroscience* [44].

Research in Europe

The scientific success of the Connectome gradients has recently persuaded two major European research centers to extend their instruments parks with a 300 mT/m machine. **The Max Planck Institute for Human Cognitive and Brain Sciences, Leipzig, Germany**, plans to develop MRI methods to reliably characterize the detailed functional and anatomical micro- structure of the human brain. Their strategy is to combine the best data from 7T and the 3T Connectom scanner. They plan for imaging the intracortical microstructure, such as myeloarchitecture and intracortical connectomics, and fine structure in the white matter. The ultimate goal is to understand the structure-function relationship in the human brain, pathological changes in neurodegeneration (e.g. amyloid plaques in Alzheimer's disease) and provide early biomarkers. A first step in methodology development will comprise high-fidelity field mapping, optical prospective motion correction and new pulse sequences, in order to achieve a spatial resolution of 600 um or higher combined with high diffusion-weighting factors.

The **Cardiff University Brain Research Imaging Centre (CUBRIC), Cardiff, UK** plans to develop MRI methods for quantifying tissue structure at the microscopic scale. The principal approach looks at how fine tissue structure impedes the movement of water. Current MRI hardware (i.e. gradient strength) restricts measurement to relatively large molecular displacements and from tissue components

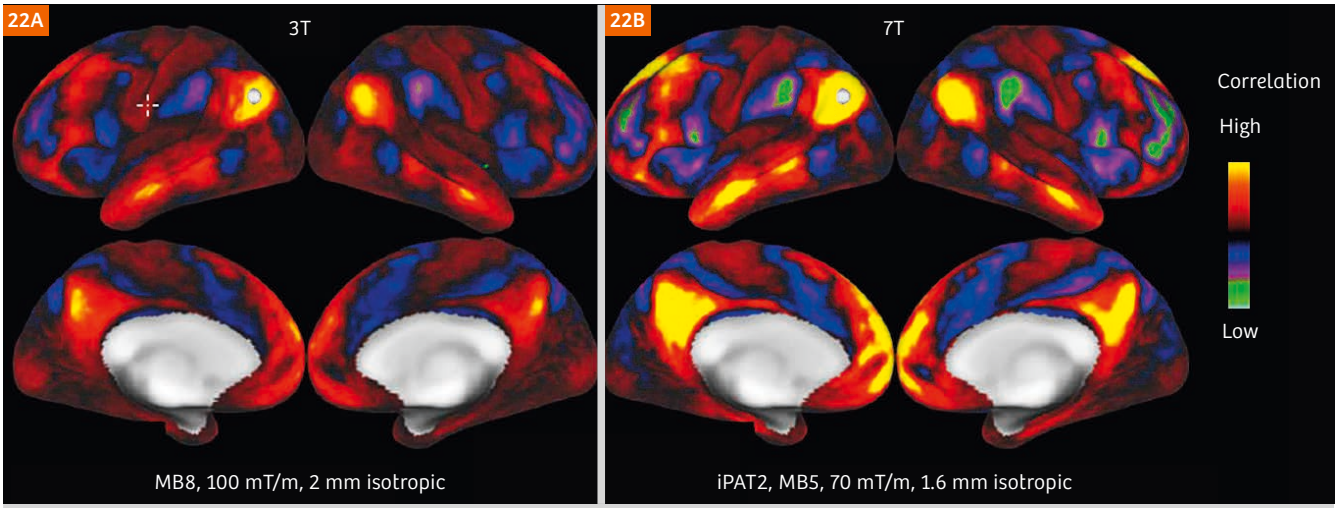

Figure 22: Exemplary composite dataset of the left and right cerebral hemispheres of the human brain (3T vs. 7T). Red and yellow sections are strongly related to the seed location in occipital parietal cortex (white dot). The correlation factor is based on data from resting state functional MRI. While the 3T data shows detailed connectivity / correlation throughout the brain, the correlation factor of 7T data is even more pronounced. *Images courtesy of Washington University – University of Minnesota – Oxford University Human Connectome Project.*

with a relatively strong and long-lived signal, prohibiting quantification of individual cell dimensions, or packing of nerve fibers. Once achieved with the new 300 mT/m machine, faster acquisition and access to newly-visible signal components will enable new mathematical models of microstructure on finer length-scales. This will help to increase understanding of tissue structure in health and disease, and to make testable predictions on important biophysical parameters such as nerve conduction velocities in the brain or cell structure in the liver. The ultimate goal is to develop the imaging software that brings this hardware to mass availability, in turn enabling a new generation of mainstream microstructure imaging and macrostructural connectivity mapping techniques to translate to frontline practice.

Conclusion

As of today, more than 140 studies have acknowledged the use of data generated by the Human Connectome Project. This reflects the goal of the NIH funding organization, which intended that the findings should be broadly applicable to clinical and scientific questions. Both MGH-UCLA and WU-Minn consortia, have successfully developed and applied new methods to map structural and functional connectivity of the brain. Gains in spatial sharpness and clarity are qualitatively analogous to those made in astronomy after the introduction of adaptive optics to overcome the atmospheric blurring. The initial thought that the human brain could be mapped in analogy to the Human Genome Project is now supported by a first, but important step. A promising next step is the extension of the Connectome user base with the new European sites, Cardiff University Brain Research Imaging Centre (CUBRIC) and Max Planck Institute for Human Cognitive and Brain Sciences, Leipzig. It remains to be seen in the future, which further methodical and instrumental steps need to be taken until the level of understanding of the human brain approaches that of *C. elegans*.

References

1 Stejskal EO, Tanner JE. Spin diffusion measurements: spin echoes in the presence of a time-dependent field gradient. Journal of Chemical Physics. 1965;42:288–292.
2 Le Bihan D, Breton E (1985). Imagerie de diffusion in-vivo par résonance magnétique nucléaire. C R Acad Sci (Paris). 301 (15): 1109–1112.
3 Basser PJ, Mattiello J, LeBihan D. Estimation of the effective self-diffusion tensor from the NMR spin echo. Journal of Magnetic Resonance. Series B. San Diego Cal 103.1994, 247–254.
4 Sulston JE, et al. The Embryonic Cell Lineage of the Nematode Caenorhabditis elegans. Developmental Biology 100, 64-119 (1983).
5 Towlson EK et al. The rich club of the C. elegans neuronal connectome. J Neurosci. 2013 Apr 10;33(15):6380-7.
6 Majka P et al. Towards a comprehensive atlas of cortical connections in a primate brain: Mapping tracer injection studies of the common marmoset into a reference digital template. J Comp Neurol. 2016 Aug 1;524(11):2161-81.
7 Zingg B, Hintiryan H, Gou L, Song MY, Bay M, Bienkowski MS, Foster NN, Yamashita S, Bowman I, Toga AW, Dong HW. Neural networks of the mouse neocortex. Cell 2014 156:1096–1111.
8 Biswal B, Yetkin FZ, Haughton VM, Hyde JS. Functional connectivity in the motor cortex of resting human brain using echo-planar MRI. Magn Reson Med. 1995 Oct; 34(4):537-41.
9 Wedeen VJ, Hagmann P, Tseng WY, Reese TG, Weisskoff RM. Mapping complex tissue architecture with diffusion spectrum magnetic resonance imaging. Magn. Reson. Med. 54, 1377–1386 (2005). (DSI).
10 Tuch D, Wedeen VJ, et al. High angular resolution diffusion imaging reveals intravoxel white matter fiber heterogeneity. MRM, 2002, 48(4):577-82.

11 Making connections. 396, Nature, vol 483, 22 March 2012.
12 Mansfield P. Multi-planar image formation using NMR spin echos. J. Phys. C, Solid State Physics 10:155 (1977).
13 Cohen MS, Weisskoff RM. Ultra-fast imaging. Magnetic Resonance Imaging 9:1 (1991).
14 Schmitt F et al. Echo-planar imaging of human brain perfusion at 1T. MRM: 116 (1991).
15 Turner R. A target field approach to optimal coil design. J Phys D 19:L147 (1986).
16 Siebold H. Gradient field coils for MR imaging with high spectral purity. IEEE Trans Magn 26:897 (1990).
17 Kimmlingen R, et al. Gradient System with Continously Variable Field Characteristics. Proc. Intl. Soc. Mag. Reson. Med. (1999).
18 Patz S et al. Novel encoding technology for ultrafast MRI in a limited spatial region. International Journal of Imaging Systems and Technology: 10.3:216 (1999).
19 Kaindl A, et al. Influence of chemo-rheological properties of silica-filled liquid epoxy resins on partial discharge behavior of coils. Proc. Coil Winding Conference (2001).
20 Irnich W. Electrostimulation by time-varying magnetic fields. MAGMA 2:43 (1994)
21 Kimmlingen R, et al. An easy to exchange high performance head gradient insert for a 3T whole body MRI system: First results. Proc. Intl. Soc. Mag. Reson. Med. (2004).
22 Takahashi E, Dai G, Wang R, Ohki K, Rosen GD, Galaburda AM, Grant PE, Wedeen VJ. Development of cerebral fiber pathways in cats revealed by diffusion spectrum imaging. Neuroimage 49(2): 1231-1240 (2010).
23 Kimmlingen R, et al. Concept and realization of high strength gradients for the Human Connectome Project. ISMRM conference (2012).
24 Budinger TF. Thresholds for physiological effects due to RF and magnetic fields used in NMR imaging. IEEE TransNucl.Sc., Vol. NS-26, No.2 April.1979.
25 Larkman DJ, Hajnal JV, Herlihy AH, Coutts GA, Young IR, Ehnholm G. Use of multicoil arrays for separation of signal from multiple slices simultaneously excited. J Magn Reson Imaging. 2001;13(2):313–317.
26 Feinberg DA, et al. Multiplexed Echo Planar Imaging for Sub-Second Whole Brain FMRI and Fast Diffusion Imaging. PLoS ONE, 2010. 5(12): p. e15710.
27 Setsompop K, Gagoski BA, Polimeni JR, Witzel T, Wedeen VJ, Wald LL. Blipped-controlled aliasing in parallel imaging for simultaneous multislice echo planar imaging with reduced g-factor penalty. Magn Reson Med. 2012 May; 67(5):1210-24.
28 Keil B, Blau JN, Biber S, Hoecht P, Tountcheva V, Setsompop K, Triantafyllou C, Wald LL. A 64-channel 3T array coil for accelerated brain MRI. Magn Reson Med. 2013 Jul; 70(1):248-58.
29 Setsompop K, Kimmlingen R, Eberlein E, Witzel T, Cohen-Adad J, McNab JA, Keil B, Tisdall MD, Hoecht P, Dietz P, Cauley SF, Tountcheva V, Matschl V, Lenz VH, Heberlein K, Potthast A, Thein H, Van Horn J, Toga A, Schmitt F, Lehne D, Rosen BR, Wedeen V, Wald LL. Pushing the limits of *in vivo* diffusion MRI for the Human Connectome Project. Neuroimage. 2013 Oct 15;80:220-33.
30 Fan Q, Nummenmaa A, Witzel T, Zanzonico R, Keil B, Cauley S, Polimeni JR, Tisdall D, Van Dijk K, Buckner RL, Wedeen V, Rosen BR, Wald LL. Investigating the capability to resolve complex white matter structures with high b-value diffusion MRI on the MGH-USC Connectome Scanner. Brain Connectivity, 2014 Nov; 4(9) p.718-26 PMID 25287963.
31 Van Wedeen J, Rosene DL, Wang R, Dai G, Mortazavi F, Hagmann P, Kaas JH, Tseng W-Y I. The Geometric Structure of the Brain Fiber Pathways: A Continuous Orthogonal Grid. Science. 2012 Mar 30; 335(6076): 1628–1634.
32 Huang SY, Nummenmaa A, Witzel T, Duval T, Cohen-Adad J, Wald LL, McNab JA. The impact of gradient strength on *in vivo* diffusion MRI estimates of axon diameter. Neuroimage 2014 Dec.9 Epub ahead of print. PMID: 25498429.
33 Huang, SY, Tobyne SM, Nummenmaa A, Witzel T, Wald LL, McNab JA, Klawiter EC Characterization of Axonal Disease in Patients with Multiple Sclerosis Using High-Gradient-Diffusion MR Imaging.
34 McNab JA, Edlow BL, Witzel T, Huang SY, Bhat H, Heberlein K, Feiweier T, Liu K, Keil B, Cohen-Adad J, Tisdall MD, Folkerth RD, Kinney HC, Wald LL. The Human Connectome Project and beyond: initial applications of 300 mT/m gradients. Neuroimage 2013;80:234-245.
35 Fan Q, Witzel T, Nummenmaa A, Van Dijk KR, Van Horn JD, Drews MK, Somerville LH, Sheridan MA, Santillana RM, Snyder J, Hedden T, Shaw EE, Hollinshead MO, Renvall V, Zanzonico R, Keil B, Cauley S, Polimeni JR, Tisdall D, Buckner RL, Wedeen VJ, Wald LL, Toga AW, Rosen BR. MGH-USC Human Connectome Project datasets with ultra-high b-value diffusion MRI. Neuroimage 2016;124(Pt B):1108-1114.
36 Smith SM, Miller KL, Moeller S, Xu J, Auerbach EJ, Woolrich MW, Beckmanna CF, Jenkinson M, Andersson J, Glasser MF, Van Essen DC, Feinberg DA, Yacoub ES, Ugurbil K. Temporally-independent functional modes of spontaneous brain activity. www.pnas.org/cgi/doi/10.1073/pnas.1121329109, 2011.
37 Van Essen DC, et al. The Human Connectome Project: A data acquisition perspective. NeuroImage (2012), j.neuroimage.2012.02.018.
38 Ugurbil K, et al. Pushing spatial and temporal resolution for functional and diffusion MRI in the Human Connectome Project. Neuroimage 80, 80–104 (2013).
39 Van Essen DC, et al. The WU-Minn Human Connectome Project: an overview. Neuroimage 80, 62–79 (2013).
40 Sotiropoulos SN, Jbabdi S, Xu J, Andersson JL, Moeller S, Auerbach EJ, Glasser MF, Hernandez M, Sapiro G, Jenkinson M, Feinberg DA, Yacoub E, Lenglet C, Van Essen DC, Ugurbil K, Behrens TE. Advances in diffusion MRI acquisition and processing in the Human Connectome Project. Neuroimage. 2013 Oct 15; 80:125-43.
41 Glasser MF, Coalson TS, Robinson EC, Hacker CD, Harwell J, Yacoub E, Ugurbil K, Andersson J, Beckmann CF, Jenkinson M, Smith SM, Van Essen DC. A multi-modal parcellation of human cerebral cortex. Nature 536, 171–178 (11 August 2016).
42 Vu AT, Auerbach E, Lenglet C, Moeller S, Sotiropoulos SN, Jbabdi S, Andersson J, Yacoub E, Ugurbil K. High resolution whole brain diffusion imaging at 7 T for the Human Connectome Project. Neuroimage. 2015 Nov 15; 122: 318–331.
43 Vu AT. High resolution whole brain diffusion imaging at 7T for the Human Connectome Project. NeuroImage (2016), http://dx.doi.org/10.1016/j.neuroimage.2016.11.049.
44 Glasser MF, Smith SM, Marcus DS, Andersson JLR, Auerbach EJ, Behrens TEJ, Coalson TS, Harms MP, Jenkinson M, Moeller S, Robinson EC, Sotiropoulos SN, Xu J, Yacoub E, Ugurbil K, Van Essen DC. The Human Connectome Project's neuroimaging approach. Nature Neuroscience 19, 1175–1187 (2016).

Contact

Ralph Kimmlingen, Ph.D.
Siemens Healthcare GmbH

Am Röthelheimpark 2
91052 Erlangen
Germany
ralph.kimmlingen@siemens.com

Gadgetron: Open Source Image Reconstruction

Michael S. Hansen; Hui Xue; Peter Kellman

Laboratory of Imaging Technology, National Heart, Lung, and Blood Institute, National Institutes of Health, Bethesda, MD, USA

Introduction

Image reconstruction plays a critical role in modern MRI methodology. Recent gains in imaging speed and quality have been driven by techniques such as parallel imaging [1–3] and compressed sensing [4]. Although there have been numerous innovations in image reconstruction, there are many new reconstruction techniques published in scientific journals that are not evaluated on a large scale and therefore never make it into clinical use. This is caused by challenges presented by the current development environments and paradigms. This paper reviews the development and deployment paradigm introduced by the Gadgetron [5] reconstruction framework as it has been used on the Siemens Healthcare platform. The concepts and information presented in this paper are based on research and are not commercially available.

While the field of image reconstruction continues to be very active, access to vendor reconstruction code has been limited. The Siemens Healthcare platform has traditionally provided a wide image reconstruction programming window through the Image Calculation Environment (ICE). This environment has enabled developers to use existing Siemens Healthcare reconstruction modules (Functors) as black box modules, but access to the source code of the full reconstruction pipeline has been limited. Modern reconstruction algorithms consist of several critical steps that form an image reconstruction pipeline [6], and when new reconstruction algorithms are developed, they must be compared to existing methodology to identify and analyze advantages and disadvantages. In many cases it is challenging to reproduce results from published papers on image reconstruction techniques. There are several reasons for this, but one important obstacle is the lack of access to the underlying source code used to produce the images. It is critical for researchers to be able to examine and reproduce each algorithmic step of previously developed methodology and consequently they have to attempt to replicate existing reconstruction methods from the descriptions in the publications. Given the cursory treatment that the actual implementation is frequently given in such publications, it can be a formidable challenge to produce a high quality, high performance implementation of existing algorithms. This makes any subsequent comparisons much less meaningful. Open access to source code of reference implementations will play an important role in advancing the field of MRI in general and MRI reconstruction in particular.

In addition to reproducibility problems, current MRI reconstruction development has also been hampered by the logistical and regulatory problems associated with deploying prototype reconstruction algorithms in a clinical environment. New techniques are often implemented in scripting environments such as MATLAB (MathWorks, Natick, MA, USA) or Python (Python Software Foundation, Wilmington, DE, USA) and they are not easily connected to clinical scanners. When researchers evaluate novel reconstruction algorithms, the workflow often involves

1

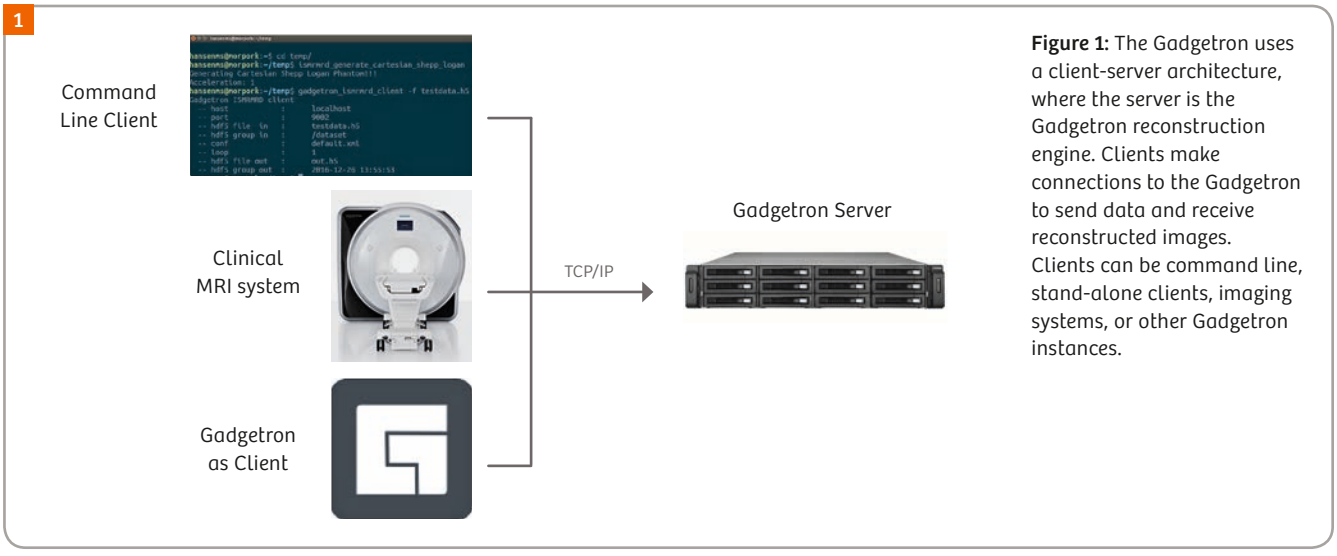

Figure 1: The Gadgetron uses a client-server architecture, where the server is the Gadgetron reconstruction engine. Clients make connections to the Gadgetron to send data and receive reconstructed images. Clients can be command line, stand-alone clients, imaging systems, or other Gadgetron instances.

transferring raw data for offline reconstruction and subsequent evaluation and comparison against existing techniques. This decouples the evaluation of reconstruction techniques from existing clinical workflows. The lack of tight scanner integration also creates a barrier for adoption and large scale testing of new techniques; the offline reconstruction workflow is manageable in small research settings where expert help is available, but it is not easily transferred to other sites. Ideally, images reconstructed with novel techniques should be available online on the scanner such that they can be used in the clinical analysis tools and immediate comparisons and evaluations become possible.

It is important to consider why developers use offline environment. One reason is that they need access to development tools and infrastructure that vendor environments such as ICE do not provide. The access to rapid prototyping scripting languages such as Python, MATLAB, or Julia (NumFocus, Austin, TX, USA) are examples of such tools, but more generally vendor reconstruction environments are relatively restrictive in terms of the hardware and software that they provide. As an example, the use of Graphical Processing Units (GPUs) was proposed [7–9] several years before such hardware became available on commercial MRI systems. Even today with the availability of the GPU hardware on commercial MRI systems, it is often older generation hardware and drivers that are not compatible with the latest development tools; the slow development cycles of commercial systems and the need to maintain backwards compatibility makes it challenging for commercial vendors to keep up with the rapidly changing field of computational hardware and software. There is a need for image reconstruction environments that can be deployed on platforms where developers can control the available hardware and the associated software components.

The Gadgetron was developed to provide solutions to the challenges outlined above. It is an open source, freely available image reconstruction server engine, which can be deployed as a stand-alone tool on a developers desktop computer or it can be connected directly and transparently to commercial Siemens Healthcare MRI systems. When connecting to a clinical MRI system, it can be deployed in several configurations:

a) directly on the available vendor hardware,

b) on a separate workstation connected to the scanner, or

c) on remote computer systems, which may provide cloud computing resources.

The framework enables developers to use the hardware and software platform of their choice. It is also modular and enables the users to use scripting languages for all or part of their image reconstruction pipeline. The following sections outline the architecture of Gadgetron and describe how it is connected to Siemens Healthcare MRI systems. A number of use cases and example applications are also provided.

Key points

- Reproducible research relies on Open Source software.
- Vendor reconstruction environments do not provide access to source code.
- It is challenging to deploy and test prototype reconstruction in a clinical environment.
- The Gadgetron is an Open Source image reconstruction framework which provides access to algorithm code, rapid prototyping, and transparent deployment on Siemens Healthcare MRI systems.
- Source code and documentation: https://gadgetron.github.io

Gadgetron architecture

The Gadgetron uses a client-server architecture as outlined in Figure 1. The reconstruction engine is the server and different types of clients can connect to the reconstruction server. Figure 1 illustrates three common scenarios. When the Gadgetron is used as a stand-alone reconstruction tool, the client would be a command line tool that reads a file with raw data and sends it to the Gadgetron. The Gadgetron instance can be local to the machine where the client is executing or it can be located on a remote server. Reconstructed images are returned to the client and written to an output file. When processing MRI datasets, the Gadgetron uses the ISMRM Raw Data (ISMRMRD) [10] format. The ISMRMRD format is a vendor neutral format for MR raw datasets and converters from most commonly used commercial vendors are available. Consequently, the ISMRMRD command line client, which is supplied with the Gadgetron source code, can be used to send data from any vendor to the Gadgetron engine for reconstruction after appropriate data conversion. The command line client is useful during reconstruction development and when processing datasets offline, but in a clinical setting, data must be sent directly by the scanner to the Gadgetron and images should be returned to the scanner host database for viewing and planning purposes. To facilitate this, an ICE based Gadgetron client (IceGadgetron) is available. The integration with Siemens Healthcare MRI systems is described in the *Siemens Healthcare Scanner Integration* section below. The Gadgetron engine itself can also act as a client. This use case is encountered when the Gadgetron is deployed in cloud computing platforms where multiple Gadgetron instances can collaborate on a reconstruction task. Some of these instances will be clients and some will be servers. This is discussed further in the *Deployment Strategies* below.

The reconstruction server engine is a pipeline architecture as shown in Figure 2. Each reconstruction program in the Gadgetron is a pipeline assembled from multiple modules

2

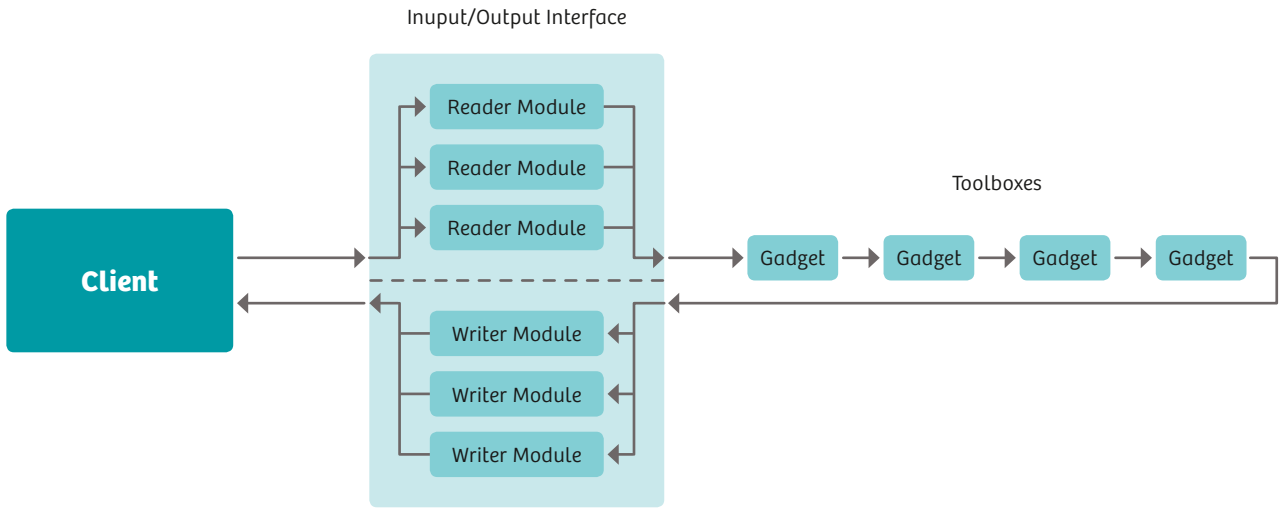

Figure 2: The Gadgetron pipeline architecture. The client connects to the Gadgetron reconstruction engine with a TCP/IP socket connection. The configurable input/output interface is responsible to deserializing incoming data and serializing outgoing data. Once data has been received, it is passed through a set of modules or Gadgets, which perform reconstruction steps. These Gadgets use a number of toolbox functions to perform the data processing.

that are assembled and configured at runtime. The data processing is modeled as a set of modules or Gadgets. As the data passes from Gadget to Gadget, it is modified and transformed until the final images are ready to be returned to the client. A configurable input/output interface is responsible for receiving data from the TCP/IP connection and transmitting reconstruction products back to the client. The configuration of this interface is done at runtime by assembling a set of modules that can handle the reading (deserialization) and writing (serialization) of particular datatypes. The Gadgetron framework does not put any restrictions on the type of data that can be sent and received, and as such it can be used to reconstruct any kind of imaging data. It can also receive and send data that it not related to the imaging experiment. Examples of such data could be physiological waveforms or other telemetry (such as subject motion data) that can be used in the reconstruction. To support a new data type, developers must implement the required reader/writer modules to deserialize/serialize the data.

The pipeline specification is provided to the Gadetron engine in the form of an XML document. This XML description lists the readers, writers, and Gadgets to include in the processing pipeline. The Gadgetron comes with a set of predefined reconstruction pipelines and the client can simply request which one to load. Alternatively, the client can transmit the XML description of the pipeline and assuming the requested Gadgets are available on the server, the pipeline will be loaded and raw data will be passed down the pipeline.

The Gadget modules are typically implemented in C/C++, but the framework also allows for modules to be implemented in scripting languages such as Python or MATLAB. The MATLAB integration requires that a MATLAB installation is available on the server that is running the Gadgetron engine. This MATLAB installation must be equipped with an appropriate license or access to a license server. The license requirements along with some performance issues associated with starting a MATLAB instance when MATLAB Gadgets load makes the MATLAB integration less attractive than the Python integration, but it is available as a prototyping tool. The scripting Gadgets provide a fast way to deploy existing prototype code on a clinical scanner. Subsequent development cycles can then be used to improve performance by moving critical pieces of the reconstruction to C/C++ Gadgets.

A set of C/C++ toolboxes are available as part of the Gadgetron framework. These toolboxes contain common components that are reused in several Gadgets. This includes data structures for storing and managing the acquisition data, filters, transforms (Fourier, wavelet, etc.), numerical solvers (conjugate gradient, nonlinear conjugate gradient, etc.), and other utilities. Much effort has been spent on tunings the computational efficiency and the use of parallel computing in these core components. The toolboxes can be used in stand-alone applications that do not use the Gadget pipeline architecture. The source code repository includes several such stand-alone applications that serve as examples of how to use key toolbox components. Of special note are several toolboxes that implement performance critical code on Graphical Processing Units (GPUs). One example is the non-Cartesian Fourier transform [7]. The GPU code uses NVIDIAs CUDA

framework [11]. The GPU based non-Cartesian FFT along with other key toolbox components (such as GPU solvers) form the basis for several high performance (real-time) implementations of non-Cartesian parallel imaging.

Siemens Healthcare scanner integration

The Gadgetron can be integrated with any commercial scanner platform, which allows sockets to be opened from the reconstruction pipeline in order to transmit data to the Gadgetron. The connection to the Gadgetron is achieved through a specialized ICE program called IceGadgetron. This ICE program is shared on the IDEA discussion board (https://www.mr-idea.com), where updated versions of binaries and source code are uploaded at regular intervals. The IceGadgetron package is known to work on *syngo* MR B, *syngo* MR D, and *syngo* MR E software versions.

The IceGadgetron package provides two key ICE Functors:
1) GadgetronEmitterFunctor (Emitter), and
2) GadgetronInjectorFunctor (Injector).
The role of these two Functors is illustrated in Figure 3. The Emitter is inserted into an existing ICE pipeline at the point where the developer would like the raw data (or images) to be transmitted to the Gadgetron and the Injector is inserted where the returned reconstruction products (usually images) are to be inserted back into the ICE pipeline. The location of the Emitter and the Injector can be controlled with a configuration file. In practice, each ICE reconstruction program that calls the IceGadgetron configurator is accompanied by a configuration document (in XML format) that specifies

3

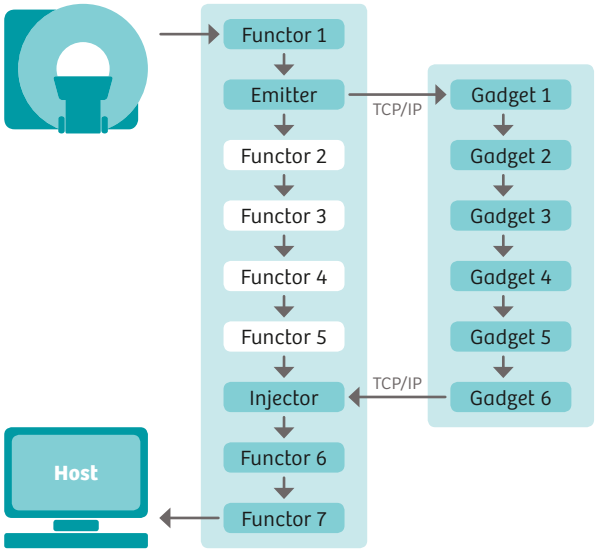

Figure 3: Schematic outline of the IceGadgetron package and connection to the Gadgetron. The IceGadgetron package provides two functors: The GadgetronEmitter, which translates the raw data to ISMRMRD format and sends it to the Gadgetron and the GadgetronInjector, which receives reconstructed images from the Gadgetron and injects them back into the ICE pipeline.

where the IceGadgetron Functors are to be inserted and other key configuration parameters such as which Gadgetron reconstruction program should be loaded. This allows the IceGadgetron program to be applied as an add-on to any existing reconstruction chain.

The Emitter plays multiple roles. Before sending any data from the current acquisition to the Gadgetron, it checks to see if there are any dependent measurements (such as noise measurements) for the current measurement and if so they are converted to ISMRMRD format and transmitted to the Gadgetron. It then converts the Siemens Healthcare specific raw data protocol (the sequences parameters) to an ISMRMRD header, which is transmitted to the Gadgetron. Finally, it does an on-the-fly conversion of each acquired raw data readout to ISMRMRD and transmits to the Gadgetron. Data is converted as it is acquired and transmitted to the Gadgetron immediately and consequently data processing on the Gadgetron starts immediately when data is available. This immediate transmission of data provides the Gadgetron framework with some performance advantages in a clinical setting compared to other prototyping environments that start data transmission when the acquisition is complete.

The Injector serves to receive images as they are returned to the Gadgetron. Once the images are back in the ICE environment, an appropriate header is attached to the images such that image numbering, timing information, etc., are attached to the image when they are inserted into the image database. After attaching a header to the images, they are passed down any remaining Functors in the ICE pipeline. This allows for post processing steps such as gradient distortion correction to be applied in the ICE environment where appropriate calibration information is available.

The Functors between the Emitter and the Injector are bypassed by default as indicated by the dotted outline in Figure 3, but it is also possible to operate IceGadgetron in such a way that the data is sent through both the Gadgetron and ICE pipelines. This may be useful for debugging and comparisons. However, since the Gadgetron is often used to deploy prototype reconstructions for which there may be no meaningful alternative in ICE, passing data through both pipelines is not always possible.

It is important to note that since conversion to DICOM images is done after the images return to the ICE environment, there is no need for patient identifying information (PII) to be sent to the Gadgetron. The ISMRMRD format defines header sections for PII (e.g., patient name), but when using the Gadgetron in conjunction with IceGadgetron, these header sections are not needed and are simply omitted. Consequently, the communication between the scanner and the Gadgetron is an anonymized stream of data. This is critical when considering deployment strategies where the Gadgetron engine is located outside the hospital firewalls. Such configuration options are discussed in more detail below.

Deployment strategies

The only requirement to connect a clinical MRI system to a Gadgetron instance is that the MRI system can open a TCP/IP network socket to either a local or remote Gadgetron instance. Some of the possible deployment topologies are outlined in Figure 4. The Siemens Healthcare reconstruction computer (the MRIR or MARS computer depending on software and hardware version) is equipped with a network interface, which is used to connect the ICE environment with the host. This network connection is configured with a local network IP address that only allows it to connect to the host, but there are two ways to utilize this network interface to provide access to a Gadgetron instance. A network switch can be inserted in the network between the MARS and the host computer. It should be noted that while such a switch used to be available *syngo* MR B line scanners, the newer *syngo* MR D and E systems do not ship with the switch since it is no longer needed. Inserting the switch is a modification of the system, which is not officially supported by Siemens Healthcare and may lead to loose the CE mark. Once the host and the reconstruction computer is connected via a switch, a Gadgetron reconstruction computer can be connected directly to this switch and given an IP address on the local network. This will allow the ICE environment to communicate directly with the Gadgetron computer. Alternatively, a Secure Shell (SSH) tunnel can be opened from the host computer and the ICE environment can connect to a remote Gadgetron through this tunnel; the connection will be made to the host, which will forward the connection. The ability to open a tunnel is built into the IceGadgetron package. Using a configuration file, the tunneling details can be specified such that the tunnel is automatically available in a way that is transparent to the user. When using a tunnel to connect to the Gadgetron, it is possible to use a Gadgetron server that is not directly connected to the MARS. This Gadgetron instance could be located somewhere else on network or it could be located at a remote location, e.g., in the cloud. Once a connection is made to cloud computing data center, it is possible to use Gadgetron topologies where multiple instances collaborate on the reconstruction thus reducing the reconstruction time of sophisticated algorithms to clinically acceptable reconstruction times [12].

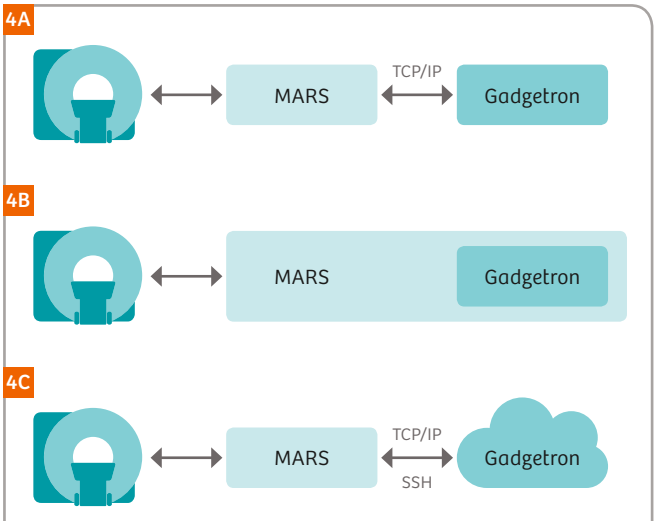

Figure 4: Gadgetron deployment topologies. The most straightforward way to connect the Gadgetron is with direct TCP/IP connection from the MARS to the Gadgetron **(4A)**. This requires a switch to be available on the local scanner network. Alternatively the Gadgetron may be deployed as a container directly on the MARS hardware **(4B)**. This enables Gadgetron operation without the installation of additional hardware. Finally the Gadgetron may be located on a remote system **(4C)**. When connecting to a remote system a Secure Shell (SSH) tunnel is opened from the host and the connection to the remote system is forwarded through this tunnel.

It is also possible to deploy the Gadgetron on Siemens Healthcare systems without installing any additional hardware. The Gadgetron development and deployment strategy (see Figure 4) makes heavy use of containers using either Docker [13] or chroot (https://en.wikipedia.org/wiki/Chroot) to manage application dependencies. It is possible to deploy such a container directly on the MARS computer and the IceGadgetron program can start and stop a Gadgetron instance automatically if configured to do so. This deployment strategy is a convenient way to deploy novel reconstruction algorithms directly on existing hardware. The Gadgetron containers can make full use of CPU and GPU hardware available on the MARS but the performance will ultimately be constrained by the hardware performance of the MARS. It should also be mentioned that ICE employs a proprietary memory management strategy that in general means that memory will not be released from the ICE environment once it has been allocated. On *syngo* MR E systems, IceGadgetron makes use of a mechanism to force the ICE environment to release reserved memory in order to make the memory available to the Gadgetron, but such a mechanism is not available on *syngo* MR D software releases. The deployment of the Gadgetron on the MARS system is only recommended for *syngo* MR E systems.

Development model

Open source software principles are key to the Gadgetron development model. The source code for the Gadgetron and ISMRMRD projects is freely available on Github (https://github.com). Changes to the source code are managed and reviewed through the online collaborative tools made available at that site. Changes are proposed as source code pull requests and after discussion and revision, they are merged into the source code. The development workflow is outlined in Figure 5. Modifications to the Gadgetron (or a dependency) triggers an automated build system to start compiling the source code on Windows, Linux, and Mac computers. If the code compiles, it is automatically tested. The test suite consists of a collection of unit tests for toolbox level components and a number of integration tests. The integration tests convert real raw data

5

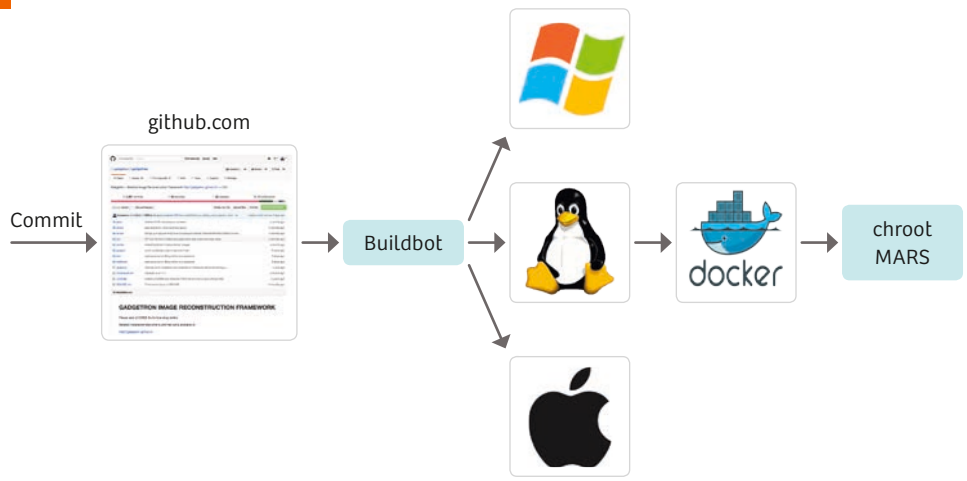

Figure 5: The Gadgetron development pipeline. Collaboration and code management is done using Github (https://github.com/gadgetron). Once code modifications are merged, the software is automatically built and tested on Windows, Linux, and Mac computers. Docker containers with all dependencies are generated and tested and the container images can be deployed directly on the Siemens Healthcare MARS computer.

sets to ISMRMRD format and reconstructs images with different image reconstruction pipelines. The reconstruction results are compared to a database with reconstruction results to detect any changes in reconstruction results. If all tests pass, the tested version of the Gadgetron with all dependencies is immediately released as a Docker image on Docker Hub (https://hub.docker.com/r/gadgetron). The build system tests multiple configuration options. In particular, multiple versions of NVIDIA CUDA are tested and Docker images based on different versions are released.

The Docker containers can be deployed immediately on any computer with the Docker engine installed. The containers will run natively on Linux and using a hypervisor on Windows and Mac computers. Consequently, it is relatively easy to install and run the Gadgetron, even for users with little or no experience in building software. The Gadgetron also comes with a script that allows the user to turn the Docker images into a chroot image that can be deployed directly on the Siemens Healthcare MARS computer as explained above. The conversion to chroot image is necessary at the moment because the MARS system does not have the required Docker engine installed.

Example applications

The Gadgetron supports a wide range of applications. Several of these applications are in the real-time imaging and cardiac imaging area due to the early developers of the Gadgetron, but as the community around the framework has grown, the applications have grown to be more generic and broadly applicable. The following sections describe four different use cases for the Gadgetron. Firstly, a generic, high performance parallel imaging reconstruction pipeline is discussed. It forms the backbone of several image reconstruction chains and provides image reconstruction performance metrics (such as g-factor maps from accelerated parallel imaging) in addition to high quality reconstructions. Secondly, interactive real-time imaging used in interventional image guidance is demonstrated. Thirdly, motion corrected, phase sensitive, inversion recovery reconstruction is highlighted as an application where the Gadgetron can be used to improve clinical workflow. Finally, retrospective respiratory motion correction for free breathing cardiac cine imaging is shown as an example of using the Gadgetron in the cloud.

Generic parallel imaging reconstruction pipeline

A multi-purpose, Cartesian parallel imaging pipeline forms the backbone of many clinical and research applications supported by the Gadgetron. The reconstruction algorithm is based on the GRAPPA algorithm [3], but the *k*-space kernels are Fourier transformed to image space and applied as coil combining coefficients in image space [14]. Based on the coil combining coefficients, parallel imaging related noise amplification is directly estimated in the form of *g*-maps. The reconstruction uses information about the receiver noise covariance matrix to maintain unit noise scaling throughout the image reconstruction pipeline and consequently, it can produce images that are reconstructed in signal-to-noise ratio (SNR) units [15, 16].

Figure 6 shows the Gadgets involved in this SNR scaled parallel imaging pipeline. Many of these Gadgets are reused in other reconstruction pipelines, which illustrates the modularity of the framework. Most Gadgetron reconstruction pipelines include the NoiseAdjust Gadget, which is responsible for noise prewhitening either based on noise samples acquired in a previous scan or inline noise measurements included with the data. After removing oversampling in the readout direction and partial Fourier (assymetric echo) adjustment, the data hits two commonly used Gadgets, the accumulation-and-triggering Gadget and the bucket-to-buffer Gadget. These two work in tandem to organize the incoming data before reconstruction. The accumulate-and-trigger Gadget simply stores the data while it waits for some trigger to occur. An example of such a trigger could be that the repetition number increases. Once the trigger occurs, the accumulated data (stored in

unorganized buckets) is passed on to the bucket to buffer mechanism, which will assemble the data in buffer structures that in the case of Cartesian imaging simply are *k*-spaces buffers. The buffers then pass into the reconstruction part of the pipeline where reference data is used to generate coil combining coefficients. After the image reconstruction there are multiple post-production steps that ready the images for return to the scanner. In this specialized reconstruction pipeline, there are also some additional Gadgets that output image and coil statistics, which are useful for evaluating reconstruction results.

Figure 7 shows example images from the generic parallel imaging reconstruction chain. The example is a rate 4 parallel imaging, real-time cine acquisition of a four-chamber view of the heart. The top image shows one frame of the real-time imaging series. The middle image is the *g*-map, which is produced by the reconstruction chain and the bottom image is the SNR scaled reconstruction. The SNR scaling feature of the Gadgetron reconstruction chain enables on-the-fly evaluation of reconstruction results and comparisons between patients and coils.

6

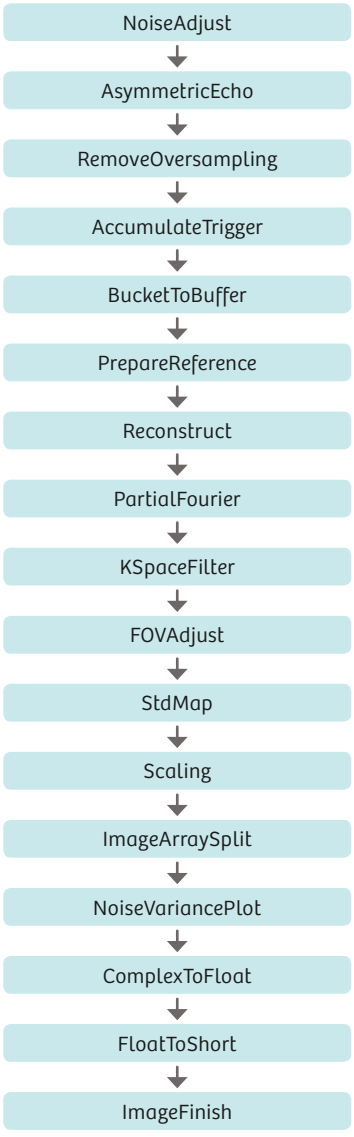

Figure 6: Generic parallel imaging reconstruction pipeline. Unit noise variance is established by the NoiseAdjust Gadget and maintained throughout the pipeline. The pipeline can produce images reconstructed in units of signal-to-noise ratio (SNR) [15].

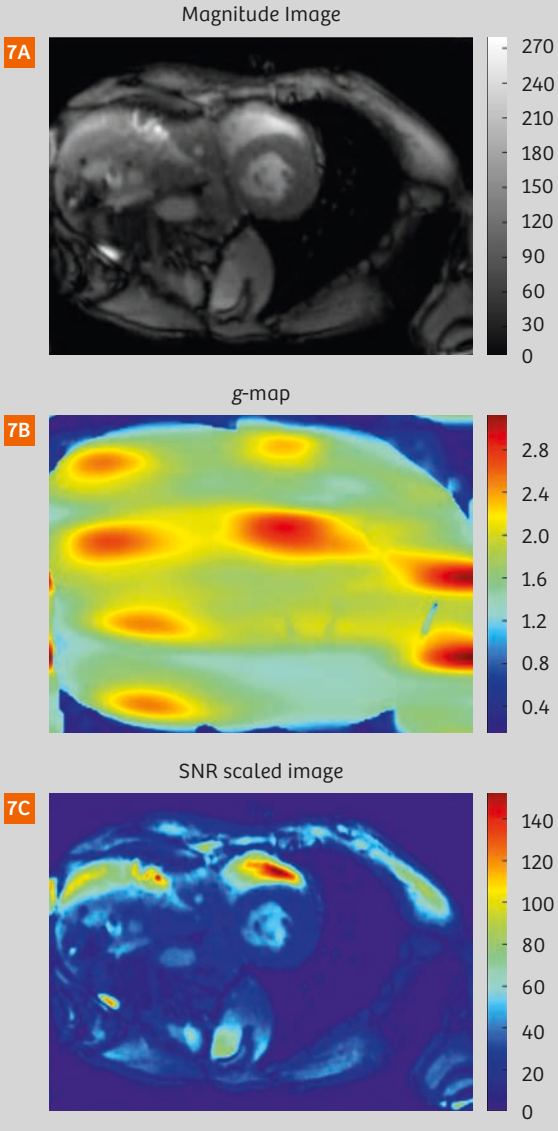

Figure 7: Example images from generic parallel imaging reconstruction pipeline. Data is from a real-time (acceleration rate 4) cardiac cine acquisition showing the heart in a four-chamber view. Top image **(7A)** is the magnitude image, middle image **(7B)** is the *g*-map, and bottom image **(7C)** is the image displayed in units of SNR. Notice how the SNR is higher closer to the coils on the chest.

8

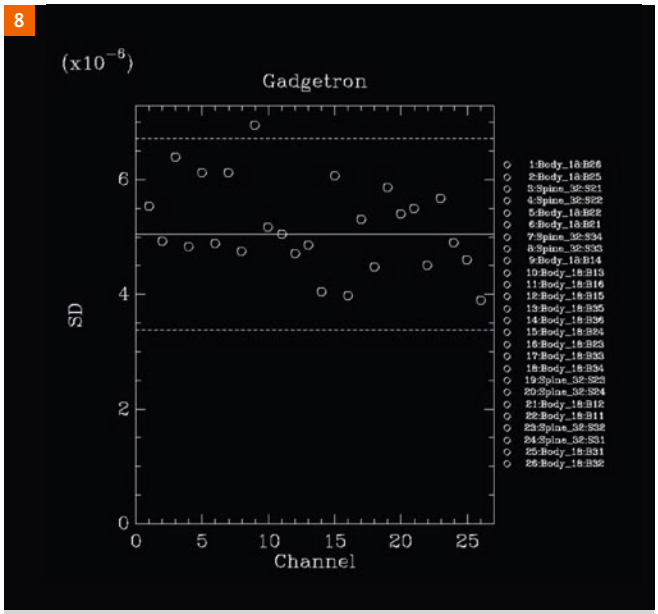

Figure 8: Noise standard deviation plot produced by the generic parallel imaging reconstruction chain. The plot shows the noise level in each employed channel and can be used to pinpoint faulty coil elements.

9

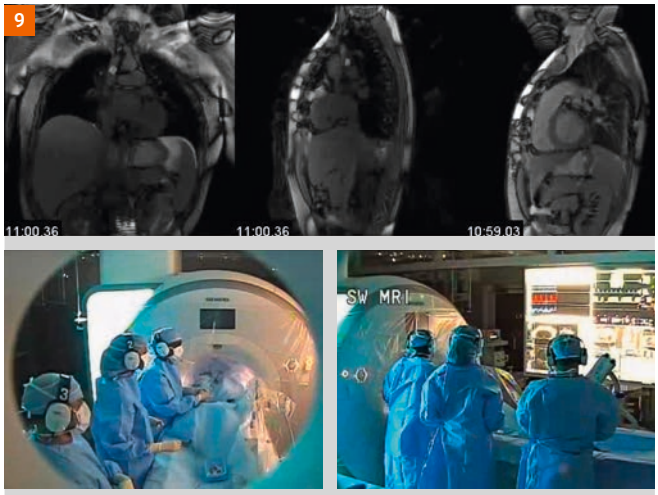

Figure 9: Real-time interventional MRI using the Gadgetron. The top row of images shows example real-time frames used to guide a passive catheter in the patient. The tip of the catheter is equipped with a balloon filled with a Gadolinium based contrast agent. An interactively controlled saturation pulse is used to provide contrast between balloon and surrounding tissue. Bottom row of images shows the interventional cardiologists using the real-time images for navigation.

Figure 8 shows another output from the generic reconstruction chain, which is a plot of the standard deviation of the noise in each channel used in the current reconstruction. This plot is useful in evaluating the performance of the currently used receive chain components. In the example plot, the coil elements have noise standard deviations in the same range, but faulty coil elements are quickly identified as having very high noise level or no noise at all. Users of the Gadgetron have found it useful to run at least one scan in each study, which outputs such an image. It can then be reviewed later as part of standard quality assurance procedures where it can help pinpoint faulty equipment.

Real-time interventional image guidance

One of the original motivations for creating the Gadgetron was to provide a high-performance environment in which to perform real-time reconstruction on the GPU. One of the driving applications for this was interventional MRI [17, 18]. For this application, real-time images must be reconstructed and displayed with low latency to allow the operator to manipulate instrumentation in the patient under MRI guidance. Figure 9 shows images from a diagnostic catheterization performed under MRI guidance. The top row shows example real-time guidance images and the bottom images show how the operator in the scanner room can use these images for navigating the catheters inside the patient. Typically one to three real-time slices are imaged simultaneously and the operator can manipulate the location of these slices interactively. Clinicians have also found it useful to be able to change imaging parameters such as parallel imaging acceleration factor on-the-fly. This enables interactive trade-off between SNR and imaging speed. The Gadgetron comes with a real-time reconstruction chain that can adapt when parallel imaging factor changes.

Siemens Healthcare has released a WIP for interventional MRI based on the BEAT_IRTTT sequence[1]. This sequence can be used with the Siemens Healthcare Interactive Front End (IFE) for interventional MRI. The distributed WIP does not ship with the Gadgetron, but the sequence has the required functionality to communicate with a Gadgetron installation running on either the MARS or an external workstation or server as described above.

Motion corrected, Phase Sensitive Inversion Recovery

Imaging of Late Gadolinium Enhancement (LGE) is the gold standard for assessing myocardial viability [19, 20]. The assessment has traditionally been done with a segmented, Inversion Recovery (IR) sequence acquired during a breath-hold [21]. It is possible to use a magnitude based reconstruction or Phase Sensitive Inversion Recovery (PSIR) [22]. The breath-holding technique can suffer from motion artifacts and thus motion corrected, free-breathing techniques [23] are gaining popularity. More recently, LGE imaging has also been combined with dark blood pre-paration to improve the blood to scar contrast [24].

[1] WIP, the product is currently under development and is not for sale in the US and in other countries. Its future availability cannot be ensured.

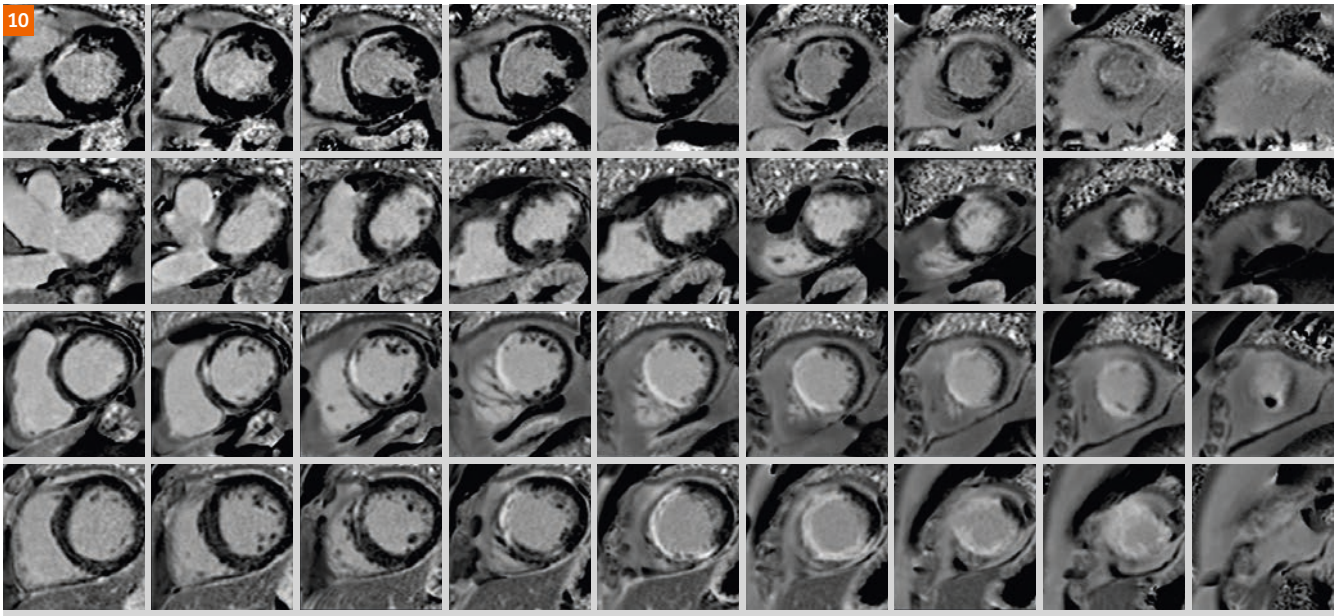

Figure 10: Example LGE stacks reconstructed with the motion corrected, PSIR reconstruction included in the Gadgetron. Stacks of 9 short-axis images can be acquired and reconstructed in approximately 2.5 minutes.

The Gadgetron incorporates reconstruction pipelines for all the popular LGE imaging options including non-rigid motion correction. The reconstruction has been implemented in such a way that multi-slice acquisitions can be reconstructed on-the-fly as they are acquired. While this is a small modification compared to current product pipelines, it has significant impact on workflow. Stacks of LGE images take a substantial amount of time to reconstruct when including motion correction. If this reconstruction does not start until the acquisition is done, it slows down the clinical workflow. Figure 10 shows example LGE short axis stacks, which have been acquired during free breathing and reconstructed using the Gadgetron. Acquisition time for a full stack of slices is on the order of 2.5 minutes. The reconstruction is complete approximately 5 seconds after the end of the scan.

Free-breathing, motion corrected cine imagine of the heart

Cardiac MRI is the gold standard for evaluating cardiac motion and function [25]. Traditionally, this evaluation has been done with a stack of short axis slices acquired during breath-holding. Typically 1–2 slices are acquired in a breath-hold and 9–13 slices are acquired to cover the ventricles. Multiple breath-holds are a significant challenge for cardiac patients in general and it represents a real impediment in pediatric[2] patients. Alternatively, a stack of real-time acquisitions can be prescribed, but the compromised spatial and/or temporal resolution makes it a less attractive option.

To overcome these problems, it was proposed that a series of real-time images acquired over multiple heart beats could be motion corrected, and the motion corrected data could be reassembled (also known as rebinning) with better temporal resolution [26, 27]. The techniques have been improved to use less data [28] and methods that handle non-Cartesian sampling have also been proposed [29]. Figure 11 shows example short axis images acquired with the free-breathing, motion corrected binning technique. The results are compared to breath-hold imaging and free-breathing with multiple averages. The motion correction algorithms increase the reconstruction time. It can be on the order of 1–2 minutes per slice, which is not tolerable clinically. The Gadgetron comes with an implementation of motion corrected binning, and it has been demonstrated that cloud computing can be used in conjunction with motion corrected binning [30]. With this approach, multiple instances of the Gadgetron collaborate on a given reconstruction, effectively assigning an independent computational node to each acquired slice. Since reconstruction of a given imaging slice can start as soon as the acquisition of that slice is complete, the reconstruction cost can be hidden by the acquisition such that the final images are reconstructed and back on the host computer within a minute of the acquisition finishing. Using the binning technique, the acquisition time of each slice is slightly longer than a breath-hold, typically 16–20 seconds, but it is acquired during free-breathing and no pause is needed between slices for the patient to catch their breath. The net result is an overall faster workflow and improved patient comfort.

[2] Siemens Healthcare Disclaimer: MR scanning has not been established as safe for imaging fetuses and infants less than two years of age. The responsible physician must evaluate the benefits of the MR examination compared to those of other imaging procedures.

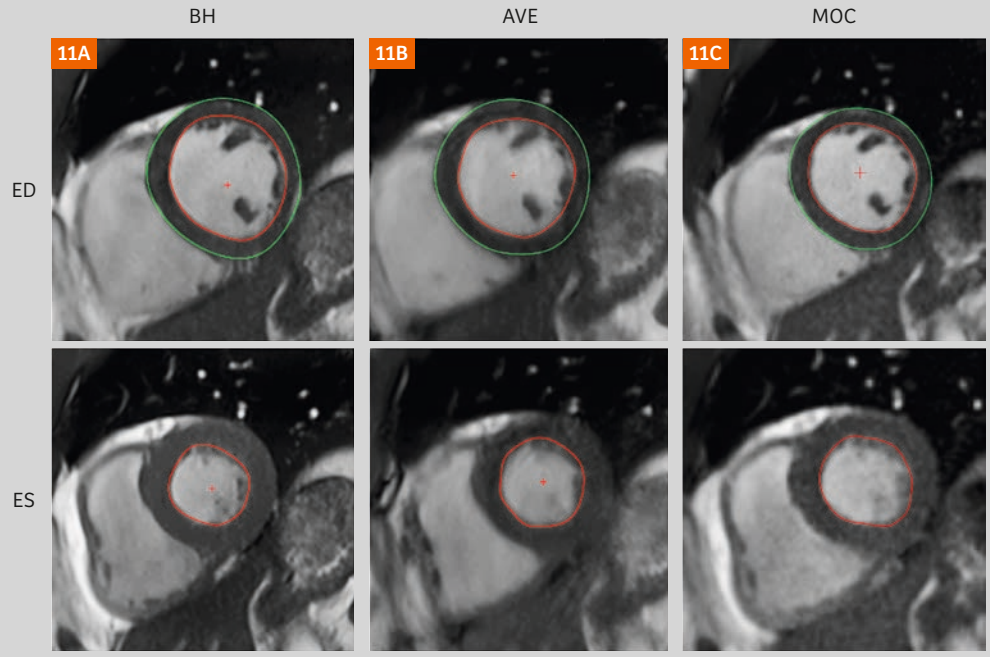

Figure 11: Example cardiac function images comparing three acquisition techniques: **(11A)** breath-hold (BH) segmented, **(11B)** free-breathing, multiple averages (AVE), **(11C)** free-breathing motion corrected (MOC) binning. Frames are shown for End Diastole (ED) and End Systole (ES).

Discussion and conclusions

The Gadgetron is an open source image reconstruction engine, which has been used extensively for MRI reconstruction. It is a client-server architecture that can be used as a stand-alone desktop image reconstruction system or it can be connected directly to clinical MRI systems by letting the vendor reconstruction act as a Gadgetron client. The internal MRI data format is the open ISMRM Raw Data standard and with converters being available for most major vendors, it can be used as a cross vendor image reconstruction platform. The framework is also cross-platform in the sense that it builds and runs on Windows, Linux, and Mac, which gives researchers flexibility to integrate it into existing work flows and infrastructure. Through the open development model, community contributions are encouraged and merged changes are continuously compiled, tested, and released for the community to use. The Gadgetron build systems produce containerized distributions that come with all necessary dependencies and can be deployed easily.

When used with Siemens Healthcare MRI scanners, a dedicated ICE program (IceGadgetron) can be used to add Gadgetron connectivity to any existing ICE program. The IceGadgetron program manages Gadgetron connection and measurement dependencies in a transparent way and the Gadgetron can be used in a clinical workflow without the need for expert research staff on site. This facilitates deployment of novel reconstruction algorithms in a clinical setting.

The Gadgetron is distributed with a wide range of ready-to-use reconstruction pipelines. These include generic parallel image reconstruction pipelines that support a wide range of parallel imaging strategies, including several commonly used strategies for acquiring calibration data. There are also several specialized reconstruction applications ranging from real-time non-Cartesian parallel imaging using GPU acceleration to cardiac imaging using free-breathing, motion correction strategies.

One of the main aims of the Gadgetron project is to provide the research community with access to completely open source implementations of robust, production quality reconstruction pipelines. The reconstruction components are a good place to start for new researches in the field and they provide a relevant reference point for reconstruction quality comparisons in scientific publications. Community participation is very much encouraged and software patches, bug fixes, and suggestions are welcomed by the growing group of people developing Gadgetron source code. The modularity of the Gadgetron also invites researchers to use it as a deployment vehicle for their own algorithms. The Gadgetron pipeline in combination with the IceGadgetron programs is a practical platform for deploying novel reconstruction algorithms in a clinical environment. External algorithms can be supplied as C/C++, Python, or Matlab code.

In conclusion, the Gadgetron aims to overcome some of the main limitations in current image reconstruction research; it provides open access to algorithm source code, is a rapid prototyping environment, and facilitates clinical deployment for rigorous testing.

References

1 Sodickson DK, Manning WJ. Simultaneous acquisition of spatial harmonics (SMASH): fast imaging with radiofrequency coil arrays. Magn Reson Med. 1997 Oct;38(4):591–603.
2 Pruessmann KP, Weiger M, Scheidegger MB, Boesiger P. SENSE: sensitivity encoding for fast MRI. Magn Reson Med. 1999 Nov;42(5):952–62.
3 Griswold MA, Jakob PM, Heidemann RM, Nittka M, Jellus V, Wang J, et al. Generalized autocalibrating partially parallel acquisitions (GRAPPA). Magn Reson Med. 2002 Jun;47(6):1202–10.
4 Lustig M, Donoho DL, Santos JM, Pauly JM. Compressed sensing MRI. Signal Process Mag IEEE. 2008;25(2):72–82.
5 Hansen MS, Sørensen TS. Gadgetron: An open source framework for medical image reconstruction. Magn Reson Med. 2012 Jul 12;
6 Hansen MS, Kellman P. Image reconstruction: An overview for clinicians. J Magn Reson Imaging. 2014 Jun 25;
7 Sorensen TS, Schaeffter T, Noe KO, Hansen MS. Accelerating the nonequispaced fast Fourier transform on commodity graphics hardware. Med Imaging, IEEE Trans. 2008;27(4):538–47.
8 Hansen MS, Atkinson D, Sorensen TS. Cartesian SENSE and k-t SENSE reconstruction using commodity graphics hardware. Magn Reson Med. 2008;59(3):463–8.
9 Sorensen TS, Atkinson D, Schaeffter T, Hansen MS. Real-time reconstruction of sensitivity encoded radial magnetic resonance imaging using a graphics processing unit. Med Imaging, IEEE Trans. 2009;28(12):1974–85.
10 Inati SJ, Naegele JD, Zwart NR, Roopchansingh V, Lizak MJ, Hansen DC, et al. ISMRM Raw data format: A proposed standard for MRI raw datasets. Magn Reson Med. 2017 Jan;77(1):411–21.
11 Nickolls J, Buck I, Garland M, Skadron K. Scalable parallel programming with CUDA. Queue. 2008 Mar 1;6(2):40.
12 Xue H, Inati S, Sørensen TS, Kellman P, Hansen MS. Distributed MRI reconstruction using gadgetron-based cloud computing. Magn Reson Med. 2015 Mar;73(3):1015–25.
13 Merkel, Dirk. Docker: lightweight Linux containers for consistent development and deployment. Linux J. 2014;2014(239):2.
14 Saybasili H, Kellman P, Griswold MA, Derbyshire JA, Guttman MA. HTGRAPPA: Real-time B 1 -weighted image domain TGRAPPA reconstruction. Magn Reson Med. 2009 Jun;61(6):1425–33.
15 Kellman P, McVeigh ER. Image reconstruction in SNR units: a general method for SNR measurement. Magn Reson Med. 2005 Dec;54(6):1439–47.
16 Kellman P. Erratum to Kellman P, McVeigh ER. Image reconstruction in SNR units: a general method for SNR measurement. Magn Reson Med. 2005;54:1439–1447. Magn Reson Med. 2007 Jul;58(1):211–2.
17 Razavi R, Hill DL, Keevil SF, Miquel ME, Muthurangu V, Hegde S, et al. Cardiac catheterisation guided by MRI in children and adults with congenital heart disease. Lancet. 2003 Dec 6;362(9399): 1877–82.
18 Ratnayaka K, Faranesh AZ, Hansen MS, Stine AM, Halabi M, Barbash IM, et al. Real-time MRI-guided right heart catheterization in adults using passive catheters. Eur Heart J. 2013Feb;34(5):380–9.
19 Kim RJ, Fieno DS, Parrish TB, Harris K, Chen EL, Simonetti O, et al. Relationship of MRI delayed contrast enhancement to irreversible injury, infarct age, and contractile function. Circulation. 1999 Nov 9;100(19):1992–2002.
20 Fieno DS, Kim RJ, Chen EL, Lomasney JW, Klocke FJ, Judd RM. Contrast-enhanced magnetic resonance imaging of myocardium at risk: Distinction between reversible and irreversible injury throughout infarct healing. J Am Coll Cardiol. 2000;36(6):1985–91.
21 Kim RJ, Shah DJ, Judd RM. How we perform delayed enhancement imaging. J Cardiovasc Magn Reson. 2003 Jul;5(3):505–14.
22 Kellman P, Arai AE, McVeigh ER, Aletras AH. Phase-sensitive inversion recovery for detecting myocardial infarction using gadolinium-delayed hyperenhancement. Magn Reson Med. 2002 Feb;47(2):372–83.
23 Ledesma-Carbayo MJ, Kellman P, Arai AE, McVeigh ER, McVeigh ER. Motion corrected free-breathing delayed-enhancement imaging of myocardial infarction using nonrigid registration. J Magn Reson Imaging. 2007 Jul;26(1):184–90.
24 Kellman P, Xue H, Olivieri LJ, Cross RR, Grant EK, Fontana M, et al. Dark blood late enhancement imaging. J Cardiovasc Magn Reson. 2017 Jan 7;18(1):77.
25 Hundley WG, Bluemke DA, Finn JP, Flamm SD, Fogel MA, Friedrich MG, et al. ACCF/ACR/AHA/NASCI/SCMR 2010 Expert Consensus Document on Cardiovascular Magnetic Resonance. J Am Coll Cardiol. 2010 Jun 8;55(23):2614–62.
26 Kellman P, Chefd'hotel C, Lorenz CH, Mancini C, Arai AE, McVeigh ER. Fully automatic, retrospective enhancement of real-time acquired cardiac cine MR images using image-based navigators and respiratory motion-corrected averaging. Magn Reson Med. 2008 Apr;59(4):771–8.
27 Kellman P, Chefd'hotel C, Lorenz CH, Mancini C, Arai AE, McVeigh ER. High spatial and temporal resolution cardiac cine MRI from retrospective reconstruction of data acquired in real time using motion correction and resorting. Magn Reson Med. 2009 Dec;62(6):1557–64.
28 Xue H, Kellman P, LaRocca G, Arai AE, Hansen MS. High spatial and temporal resolution retrospective cine cardiovascular magnetic resonance from shortened free breathing real-time acquisitions. J Cardiovasc Magn Reson. 2013 Nov 14;15(1):102.
29 Hansen MS, Sørensen TS, Arai AE, Kellman P. Retrospective reconstruction of high temporal resolution cine images from real-time MRI using iterative motion correction. Magn Reson Med. 2012Sep;68(3):741–50.
30 Cross R, Olivieri L, O'Brien K, Kellman P, Xue H, Hansen M. Improved workflow for quantification of left ventricular volumes and mass using free-breathing motion corrected cine imaging. J Cardiovasc Magn Reson. 2016 Feb 25;18:10.

Contact

Michael S. Hansen, Ph.D.
Laboratory of Imaging Technology
National Heart, Lung, and
Blood Institute
National Institutes of Health

Building 10 Room B1D405
9000 Rockville Pike
Bethesda, MD 20814
USA
Phone: +1-301-496-1457
Cell: +1-301-412-9671
michael.hansen@nih.gov

MRI at UK Biobank

Niels Oesingmann[1]; Paul M. Matthews[2]; Karla Miller[3]; Stephen Smith[3]; Stefan Neubauer[4]; Steffen E. Petersen[5]; Jimmy Bell[6]

[1] UK Biobank, Stockport, Cheshire, UK
[2] Imperial College, Edmond and Lily Safra Chair, Division of Brain Sciences, Imperial College London, UK
[3] Oxford Centre for Functional Magnetic Resonance Imaging of the Brain (FMRIB), Oxford, UK
[4] John Radcliffe Hospital, Oxford, UK
[5] William Harvey Research Institute, London, UK
[6] University of Westminster, London, UK

Introduction

UK Biobank is a large prospective cohort study designed to understand the causes of common chronic disease with the aim of improving the prevention, diagnosis, and treatment of a wide range of serious and life-threatening illnesses – including cancer, heart diseases, stroke, diabetes, arthritis, osteoporosis, eye disorders, depression, and forms of dementia. UK Biobank recruited 500,000 people aged between 40–69 years in 2006–2010 from across Great Britain to take part in this project. They have undergone a range of physical measures, provided detailed information about themselves, and have given blood, urine, and saliva samples for future analysis. Also, participants agreed to have their health followed throughout their lives through linkage to their medical records. This will help scientists clarify why some people develop particular diseases and others do not.

In 2012, a proposal for an imaging enhancement in 100,000 participants was made to quantify detailed phenotypes that may be associated with disease and enhance the power to detect associations with incident health outcomes. The simultaneous imaging of brain, heart, arteries, abdomen, and bone in each individual participating in the imaging enhancement and the combination of these data would provide a dataset that is uniquely able to allow questions to be addressed regarding the relationships between phenotypes across organ systems and allowing assessment of pathophysiological mechanisms operating at a systemic level. For example, the relationships between obesity and aging-related macrostructural brain changes with later-life cognitive dysfunction [1] may suggest specific mechanisms and associations with incident disease and need further exploration in much larger datasets. Such correlations, which are based on prevalent disease, also need to be extended to studies of the associations of pre-symptomatic measures of body phenotype (e.g. body MRI and dual-energy X-ray absorptiometry (DXA)) with future brain health outcomes. The potential to relate longer term clinical and cognitive dysfunction outcomes to sensitive brain structural and functional markers, cardiac and body composition phenotypes (as well as to information on blood markers, lifestyle, and clinical history) would allow new depths of exploration of risk and pathogenic mechanisms, and the generation of new hypotheses regarding possible modifying factors. In the shorter term, value of the imaging enhancements in UK Biobank can be realised through cross-sectional case-control studies, e.g., relating brain imaging differences to prevalent brain disease or to independent phenotypic measures.

The pilot phase of imaging 5,500 participants was completed in September 2015. Further funding allowed for the main phase to start in 2016. In total, over 14,000 participants have already been scanned and imaging data from 10,000 subjects has been released for use by the international research community (http://www.ukbiobank.ac.uk/2017/02/new-data-from-brain-imaging-and-on-heart-attacks-and-strokes-available/). As many as 100 research groups are accessing the imaging data for their research.

The imaging methods employed are: magnetic resonance imaging (MRI), carotid ultrasound, and dual-energy X-ray absorptiometry. For MRI, three specific areas of interest were identified: brain, heart, and body imaging. The specifics of each MR application are described in the following sections.

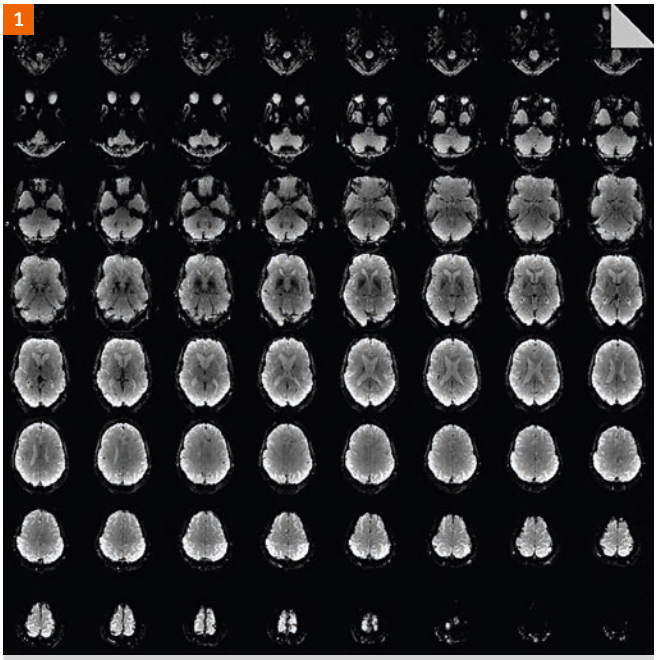

Figure 1: fMRI time point with simultaneous excitation of 8 slices.

MR imaging

To meet the temporal, financial, and geographic constraints of scanning 100,000 participants, the measurements are made in three different locations each fitted with two scanners (one 3T MAGNETOM Skyra and one 1.5T MAGNETOM Aera). Scanning sites were selected to allow maximize volunteer recruitment from UK Biobank participants across the UK. Currently, the primary site in Stockport, near Manchester, UK, is running with an average of 17 participants scanned per day (strictly within 12 h) on 7 days per week. The second site in Newcastle, UK, will be operational in April 2017 using the identical software and protocols. A third site in Reading, UK, will receive participants at the end of 2017. The brain program runs for about 30 minutes exclusively on the 3T systems, while an integrated body and cardiac program is measured on the 1.5T scanners for 10 and 20 minutes, respectively.

Major challenges, as one might expect, centre on the selection of the specific applications within each body region, the choice of measurement techniques, and the setting of protocol parameters. The need for data harmonization means that these decisions, which were made based on experience in the pilot phase, will be applied for all data acquisition in the next phase of development of the resource. Many developers and subject matter experts worldwide have contributed to the selection and optimization of the final imaging sequences and data management. An externally chaired imaging working group (constituted from leading UK academic researchers in relevant areas) has been responsible for the design of the imaging enhancements. Pre-piloting the feasibility of the proposed imaging protocols for each of the separate elements of the imaging assessment visit informed the final program further. There has also been careful consideration and consultation on the issue of providing feedback on incidental findings from imaging, including the implementation of a prospective study of unexpected findings of potential medical significance and both their clinical consequences and impact on lives of the volunteers affected.

Considerable effort within and outside Biobank is devoted to data transfer and security. This includes the encoding and separation of personal information to allow complete DICOM streams to be provided.

Along with the protocol for examinations, a quality assurance procedure was developed. There are three different quality aspects to consider over time: the status of the scanners, the actual scanning of participants, and the evaluation of data. The first aspect is realized by a regular high resolution phantom scan which detects B_0 and B_1 variations of the hardware as early as possible. Close cooperation with the service department is important in order to resolve potential issues as fast as possible and the proactive effort of the service employees is much appreciated. The second aspect requires the active participation of radiographers in an unconventional way. The scan protocol must change as little as possible while the circumstances and constancy of parameters must be checked as often as possible. While the orientation and position of an oblique protocol is slightly adjusted to the tilt of the head, none of the other scan parameters are modified. This also means, for example, that exactly 6 stages for the complete body are scanned irrespective of the height of the participant. This is a consequence of the decisions to keep both the measurement and acquisition time fixed. Hence, one must not underestimate the role of education and the challenges of an environment where the creative optimization and adjustment of protocols to the subject are neither desirable nor permitted. Tools are currently being developed to provide automatic checks against constancy of relevant parameters. The third aspect requires an evaluation of the resulting scans via the review of a number of defined image parameters. This depends on the evaluation chain of developers and it is important to establish a close feedback process.

Brain imaging

The brain MRI protocol will provide researchers with data concerning both brain structure and function from a single, short examination, including data to reconstruct the major white matter connection pathways. Each participant undergoes a 32-minute brain MRI protocol using a 3 Tesla MAGNETOM Skyra. This provides T1- and T2-weighted FLAIR structural 3D MRI, functional MRI during rest and task performance, whole-brain diffusion tensor imaging, susceptibility-weighted imaging (SWI), and arterial spin labeling (ASL).

The brain program comprises the following protocols:

- AutoAlign Scout images
- T1-weighted structural morphology MPRAGE with iPAT 2
- fMRI resting state protocol with simultaneous excitation of 8 slices
- fMRI task performance protocol with simultaneous excitation of 8 slices
- T2-weighted 3D FLAIR with iPAT 2
- Diffusion AP b = 0, b = 2 ms/μm^2 with 6 directions and simultaneous excitation of 3 slices
- Diffusion PA b = 0, 104 directions in total distributed over two shells with b = 1 and 2 ms/μm^2 with simultaneous excitation of 3 slices
- 3D SWI iPAT 2
- 3D pcASL

Highly efficient scanning protocols are needed to allow the full range of imaging and other phenotype measures to be obtained on each volunteer. To perform this imaging program within the limited time allocated, the use of acceleration techniques, in particular the simultaneous excitation of multiple slices, is required. It is also apparent

that the acquisition of data is tuned to the minimum required while the data quality and contrast aims to be the best per unit time of acquisition.

Cardiac imaging

Cardiovascular MRI is considered the most versatile and precise technique for simultaneous assessment of multiple cardiac parameters. Its reproducibility and non-invasiveness are key advantages for large-scale population studies over other imaging modalities such as echocardiography. An additional attractive feature for large scale population studies is that volunteers are not subjected to any potentially harmful radiation (as with cardiac CT). A major strength of CMR is the ability to obtain multi-parametric images in one imaging session related to both structure and function of the heart. A 20-minute protocol using a 1.5 Tesla scanner provides time-dependent heart chamber volumes, cardiac wall thickness and mass, tissue motion using tagging, and aortic size and compliance. In addition, the aortic flow quantitation is performed and the myocardial T1 is estimated.

The cardiovascular program consists of the following protocols:

- Cine scanning of the left ventricular long and short axis views
- Cine scan of the left ventricular outflow tract with ascending aorta
- Cine tagging of 3 short axis planes around the middle of the left ventricle
- Cine cross section of ascending aorta and proximal descending aorta
- Through-plane flow measurement of ascending aorta
- T1 mapping of mid-ventricular slice

Body imaging

There are a number of methods for estimating body fat content (such as the BMI, waist-hip circumference, and bio-impedance measures already included in UK Biobank). However, such estimates are imprecise (although still have predictive power) and cannot be used to assess adipose tissue distribution, which is both an individually distinctive phenotype and a determinant of relative disease risk. MRI can provide much more accurate information on fat content and distribution, muscle mass, and organ volume. A wide variation has been found between individuals in the amount of visceral, muscle, and liver fat for any given body mass index (BMI), waist-to-hip ratio (WHR), and total amount of body fat [5]. There is increasing evidence to suggest that fat distribution, rather than amount of fat, is important for determining an individual's risk of future disease [2, 3]. Body MRI provides an opportunity to examine the predictive importance of particular fat deposits (visceral, liver and pancreas) and the relative distribution of fat for the development of particular conditions (e.g. vascular disease, diabetes, and certain types of cancer). The 10-minute protocol on a 1.5 Tesla scanner provides quantitative information on subcutaneous-abdominal and visceral adipose tissue volumes and distribution and on intra-hepatocellular and intra-pancreatic lipid.

The body program comprises the following protocols:

- Dixon imaging of 6 contiguous stages beginning from neck downwards to the knees
- T1-weighted VIBE of pancreas

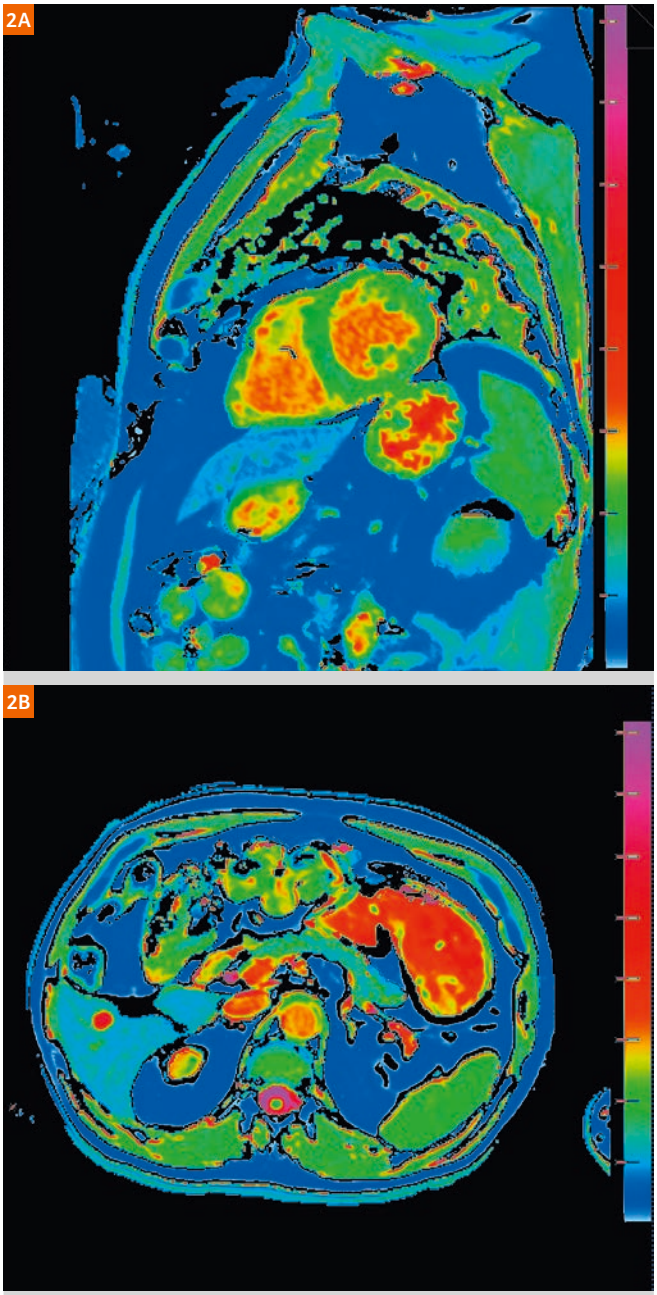

Figure 2: Computed T1 maps of heart and pancreas after acquisition of shMOLLI.

- T1 mapping of mid-liver axial cross-section
- T2*-weighted multi-echo imaging of liver cross-section
- T1-mapping of pancreas cross-section
- T2*-weighted multi-echo imaging of pancreas cross-section

Summary

The multi-modal imaging enhancement of 100,000 UK Biobank participants is well underway. This brief article presents an overview of the measurements within 1 hour of scan time with excellent quality. This, however, requires a strict regime of timing and scheduling to be performed successfully. UK Biobank solved a variety of challenges related to the infrastructure and logistics of the daily throughput. We would like to further stimulate the interest of researchers in using the unique dataset for research for many years to come. It is our hope that the community finds the data (depth, breadth, and quality) useful in answering a range of research questions.

The data and information UK Biobank presents is the result of the work of many people. The developers who programmed the sequences and those who provided the programming environment in the first place are as important as the final authors of the research publications that make use of the measurements. The insight and vision of funders provide a sound backbone of the activities of the many different departments of UK Biobank; MR images are now an exciting part of the growing data set within the UK Biobank data repository. We would like to thank and acknowledge the many contributors to this work inside and outside of UK Biobank. Specifically the use of the multiband implementation from CMRR (University of Minnesota) and the pcASL sequence from Fraunhofer MEVIS are acknowledged.

References

1 Stanek HM. Grieve SM, Brickman AM, et al. Obesity is associated with reduced white matter integrity in otherwise healthy adults. Obesity 2011; 19: 500-4.
2 Goldstone AP, Thomas EL, Brynes AE, et al. Elevated fasting plasma ghrelin in Prader–Willi syndrome adults is not solely explained by their reduced visceral adiposity and insulin resistance. J Clin Endocrinol Metab 2004; 89: 1718-26.
3 Thomas EL, Parkinson JR, Frost G, et al. The missing risk: MRI and MRS phenotyping of abdominal adiposity and ectopic fat. Obesity 2012; 20: 76-87.
4 Thomas EL, Hamilton G, Patel N, et al. Hepatic triglyceride content and its relation to body adiposity: a magnetic resonance imaging and proton magnetic resonance spectroscopy study. Gut 2005; 54: 122-7.
5 Thomas EL, Bell JD. Influence of undersampling on magnetic resonance imaging measurements of intra–abdominal adipose tissue. Int J Obes Relat Metab Disord 2003; 27: 211-8.

Further information

A primary portal for information on UK Biobank and how to access the data, which is available for all researchers, is:	www.ukbiobank.ac.uk/
In 2016, several milestones were achieved. Together, these describe the developing resource well:	www.ukbiobank.ac.uk/2016/11/scanning-study-launched/ www.ukbiobank.ac.uk/2016/09/brain-imaging-results-from-5000-subjects/ www.ukbiobank.ac.uk/2016/03/uk-biobank-looking-at-the-whole-person
Reports presented in annual UK Biobank meeting (2016) can be accessed through:	www.ukbiobank.ac.uk/listen-again-annual-meetings/
The actual publications can be found easily with a specific search term, for example, the cardiac, abdominal, and neuro publications, respectively, are listed here:	www.ukbiobank.ac.uk/published-papers/?tps=cardiac&tps_button=Search www.ukbiobank.ac.uk/published-papers/?tps=body&tps_button=Search www.ukbiobank.ac.uk/published-papers/?tps=neuro&tps_button=Search
Information on how to access the DICOM data and how to apply for downloading keys can be found at:	www.ukbiobank.ac.uk/register-apply/

Contact

Niels Oesingmann, Ph.D.
MR Physicist
UK Biobank

Units 1–4 Spectrum Way, Adswood
Stockport, Cheshire, SK3 0SA, UK
Phone: +44 (0)161.475 5360
Direct: +44 (0)161.475 1423
Mobile: +1 347.443 4328
Fax: +44 (0)161 475 5361
Niels.Oesingmann@ukbiobank.ac.uk

Professor Paul M. Matthews OBE, MD, DPhil, FRCP, FMedSci
Head of the Imaging Working Group
Imperial College London, Faculty of Medicine
Edmond and Lily Safra Chair
Head of Brain Sciences Division

E515
Burlington Danes
Hammersmith Campus

London SW7 2AZ, UK
Phone: +44 (0)20 7594 2855
P.Matthews@imperial.ac.uk

Meet Siemens Healthineers

Our brand name Siemens Healthineers embodies our pioneering spirit and engineering expertise in the healthcare industry. The people working for Siemens Healthineers are highly passionate about the technology and the company they work for and their engineering capabilities and pioneering spirit are unique in this industry. In this section we introduce colleagues from all over the world to you – people who put their hearts into what they do.

Edgar Müller

Erlangen, Germany

Edgar Müller graduated in physics from the University of Stuttgart, Germany in 1983. Straight after, he joined Siemens in Erlangen to participate in the development of first-generation MRI systems. In the early years, up to 1991, he developed the first Siemens local coil (breast coil) and the first sequences for flow quantification. Later Edgar headed a neuro-functional MR team that developed fMRI and DTI sequences and post-processing software. This period also saw the strengthening of a huge cooperational network. Between 2005 and 2016 Edgar headed global cardiovascular MRI Applications development. Highlights of this period included the initiation of workflow prototypes, leading to the development of Dot engines.

Since November 2016 Edgar has been Head of the Siemens MR Technology and Innovation Management Team that encompasses MR innovation and IP management, the MR technology incubator and the key expert network. Besides being responsible for the MR innovation process across all clinical imaging and technology fields, Edgar and his team establish and manage large-scale strategic collaborations that focus on the development and validation of hardware innovations or groundbreaking new applications such as Compressed Sensing or MR Fingerprinting.

How did you first come in contact with MRI?
While completing my master thesis in physics, I heard about a fascinating new possibility to obtain images from the human body with a new method based on magnetic resonance. At that time Siemens had launched a huge program to develop MRI and I successfully applied for a job in Erlangen at the age of 26 years. I have had the privilege of being involved from the very first Siemens product operating at 0.35 Tesla in 1983 through many generations of MRI scanners to the present system portfolio.

What is most motivating about your job?
If you compare MRI to other imaging modalities, there is a fundamental difference: while other modalities rely on more or less one physics observable (e.g. attenuation of X-rays) MRI images are influenced by many independent physics observables: human tissue differs in relaxation times T1, T2, diffusion properties, chemical shift, magnetization transfer, velocity behavior, magnetic susceptibility, to name just a few important ones. This allows us to design pulse sequences, which can create virtually every desired imaging contrast between different tissues. There is a brilliant physics and technology behind MRI which is hugely fascinating not only for me, but for many colleagues I have had the privilege to work alongside.

But what has most motivated at a personal level is the outstanding friendships I have forged with people working with the same spirit of innovation over decades: within Siemens as well as at many institutions worldwide, where we were able to brainstorm and realize things that people could scarcely have contemplated just a few years earlier.

What do you think are the most important developments in MRI?
The current reality is that more than 90% of all MRI procedures are covered by innovations from the 1980's, like affordable high-field superconducting magnets including high-quality gradient and RF hardware, accompanied by inventions of fast imaging sequences like Turbo Spin Echo and FISP/FLASH.

What we experienced then was a race in magnetic field strength, followed by a decade of gradient power and then a decade of RF channel density. However, I sense that we are now at the dawn of a new age in MRI, which will be driven by the use of artificial intelligence, deep learning methods, cloud computing, etc. This will guide us to MRI scanners that are really simple to use, robust, and fast.

What would you do, if you could do for one month whatever you wanted?
There is nothing I could wish for, since I have always had the freedom to do just what I wanted to do in my professional life. For example, in October 1991 I heard about fascinating experiments going on in both the USA and in the UK with regard to fMRI. What started out as a hobby became my official profession at Siemens MR in 1992. What followed where the most wonderful ten years of my professional life. I was able to ramp up a research team under the guidance of former Siemens Healthcare CEO Hermann Requardt and we had total freedom in what we developed, with successful outcomes. When we came up with first ideas about Compressed Sensing, my former boss Christoph Zindel realized the potential immediately and again I could do for years exactly what I wanted to do.

My private life is a completely different world. At home there is a wonderful woman to whom I have been married for more than 35 years, six children – three girls and three boys aged between 16 and 35. All the interaction with them and with their partners keeps me busy and young. And there are hobbies, which I wish I could devote more time to: I like hiking and skiing in the mountains, having grown up close to the Austrian Alps; listening to pop music by bands such as Dire Straits; and still occasionally playing the piano, which had been a big hobby in my youth. And, last but not least, playing chess and reading good books such as Astrid Lindgren's "Karlsson on the Roof".

Aurélien Stalder is from Geneva, in the French-speaking part of Switzerland and has joint French and Swiss citizenship. He graduated in micro-engineering from EPFL in Lausanne, Switzerland in 2005. He then studied for his Ph.D. in the field of 4D Flow MRI at the University of Freiburg, Germany. In 2009, he was awarded an EU Science and Technology Fellowship to undertake a two-year post-doctoral research program at the Xuanwu Hospital in Beijing, China. Aurélien joined Siemens in 2011, as application developer in Erlangen and participated in the predevelopment of some new key technologies such as quiet MRI or compressed sensing MRA. Based on his extensive knowledge of the MRI research and of the academic world in China, he took over the lead of the Siemens Healthineers MR Collaboration team for Greater China in 2015.

Shanghai, China

How did you first come in contact with MRI?
Following my master's thesis in image processing, I was looking for a Ph.D. position in biomedical imaging. Michael Markl introduced me to the exciting research work on 4D Flow MRI that he was leading in Freiburg within the Jürgen Hennig group. I was captivated by the possibilities offered by MR and delighted to join their team.

What fascinates you most about MRI?
The incredible quantity of information and imaging contrasts that MR can produce both for anatomy and function. The possibilities seem endless, and the research community keeps working to improve existing MR contrast mechanisms and discover new ones. For me, this really makes MRI stand out among all other imaging modalities.

What do you think are the most important developments in Healthcare?
We are moving toward the integration of all possible sources of patient data and information to provide the best patient screening, diagnostic, and treatment. Artificial intelligence will play a key role in helping radiologists and doctors integrate this growing quantity of information. I believe that MRI will play a central role here due to the vast range of image contrasts and the quantitative information it can produce, while being non-invasive and radiation-free.

What motivates you most about your job?
Each day I meet people that share the same passion for MRI. My heart is with MRI so I may be biased, but I see no other modality where people share such a strong fascination for the technology they use. It is a passion that crosses many borders, shared by clinicians, engineers, technicians, and physicists. The commitment that I see from our collaboration partners in China is incredible. Some are still developing their research experience, but they work hard – often alongside the collaboration scientists in my team – to bring MRI to the next step!

What are the biggest challenges in your job?
First and foremost, communications! And here I also include intercultural aspects. Everyone – no matter what their mother tongue is – express themselves differently due to our cultural differences, which is important to understand and respect. The role of my team is to act as the interface between MR research sites in greater China, Siemens Healthcare in China, and the predevelopment and R&D teams in our headquarter in Erlangen, Germany. For our projects it is very important that, for example, a developer in Germany understands the goals of a Chinese doctor and vice-versa. I have lived in China for over 3 years now (2 years for my post-doc, 1.5 years in my current role) and speak decent Chinese; this helps me a lot to understand what our Chinese partners expect.

What would you do, if you could do for one month whatever you wanted?
Like every Healthineer, I would like to spend time in a clinical setting. Learning more about the daily clinical routine and the important clinical challenges. Although I visit customers almost every week, I feel that there is always more to learn.

However, if I had this free time now, I would probably travel through Europe with my fiancé. I would love to have the time to travel by bike and visit our friends all over Europe. I like very much traveling and I have been to many countries already. When I lived in Switzerland or Germany, I often travelled to exotic destinations, such as China. Now, living in China, where everything moves at an incredible pace, it would be a great contrast to take the time to travel at a slower pace through Europe.

The entire editorial staff at University Hospital Tübingen and at Siemens Healthineers extends their appreciation to all the radiologists, technologists, physicists, experts, and scholars who donate their time and energy – without payment – in order to share their expertise with the readers of MAGNETOM Flash.

MAGNETOM Flash – Imprint

Publisher:
Siemens Healthcare GmbH
Magnetic Resonance,
Karl-Schall-Str. 6, D-91052 Erlangen, Germany

Editor-in-chief:
Antje Hellwich
(antje.hellwich@siemens-healthineers.com)

Guest Editor:
Professor Konstantin Nikolaou
University Hospital Tübingen
Diagnostic and Interventional Radiology
Hoppe-Seyler-Str. 3
72076 Tübingen
Germany

Editorial Board:
Reto Merges; Wellesley Were; Sunil Kumar S.L., Ph.D.; Gary R. McNeal, MS (BME)

Review Board:
Lisa Chuah, Ph.D.; Daniel Fischer; Berthold Kiefer, Ph.D.; Heiko Meyer, Ph.D.; Efren Ojeda; Gregor Thörmer, Ph.D.

Production:
Norbert Moser,
Siemens Healthcare GmbH

Layout:
Agentur Baumgärtner,
Friedrichstr. 4, D-90762 Fürth, Germany

Printer:
G. Peschke Druckerei GmbH,
Taxetstr. 4, D-85599 Parsdorf b. Munich, Germany

Note in accordance with § 33 Para.1 of the German Federal Data Protection Law: Despatch is made using an address file which is maintained with the aid of an automated data processing system.

MAGNETOM Flash is sent free of charge to Siemens MR customers, qualified physicians, technologists, physicists and radiology departments throughout the world. It includes reports in the English language on magnetic resonance: diagnostic and therapeutic methods and their application as well as results and experience gained with corresponding systems and solutions. It introduces from case to case new principles and procedures and discusses their clinical potential. The statements and views of the authors in the individual contributions do not necessarily reflect the opinion of the publisher.

The information presented in these articles and case reports is for illustration only and is not intended to be relied upon by the reader for instruction as to the practice of medicine. Any health care practitioner reading this information is reminded that they must use their own learning, training and expertise in dealing with their individual patients. This material does not substitute for that duty and is not intended by Siemens Healthcare to be used for any purpose in that regard. The drugs and doses mentioned herein are consistent with the approval labeling for uses and/or indications of the drug. The treating physician bears the sole responsibility for the diagnosis and treatment of patients, including drugs and doses prescribed in connection with such use. The Operating Instructions must always be strictly followed when operating the MR system. The sources for the technical data are the corresponding data sheets. Results may vary.

Partial reproduction in printed form of individual contributions is permitted, provided the customary bibliographical data such as author's name and title of the contribution as well as year, issue number and pages of MAGNETOM Flash are named, but the editors request that two copies be sent to them. The written consent of the authors and publisher is required for the complete reprinting of an article.

We welcome your questions and comments about the editorial content of MAGNETOM Flash. Please contact us at magnetomworld.med@siemens.com.

Manuscripts as well as suggestions, proposals and information are always welcome; they are carefully examined and submitted to the editorial board for attention. MAGNETOM Flash is not responsible for loss, damage, or any other injury to unsolicited manuscripts or other materials. We reserve the right to edit for clarity, accuracy, and space. Include your name, address, and phone number and send to the editors, address above.

MAGNETOM Flash is also available online:

www.siemens.com/magnetom-world

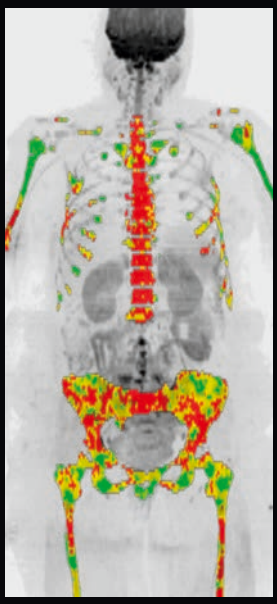

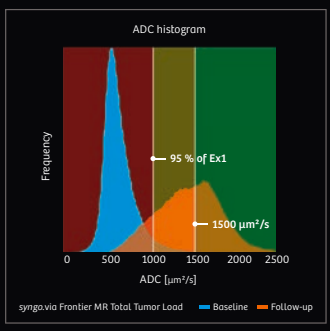

MAGNETOM Flash

Issue Number 68, 2/2017
ISMRM Edition

siemens.com/magnetom-world

SIEMENS Healthineers

Please enter your business address

Institution
Department
Function
Title
Name
Street
Postal Code
City
State
Country
MR system used

Please include me in your mailing list for the following Siemens Healthcare customer magazine(s):

☐ MAGNETOM Flash
☐ SOMATOM Sessions
☐ Imaging Life
☐ AXIOM Innovations
☐ Go HYBRID!

Stay up to date with the latest information
Register for:

E-mail

☐ Yes, I consent to the above information being used for future contact regarding product updates and other important news from Siemens.
☐ unsubscribe from info service

Please print clearly!

→ **Visit www.siemens.com/magnetom-world** for case reports, clinical methods, application tips, talks and much more clinical information.

Subscribe now!

– and get your free copy of future MAGNETOM Flash!

Relevant information from the world of magnetic resonance – gratis to your desk. Send us this postcard, or subscribe online at

www.siemens.com/magnetom-world

Siemens Healthcare GmbH
Antje Hellwich
HC DI MR CRM SCI
Karl-Schall-Str. 6
91052 Erlangen
Germany

MAGNETOM Flash

On account of certain regional limitations of sales rights and service availability, we cannot guarantee that all products included in this brochure are available through the Siemens sales organization worldwide. Availability and packaging may vary by country and is subject to change without prior notice. Some/All of the features and products described herein may not be available in the United States.

The information in this document contains general technical descriptions of specifications and options as well as standard and optional features which do not always have to be present in individual cases, and which may not be commercially available in all countries.

Due to regulatory reasons their future availability cannot be guaranteed. Please contact your local Siemens organization for further details.

Siemens reserves the right to modify the design, packaging, specifications, and options described herein without prior notice. Please contact your local Siemens sales representative for the most current information.

Note: Any technical data contained in this document may vary within defined tolerances. Original images always lose a certain amount of detail when reproduced.

Siemens Healthineers Headquarters
Siemens Healthcare GmbH
Henkestr. 127
91052 Erlangen
Germany
Phone: +49 9131 84 0
siemens.com/healthineers

A91MR-1000-125M-7600 Printed in Germany | PS MR 4716 041710.